The Explosion and Dispersion Potential of Engineered Nanoparticles

By

Georgios Fokion Kylafis

Submitted in accordance with the requirements for the degree of
Doctor of Philosophy

The University of Leeds
Energy Research Institute
School of Chemical and Process Engineering

September, 2016

The candidate confirms that the work submitted is his own and that appropriate credit has been given where reference has been made to the work of others.

Acknowledgements

I would like to forward my thanks to my supervisors Prof Tomlin, A., Dr Sleigh, A. and Dr Lawes, M. for their support, directions and valuable discussions throughout the period of this study. My thanks are also forward to Dr Biskos, G. (TU Delft) for his valuable assistance and discussion during the period conducting the experimental work. I also wish to thank departmental colleagues who have provided invaluable practical assistance and support over the past four years, including Francis Emejeamara and Ben Thorne. In addition, I would like to thank Mr Chris Nickolaus (Cambustion Ltd) who was always there to provide me with his high technical knowledge on issues related to specific particulate instrumentation used in this work. I am also grateful for the financial support provided for this research by the EU through the 7th Framework Programme (managing risks of nanoparticles, MARINA).

I would also like to thank my friends for their unending support, their patience and tolerance during the ups and downs I experienced while carrying out this work. Finally I would like to thank my family, especially my Mum and Dad, to whom I am indebted, as they have provided me with permanent support, encouragement and motivation throughout the whole of my education.

Presentation of work

Conferences attended:

- Oral Presentation at the Nanosafety Forum for Young Scientists, 8-9 October, 2014, Sicily (Italy)
  Paper Title: Accidental release and dispersion of engineered nanoparticles: an example of the dispersion of TiO_2 nanopowder within indoor environments.
- Oral Presentation at the 4th Annual Postgraduate Symposium on Nanotechnology, 15 December, 2015, School of Chemistry, University of Birmingham.
  Paper Title: Accidental release and dispersion of engineered nanoparticles: dispersion of TiO_2 nanopowder within an indoor environment.
- Oral Presentation at the Cambridge Particle Meeting, 3 July, 2015, University of Cambridge, Department of Engineering.
  Paper Title: Accidental release and dispersion of engineered nanoparticles: an example of the dispersion of TiO_2 nanopowder within indoor environments.
- Poster Presentation at the final Marina-NanoValid Conference, 29-30 September, 2015, OECD Conference Center, Paris.
  Paper Title: Accidental release and dispersion of engineered nanoparticles: an example of the dispersion of TiO_2 nanopowder within indoor environments.

Abstract

This work investigates the explosion and dispersion potential of engineered nanoparticles (ENP). The European Union (EU) sponsored this investigation, firstly to predict or estimate risks posed by the use of engineered nanomaterials (ENM), and secondly to implement procedures for the purpose of risk mitigation. These include establishing exposure control limits and controlling and monitoring exposure, including the accidental explosive or massive release of ENP into the environment.

To this end, the release of ENP originating from specific nanopowders was simulated in a 31 m^3 airtight chamber of controllable environment. Their loss and dispersion characteristics were studied under ventilated and unventilated conditions. The explosion characteristics of specific ENP in lean hybrid blends of nanoparticles with methane and air, were studied in a 23 L cylindrical combustion vessel providing the adjustment of isotropic turbulence induced by specially designed fans. The influence of ENP on the explosion severity was evaluated by comparing the results obtained for pure methane explosions. Via a 6-jet Collison nebuliser (CN) combined with a considerably modified preparatory process of the tested nanopowders suspensions in water, ENP of Titanium and Silica Dioxide (TiO_2 and SiO_2) were injected continuously into the dispersion chamber. A specially designed dust injector was used for the introduction of two types of carbon black (CB) nanopowders (Corax N550 and Printex XE2) into the combustion vessel. An arrangement of particulate instrumentation was applied for tracking the evolution of particle number concentration (PNC) and particle size distribution (PSD) at points near to the source within the dispersion chamber. In addition, PSD measurements were conducted in the dust clouds generated for the explosion tests. Using a Log_{10}-normal modal fitting program, the characteristics of groups present within the PSDs, were mathematically described. An indoor aerosol model for the study of the differential effect of coagulation and deposition on the changes of PNC with time in the dispersion chamber, was applied. Finally, the explosion severity was characterised by measurements of the explosion pressure history and of flame speed derived from high speed Schlieren cine photographs.

Results indicated that by reducing the ventilation rate the leftover PNC of ultrafine particles (diameter ≤ 100 nm) was gradually increased at the end of the evacuation process. In parallel, at the high ventilation rates the spatial ventilation efficiency was shown to be optimal close to the inlet diffuser. However, by decreasing the ventilation rate, ventilation efficiency was shown to be independent of the location in the chamber. The study of particle interactions under unventilated conditions indicated that different growth rates due to agglomeration were induced on the two types of dispersed ENP. For fine particles (diameter > 100 nm) of both

materials, the model indicated that their losses were dominated by deposition at high PNC, whereas for ultrafine particles, heterogeneous coagulation was the main removal mechanism. However, the model indicated stronger deposition at low PNC, and weaker homogeneous coagulation at high PNC, for ultrafine and fine SiO_2 particles respectively, compared to their TiO_2 counterparts. The explosion tests indicated that the addition of variable concentrations of ENP in methane resulted in higher burning rates and flame acceleration than those demonstrated by the respective particle-free methane air mixtures. In addition, the mixture of the highest fraction in ultrafine ENP yielded the most severe explosion, while this mixture was of the lowest dust concentration. Finally, hybrid mixtures with methane below its lower flammability limit (LFL) were shown to be ignitable. Furthermore, the level of this extension below LFL was shown to be dependent to the material as different extensions were performed by Corax N550 and Printex XE2 hybrid mixtures.

The investigation recommends that in order to design efficient ventilation systems for nanotechnology workplace, only specific ventilation rates and arrangements of inlet/outlet diffusers, should be considered. Exposure to accidentally released ENP is expected to be different for different materials and strongly related to their emission profile. Finally, the generation of a dust cloud from a minor amount of a nanopowder combined with a low amount of a flammable gas and an electrostatic spark may result in a severe explosion of higher impacts for human health and installations than those induced by the explosion of a higher dust concentration hybrid mixture. Also this work demonstrated that as the mean particle size in the dust cloud decreases, a hybrid mixture of an extremely low content of gas could become ignitable. The latter could be applicable not only in the field relating to the risk assessment of ENP but also in generic technological applications involving airborne nanoparticles (e.g. soot particles) suspended in flammable gases (e.g. automotive applications that use natural gas).

Table of Contents

List of Tables

List of Figures

Nomenclature

A		
	ACH	Air Changes per Hour
	ADC	Analogue Digital Converter
	APS	Aerodynamic Particle Sizer
	Al_2O_3	Aluminium Oxide
	ACGIH	American Conference of Governmental Industrial Hygienists
B		
	BG	Background particles
C		
	C	Concentration
	CB	Carbon Black
	CFE	Cold Field Emission
	CN	Collison Nebuliser
	CMD	Count Mean Diameter (nm)
	CoagS	Coagulation Sink (s^{-1})
	CPC	Condensation Particle Counter
D		
	D	Diffusion Coefficient ($cm^2\ s^{-1}$)
	d	Particle Diameter (nm)
	d_p	Particle Diameter based on Electrical Mobility (nm)
	D_{real}	Dispersibility of powder
	DLS	Dynamic Light Scattering
	DMA	Differential Mobility Analyser
	DMS	Differential Mobility Spectrometer
	dP/dt_{max}	Peak maximum rate of pressure rise ($bars^{-1}$)
E		
	E	Relative ventilation efficiency
	EEPS	Engine Exhaust Particle Analyser
	ENP	Engineered Nanoparticles
	ENM	Engineered Nanomaterials
	EPA	Environmental Protection Agency
	ELPI	Electrical Low Pressure Impactor
F		
	FDV	File and Discharge Valve
	FEG	Field Emission Gun
	FMPS	Fast Mobility Particle Sizer
	FeO(OH)	Iron Oxide-Hydroxide
H		
	HHCPC	Handheld Condensation Particle Counter
	HOE	Heat of Explosion (cal/gram)
I		
	IPHE	Institute for Public Health Environment
J		
	J_{d1}	Measured Particle Formation Rate ($cm^{-3}\ s^{-1}$)
	JRC	Joint Research Center

K

K_{st}	Volume invariant dust explosion severity index
$K_{i,j}$	Coagulation Coefficient ($cm^3\ s^{-1}$)
Kn	Knudsen Number
*k**	Efficiency factor
k	Boltzmann's constant

L

LFL	Lower Flammability Limit
LDMA	Long Differential Mobility Analyser
LPM	Litres Per Minute

M

m_g	Mass of gaseous species
mPNC	modal Particle Number Concentration (cm^{-3})
M_g	Average molecular weight of gaseous species
MEC	Minimum Explosible dust Concentration
MIE	Minimum Ignition Energy (J)
MOUDI	Micron-Orifice Uniform Deposit Impactor
$Mg_3Si_4O_{10}(OH)_2$	Magnesium Silicate Hydroxide
MWCNT	Multi-walled Carbon Nanotube
MV	Mixing Ventilation

N

n_g	Moles of gaseous species
N	Number
NP	Nanoparticle
NDMA	Nano-Differential Mobility Analyser
NIOSH	National Institute of Occupational Health
NIST	National Institute of Standards and Technology

O

OPC	Optical Particle Counter

P

P	Absolute pressure
P_{max}	Peak maximum explosion pressure (bar)
Pt	Platinum
PPE	Personal Protective Equipment
PMC	Particle Mass Concentration ($\mu g\ m^{-3}$)
PNC	Particle Number Concentration (cm^{-3})
PSD	Particle Number Size Distribution
PSU	Power Supply Unit

R

r_{sch}	Schlieren radius
R	Universal gas constant ($JK^{-1}mol^{-1}$)
RD	Rotating Drum
RNG	Re-normalisation Group model
RSM	Reynold Stress Model

S

S	Source rate (particles/s)
SEM	Scanning Electron Microscopy

	SiO_2	Silica Dioxide
	SWCNT	Single-walled Carbon Nanotube
	SMPS	Scanning Mobility Particle Sizer
T		
	T	Temperature (°C or K)
	TiO_2	Titanium Dioxide
	TEM	Transmission Electron Microscopy
	t	Time (s)
U		
	u’	Root mean square (rms) velocity (ms^{-1})
	u·	Friction velocity
	USA	United States of America
	UFAD	Underfloor and Distribution System
V		
	V	Volume
	VS	Vortex Shaker
W		
	W_{min}	Total minimum work
Z		
	ZnO	Zinc Oxide

Greek Symbols

α	air change rate (h^{-1})
β	Particle decay rate (h^{-1})
λ_{air}	Air Mean Free Path
μ*	Mean
μ	Viscosity ($cm^{-1}\ s^{-1}$)
π	Mathematical Constant ~ 3.14 (2 d.p.)
ρ	Particle Density ($g\ cm^{-3}$)
σ	Standard Deviation
σ_g	Geometric Standard Deviation

Common Technical Descriptive Terms

Aerosol	A suspension of solid or liquid (or a mixture of both) particles in the air
Accumulation Mode	A mode of particles $100 < d \leq 1000$ nm formed primarily by coagulation of smaller particles
Aerodynamic Diameter	Diameter of a unit-density sphere having the same gravitational settling velocity as the particle in question
Agglomerate	a collection of loosely bound particles or aggregates or mixtures of the two held together by weak forces where the resulting external surface area is similar to the sum of the surface areas of the individual components
Aggregate	a collection of particles bind strongly to each other such that their total surface is less than the sum of surfaces of the individual particles
Aitken Mode	Particles $25 < d \leq 100$ nm
Coarse Mode	Particles with diameter > 1000 nm
Coagulation	An aerosol growth process resulting from the collision of aerosol particles with each other
Condensation	A process with more vapour molecules arriving at a particle's surface than leaving the surface, resulting in particle growth
Electrical Mobility Diameter	Diameter of a unit-density sphere having the same migration velocity within a constant electric field as the particle in question
ENM	A material that consists of particles with one or more external dimensions in the size range 1 nm – 100 nm for more than 1 % of their number
ENP	Intentionally created particle with one or more external dimensions in the size range 1 nm – 100 nm
Evaporation	A process with more vapour molecules leaving a particle's surface than arriving at the surface, resulting in particle shrinkage
Fine Particles	Particles within the fine mode, less than 2.5 μm in diameter. Also known as $PM_{2.5}$
Nucleation Mode	The smallest mode of atmospheric aerosol containing particles $0 \leq d \leq 25$ nm
Poly-disperse Aerosol	An aerosol containing a mixture of widely varying particle sizes

Primary Particle	A particle introduced into the air in solid or liquid form which has been emitted directly from the source.
Ultrafine Particles	Particles with diameter ≤ 100 nm

(Adapted from Baron and Willeke, 2001; DeCarlo et al., 2004; Agus, 2008; Maynard, 2011)

Chapter 1

1 Introduction

1.1 Background

Engineered nanoparticles (ENP) are increasingly produced and used in various consumer and industrial products. While enhanced functionality is achieved due to nano-specific properties, ENP can be released into the environment over the entire life cycle of nano-enabled products with possibly harmful consequences (Walser et al., 2012). As these new materials go through their life cycle-from development, to manufacture, to consumer usage, to final disposal, different human groups (workers, bystanders, consumers), environmental compartments (air, soil, sediment, water) and species (e.g. worm, fish or humans) will be exposed to these materials. As a new technology, it is important to establish the pathways of such potential impacts in order to plan for the safe and environmentally friendly production and utilisation of engineered nanomaterials (ENM).

A first and important step to achieve this is to establish appropriate schemes of risk management within the production sector where an accidental release could involve both high amounts of ENM and worker population in confined areas leading to the potential for high exposures (Nowack et al., 2014). Population intake fractions of chemical compounds are commonly several orders of magnitude higher for indoor releases according to Hellweg et al. (2009) and this might also be true for ENP indoor emissions. In combination, many toxicological studies have shown that nanoparticles are more harmful to health than large particles because of their orders of magnitude higher particle number concentration and surface area than large particles of the same mass (Zumwalde and Hodson, 2009). Furthermore, it has been shown experimentally that flammable dust clouds of most solid combustible materials will become more sensitive to electric spark ignition and burn with increasing violence as the size of the primary particles in the cloud decreases down to the order of 1-10 μm (Eckhoff, 2012). Considering that this trend could be extrapolated in the nm-particle range then extreme explosion characteristics would be predicted.

1.2 Research Objectives

In order to study accidental scenarios, a fundamental understanding of agglomeration, of dispersion and combustion mechanisms of ENP should be developed so as to provide

experimental and modelling tools to assess risks associated with accidental scenarios, and to be able to propose technical and organisational strategies to lower accidental risk. With the above issues in mind, this research aims to;

- **Objective 1**: Evaluate the possible effects of an accidental large-scale release of nanoparticles involved in a particular activity such as particle manufacturing, formulation, transport, recycling/disposal and storage. The goal of this work is to provide information to construct reference tools that will allow the modelling of the time evolution of a massive release of specific ENP. To this end, methods for the effective de-agglomeration and injection of the processed tested materials, will be investigated. Subsequently, indoor experiments in a dispersion chamber will be performed in order to assess the near-field emission sources induced by a reference accidental scenario leading to the massive release and dispersion of particles under unventilated conditions, i.e. for example the continuous, severe, leakage of nanoparticles which corresponds to the fall or rupture of a tank or the rupture of a pipe. The evolution of particle size distribution (PSD) will be tracked by measurement devices operating in parallel near to the source. Images of the deposited matter on the surfaces of test room will allow the optical assessment of those morphological characteristics of the dispersed materials that will enable correlations to take place between the type of particles and their resulting human exposure.
- **Objective 2**: For the same accidental scenario described in Objective 1, to develop strategies of mitigation based on ventilation using the calibrated volume air flow rate (measured in terms of air changes per hour, ACH) of the chamber. This will allow the examination of the efficiency of particle removal of the accumulated aerosol immediately after the cessation of the continuous release. Particle removal will be evaluated through the measurement of particle number concentration (PNC) by spatially distributed measurement devices. In addition, the spatial ventilation efficiency will be determined for the different ventilation rates in order to evaluate the relationship between the ventilation performance and the location in the chamber.
- **Objective 3**: Investigate the explosion characteristics of accidentally released ENP. This will be examined by forming a dust cloud in turbulent methane-air mixtures of very low gas content that is ignited by a spark plug (low nominal ignition energy). The influence of the added nanoparticles on the explosion severity will be determined by comparing the results obtained for the hybrid mixtures with those obtained for similar pure methane-air scenarios. The explosion severity of mixtures will be evaluated by the application of two completely different measurement techniques (dynamic pressure transducer and Schlieren flame photography). The level of

influence will be linked to the particle size characteristics of the tested dust clouds. In addition, the ignition potential of hybrid mixtures of methane content below its lower flammability limit (LFL) will be studied. Finally, the explosion characteristics of a hybrid mixture ignited by an additional ignition system of moderate nominal ignition energy will be compared to those obtained from the same mixture ignited by the conventional low energy spark plug ignition system.

This research is divided into different stages, each one with distinct intermediate goals:

a) First, the fundamental dispersion characteristics and explosion properties of nanoparticles as have been reviewed by the current literature, are presented in Chapter 2. This includes their airborne behaviour when introduced into the gas phase, and problems related to the dispersion ability of nanopowders using different dispersion methods. Furthermore, descriptions of measurement strategies and related studies on indoor particle exposure, are cited. Finally, related studies and a brief collection of results of nanopowder's explosion characteristics as well as of hybrid mixtures involving nanoparticles, are discussed.

b) In Chapter 3, a description of the methodology used within this study is presented. Firstly an overview of the dispersion and explosion facilities as well as the basic measurement instrumentation and auxiliary equipment used in the experimental procedure, are presented. Description of the methods of processing data is also included along with information on the data quality assurance procedures. Comparisons between the particulate instruments used in this work is also conducted and presented in this chapter. Finally, the techniques applied for the introduction of nanopowders into the experimental facilities are described along with the methods applied for the preparation of samples and mixtures before the main experimental stages.

c) Chapter 4 presents the applied optimisation steps for the preparation of the liquid nano-dispersions which utilised in the subsequent dispersion tests. Each step is accompanied by the presentation of the resulting volume-based PSD in the sonicated samples. Following this, the experimental-set-up is presented as applied to the evacuation experiments where the liquid nano-dispersions were injected. The evolution of total PNC and PSD measured by spatially distributed devices during injection and during the following decay period induced by various ventilation settings, are demonstrated. The different modal groups present within the measured PSD of the accumulated aerosol at the end of injection are

characterised and the evolution with time of the modal PNCs during the decay period is investigated. Finally, the estimation of the spatial particle decay rates as well as of the size-resolved particle decay rates are presented along with the estimation of the spatial ventilation efficiency corresponding to each tested ventilation rate.

d) Chapter 5 presents the experimental set-up configured for the study of titanium dioxide (TiO_2) and silica dioxide (SiO_2) particle interactions during and after their continuous injection. The continuous monitoring of the PSDs in the dispersed aerosols, over the nano and micron-scale, is demonstrated for both experimental periods: continuous injection followed by a prolonged period when aerosols are allowed to decay under unventilated conditions. Similarly to Chapter 4, different modal groups are identified within the measured PSDs, thus highlighting the interactions between these. An indoor aerosol model for the study of the differential effect of coagulation and deposition on the changes of PNC with time for both experimental periods, is presented. The estimated changes in PNC are compared with the experimental measurements and serve to highlight the importance of the different physical experimental processes in the change of exposure during and after the simulated accidental release. Finally, transmission electron microscopy (TEM) images of deposited matter of each material collected during the experiments, are also provided.

e) Chapter 6 demonstrates the particle size characterisation conducted in the powder form of two types of carbon black (CB) nanopowders, as well as in their airborne state within the clouds of dust concentrations used in the explosion tests. Comparisons are then presented between the explosion severity of a laminar and a turbulent methane-air mixture of low equivalence ratio. In addition, the identification of methane LFL corresponding to the specific conditions applied for the explosion tests conducted in this work is presented. For the study of the influence of ENP on the explosion severity of methane-air mixtures, the comparisons between methane-air and their respective hybrid mixtures of variable dust concentration of each tested material, are provided. The explosion pressure results obtained from the tests conducted on hybrid mixtures of methane content below its LFL, are also presented. The chapter ends with the comparison between the explosion pressure measurements obtained from the same hybrid mixtures of methane content below the LFL, ignited by two different ignition energy systems.

f) Finally, in Chapter 7, conclusions of the research study are summarised and their implications and impacts discussed.

Chapter 2

2. Background Information

2.1 Issues relevant to ENM risk assessment

Today ENM have been defined as materials having at least one dimension that is ≤ 100 nm (Elder et al., 2009). Due to their often novel and outstanding performance, a significant amount of research has been motivated in a variety of fields resulting in many new nano-technological applications. The acceleration of the manufacture and use of ENM has led to an increase in the probability of the accidental release of engineered nanoparticles (ENP) into the air and the concern that these will have possibly harmful effects. ENP emissions at nanotechnology work-places where large amounts of ENM are involved, under normal operating conditions have been shown to be very limited (Walser et al., 2012; Kuhlbusch et al. 2011; Wang et al., 2011). However processes like bagging, packaging, or cleaning of process equipment can significantly increase the ENPs indoor concentrations and consequently the exposure of workers to various risks (Kuhlbusch et al., 2011). Further unwanted exposure situations to ENP at the workplace could occur, with accidental emissions representing the worst case scenarios. This case would be unpredictable possibly resulting in massive releases, which in the case of indoor accidents, could dramatically increase the exposure levels. To date, no major accidents with ENM are known according to Nowack et al. (2014). Therefore, the knowledge available on the dissipation behaviour of ENM after an accident is limited.

2.1.1 Definition of risk and hazards

In order to define the term “risk”, it is important first to define the term “hazard”. According to the Environmental Protection Agency (EPA) (2007) of the USA, hazard is defined as the inherent toxicity of a compound. Any exposure to a hazardous substance can result in adverse health effects in individuals or even in death. With respect to the above definition, risk could be utilised as a measure of the probability of the exposure to a hazardous material that causes damage to life, health, property, and/or the environment as a result of a given hazard (Hristozov and Malsch, 2009). Therefore, if the probability of exposure to a hazardous material is high then the risk is considered to be high. Especially in the case of an accidental release of a hazardous substance, such as ENP released into atmosphere, the risks posed could be increased enormously due their size and structural characteristics.

2.1.2 Potential of ENM for major accidents

It is important to define first the potential of major ENM accidents. A major accident can take place whenever large amounts of a potentially toxic or reactive substance is present. According to Nowack et al. (2014), the scenarios for major accidents strongly depend on the type of ENM used and other chemicals present on the same site. Other factors specific for the situation or the site may influence the severity of the accident:

- Form of ENM: suspended or as powder
- Presence of flammable or explosive substances e.g. metallic ENM or organic solvents
- Risk of accident during transport
- Safety measures

In the case of ENM in the form of powders it could be assumed that the potential for major accidents is high because they are more dispersible than suspended ENM (Kuhlbusch et al., 2011). The aerosol produced by a nano-powder following a large energy input into the sample could potentially be composed by large fractions of airborne NPs.

NPs are particulates with lengths between 1 and 100 nm in at least two of three dimensions. ENM usually are composed of organic materials or metals and their structural units can come in a variety of shapes including nanotubes, nanowires and crystalline structures. Compared to micrometer-sized materials, ENMs are characterised by large specific surface area and a large number of atoms on the surface of NPs forming these. Due to these characteristics, properties such as reactivity, strength, fluorescence and conduction are enhanced for ENM (Hallock et al., 2009).

However, the extremely small size of ENM enables these to be respirable and it is believed that their inhalation may result in adverse respiratory and cardiovascular effects (Biskos, 2012). Furthermore, it has been found that as particle size decreases, the severity of explosion involving airborne ENP increases (Worsfold et al., 2012). However, in order to understand and to develop strategies for the control of risks derived from an accidental release of ENP, the dispersion and explosion characteristics presented in publications should be discussed and clarified.

2.2 Accidental release and dispersion in indoor environments

After an accidental release the new properties and the high mobility of some nanomaterials may lead to health and environmental effects. ENP are increasingly produced and used in various consumer and industrial products. For this reason they can be released into the

environment over the entire life cycle of nano enabled products with possibly harmful consequences. From a human health perspective, indoor workplaces require particular attention because of the possibility of inhaling ENP during production (Oberdörster et al., 1995). Humbert et al. (2011) claimed that if the population intake fractions of chemical compounds are commonly several orders of magnitude higher for indoor releases than for outdoor then this might also be true for ENP indoor emissions. However, only a few studies regarding workplace air monitoring of nanoparticle production are available and these are often focused on carbon compounds produced with laboratory equipment (Maynard et al., 2004), or from investigating other processing activities such as bag filling and packaging (Kuhlbusch et al., 2004). On the other hand, for studies basing their process in simulated workplaces and of simulated work processes, there are two important parameters which have to be evaluated precisely: release rates and methods of release; and devices and measurement strategies used for airborne nanomaterials quantification after their indoor dispersion (Schneider, 2011). The first category of studies could be useful inputs for the evaluation of characteristics which should be applied in the studies of the second category as a part of an effective simulation and implementation in real life conditions.

2.2.1 Release potentials of nano-objects sourced from ENM and dispersion techniques for experimental studies

The emission or release of nano-objects (materials with one, two or three external dimensions in the nanoscale) into the surrounding air from powdered nanostructured materials resulting from handling is an important consideration in the design and operation of many industrial processes. The propensity of nanomaterials to release nano- objects into the air is determined by test methods devised to apply energy to a sample to stress the inter-particle bonds. This stressing induces abrasion, erosion or comminution, which causes dissemination of the particles in the gaseous phase (ISO/TS-12025, 2015).

ISO/TS-12025 indicates that aerosols of nano-objects are more dynamic than micrometer sized particles because of greater sensitivity to physical effects such as Brownian diffusion. Porosity and cohesion of the powder can be much higher than those containing larger particles with more resistance to flow and lower ratio volume to specific surface area. Nano-objects in powdered materials can dominate relevant properties of the bulk material by particle to particle interactions that form clusters like agglomerates and characterized as secondary nano-structured particles consisting of primary nano-objects.

2.2.1.1 Analysis of the dispersion problem

Hamelmann and Schmidt (2003) suggested that to meet the requirements of occupational health, hygiene and safety as well as those of fire and explosion prevention, the estimation of dustiness is becoming more and more important. A given mass of powder at equilibrium with the ambient atmosphere contains a finite number of inter-particle bonds, each of which requires a specific amount of work to be broken. The total minimum work W_{min} necessary to break all these bonds in one unit mass of powder could in principle be calculated by integrating the work required for breaking all the individual inter-particle bonds. According to Eckhoff (2012), the 'dispersibility' (D_{real}) is defined by the following equation:

$$D_{real} = \frac{k*}{W_{\min}} \qquad \text{Eq. 2. 1}$$

Where k* is an efficiency factor and depends on the chosen dispersion method considering that no realistic dispersion process is one-hundred percent efficient. The particle size distribution has a great influence on W_{min} for a given powder with specific density. Furthermore the degree of compaction of a cohesive powder will determine the value of its bulk density. When cohesiveness is combined with small particle distribution then W_{min} increases. In other words, the number of inter-particle bonds per unit mass of cohesive powder will increase with increasing the level of powder compaction and the size of particles will enhance the inter-particle forces as the particle size decreases. However, the efficiency factor k allows D_{real} to have any value between zero and a maximum value, depending on the way the work W_{min} is applied to the powder to be dispersed (Eckhoff, 2012). In turn that means that the geometrical arrangement of the powder and the form of the energy available for the dispersion process are playing major role in the resulting dispersion. Especially in the case of cohesive powders containing very small particles, the existence of strong inter-particle forces may not be broken unless the particle agglomerates are exposed to high velocity flow fields and consequently high shear forces, or strong agitations or a combination of both. In conclusion, the release rates are strongly dependent on the energy applied during the dispersion method, a factor which is going to determine the dispersion device to be used in the experimental process of the present work.

2.2.1.2 Dispersion methods and previous studies

It is important to measure the propensity of ENM for exposure assessment, control and mitigation purposes. Different particle generation methods were proposed for testing the dustiness of nano-materials in ISO standard (ISO/TS-12025, 2015) including the rotating drum dustiness tester (RD), the Vortex Shaker (VS) and dynamic methods. Furthermore, free

fall experiments make it possible to check the presence (or the absence) of ultrafine particles suspended in air due to free-falling nano-structured powders. The technical description of these dispersion mechanisms is not essential for the current chapter, although results obtained from previous studies will be presented in order to determine the reasons for the choice of the selected dispersion device in our experimental procedure. Because the research presented here is based on the simulation of accidental scenarios of nano-powder release in an indoor testing room, it is considered that the outcomes in terms of PNC and PSD occurred by the chosen dispersion method would represent the corresponding levels of real accidental conditions. Methods like the RD, VS and free fall are representative of levels of dust emitted in a handling process or to the occupational exposure of workers under normal working conditions in the workplace.

The research focuses on measuring the number concentration and distributions of generated particles from test nanomaterials. Table 2.1 presents the ENMs which were tested experimentally, as well as the characteristics of the generated airborne nanoparticles for dispersion methods based on dry and wet techniques. The last column of the table presents the fractions of ultrafine particles (diameter $\leq$ 100 nm) within the population of the generated aerosol.

The dry dispersion methods for nano-powders suffers from incomplete determination of the energy input during sample treatment. For example, studies describing the VS method do not connect the frequency of the rotations (energy input) with the results. Furthermore, repeated treatment of powders in processes like the RD can generate secondary agglomerates. Thus in this case the number of released nanoparticles rapidly decreases during the test.

Regarding the wet dispersion techniques, as can been seen in Table 2.1, the measurements of the PNC showed an increase in concentrations by sonication in comparison to the dry powders bulk handling. At the same time measurements in the micro-meter range showed a decrease in concentration of the coarse particles. An interesting feature can been shown in the case of spray simulations with nano-silver and nanoparticle-free suspensions conducted by Hagendorfer et al. (2010) in a particle free glove box. This work indicated that the measured PSDs on the generated aerosol showed a fraction of around 80% for ultrafine particles.

The results presented in Table 2.1 are based on a low energy input to the powder. Accidental dispersion involves high energy processes which result in significantly higher energy input to the nanomaterial. To this end, Stahlmecke et al. (2009) attempted to mimic the particle release of metal oxide powders due to a leak in a pressurized vessel. They used a pressurized beaker in combination with a magnetic stirrer and an orifice in order to measure the PSDs

Study	Dustiness device	Materials	Measurement devices	Metric	Results
Dry dispersion methods					
Tsai et al. (2009)	RD	TiO_2 (Aeroxide P25), ZnO	SMPS, APS, MOUDI	PSD (15 nm – 20 μm)	less than 10% of particles < 100 nm and less than 60% of particles < 1 μm
Schneider and Jensen (2008)	RD	TiO_2,SiO_2, FeO(OH), $Mg_3Si_4O_{10}(OH)_2$, Al_2O_3	FMPS, APS, filtration	PSD (5.6 nm-20 μm)	Undefined fraction of particles < 100 nm
Jensen et al. (2009)	RD	Organoclay, Bentonite	FMPS, APS, filtration	PSD (5.6 nm-20 μm)	Undefined fraction of particles < 100 nm
Tsai et al. (2012)	RD	TiO_2, ZnO, SiO_2	SMPS, APS, MOUDI	PSD (15 nm – 20 μm)	Nearly no nanoparticles < 100 nm generated during the test
Maynard et al. (2004) & Baron et al. (2003)	VS combined with fluidized bed	SWCNT, alumina powder	SMPS (LDMA,NDMA), APS	PSD (4 nm – 20 μm)	Fraction of particles < 100 nm, alumina powder released more NP than SWCNT
Ogura et al. (2009)	VS(fluidized bed)	SWCNT, MWCNT, TiO_2, ZnO	SMPS, HHCPC, APS, OPC	PSD (10 nm-20 μm)	Fraction of particles < 100 nm
Lee et al. (2010)	VS	MWCNT	SMPS, APS,TEM	PSD (14 nm- 20 μm)	Fraction of particles < 100 nm having peak at 200-300 nm

Tsai et al. (2012)	VS	TiO_2, ZnO, SiO_2	SMPS, APS, MOUDI	PSD (20 nm – 20 μm)	Fraction of particles < 100 nm
Isabeta and Biscans (2007)	Free fall device	TiO_2 (G5), SiO_2 (Aerosil 200)	ELPI, SEM	PSD (30 nm – 10 μm)	Fraction of particles < 100 nm
Wet dispersion methods					
Johnson et al. (2010)	Weighing/transferring powders and sonication of suspensions	Fullerenes, MWCNT,CB	CPC, TEM	PSD (0.3 μm – 20 μm) NC(10 nm-1 μm)	Suspension sonication leads to droplets with embedded ENM
Hagendorfer et al. (2010)	Spraying	Suspension with and without Ag	SMPS, TEM	PSD (10 nm – 500 nm, NC<500 nm	High fraction of particles < 100 nm

Table 2.1: Studies focused on the dispersion methods of nano-structured powders

resulting from the de-pressurization process. Number weighted distributions of particles in the size range < 736 nm showed that the amount of ultrafine particles was increased from 1% up to 12% with increasing overpressure from 0 KPa to 140 KPa.

Well-defined samples in combination with well-defined flow rate conditions and a detailed record of energy input could ensure a repeatability and accuracy of the results. Specific conditions of handling during the preparation of the powder sample could modify the dispersion state of the test material. Moreover, conditions established of air humidity during the day of the experiment conduction could significantly change the results. Morphological characteristics of the powder could also be changed during the transportation of the material from the factory to the supplier. Thus the work applied on the powder during the dispersion should be representative of forces which could overcome the agglomeration level of each powder in order to provide realistic experiments of airborne nanoparticles.

2.2.2 Devices and measurement strategies for airborne nano-objects and nanomaterials

There are three main metrics for the exposure assessment to airborne NPs. These are: i) mass concentration (mg m^{-3}); ii) number concentration (n m^{-3}) and; iii) surface area concentration (m^2 m^{-3}). Instrumentation is available to measure each of these metrics. For mass, Tsai et al. (2012) reported a lack of sensitivity towards the NPs of interest. On the other hand, measurement of number concentration is highly sensitive and the integration limits on which a particular instrument operates are critical to the reported results (ECHA, 2012). The real time measurement of particle surface area concentration is possible according to the latest progress of the particle instrumentation technology. However, there is very limited practical experience with these instruments. All the above indicate that the choice of devices and measurement strategies is very important for better understanding and for efficient performance of simulations related to ENP emissions.

2.2.2.1 Measurement devices for airborne NPs

There are a number of instruments available which measure the metrics discussed in the previous paragraph. These devices operate on different physical principles and they are serving different aims depending to the purpose of the investigation each time. The operation principles of two categories of devices which will be used in the frame of the current experiments are: size resolved and time resolved devices and size integrated and time resolved devices. However, it is necessary first to define the main physical principles on which particles are detected and classifying these by devices.

According to Mark (1998), the three main physical principles on which particles are classified are by light-scattering, inertial properties and electrical mobility. Light scattering instruments, or 'optical particle counters', operate on the principle of light interaction with airborne particles.

However, most often particles are classified by their aerodynamic diameter. The aerodynamic diameter is defined as the diameter of a unit density sphere (1 g cm^{-3}) that settles through the air with a gravitational settling velocity equal to that of the particle in question. It is an important aerosol size parameter because it determines a particle's behaviour whilst airborne. Therefore, particles with the same aerodynamic behaviour will have the same aerodynamic diameter, in spite of their physical shape, size, density or composition. Knowledge of a particle aerodynamic diameter enables determination of where a particle will be deposited in the human respiratory tract, how long the duration during which particle remains airborne in the atmosphere or in an aerosol, and whether the particle will penetrate a removing device, a particle sampling system or a pipe, tube, duct or channel (Agus, 2008).

On the other hand, a number of particulate measurement instrument classify particles by knowledge of their electrical mobility diameter. The electrical mobility is a measure of the velocity of motion resulting from the force experienced in an electric field. It is defined as the diameter of a unit density sphere with the same migration velocity within a constant electric field as the particle in question (DeCarlo, 2004). The electrical mobility diameter increases with increasing deviation from the spherical shape. The irregular shaped particle, which is identical in volume to the smaller particle, is shown to have the same trajectory as the larger spherical particle. Therefore, the diameter of the larger particle is equal to the electrical mobility diameter of the irregular shaped particle (DeCarlo, 2004).

In general, DeCarlo (2004) suggested that comparison of the aerodynamic diameter and the electrical mobility diameter for an irregular particle of standard density indicates that the electrical mobility diameter is greater than the aerodynamic diameter. Therefore, irregular shaped particle populations will show significant differences in their size distributions when measured by these techniques (Agus, 2008). According to Agus (2008), these are not real differences, but simply capture differences.

The size resolved-time resolved devices use detection principles based on the particles' optical-aerodynamic properties or electrical mobility. Hence the results are based on optically or electrically equivalent spheres or furthermore aerodynamic spheres after the conversion of electrical signals into particle size. For this reason there is an issue of equivalency in the case of non-spherical particles and hence bias in the measurement accuracy. Another distinction

between devices of this category is that of time resolution. Particle size distribution may vary over time scales of second thus of great importance is the real time recording. An example of a fast particle sizer is the differential mobility spectrometer (DMS) which could be employed to analyse fast changes in the particle size distributions.

The size integrated-time resolved devices have a more simplified operation based on the detection of the number of particles. A particle is signalled by a detector independently of its size and the results are recorded in real time. An example of these devices is the condensation particle counter (CPC) which detects particles from a few nanometers to a few micrometers (Farnsworth and Caldow, 2010), depending on the device used. Furthermore these counters are characterized by a counting efficiency number which configures their lower detection limit, which is defined as the particle diameter at which 50% of particles are detected.

The main particulate classifier in the nanoscale used within this study operates on the basis of the electrical mobility principle, and therefore the particle diameter, d_p, reported throughout this work is equivalent to the electrical mobility diameter. Measurements based on the aerodynamic diameter were also obtained by a device employed for particle detection in the micro-meter scale. The main particulate instruments are described in Chapter 3.

2.2.2.2 Measurement strategies

Measurement techniques and strategies have to be optimally combined to allow sensitive and cost effective determination of airborne engineered nanomaterials dispersed within indoor environments. The first step is a real time screening for the identification of possible 'hot-spots' (Methner, 2009). These points are characterized by increased concentration levels and indicate the need for a further more detailed investigation in the frame of a tiered approach. In the next step, size information of nanoparticle concentrations within the indoor environment should be obtained by classifiers as described previously. This is because a detailed assessment of effects requires knowledge about the evolution of particle morphology and size distribution from emission source to the sampling point (Walser et al., 2012). According to Kuhlbusch et al. (2011), one considerable problem is the distinction of nanomaterial from the background aerosol. The combined use of the measurement devices significantly enhances possibilities for the distinction of nano-objects from the background. However, by-product particles either from the production process itself or from other sources such as electrical devices may influence the measurements.

Beside these general measurement strategies, the environment where engineered nano-objects and their agglomerates or products using nanomaterials are processed or used needs to be

examined and assessed. The conditions existing in the workplace, as will be shown in the following paragraphs, play a dominant role in the evolution of the particles' behaviour during their dispersion in the indoor environment.

2.2.3 ENP and their airborne behaviour

As mentioned above, the definition of ENM describes those materials with at least one of their dimensions ranging between 1 and 100 nm, and they have different properties than particles of micrometer scale made of the same material. Therefore, due to their small size, any airborne product sourced from these is potentially involved in different processes like diffusion, coagulation, aggregation, agglomeration as well as re-suspension.

2.2.3.1 Diffusion

Diffusion is described by Friedlander (1977) as a random dancing motion of small particles under which these are subjected when suspended in a fluid. Maynard and Kuempel (2005) stated that the smaller the particle, the more rapidly it disperses. For instance at 1 nm, a particle's diffusion coefficient is about the 5% of the diffusion coefficient of the gases. That means that a nanoparticle will not remain localized in the field near to a leak, instead it is going to diffuse rapidly over a great distance and potentially may expose many individuals far from the leak. Furthermore, the airborne nanoparticle motion is influenced by its collisions with gas molecules. This bombardment of the gas molecules against particles results in an irregular wriggling movement, the so called Brownian motion (Hinds, 1982).

2.2.3.2 Agglomeration and coagulation

Agglomeration is another process in which nanoparticles participate during dispersion to the air. A correct definition of agglomeration is given by ISO/TS-12025 (2015) and specifies the differentiation of this phenomenon from aggregation. According to this, agglomeration is a collection of loosely bound particles or aggregates or mixtures of the two held together by weak forces where the resulting external surface area is similar to the sum of the surface areas of the individual components. However, in aggregation, particles bind strongly to each other such that their total surface is less than the sum of surfaces of the individual particles.

Agglomeration is a natural trend of airborne nanoparticles and is enhanced further by the diffusion caused by the Brownian effect. The total result of this process, according to Maynard and Kuempel (2005), is an increase in the aerodynamic diameter of aggregated or agglomerated particles, thereby causing a decrease in the number of particles. Agglomeration is directly related to coagulation which is the most important interparticle phenomenon for

aerosols. Hinds (1982) claimed that the term “agglomeration” started being used in order to describe the coagulation taking place between solid particles. By that way it established a distinction between coagulation in liquids and coagulation in aerosols.

Coagulation moves to a state of equilibrium for the very small particles, including those ranging from 1 to 100 nm. These particles after their dispersion in high rates start to form bigger, less mobile and less numerous particles whereas through coagulation their growth becomes much slower. A characteristic example was given by Hinds (1982) for the case of a spherical particle with diameter <100 nm. This reaches a size of around 100 nm rapidly, and then it will grow less rapidly up to a size of about 2000 nm. The change in diameter contributes to increasing the effect of gravity on the movement. Particles become heavier in relation to air through the process of coagulation and gravitational sedimentation starts to play a major role in the particle’s movement. Under identical turbulent conditions, the rate of sedimentation is increased for the heavier airborne particles.

2.2.3.3 Deposition

Particle deposition on surfaces by diffusional transport is of fundamental importance in the study of the aerosols behaviour and fate. This type of diffusion is called convective diffusion and is effective for particles < 1 μm. However, in the nanoscale this effect of deposition on airborne NPs is size dependant. More details about the relationship between particle size and deposition rates are given in Section 2.2.6.2. Deposition losses, according to Seipenbusch (2014), are a group of mechanisms leading to changes in particle number and size distribution. These losses could occur due to: a) gravitational settling, b) thermophoresis, c) electrostatic forces and d) Brownian and turbulent diffusion. However, information allowing estimation of losses due to thermophoresis is not available and they are usually neglected (Schneider, 2011). Furthermore, Schneider (2009) claimed that the increased deposition velocity of charged airborne ENP at surfaces due to electrical fields can be expected to cause a negligible loss rate.

All the above phenomena lead to the conclusion that the smaller the particles, the longer distances they can travel, with their dimensions slowly increasing and their composition evolving over time through impacts with other particles. These factors are responsible for changes in the number concentration and size distribution of an aerosol. At the same time, these factors, according to Anand (2012), are linked to the characteristics of a nanoparticle source, the interaction with pre-existing particles, as well as the transport, mixing and dilution conditions specific to a given environment.

2.2.3.4 Large scale particle processes

The analysis of aerosol motion given above has focused exclusively on the motion of individual particles. There are, however, some situations in which individual particle motion is negligible compared with motion on a larger scale (Hinds, 1982). Nazaroff (2004) indicated that the effects of direct emissions on inhalation exposure, to an extent, depend on indoor-air mixing processes and the term 'mixing' is defined as the transport and dispersion of a species within a single room which is induced by bulk advective flow combined with turbulent fluctuations about the mean flow. Indoor airflow may be induced by mechanical means, such as air discharge from ventilation registers. Therefore, in the case of application of control strategies in the chamber it is expected that all the above transport aerosol mechanisms will be very small compared to the bulk motion of aerosol caused by mechanical means. Simultaneously, in intense bulk aerosol motions induced by the application of mechanical ventilation, possibly other mechanisms, e.g. resuspension, are going to have a more enhanced role.

Resuspension is a process that is difficult to predict and quantify accurately despite its understandable nature. Hinds (1982) defined resuspension as the detachment of particles from a surface and its transport away from the surface. Air jets and mechanical forces could be the main reasons of the resuspension occurrence. Resuspension potentially causes the entrainment of individual particles or small clusters and subsequently their re-circulation into the air. This process increases with the increase of the exposure duration of the surface to an air jet.

2.2.4 Modes for the analysis of dispersed ENP

In atmospheric studies, the size distribution of particles are characterized by size modes caused by the aerodynamic processes described in the previous paragraph. These modes according to Schneider (2011) are: nucleation mode (< 20 nm), Aitken mode (20 – 80 nm) which is the transition mode between nucleation and accumulation modes, accumulation mode (80 – 1000 nm), and coarse mode (> 1000 nm). Similar physical processes resulting in these distinct modes can be considered in indoor studies related to workplaces of ENMs. Brouwer (2010) indicated that field measurements of ENM production and downstream scenarios showed the existence of a submicron mode and of a mode above 1 μm. Therefore, in the present work the size class boundaries used are 25, 100 and 1000 nm.

2.2.5 Studies for the risks of occupational exposure in workplaces

For the current literature review, exposure related nanoparticle measurements at workplaces are taken into account, where engineered nano-objects and their agglomerates or products

using nanomaterials are processed or used. For the purpose of this research a review of these studies is considered to be a useful index for the evaluation of the exposure levels in the dispersion chamber determined by the conduction of simulation accidental release tests. The investigations can be structured along the production pathway: production, handling and refinement of the raw material, bagging and shipping of the nanomaterial and work processes with nanomaterial products.

In Table 2.2, taken from a review by Ding et al. (2016), are presented the most recent studies on exposures related to specific workplaces. Different measurement strategies and techniques complicate the summary of these studies. Number concentrations of particles could be derived directly by size integrated and time resolved devices (e.g. CPC) or indirectly by size resolved and time resolved devices (e.g. ELPI, SMPS etc.). However, this may result in difficulties in the comparison of absolute values especially in case of number concentrations where contributions of sub-10 nm particles can be significant. Furthermore, according to Kuhlbusch et al. (2011), using devices which classify particles either by mobility diameter or by aerodynamic diameter, those measurements are based on diameters of equivalent spheres thus these may not be representative for non-spherical particles.

In more detail, Table 2.2 presents the measurement results for airborne particle types, number concentrations, mean sizes and agglomeration states. As can been seen, processes like cleaning, packing and bagging, weighing-mixing and transferring associated with the release of airborne particles of large size of minor or moderate concentrations. Processes related to machining and abrasion of nanocomposites shown to release ENPs embedded in matrix particles, although airborne NPs of primary size were not identified in the released particles. On the other hand, processes in the production stage like physical and chemical synthesis were associated with potential releases of ENP in small sizes. According to Ding (2016), studies focused in production claimed that the measured particle mass concentrations were low, an indication of the presence of very small sized airborne particles. Finally, in spraying processes the highest levels of airborne NPs of very small size have been detected. A characteristic example of these cases are the measurements on particle concentrations conducted during flame-spray process. The highest releases were seen during the active phase of the process were 1.6-2.1 10^5 particles cm^{-3} (Ding et al., 2016).

The main conclusion extracted by this summary of studies is that agglomerated particles were the most frequently found form of particles. Furthermore, the identification of nanomaterial exposure is not straight forward and that well described and harmonized methodologies are needed to unambiguously link elevated particle concentrations to the nanomaterial under

investigation and to obtain quantitative results. The latter is extremely difficult and demands careful process studies on the laboratory scale.

	Ref	Material	Background, #/cm^3	During activity, #/cm^3	Sampling size range, nm	Mean size**	A.*
Weighing Mixing Transferring	Methner et al. (2010)	Composite materials	700-19,500	4,000	10-1000	0.5-3 µm	A.
	Methner et al. (2010)	MWCNT	14,700	57,000-157,800	10-1000	0.5-1 µm	A.
	Koivisto et al. (2014)	Nanodiamonds	4,600± 2,900	6,000-20,000	10-1000 14-573	0.5 µm	A.
	Bekker et al. (2015)	SiO_2	13,357-85,272	72,096-100,856	10-300	0.5-25 µm	A.
	Bekker et al. (2015)	Al_2O_3	8,664-10,641	88,699-134,403	5-500	0.05-10 µm	A./I.
Sonication	Johnson et al. (2010)	MWCNT, CB	724–1,250	1,450–3,500	10-1000	300–500 nm	A.
	Methner et al. (2010)	C60, MWCNT	N/A	2200–2800	10-1000	~ 200 nm	A.
Packing	Kuhlbusch et al. (2004)	CB	N/A	1,000-5,000	200-700	>0.4 µm	A.
	Huang et al. (2010)	TiO_2	N/A	N/A	56 nm - 18 µm	5.52–7.25 µm	N/A
	Bekker et al. (2015)		12,103 – 20,051	64,489–130,424	5-500	0.05-20 µm	N/A
Spraying	Methner et al. (2010)	Silica-iron	13,300 – 20,300	79,700	10-1000	200–1000 nm	A.
	Methner et al. (2010)	TiO_2	33,500	144,800	10-1000	N/A	N/A
	Bekker et al. (2015)	SiO_2	19,404 – 51,348	382,976–1,789,544	10-300	0.5–5 µm	A.
	Bekker et al. (2015)	SiO_2	9,909–14,200	121,13–201,38	10-300	0.1-25 µm	A./I.
Production (physical & chemical synthesis)	Plitzko (2009)	TiO_2	7,000–20,000	21,000	5 nm to >32 µm	0.5–1 µm	A.
	Plitzko (2009)	Specific ENMs	5,500–15,000	62,000 (477,000)	5 nm to >32 µm	2 µm	A.
	Demou et al. (2009)	Metals/metal oxides	2,109	Peaks: 35,494–102,708	20-673	112–188 nm	N/A
	Hedmer et al. (2014)	MWCNT	N/A	500-34,000	10-300	59-65 nm	N/A
	Lee et al. (2012)	silver	877,364	224,622 – 2,328,200	15-711	<100 nm	A.
Machining (sawing, grinding etc.)	Bello et al. (2009)	Carbon fiber	4,820	94,000	5.6-560	165 nm	N/A
	Mazzuckelli et al. (2007)	Carbon nanofiber	10,000 – 20,000	10,000–20,000	10-1000	400 nm	A.

	Hedmer et al. (2014)	Graphite	N/A	Up to 34,000	10-300	30-40 nm	N/A
	Boonruksa et al. (2016)	CNT/polymer	BG corrected	4,500 – 430,000	6-560	<10 nm, 150 nm	A.
Cleaning	Methner et al. (2010)	Oxides(Ag,Mn,Co)	N/A	62,000-74,000	500-1000	0.5-1 μm	A.
	Methner (2010)	Ag,Cu,Ni,Fe,Mn	N/A	1,300–16,000 (BG subtracted)	10-1000	0.5–5 μm	A.
	Plitzko (2009)	TiO_2	7,000–20,000	22,000	5 nm to >32 μm	0.5–1 μm	A.

*Agglomeration state: A.: agglomerated or aggregated, I.: individual nanoparticles.
**Mean particle size was taken from the mode sizes in number size distributions or estimated from TEM/SEM images.

Table 2.2: Release characterizations grouped into different activity types (Ding et al, 2016)

2.2.6 Studies on the dynamic potentials of airborne NPs in a well-controlled indoor environment

A question of great importance for assessing the possible risks in accidental situations is to identify and quantify the aerosol transport processes driving changes in the morphological characteristics, such as particle size, of accidentally released airborne ENP, from a source to the receptor. Systematic and quantitative analysis of processes and materials can be carried out under controlled boundary conditions in the laboratory. To this end, various studies investigated and simulated the accidental release of NPs in controllable indoor environments in order to model important aerosol processes like coagulation and deposition.

2.2.6.1 Experimental studies modelling coagulation and scavenging

Modelling studies on the coagulation of accidentally emitted ENPs in dispersion test rooms have taken into account two types of coagulation: i) homogenous coagulation of ENPs, in which high concentrations of primary NPs or nano-sized agglomerates may be present, and ii) scavenging of emitted NPs by background or associated particles (heterogeneous coagulation).

Seipenbusch (2008) conducted one of the first studies to introduce aerosol dynamic principles in tracking the changes in measured PSD of released NPs in a simulated workplace environment of a 2 m^3 volume metallic chamber. The evolution in time of a nanoparticle aerosol release was investigated for different starting scenarios: (i) nanoparticle release into a particle free atmosphere and (ii) release in the presence of a pre-existing background aerosol. Both scenarios monitored over several hours. An interesting facet of that study is the production and dispersion of very small ultrafine platinum (Pt) nanoparticles having median

diameters of 7-8 nm in the chamber. The concentrations of the background aerosols were chosen to be representative of indoor aerosols with concentrations of typically ~10^3 to 10^4 #/cm^3 and particle sizes in the range of 0.1-1 μm (oil droplets and silica particles). A fan was used to establish turbulence and thus rapid mixing of the aerosols whereas an external pump was flushing the chamber with filtered air in order to obtain a particle-free environment and which was shut-off during experiments. The results in Figure 2.1 describe the evolution of the particle size distributions, obtained by an SMPS (Scanning Mobility Particle Sizer), of Pt nanoparticles in time corresponding to each scenario.

In the first scenario after 3 h aerosol injection and measurements, initially a single peak approximately 15 nm appeared when the first size distribution was measured (Figure 2.1a). The following measurements illustrated a rapid emergence of a secondary peak which travelled to larger particle sizes with a continuing drop in magnitude of particle concentrations. These results indicate the creation of 'aged' nanoparticles consisting of large, loose agglomerates during the injection process. According to Hinds (1982), the coagulation rate of a mono-disperse aerosol is proportional to N^2 (N is the particle number concentration in an enclosed media) and thus rises rapidly as the chamber fills, leading to the emergence of a secondary mode by homogeneous coagulation and to a slight decrease in total chamber concentration. Furthermore the resulting agglomerates of the secondary mode are operating as scavengers of the primary particles thus the coagulation rate increases to a point where it outpaces the source rate resulting in a decrease in number concentration with time. Finally, a steady state occurs when the coagulation rate equals the source rate.

The second scenario, in the presence of background particles leads to a quasi-steady state of the size distributions (Figure 2.1b). The concentration of the background particles is a regulator of the level of vanishing primary nanoparticles by attachment on the larger background particles and determines the visibility of the continuous nanoparticle source in the size spectrum. At the high end of the background particle concentrations, almost all the nanoparticles of diameter 15 nm are removed by the larger particles and at the lower end the evolution is much slower. Note that the nanoparticle injection is being continually compared to the background particles which are not replenished.

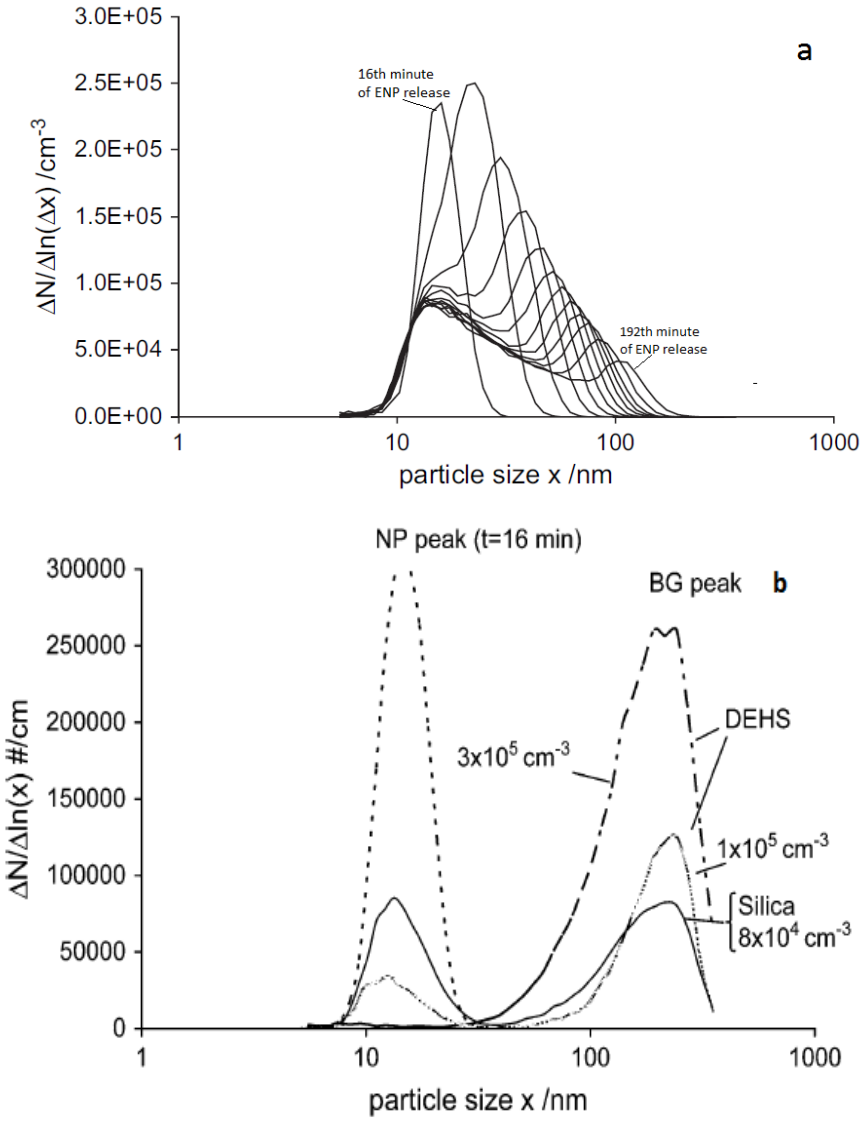

Figure 2.1: Particle size distributions of Pt nanoparticles in the dispersion chamber for (a) scenario (i) and (b) scenario (ii) (Seipenbusch, 2008)

In another study, Koch (2003) estimated the coagulation of airborne NPs under the presence of 1 μm in size particles for masses of 0.01 to 1 mg/m^3 and 0.5 to 50 mg/m^3 respectively. The applied residence time was 1-10000 s. The results of this work indicated that homogeneous coagulation would be negligible for concentrations of nano-sized particles below 0.1 mg/m^3. Additionally, for concentrations of nano-sized particles above 0.1 mg/m^3 homogeneous coagulation was strong enough to increase the size of the primary particles and in parallel to reduce the scavenging rates. On the other hand, for background concentrations of 5 mg/m^3 (~ 10^4 particles cm^{-3}) heterogeneous coagulation (scavenging) was negligible.

In conclusion, according to the above studies some indications could be extracted for the interpretation of the results to be presented in the next chapters. The first one is the importance of the background particle concentration or large associated particles in the fate and behaviour

of the smaller particles. Considering the polydisperse nature of the aerosol formulated by nanopowders then it is expected that large airborne agglomerates/aggregates are going to be released in the dispersion tests and will enhance the scavenging effect. The second conclusion is that dispersed NPs do not reach the receptor in the form of primary released aerosol. They change their size and number concentration by coagulation, homogeneously by coagulation within the NPs size class or heterogeneously by interaction with the background particles.

2.2.6.2 Experimental studies modelling surface deposition

Lai (2000) analysed experimental measurements of surface particle deposition velocities as obtained by various studies. Figure 2.2 illustrates the U-shape feature of the diameter-dependent deposition velocity. As can been seen, the minimum deposition velocity is observed for particles with diameter ~300 nm. For particles below 300 nm the gravity effect can be neglected. On the other hand, as moving toward to larger sizes the decreasing deposition velocity is counterbalanced gradually by the acceleration of sedimentation. Turbulent diffusion is also an important mechanism strongly correlated to the turbulence of the system. The quantity u_* in Figure 2.2 represents the friction velocity which characterises the intensity of the turbulent flow near at the surface.

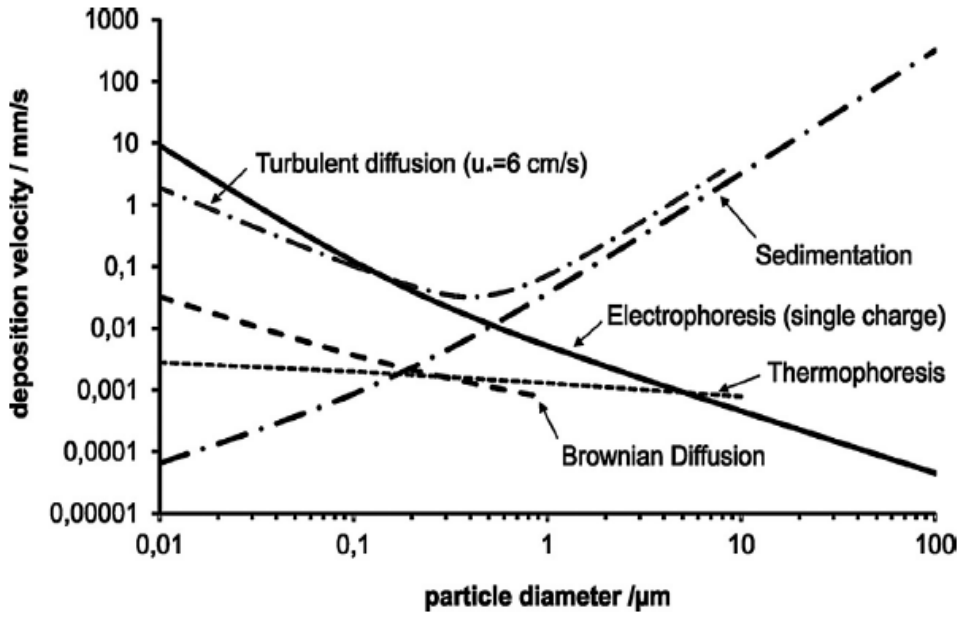

Figure 2.2: Deposition velocities of various surface loss mechanisms as functions of particle size. Modelling conducted by Lai (2000) (adapted from Seipenbusch et al., 2014)

Other studies, according to Schneider (2011), have reported deposition rates of the order 10 h^{-1} for 10 nm particles. Similar values of deposition rates have been estimated for 10 µm particles. Lai and Chen (2006) used computational fluid dynamics to calculate the fractions of

airborne ENP deposited on the internal surfaces in a ventilated enclosure. Their results showed that high concentrations of ENP can cause significant surface contamination under ventilation conditions after short periods of time. He et al. (2005) reviewed various surface deposition studies and concluded that the deposition rates of particles <80 and >1000 nm were not influenced by ventilation conditions.

In conclusion, surface deposition could cause considerable losses of primary airborne ENPs. Every realistic scenario should include this mechanism as part of its calculations. Due to the high possibility of a primary ENP to grow by homogeneous coagulation or to become scavenged by sub-micron size particles, they could enter in a size range where surface deposition has a minimum. However, as indicated in Section 2.2.1, the possibilities for the release of large fractions of primary ENP by a nano-powder are very low. Even under high energy input primary aggregates could be released into the air, thus losses by surface deposition would be considerable.

2.3 Engineering control strategies for the mitigation of accidentally released ENP in indoor environments

Controlling exposure to occupational hazards plays an important role in preventing or reducing personal exposure to hazardous substances in workplaces. According to the National Institute of Occupational health, NIOSH (2013), a hierarchy of controls have to be considered and applied in order to implement effective protection of the individuals involved in the production process of ENM. Figure 2.3 illustrates this hierarchy. From these five categories of controls, the engineering controls represents the most fast response measure to protect workers by hazardous conditions. For instance, elimination and substitution are not feasible if the production process is the design or development stage, whereas the administrative controls serve as back-up in the case of failure of the engineering control measures. Personal protective equipment (PPE) is the most effective measure for the protection of workers, although requires employee training and over the long term operating costs could become high especially for high risk process areas. However, the major advantage of the engineering control measures over the others is the inherent safety of the worker under a variety of conditions and stress levels (NIOSH, 2013). Engineering controls are divided into two broad categories: ventilation and non-ventilation controls. For the purpose of the present work, ventilation will be described in detail below.

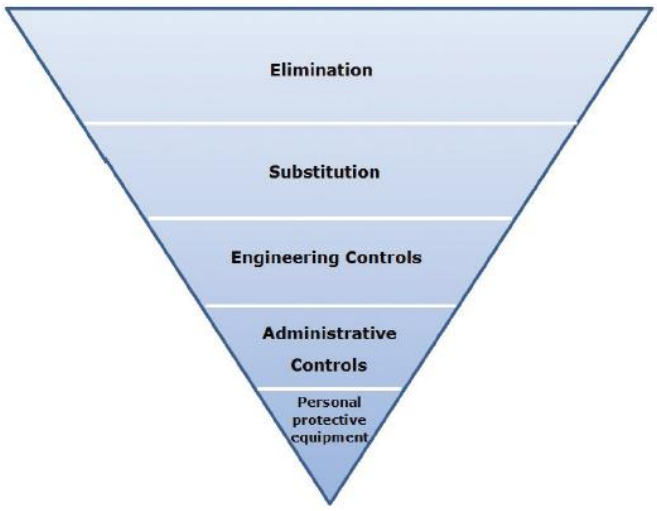

Figure 2.3: The hierarchy of controls for the mitigation of exposure to ENPs in the indoor environments (NIOSH, 2013)

2.3.1 Ventilation

The concept behind ventilation is the removal of contaminated air from the environment. According to Ding (2016), workplace ventilation controls can be broadly grouped into the following categories: a) laboratory fume hood, b) local exhaust ventilation (LEV), c) process-specific enclosures and d) general centralized ventilation. Due to the experimental work of the current study, described in Chapter 4, the general centralized ventilation has been chosen to be described in the present paragraph. In general, it is necessary for a well-designed ventilation system to have the right configuration in order to provide balance between the exhaust and supply air. Without air replacement, uncontrolled draughts will cause problems at doors, windows and other openings. In addition, turbulence established through high pressure differentials may result in the failure of the design goal of the ventilation.

The maintenance of proper pressurisation between production and nonproduction areas is a reasonable method for reducing the possibilities of emitted NPs escaping outside of the immediate work zone. Infiltration of particles is the main reason for fugitive emissions from the production and processing areas to nonproduction areas (e.g. offices and control labs). Therefore, according to NIOSH (2013) a negative air pressure differential should be maintained in the ENM production areas. To achieve a slight negative pressure, the exhaust air should be slightly more than the room supply air volume. A general guide is provided by the American conference of governmental industrial hygienists (ACGIH, 2013) and determines a 5 % flow difference between supply and exhaust air flow rates but no less than 0.85 m^3/min. From the above, it is apparent that a proper design of the ventilation can provide plant ventilation, building pressurization and exhaust air replacement. Before introducing

studies related to ventilation strategies it is proper to present the physical process behind ventilation resulting in the drop of the number concentrations after an accidental release of ENPs in an indoor environment.

2.3.1.1 Dilution

Dilution due to ventilation is a major process in reducing the concentration levels of dispersed ENP in workplaces. Figure 2.4 shows the mathematically determined particle concentration in a completely mixed room at different ACH. For the highest ACH (20 h^{-1}), a reduction to half of the initial concentration can be achieved after about two minutes. However, in a real workplace, conditions could be assumed such that the mixing of air would not be quite as efficient as in the theoretical description (of a well-mixed room). Furthermore, particle formation processes like resuspension due to the air jets established by ventilation may result in the decrease of the particle removal effect. Resuspension as mentioned in Section 2.2.3, is difficult to quantify, although the use of measurement devices could give an indication of whether these phenomena are taking place.

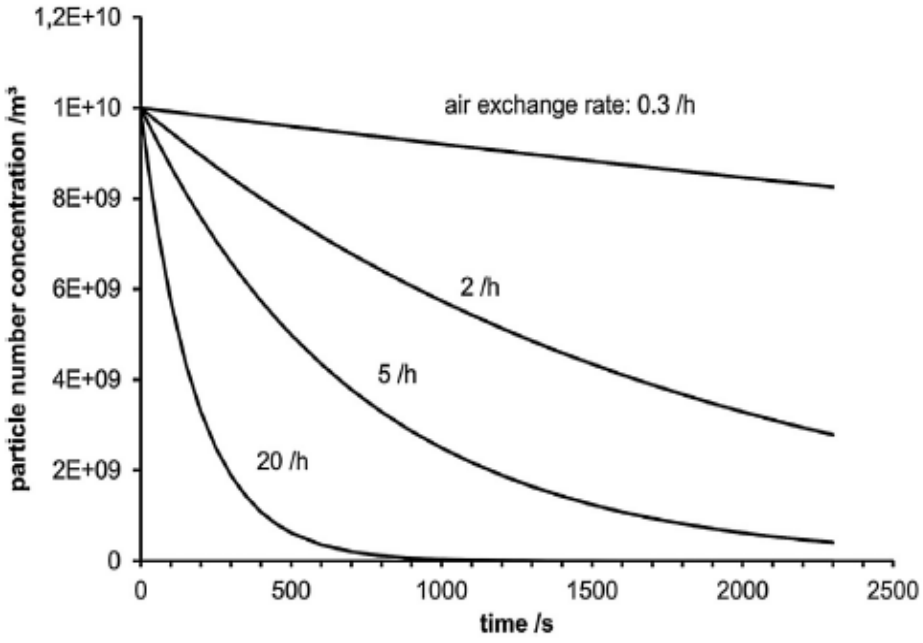

Figure 2.4: Mathematical representation of the dilution due to ventilation of an aerosol taking place in a completely mixed chamber at various ACH (Seipenbusch et al., 2014)

2.3.1.2 Experimental studies on the ventilation strategies for the mitigation of released nano-particulates in well-controlled indoor environments

According to Ding (2016), in a review of studies conducted between 2004 and 2016, types of engineering controls on ENP were frequently provided as contextual information. Regarding the most recent literature (2011-2016), studies are mainly related to PPE controls while

research on the removal efficiency in a simulated accidental release of ENP in relation to various ventilation settings is something which has not yet been conducted. However, there are various studies that indicate a very well established framework into which the current project was based some design aspects of the experimental process.

Bouilly et al. (2005) studied the impact of ventilation strategies on the indoor particle concentrations in a cubic experimental chamber (15 m^3). The combined effect of ventilation (0.5 and 1 ACH) and the inlet and outlet of air locations were tested. The instant particle injection into the test room was achieved via a compressed air device. The dispersion material was polyamide powder with size range 0.3-15 μm of spherical shaped particles. Two ventilation strategies were examined: Top-Top and Bottom-Top inlet/outlet configuration. They confirmed through numerical results that the particle removal depended on the air flow rate pattern within the room. Due to the influence of inlet and outlet location over fine particles (in the particular study fine particles were considered particles with diameter < 5 μm in diameter), the choice of the ventilation strategy has to be carefully taken into account in order to limit the particle pollution indoors.

Zhong et al. (2010) used a computer model to predict aerosol dispersion in an indoor room and they validated this with experimental data found in the literature. In this work the particle removal efficiency of two different ventilation strategies: mixing ventilation (MV) and underfloor air distribution (UFAD) system were tested. The air supply volume was considered to be the same (3.2 ACH) for both ventilation scenarios. The experimental data used for validation was obtained from the work of Zhang and Chen (2006) who injected monodisperse liquid droplets of average diameter 0.7 μm into a full scale chamber. The results showed that in the MV room the indoor particles were found to be more uniformly distributed than in the UFAD room. Additionally, the source location did not have a strong effect on the particle distribution, whereas the airborne particles due to resuspension were detected in the MV system.

Walser et al. (2012), in a study more related to ENP, introduced the spatial measurement of the size distribution over dispersed ENPs accidentally released in a 300 m^3 room. In more detail, during the production process of nano-particulate $CaCO_3$ by flame spray pyrolysis, scenarios of equipment failure were simulated in order to study the emission plume of NPs. The NPs produced by this process had primary particle size 50 nm and were characterised by high crystallinity. The experiment took place in a ventilated production room isolated from the outdoors and the incoming air was filtered, whereas the production facility was placed under a fume hood. For adjusted ventilation rates in the room (4 ventilation zones), the

corresponding background concentration was established before the production process started. The maximum ventilation rate was 6.5 ACH and was driven by the combined operation of the main room ventilation, the fume hood under which was placed the production facility and two more ventilation sinks of lower power. The results showed that at high ventilation rates and multiple ventilation sinks the emitted ENPs were dispersed quickly in the whole production room. Furthermore, within a minute after the release spatially uniform concentrations were reached. Even when the fume hood stopped working the general ventilation system was quite efficient for the removal of the dispersed ENP.

In conclusion, from the above studies it is apparent that a dispersed aerosol under ventilation conditions develops a bulk motion resulting in spatially the uniform concentrations in a dispersion room. Also the existing literature indicates a strong relationship between the location of the inlet/outlet air diffusers and the established flow pattern in the indoor environment. Therefore, it could be assumed that the exposure of an individual being in a room occupied by accidentally released ENPs would be determined by the relative location of this to the location of air inlet and outlet. Furthermore, the resuspension of deposited particles due to the air jets induced by ventilation should be considered as a factor potentially dropping the ventilation efficiency. However, there appears to be gap in published work on the estimation of the optimum ventilation power settings which could eliminate formation phenomena such as resuspension, and ensure the most efficient particle removal in an indoor environment after an accidental release.

2.4 Fire and explosion properties of ENP

A dust explosion may occur as the result of dust particle suspension in the air under confinement and the presence of an ignition source. Amyotte and Eckhoff (2010) stated that the severity of the incident is comparable to a gas explosion event. The process industry along its development in time has been stigmatized by a number of hazardous explosions, sometimes very severe. Among the earliest records of the cause of an industrial accident being attributed to a dust explosion, took place in a silo during discharge of contained plastic powder. According to Lüttgens (2005), the creation of a dust cloud during this process combined with a type of spark discharge resulted in the dust explosion. Despite significant research, the risks of dust explosions are still not well-known in industry, and dust explosions continue to occur (Worsfold et al., 2012). Nanotechnology is a rapidly expanding technology and consequently production and use are very likely to increase in the next few years (Bouillard et al., 2010) thus there will be more and more associated risks. Information on the explosion characteristics of ENM is necessary to predict the likelihood and severity of explosions and consequently to design proper explosion prevention and mitigation measures. Therefore it is essential to

develop initially the basic properties of ENM which are related indirectly and directly with the combustion-explosion topic.

Many nano-powders are known to be an explosion risk, particularly organic and metallic powders. In the event of a large release of ENP into the atmosphere an explosive dust cloud could be formed and if the cloud is within the explosive dust concentration range and an ignition source is available could ignite. It is essential to know the explosive characteristics of such a dust cloud in order to provide prevention/protective systems as part of a risk assessment. It has been shown experimentally that as the particle size decreases, an explosion could reach its maximum severity and this could be in the nanometer range (Eckhoff, 2012). Furthermore, the combustion regime is changing, as will be shown below, in the nanometer range, the process is leading to the acceleration of the flame front. This combustion regime is additionally the indication that the observed instabilities of flame development during the combustion process could be explained and understood for gaseous flames but have not been adequately investigated for ENP explosions. In order to accomplish safe dimensioning of prevention/protection systems, an adequate knowledge is required about the burning rate of an aerosol cloud in the actual process situation.

2.4.1 Constant volume explosion pressure of dust clouds

The most common method for the estimation of the rate of energy release during a dust explosion inside a constant-volume vessel is to measure the pressure rise as a function of time during the explosion. Without considering the volume of any solid, it is assumed that the gaseous species in the explosion process obey the ideal gas law:

$$PV = n_g RT = \frac{m_g}{M_g} RT \qquad \text{Eq. 2. 2}$$

where P, V, n_g, m_g, M_g, R and T are absolute pressure, volume of explosion vessel, moles of gaseous species, mass of gaseous species, average molecular weight of gaseous species, the universal gas constant and the absolute temperature, respectively. Since the volume is constant, the pressure rise is determined by the change in gaseous species and the net temperature increase due to the chemical reactions. The molar change contribution is usually far less important than that due to increases in temperature (Skjold, 2003).

The maximum constant volume explosion pressure is considered a static explosion parameter in gas explosion studies. The measurement of this parameter could be conducted through stoichiometric and thermodynamic considerations. However, in the case of combustible air-

dust mixtures, these calculations are insufficient because reactions are seldom complete (Lee, 1988). The traditional approach of determining the severity of a dust explosion is the measurement of pressure as a function of time in a constant-volume bomb. An additional tool for the evaluation of the explosion severity is the flame speed. Several researchers have calculated a theoretical flame speed using dynamic pressure data (Santhanam et al., 2010). This use of pressure data is due to the lack of optical access associated with the constant-volume bomb technique.

2.4.1.1 Explosion severity and ignitability of nano-powders

The procedure for measuring the explosion severity of dust/air mixtures is described in the European standard EN-14034 (2011) and the International standard ASTM (2010). These Standards determine the basic explosion characteristics of dust clouds and set the lower explosion limits as much as the limiting oxygen concentration appropriate for a potential dust explosion. To further understand the description of the parameters related to the dust explosion, first there should be identified the basic stages which constitute a typical scenario of a dust explosion, as described in Figure 2.5. Where ENP are dispersed into the atmosphere an explosive dust cloud could be formed and if the cloud is within the explosive dust concentration range and an ignition source is available it could ignite increasing in parallel the pressure of the enclosure space and causing damage to humans and installations.

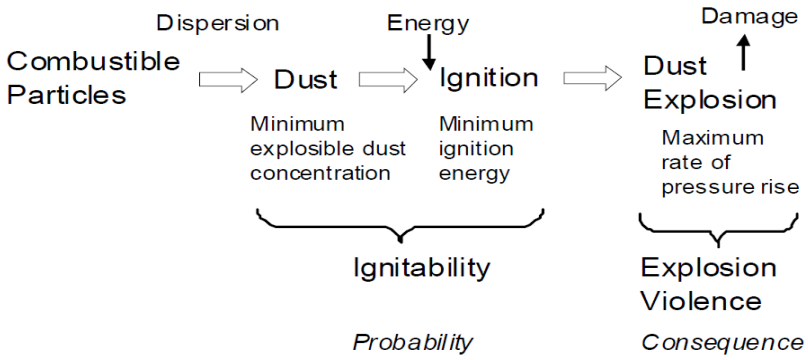

Figure 2.5: Typical scenario of a dust explosion Dobashi (2009)

This typical explosion scenario is applied in controllable atmospheres of enclosures with specific geometrical characteristics. Thus experimentally determined burning rates for dust-air mixtures are usually limited to the information that can be extracted from measurements of the pressure development in constant volume explosions. The standardised explosion vessel employed for the conduction of these tests in the current work is described in detail in Chapter 3.

Explosion severity of dust-air mixtures

The peak maximum explosion pressure, P_{max}, and the peak maximum rate of pressure rise, dP/dt_{max}, are measured in the standardised test procedure. Both parameters are used as indicators of explosion severity and violence and, according to Bradley et al. (2003), the measurement of the increase in pressure is associated with the rate of formation of burned gas. On the other hand, the optical access into spherical and cylindrical vessels provided by a small number of facilities, allows the application of optical techniques, such as schlieren photography, which can be used for the measurement of flame speeds. These techniques track the progress of the flame front relative to the unburnt mass (solid and gas) and are associated with the apparent rate of disappearance of cold reactants. However, direct measurement of flame propagation in these heterogeneous mixtures using the constant-volume bomb technique is uncommon in the literature.

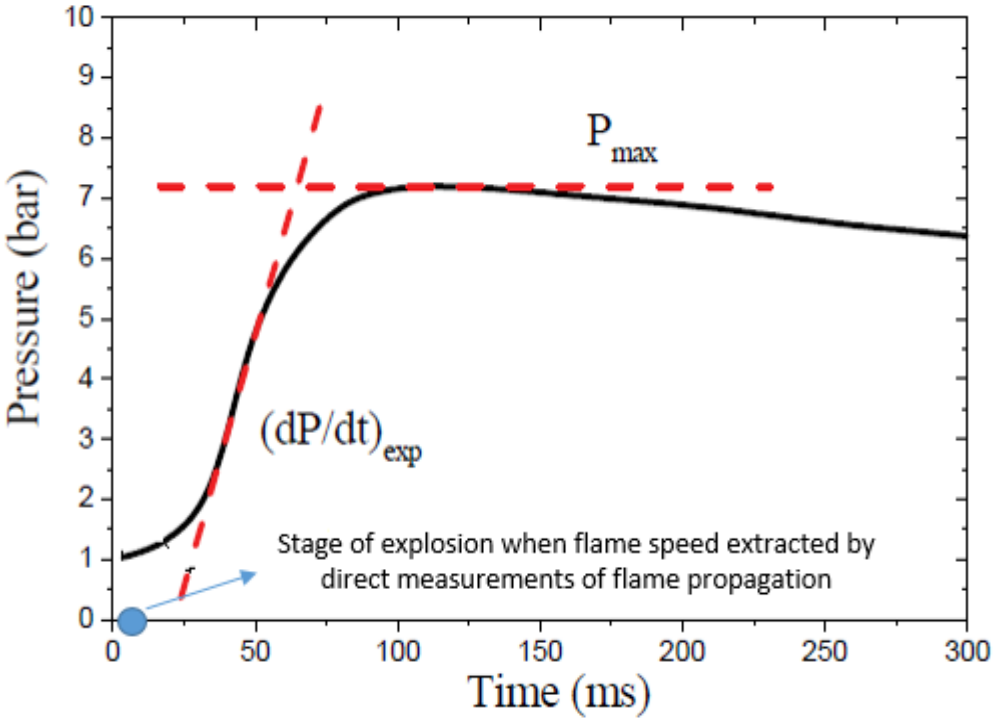

Figure 2.6: Pressure curve as a function of time for a typical dust-air explosion test in a closed vessel and the location of flame speed measurement (Dahoe et al., 1996)

A typical pressure trace for a constant volume vessel is illustrated in Figure 2.6. In the particular figure is also indicated this period of explosion during which flame speed is experimentally determined when optical access is provided by the facility. It should be noticed that pressure rise during the flame speed measurement based on optical access to the flame is negligible. In terms of risk assessment, in order to evaluate how fast a flame travels in space during the first milliseconds of an explosion then flame speed is the proper indicator for that

purpose. On the other hand, pressure measurements refer to a most extended period of explosion. After ignition, the pressure rises quickly due to the rapid release of energy from the burning dust. During this period the pressure parameters P_{max} and dP/dt_{max} are measured which corresponds to the stage when the flame has been stabilised within the vessel and has already passed out from the region where optical access is provided. After the maximum pressure is reached, the pressure within the vessel gradually decreases due to the heat exchange between the hot production products and the vessel wall. The utility behind the concept of knowing P_{max} for particular dusts is to design explosion-proof enclosures which will be able to withstand the high pressures of an accidental explosion. Furthermore, the dP/dt_{max} parameter is a useful inlet factor for the design of explosion relief venting and explosion suppression equipment (Amyotte et al., 1988).

Ignition sensitivity parameters

The parameters describing ignition sensitivity are the minimum ignition energy (MIE) and minimum explosible dust concentration (MEC). These parameters are experimentally determined by MIKE 3 apparatus, although it is not within the scope of the present work to give technical details of the MIKE3 mechanism. MIE is the minimum value of the energy that is needed to ignite the dust, whereas MEC is the lower flammable limit of flammable dust concentration. Both parameters have been found experimentally to become smaller for dust of smaller particle (Eckhoff, 2003).

2.4.1.2 Standard test apparatus for the determination of nano-powders' explosion severity

A typical standardised vessel consists of a hollow sphere of 20 L internal volume constructed by stainless steel. The typical procedure followed for dust explosion experiments in closed-vessel facilities is shown in Figure 2.7, where the process is divided into three stages. First, the rigid vessel is filled with approximately 1 atm air, depending on the desired conditions. Particles of interest are loaded into a container at the bottom of the rigid vessel. The particle container is commonly a smaller pressure vessel and is pressurized to a level that will transfer all the dust into the main experimental apparatus when a valve is actuated. Specific designs and geometries of the dust container and dispersion nozzle system vary throughout the literature, but the concept remains the same. The pressure within the experimental chamber is evacuated to a level such that the equilibrium pressure is 1 atm between the two vessels.

Second, particles are dispersed into the test chamber usinga controlled, strong blast of compressed air, which consequently produces turbulence within the facility. There is also an

inherent concern about the dust uniformity and test-to-test repeatability of the particle distribution as a result of the dispersion process

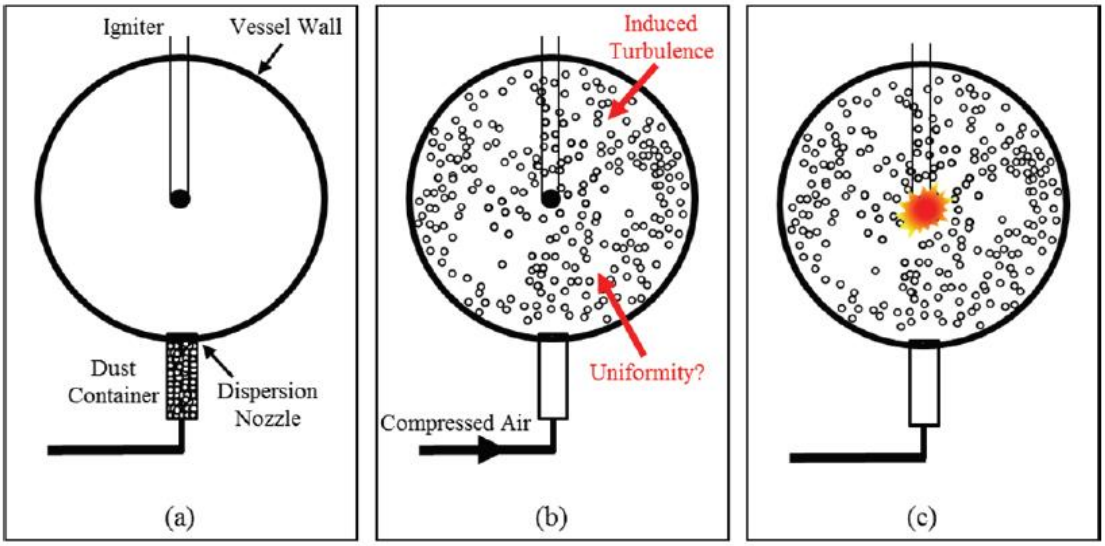

Figure 2.7: Typical procedure for constant-volume bombs: a) dust particles loaded into the container, b) particles are dispersed through a strong blast of air, and c) ignition occurs at the centre of the vessel shortly after dispersion (Vissotski, 2012)

The third step occurs several milliseconds after the particles have been dispersed. At this point, the dust-air mixture is ignited at the vessel centre, and the resulting flame will propagate outward. Again, the delay time between dispersion and ignition varies throughout the literature but is generally less than one second (Skjold, 2003). The pressure rise produced from the combusting dust within the vessel is typically the primary, if not the only, data recorded during the experiment. There is also additional uncertainty about the pressure rise, associated with the use of strong pyrotechnic igniters.

2.4.1.3 Cube-root law and its application to dust explosion

According to Dahoe et al. (1996), an important parameter for assessing venting requirements and for specifying automatic dust explosion suppression equipment is the maximum rate of pressure rise, dP/dt_{max}, obtained from closed vessel experiments. Since this parameter depends on the size of the vessel, it is normalized with respect to the volume of the vessel in question according to the 'cube-root law':

$$K_{St} = dP/dt_{max} V^{1/3} \qquad \text{Eq. 2. 3}$$

Where K_{St} is the volume-invariant dust explosion severity index and V is the volume of the vessel. Practically the cube-root law is used as a scale-up equation for the expansion of the

standard test results from laboratory-sized vessels to industrial-size equipment. Inaccuracy of this could result in sizing a vent improperly. According to Abbasi (2007), it will not be ensured that the vent becomes operative as soon as the overpressure exceeds a certain safe threshold.

Dust explosion class	Kst (bar m/s)	Characteristics
St 0	0	no explosion
St 1	>0 - <200	weak explosion
St 2	>200 - <300	strong explosion
St 3	>300	very strong explosion

Table 2.3: Classification of powders severity according to their explosion severity index (Bissel, 2008)

Bissel (2008) has assigned an explosion class to the nano-powders evaluated so far according to their explosion severity index (Table 2.3). Nano-aluminum powders, as we are going to see below, have high explosion sensibility making them more likely to ignite and the severity of explosion is classified as strong or very strong (St 2 or St 3) depending on the particle size. The question then arises is "which are the properties of the airborne ENPs that influence the severity of explosions being involved?"

2.4.2 Explosion characteristics correlated with nanoparticles' properties

Nano-scale materials are known to exhibit significantly different physical, chemical, electrical and optical properties compared to their properties at the macroscale (Yetter et al., 2009). Accidental release of nanoparticles into the atmosphere is outlined by behaviour of the airborne matter which determines the intensity of consequences related to public health. Therefore the description of the basic properties of nanoparticles related to their explosion potential is of great importance. Before starting the development of the nanoparticle's properties related to their explosion severity, it is also important to discuss the main groups of combustible particle materials. According to Eckhoff (2012), the main groups of this category are:

- Natural organic materials (grain, linen, sugar etc.)
- Synthetic organic materials (plastics, pigments, pesticides etc.)
- Carbon, coal and peat

- Metals (aluminium, magnesium, silicon, zinc, iron, titanium etc.) including their metal oxides

Based on the mechanisms governing the combustion process, as going to be shown below, a wider division of nano-powders could be into metallic and non-metallic.

2.4.2.1 Agglomeration and sedimentation

Agglomeration has been discussed extensively in Section 2.2.3.2. As indicated also in the same section, the change in diameter due to agglomeration contributes to increasing the effect of gravity on particle movement. Particles become heavier in relation to air through the process of coagulation, and gravitational sedimentation starts to play a major role in a particle's movement. Also, as indicated in Section 2.2.1, high mechanical energy should be applied to a nano-powder sample in order to release high fractions of nano-agglomerates in air. Therefore, if the provided energy is not efficient, then particles of various diameters would be released including particles in the μm-size range which sediment and are removed quickly from air. The level of sedimentation is actually regulating the residence time of the nanoparticles in air because the increased surface area of the large particles under sedimentation provides a surface for the smaller in diameter particles to diffuse onto. This subsequently works as a removal mechanism and determines the duration of the existence of an explosive atmosphere consisting mainly of submicron particles. The question then arises is "could the dispersion processes of a given nano-powder lead to large agglomerates capable of significant sedimentation?"

2.4.2.2 Oxidation sensitivity of NPs

The oxidation sensitivity of nanoparticles is another property, important in connection with serious accidents, which has a decisive influence on the fire and explosion properties of the particles. According to Eisenreich et al. (2008) oxidation is related not only to the surface area of the particle but also to whether or not the surface is covered by a protecting layer. However, as will be shown below, metallic and non-metallic nano-powders display different oxidation sensitivity.

Metallic nanoparticles e.g. aluminium, magnesium and titanium are pyrophorous which means that they could ignite in contact with air at low temperature. Their ignitability has been experimentally clarified and their particle size can significantly change properties related to the explosion characteristics of a powder which become more intense as the particle size decreases. Furthermore, Eisenreich et al. (2008) claimed that metallic nanoparticles freshly manufactured in an inert atmosphere display a significantly higher sensitivity to oxygen and thus are more sensitive in a potential explosion. This is due to the absence of oxygen on their

surface which, according to Yetter et al. (2009), determines the explosion properties of nano-powders when they are in an oxygen containing environment (creation of a condensed oxide protecting layer). However, the above does not mean that all the metallic nanoparticles are pyrophorous, for example metals used in nanotechnology such as nano-silver do not display this characteristic. On the contrary, they have been examined for use as fire retardants in the wood industry (Taghiyari, 2012).

2.4.2.3 Turbulence

Turbulence in a dust cloud causes a random movement of the dust cloud elements relative to each other in three dimensions. In quiescent conditions a dust cloud in an explosion demonstrates distinct orientations between burnt, burning and unburnt zones. On the other hand, in turbulent conditions, turbulence will generate local variations in particle concentration and local size distributions due to vorticity (Jarosinski et al., 2000). As a result, this is causing a three dimensional structure of burn/burning/unburnt with complicating characteristics and the cloud burns much faster. Furthermore, according to Eckhoff (2009), turbulence is affecting the ignition zone by removing the heat from this by rapid convention. Therefore, the explosion of a turbulent cloud requires higher energy inputs to get triggered than the explosion of a cloud under laminar conditions.

Initial turbulence

The turbulence generated by the industrial process itself could affect the burning rates of a dust cloud formed within a workplace. In real industrial operation conditions turbulence generated by fans or by other moving machinery may cause the formation of a combustible dust cloud. According to Eckhoff (2009), this kind of turbulence is described as initial turbulence and its direct effect is the increase of the minimum ignition energy (MIE) for the reason described above. Although when it comes to the violence of the explosion, the effect of initial turbulence is to increase the hazard.

Turbulence induced by explosion

Eckhoff (2009) defined another type of turbulence, that induced by the explosion itself. This turbulence is attributed to expansion of the unburned dust cloud ahead of the propagating flame. This “in situ” turbulence depends on the speed of the flow and the geometry of the confinement within which the explosion takes place. Therefore, it is clear that this type of turbulence varies from one apparatus to the next and this is one of the reasons for the observed discrepancy between the results in the literature.

2.4.3 Reaction steps of ENP ignition process

In order to understand better the explosion process of each powder in the airborne phase we should first focus on the combustion regime of each category of nano-powder (metallic and non-metallic) and the reactions related to the process of combustion.

2.4.3.1 Non-metallic ENP

The reason for a limiting particle size can be explained if one considers the various steps in the reaction mechanism. In the case of a dust explosion involving non-metallic nanoparticles e.g. coal or any other organic material, Pritchard (2004) argued that pyrolysis and devolatilization always precedes combustion, which primarily occurs in the homogeneous gas phase. The limiting particle size below which the combustion rate of the dust cloud ceases to increase, depends on the ratios between the time constants of the three consecutive steps of devolatilization, gas phase mixing and gas phase combustion. The above process is illustrated schematically in Figure 2.8. Particle size contribution in the process is described by its influence on the devolatilization rate as a higher specific area allows faster devolatilization. Therefore, if the gas phase combustion is the slowest of the three steps, increasing the volatilisation rate by decreasing the particle size will not increase the overall combustion rate. In the case of materials which yield gaseous pyrolysis products, the combustion gas phase is expected to be accelerated leading to smaller process times and consequently more severe explosions. For these materials the limiting particle size will be lower and probably in the nm-size range of diameters.

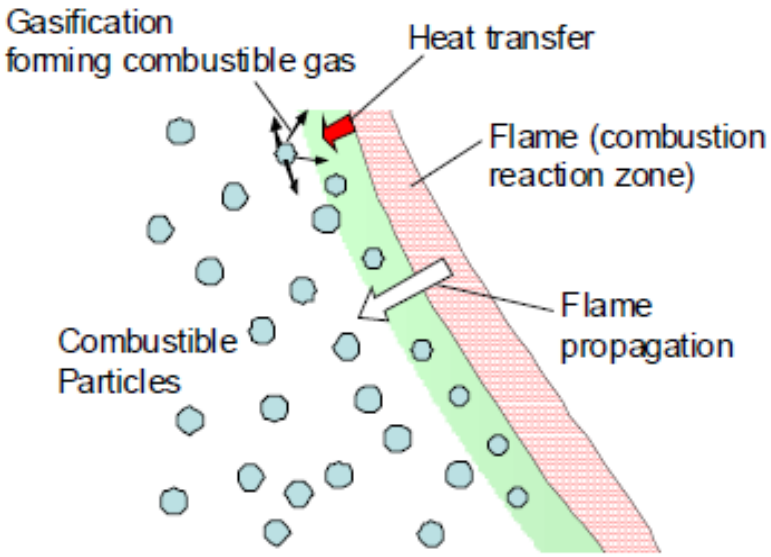

Figure 2.8: Combustion process during the dust explosion of non-metallic nanoparticles (Dobashi, 2009)

2.4.3.2 Metallic ENP

For metal dusts, especially the more reactive metals like aluminium and magnesium, the limiting particle size should be even smaller than for organic (non-metallic) dusts. The reason for the lower limiting size is that the reaction steps for a metal dust explosion are different and thus the rate limiting step will be different. According to Pritchard (2004), metal particles do not devolatilise or pyrolyse, but melt, evaporate and burn as discrete entities.

Yetter et al. (2009) going deeper into the limiting particle size issue, mentioned that as the particle size decreased, dimensionless numbers describing the heat conduction between the particle and the environment e.g. Fourier number and Biot number, are becoming small indicating that the particle temperature will quickly equilibrate to the surrounding temperature and become uniform throughout the particle mass. Therefore the heat released from the combustion would preheat faster the unburned particles by gas convective heat transfer and flame thermal radiation. As the particle temperature reaches the ignition temperature then, according to Li et al. (2011), the preheat zone becomes the combustion zone and the burning rate increases leading to an increase of the explosion severity accelerating the flame spread until all dust particles will burn out.

2.4.4 Relation between particle size and explosion severity

According to Eckhoff (2012), the flammable dust clouds of most solid combustible materials experimentally have been shown to become more sensitive to electric spark ignition and burn with increasing violence as the size of the primary particles in the dispersed phase decreases down to the order of 1-10 μm. For both metallic and non-metallic carbon nanoparticles, studies have shown that their explosion severity increases with decreasing particle diameter but appears to level out below a specific particle diameter value for each powder. This observation on the experimental results described as a ‘plateau’ effect and has been detected for both types of nano-powders, non-metallic and metallic.

2.4.4.1 “Plateau” effect of non-metallic nano-powders

The ‘plateau’ effect for non-metallic powders, specifically for organic powders (methyl cellulose, polyethylene and flour), have been described by Pritchard (2004) and accepted experimentally by Beck et al. (1997). When the particle size decreases the explosion severity parameters increase up to a plateau of approximately 50 μm. When the particle size decreases further, parameters increase only slightly. The only exception is observed for PVC powder which for large particles >150 μm gave no explosion detected, between 150 μm and 50 μm the increase is almost linear, although still low below the other three substances and for further

decreases the explosion severity parameters continue to increase. This differentiated behaviour shows that caution is needed in making statements in the nanometer range.

2.4.4.2 "Plateau" effect of metallic nano-powders

In the case of metal powders such as aluminium and magnesium, a plateau effect must be anticipated at smaller particle diameters than for organic powders (Pritchard, 2004). No experimental values could be found in the literature. However, based on computations, Pritchard et al. (2004) were able to show that the plateau effect should occur for aluminium at a specific surface of 6.5 m²/g. This would correspond to a particle diameter of 0.34 µm. Mechanistically, since metal powder explosions proceed unlike powder explosions with organic particles, the process stage that determines the combustion rate is different, so that the particle diameter at the point where the plateau effect occurs appears to become smaller.

For aluminium nanoparticles, the plateau effect probably applies to particle sizes in the nanometre range. A comparison of experimental values measured by Bouillard et al. (2010) and Dufaud et al. (2008) shows that the maximum explosion overpressure of aluminium nanoparticles with a diameter of 100 nm (8.2 bar) and 200 nm (9.5 bar) does not increase in comparison to that for aluminium powder with a diameter of < 63 µm (12.5 bar). On the contrary, it actually decreases further.

2.4.5 Studies on the explosion violence and ignitability of nano-powders

Explosion severity tests have been conducted and presented by several studies investigating the final question: is the explosion of nano-powders more violent compared to conventional micron-scale powders? Furthermore are the nano-powders more sensitive to ignition? Most of the tests have been accomplished in the 20 litre standard test vessel whereas the vessel described in EN-14034 (2011) has 1 m^3 volume. The reason is that vessels of smaller volume reduced the quantity of test material required for the test procedure. The most popular tested material in the greatest number of studies is aluminium as the micron-scale dust has given the strongest indications of explosion violence.

2.4.5.1 Studies investigating the explosion sensibility of nanopowders

As indicated above, the MIE decreases with decreasing particle size. Experiments on metallic nano-powders have shown that they can explode with nominal ignition energies less than 1 mJ (Eckhoff, 2011; Wu et al., 2010a; Wu et al., 2009). The nanopowders tested in these works were titanium, iron and aluminum and the 1 mJ was the lowest energy that can be tested by a

MIKE 3 apparatus. The low MIE shifts these powders to higher ignition risk than similar micro-meter sized dusts.

Minimum ignition temperature has also been found to decrease with decreasing particle size, increasing the explosion potential of nanoscale particles over larger particles. As described in paragraph 2.4.2.2, oxidation sensitivity is a process significantly affecting the explosion sensibility especially to metallic NPs. Nano-aluminium has been found to ignite at a rather low ignition temperature of approximately 900 K, which is below the aluminium's melting point (Kwok et al., 2002; Huang et al., 2009). Finally, another extreme example of minimum ignition temperature, according to Dreizin (2009), is the preparation of thermites with nano- and micro metre particles. The comparison between these two materials indicated that micron powders were ignited at 610 ^{o}C whereas nanopowders ignited at 100 ^{o}C.

2.4.5.2 Studies investigating the explosion severity of nanopowders

Li et al. (2011) tested aluminium nanopowder explosion characteristics in the standard 20 litre test vessel. Without evaluating the particle size distribution of the dust cloud, the study indicated that the dispersion of nano-aluminium powder of primary particle size of 100 nm followed a rapid combustion process which had no evident difference from the micro-aluminium dust explosion. However, in spite of the P_{max} being nearly the same as each other, the dP/dt_{max} of nano-aluminium powder (59.6 bar·m/s) was much higher than for micro aluminium powders (17.2 bar·m/s), indicating that the finer particles resulted in higher burning rates due to their higher specific surface area. Also the combustion time of the nanoparticles (105 ms) was much shorter than 159 ms for the micro-aluminium powder. According to the authors, this may be due to the fact that the alumina oxidation layer covering the particles has lower intensity due to the lower specific surface area of the particle allowing the cracking to occur more easily.

Bouillard et al. (2010) studied the explosion severity parameters of CB and aluminium micro and nano-powders over a wide range of dust concentrations as illustrated in Figure 2.9. As can been seen, powder concentration comes to play an important role in the phenomenology of the explosion. However, the writers noted that the influence of the specific surface area in particle explosivity was minor. To support this they compared multi-walled carbon nanotubes (MWCNT) explosivity, found in the literature, to that of Corax nanoparticles, both originated from carbon black nanopowders, with specific surface area of 195 and 40 m^2/g, respectively. Despite the rather high specific surface area of MWCNT compared to Corax in powder form, the explosivity of both materials was almost equal. This difference in explosivity between the two powders could be attributed to the different size of the agglomerates in the powder form

(200 μm for MWCNT and 15 μm for Corax). Regarding the aluminium particles, as seen in Figure 2.10b, the 200 nm in diameter particles explode more violently than the 100 nm. This is also an indication of agglomeration affects taking place in the airborne phase of particles where the cloud originated from the dispersion of the smaller in primary particle size powder having a higher potential to agglomerate compared to the larger ones.

Turkevich et al. (2015) conducted explosion experiments on several carbonaceous nanopowders in a 20 litre explosion vessel. The goal of this study was the determination of the explosion severity and sensibility of the tested materials. They also measured the size distribution through a light scattering method of the dust clouds before the explosion. According to their results, carbonaceous nanopowders could be classified in the St 1 dust explosion class (according to table 2 St 1 class is characterised by weak explosion). These materials exhibited MEC in the range 10^{1}-10^{2} gm^{-3} whereas their MIE was estimated in the range 0.25 – 2.5 kJ. Regarding the particle characterisation in the airborne phase they concluded that through the statistical analysis of their results, there was no evident correlation between the explosion severity and the aggregate particle size.

The two studies conducted by Wu et al. (2010b) and Dufaud et al. (2011) present a more extreme combustion and explosion behaviour of nano-metallic particles compared to the micron-size range. Wu et al. (2010) were the first who plugged into the test vessel a sampling tube directly connected to a particle size distribution analyser (Engine Exhaust Particle Analyser, EEPS) in order to record the evolution of the dispersed particle mass and to determine the level of agglomeration. Results in this study showed that the diameters of the dispersed nano-aluminium particles (165 nm and 167 nm) were greater than the primary particle diameters (35 nm and 100 nm respectively) due to the agglomeration effect taking place in the airborne state. Continuing the analysis, the maximum explosion pressure appears to increase as it transitions from the micrometer to nano-range. However, once within the nanorange, the explosion pressure decreases. The maximum rate of pressure rise also shows an increase with decreasing particle size and this trend continues into the nanoparticle range. MIE is quite small at less than 1 mJ for both nano sized powders. Aluminium nanopowders present the same trends in Dufaud et al. (2011) in contrast to the Zinc nanopowder which has quite similar explosion behaviour to the micron-scale particles. However, MIE was extremely low for nanoparticles making the nanopowder extremely sensitive to ignition. In the micron range aluminium follows an increasing trend as the particle diameter decreases, in agreement with the wide study that has been conducted so far on the explosion characteristics of the micro meter powders.

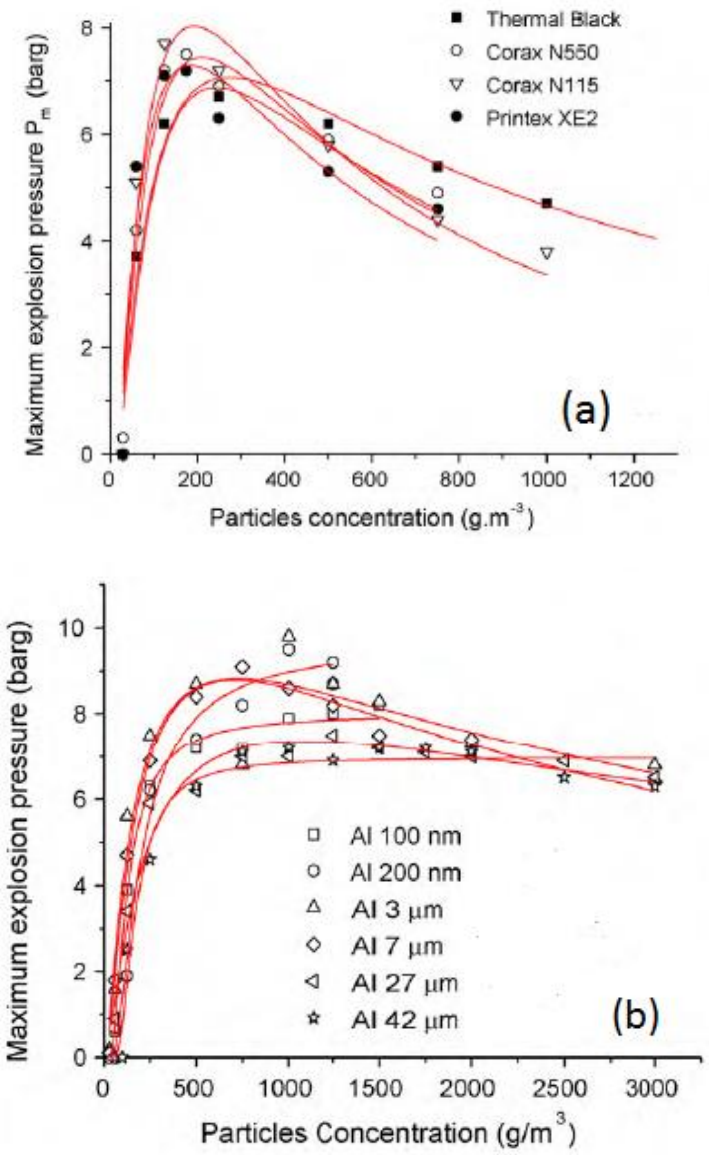

Figure 2.9: Comparison of experimental explosion pressures with best fit curves for (a) carbon black nano-powders and (b) aluminium micro and nano-powders (Bouillard et al., 2010)

In conclusion, it is clear that parameters like explosion severity and ignitability of powders are increased as the particle size decreases, although the majority of works presented above suffer from a lack of knowledge on the particle size characteristics in the airborne state. The estimation of the average particle size within a dust cloud at the initiation of its ignition is an information of crucial importance which should be included in the studies related to the explosion characteristics of nanopowders. Additionally, among the results on the explosion severity presented by the current literature is illustrated an agreement on the tendency presented by the explosion parameters to be increased by the decrease of the primary particle size. However, the measurements of those demonstrate a large deviation and this could be attributed to the utilisation of igniters of different ignition energy. More details on the effect

of ignition energy on the explosion parameters of a heterogeneous mixture are presented in Section 2.4.7.

Although in the nano-meter range, scientific observations on the explosion characteristics are synthesized by different conditions of the experimental process which affect the experimental results as the nature of mass, in the nanometer range becomes more complicated and sensitive to the changes of conditions. According to Worsfold et al. (2012) there are two physical processes that are believed to reduce explosion severity: limited dispersibility and high coagulation rates. The dispersibility problem, described extensively in section 2.2.1.1, is directly connected with the choice of the dispersion mechanism as much as with the physical-chemical properties of the considered dust (particle size distribution, morphology, humidity etc.). Furthermore after an incomplete dispersion, agglomerates will continue to form as a result of collision between particles. As a result of both of the above processes, the effective size will be greater than the particles' primary nanometer size. Therefore more research is required to reach a better understanding of nanomaterial ignition behaviour, in particular, the effects of agglomeration on ignitability and subsequent explosion development of nanopowders.

2.4.6 Hybrid mixtures

A hybrid mixture is caused by the combination of a combustible dust and a flammable gas. According to Worsfold et al. (2012), within the form of a hybrid mixture, the dust may be present below its MEC and the gas may be present below its LFL. The combination of both conditions creates a potentially explosive mixture. Therefore, it is important to identify the changes in the thermodynamic parameters of an explosion by the addition of a flammable gas in a dust-air mixture.

2.4.6.1 Explosion parameters of dust and flammable gas in hybrid mixtures

As will be shown below, it has been experimentally proven that the addition of a flammable gas to a dust results in the increase of the explosion parameters of the dust alone. Regarding the maximum explosion pressure, which is a thermodynamic parameter, both gas and dust bring their own combustion enthalpy to the mixture (Worsfold et al., 2012). However, in the case of the maximum rate of pressure rise which is considered a kinematic parameter, there are more than additive effects. According to Worsfold et al. (2012), these effects depend on the fuel-air ratio and are difficult to predict. Following Amyotte et al. (2010), both explosion parameters have been found to be promoted and to be greater than for either the dust or the

gas alone, although the maximum rate of pressure rise has been proven to be more apparently affected.

The effect on the MEC by the presence of a flammable gas

Explosions may occur in hybrid mixtures below the MEC of the dust alone. In that case, the explosion pressure is to a certain extent dependent upon the flammable gas equivalence ratio (partial pressure of gas in the mixture). However, for dust concentrations above the MEC, the explosion pressure becomes independent of the concentration of flammable gas and instead depends upon the oxygen levels (Garcia-Agreda et al., 2011). On the other hand, the maximum rate of pressure rise parameter has presented to be influenced by the flammable gas concentration, even above the MEC, and this effect is diminished as the dust concentration increases above the MEC (Garcia-Agreda et al., 2011). At the leaner dust concentrations the presence of the flammable gas has the maximum effect on the explosion parameters as the controlling variable of the combustion kinetics is led by the gas (Dufaud et al., 2009).

The effect on the LFL by the presence of dust

It has been proven that the LFL of a flammable gas could be affected by the presence of a dust in the mixture. According to Worsfold et al. (2012) the LFL is reduced by the addition of a small amount of dust. An example of that is given by Dufaud et al. (2009) who indicated that the LFL of toluene is 8 %, although, it has been shown to explode at a concentration of 4 % after addition of combustible dust. Also, methane, due to its unique oxidation characteristics, has been found to be less ignitable in methane-air mixtures compared to other hydrocarbons. This is due to the high energy required to break the C-H bond of methane gas (Pilão et al., 2006). Although, increased explosion risks have been reported in methane/dust mixtures according to Worsfold et al. (2012). Furthermore, explosion could occur when the dust is below the MEC and the flammable gas is below its LFL and this explosion can still be violent (Dufaud et al., 2008). However, the influence in the LFL of a gas after the addition of airborne ENP originating from low nominal dust concentrations is something which has not been studied yet.

2.4.6.2 Studies investigating the explosion characteristics of hybrid mixtures

Several works studied the explosions in hybrid mixtures in the past, although there are still unanswered questions about the phenomena involved. If we consider the average particle size of the dusts tested in these works, then a minor number of studies have focused on hybrid explosions involving ENM.

Kosinski et al. (2013) focused on explosions of carbon black nanopowders under the addition of some quantities of propane in a 20 litre explosion vessel. The specific tested material according to the authors had a very low volatiles content. The igniters used in this work were 1 kJ and 2x5 kJ. The results showed that for lean gaseous mixtures, the addition of nanopowders increased the explosion pressure and maximum rate of pressure rise. Similar trends were observed for the rich gaseous mixtures. For the highest nominal dust concentration (500 gm^{-3}) no explosion was recorded and according to the authors this could be attributed to high deposition of the suspended NPs in piping and dispersion nozzles. The SEM images on the explosion residues revealed the formation of large agglomerates. This phenomenon probably makes the explosion study more complicated than it would be for individual particles. Two very interesting features were displayed in this work. The first is that in order to initiate the flame propagation of the hybrid mixture, the propane concentrations had to be above its LFL. The second is that in this work was attempted the ignition of the dispersed nanopowder without the flammable gas and it was not feasible.

Torrado (2016) studied the influence of carbon black nanopowders (Printex XE2 and Corax N550) in methane-air mixture explosions conducted in a 20 litre spherical vessel and a propagation tube. They also studied the effect of the initial turbulence by varying the ignition delay time (the time between the start of the air pulse for the injection of powder and the triggering of ignition) through Particle Image Velocimetry (PIV). They applied ignition at 100 J with chemical igniters. At a low dust concentration (0.5 gm^{-3}) of Printex nanopowder, they found that the explosion pressure was not modified significantly whatever the gas concentration and level of turbulence was. However, a slight but not noticeable decrease in the maximum rate of pressure rise was observed especially for high turbulence levels and rich fuel mixtures. For Corax nanopowder tests of the same concentration demonstrated similar trends with a slight difference observed at high turbulence levels where the negative effect of carbon black insertion on the explosion severity was less noticeable for Corax than for Printex. Furthermore by increasing the dust concentration from 0.5 to 2.5 g m^{-3}, the maximum rate of pressure rise was further decreased.

2.4.7 The Ignition Effect in homogeneous and heterogeneous mixture explosion tests

As two ignitors of different energy will be used in this work, it is important to investigate the findings of other works which have investigated the effect of ignition energy on the explosion phenomenology of homogeneous and heterogeneous explosive mixtures. The role of ignition energy on the explosion parameters of gas-air (Hertzberg et al., 1988), dust-air (Hertzberg et al., 1988; Pilão et al., 2006) and gas-dust-air (Landman, 1995; Di Benedetto et al., 2011) has

been studied and indicating that this particular factor significantly contributes in the explosion severity. All the above studies have confirmed a relationship between the amount of the provided energy and the volume of the vessel. More specifically, strong ignitors applied in small volume vessels have been proven to overdrive the explosion characteristics of a specified mixture through the conduction of tests under the same conditions on the same mixture in large volume vessels (Zhen and Leuckel, 1997).

In the case of an ignition point source, a device similar to the spark plug which will be used in the explosion tests of this work, which due to its low energy can be considered as an ideal ignition tool relative to the size of the test chamber. More information about the explosion chamber will be given in Chapter 3. Bradley et al. (1996) have shown that the flame propagation in a mixture of methane-air initiated by a central ignition point (spark discharge) stops being influenced by the ignition effect for radii larger than a few millimetres.

On the other hand, according to Zhen and Leuckel (1997), in a dust explosion triggered by a 5 kJ chemical ignitor in a 20 litre vessel with a maximum explosion pressure of 9.5 bar, it is expected that the volume of the flame kernel governed by the ignition effect will be 35 % of the total volume of the vessel. However, in the present work, as will be shown in Chapter 3, a much lower nominal ignition energy will be provided by the additional ignitor employed in the explosion tests. Therefore, it would be interesting to access the contribution of the excessive energy in the explosion characteristics of the mixtures which will be tested in this work.

2.5 Summary

It is clear from the discussion above that the simulation of the accidental release of ENP in a specially designed indoor environment to investigate their dispersion and explosion characteristics is something which has not yet been studied. In order to achieve realistic simulations representative of the conditions found in an accident, techniques should be developed that could overcome the agglomeration state existing in the cohesive nanopowders and provide realistic experiments of airborne ENP. In addition, the expected polydisperse nature of aerosols generated from nanopowders is a further complication in the airborne behaviour of the released ENP. Therefore, identification and quantification of the main aerosol processes driving changes in the morphological characteristics (e.g. size) of ENP, from the source to the receptor, is of high importance. Furthermore, as indicated in this chapter, the engineering controls for accidentally released ENP were frequently provided as contextual information. Therefore, there is a gap in the identification of these optimum ventilation

settings which would be able to eliminate phenomena such as re-suspension and ensure the most efficient removal in an indoor environment after an accidental release.

Additionally, as outlined in this chapter, the combustion regime of ENP has been reported by various works to cause instabilities in the flame development. While these instabilities have been explained and understood for gaseous flames, for ENP explosions they have not been adequately investigated. So far, the traditional approach for determining explosion severity through the measurement of pressure history in constant-volume bombs, has been used in the explosion studies of ENP. The acquired pressure data has been used for a theoretical calculation of the flame velocity due to the lack of optical access associated with the standard instruments such as the 20 litre sphere utilised so far in the study of nanopowders' explosivity. Therefore, it is important to obtain a knowledge of the real turbulent flame velocity through optical techniques in mixtures containing airborne ENP that will allow the accomplishment of safe dimensioning of prevention/protection systems in the future. To this end, the Leeds explosion rig, which includes excellent optical access, will enable the measurement of the fundamental quantities of burning rates, and turbulent flame structure and their evolution throughout the explosion.

In addition, an important factor that has not been studied in detail is the uncertainty in the correlation between the explosion severity of a dust cloud of ENP and the aggregate particle size in the cloud. Finally, the influence of dust in hybrid mixtures with a gas below its LFL has been studied with several indications that explosions can occur even at these low equivalence ratio values. However, these studies have not included ENP and currently there is no knowledge on the explosion potential below the LFL of gas when ENP are added in gas-air mixtures. Additionally, there is no knowledge on the level of extension below the LFL of gas and the role of the particle size in this process.

This chapter has provided a brief introduction to all these dispersion and explosion properties of ENP that make these hazardous for public health, especially in the case of an accidental release within indoor environment. The context for further research was presented via the uncertainty that surrounds current conclusions on the dispersion and explosion potentials of ENP. The following chapter provides details on the methodologies used to achieve the aims and objectives listed in Chapter 1.

Chapter 3

3. Experimental Apparatus and Measurement Techniques

3.1 Introduction

As indicated in Chapter 2, nanoparticle release studies under laboratory conditions could allow a systematic and quantitative analysis of processes and materials. Worst case scenarios, such as an accidental ENP emission to the workplace could result in further unwanted exposure situations which still need to be investigated. Additionally, the mitigation and control of exposure derived from accidental conditions in an indoor environment is another unquestioned issue which needs to be approached through experimental investigation. In order to derive detailed conclusions on the aerosol transport processes as well as the mitigation control performance in an indoor ENP accidental release, experimental data on temporal PNCs and PSDs needs to be collected. Whilst great progress has been achieved in recent years in the measurement techniques and strategies for the development of exposure assessments to airborne ENPs, there is still a lack of comparability among these and concerns over their performance. As PNC is worthy of consideration as a concentration metric in exposure studies, instrumentation for such measurements needs to developed, tested and compared.

Various types of apparatus have been used in previous nanopowder explosion studies for the determination of their burning rates. However, explosion studies on aerosolised nanopowders and flammable gas-air mixtures under isotropic turbulence in constant volume vessels have not been previously carried out. Furthermore, visualisation of flame development involving dust particles sourced from nanopowders can be linked to the flame velocity, as another means of assessing explosion severity parameters. As outlined in Chapter 2, one parameter affecting the explosion severity of dust particles is their size in suspended state when an explosion is triggered. As the particle size decreases, an explosion could reach its maximum severity and this could be in the nanometre range. Therefore, it is of great importance to obtain knowledge of the size of dust particles suspended in air at the moment when an explosion initiates, through the utilisation of real-time particulate measurement equipment.

To this end, the study of dispersion and explosion characteristics of ENP sourced from specific nanopowders have been conducted in the Leeds experimental facilities. Metallic nanopowders, given their strong tendency to agglomerate, were initially subjected to a particular processing technique to re-entrain them. The material form resulting from this was utilised in a device in order to be continuously injected in the Leeds dispersion facility.

Nearfield PNC and PSD were estimated using particulate characterisation instrumentation installed close to the spillage location, from which samples were taken. The decay characteristics of the accumulated aerosol following the end of injection, under different ventilation settings, were studied. Furthermore, the subsequent behaviour of the suspended ENP in the air in terms of dispersion, agglomeration and deposition were investigated for the periods during the injection and a prolonged time following the end of injection under unventilated conditions.

Additionally, the explosion characteristics of ENP generated from the dispersion of specific CB nanopowders in the Leeds explosion facility have been studied in the present work. Specifically, CB ENP was dispersed in lean methane-air mixtures and ignited under low isotropic turbulence (characterised by 0.83 m/s rms of the velocity) and by two different types of ignition system. By adding predetermined powder concentrations in methane-air mixtures, then the influence of the CB ENP on the explosion characteristics have been appreciated by comparing the results obtained for pure methane explosions. Furthermore, the LFL of methane-air for the determined condition applied in the explosion experiments of this work, was identified in order to evaluate any potential change after the addition of CB ENP. Particle size characterisation was conducted in the powder form as well as in the dust clouds originating from the predetermined powder concentrations. All the above were linked together in order to identify any correlation between the average particle size and the explosion violence in the relevant hybrid mixture.

This chapter describes the methodology used within this study. Firstly an overview of the dispersion and explosion facilities is presented as well as the auxiliary equipment used in the experimental procedure. Description of the methods of processing data is also included along with information on the data quality assurance procedures. Comparisons between the particulate instruments used in this work is also conducted and presented in this chapter. Finally, the methods applied for the introduction of nanopowders into the experimental facilities are described as are the protocols followed for the preparation of samples and mixtures before the main experimental stages.

3.2 Controlled indoor experimental facility

For the study of the dispersion characteristics of specified nanopowders, experiments were conducted in the aerobiological test facility of the Institute for Public Health Environment (IPHE) of the University of Leeds. The aerobiology chamber has been used in the past for aerial dispersion of pathogenic microorganism studies and is specially designed to simulate indoor environments and exposure conditions to carry out hazardous measurements without

the costs and difficulties presented for real life scenarios. The particular facility is described in more detail in the following section.

3.2.1 Room-sized dispersion chamber

The release of hazardous nanoparticulate matter originating from specific nanopowders in accidental situations was simulated in a specially designed airtight chamber. The main test chamber (32 m^3), as shown in Figure 3.1, and a smaller anteroom (8.75 m^3), were constructed from prefabricated, plastic coated, wipe clean panels. Two vertical locations indicated in Figure 3.1 have been considered in previous work (King et al., 2013) for the estimation of air velocities at the particular points. The reason for including these two locations in the schematic is presented in Section 3.2.1.2. Access into the main test chamber was via a sealed door which contains a window to allow observation of the inner space whilst the door was closed. Control of the power supply, air flow rates for the supply and extractor fans for the main test chamber was undertaken from panels outside of the facility. A pressure gauge indicating pressure within the main chamber was located alongside these panels.

The main test chamber was hermetically sealed with its own sterile inlet supply and was always operated under negative pressure conditions. There were two air inlets into the main test chamber, one located at a low level on the left hand wall and the other located in the ceiling. Air entering the test chamber was taken from outside the building through a pipe network and was pre-filtered before passing through an HEPA filter in order to ensure that the inlet air was sterile and contained very low concentrations of fine particles. The same set-up was installed for the exhaust air from the main test chamber to ensure its safety standards before being vented to the outside of the building. The main test chamber had six access ports situated around the walls which were used for sampling and for the introduction of nanoparticles into the chamber. Details on the injection mechanism applied in the present work are provided in Section 3.2.3.2. Moreover, the arrangements of the sampling instrumentation designed for the two different sets of experiments are presented in Chapters 4 and 5. When not in use, these access ports were sealed using threaded screw caps. Finally, shut-off dampers were present in both the inlet and outlet in order to ensure the internal volume was isolated during the release tests and were opened before the ventilation was activated.

One accidental scenario has been simulated and tested as reported in Chapters 4 and 5: the continuous severe leakage of ENPs which corresponds to the tip or rupture of a tank or the rupture of a pipe (aerosol injection). The ventilation rate varied from 0.5 to 12 ACH. Therefore various strategies can be studied for a given accident scenario, to assess the best strategy to reduce risks. Additionally, the hermetically sealed and adiabatic structure of the chamber

allowed the conduction of experiments on accidental ENP release and the study of aerosol characteristics under unventilated conditions.

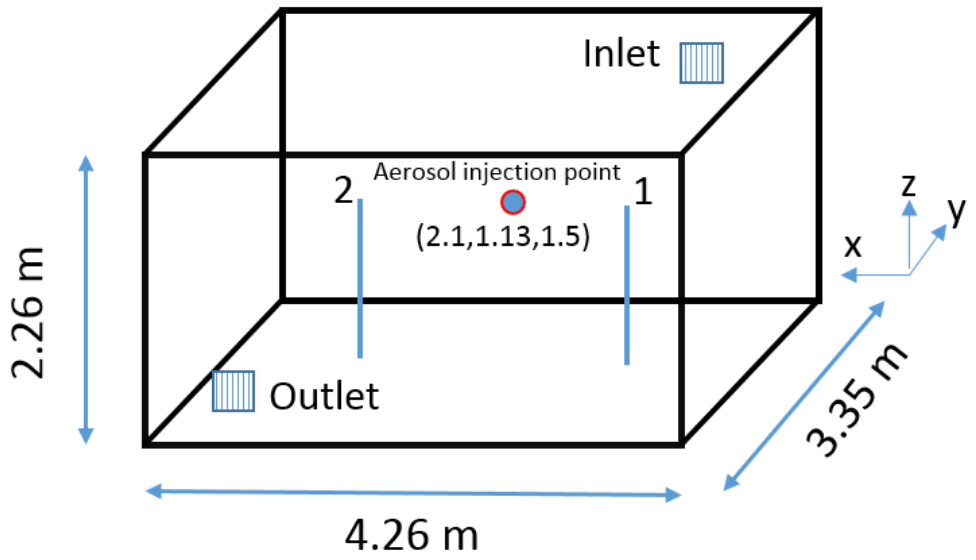

Figure 3.1: The dispersion chamber of IPHE of the University of Leeds

Prior to the addition of ENP to the chamber, it was necessary to establish a low background (BG) particle concentration in the chamber, for reasons explained in Chapter 2. In order to reduce the BG particle concentration, the chamber was ventilated for a 10 min period at the highest number of ACH prior to each experiment. Given the importance of the flow conditions in an indoor environment over the exposure levels, a specific sampling strategy should be applied in the indoor dispersion experiments. The designed sampling strategy was based on the inherent flow characteristics of the chamber under operational mode (ventilation on). These chamber's characteristics as well as the levels of BG particle concentration prior to each experiment are presented in the following two sections.

3.2.1.1 Background particle concentration in the chamber before the release of ENP

A major drawback of particle measurement devices is the lack of differentiation of BG particles from nanomaterial related particles. In order to ensure that any elevated PNC in the chamber was due to the ENP release process, the BG particle concentrations first had to be reduced to the minimum level by applying ventilation at 12 ACH. Several tests were conducted to ensure the stability of the evacuation performance of the chamber with regards to BG particles. A CPC, part of the experimental set up in the dispersion tests, was set to sample air from the room prior to each experiment. A typical evolution with time of measured

PNC obtained by a CPC is presented in Figure 3.2. The operational principles of the particular instrument is described in Section 3.2.2.3.

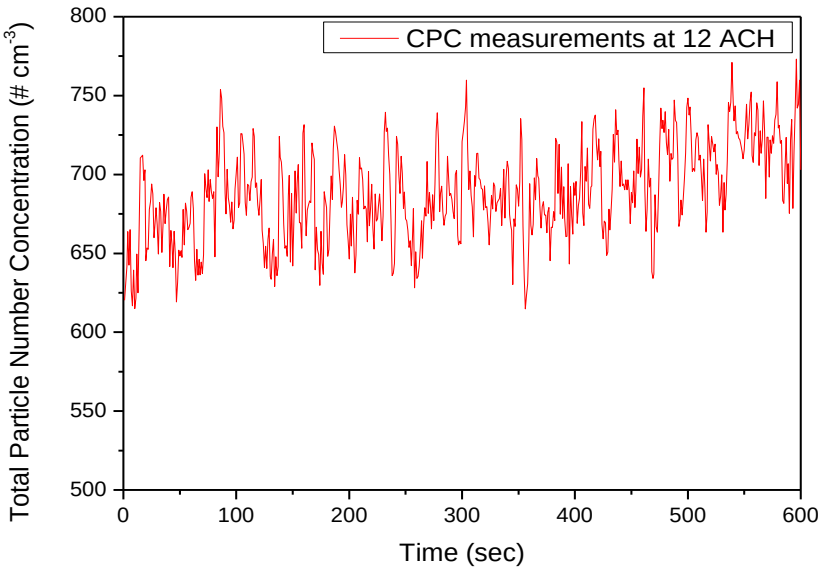

Figure 3.2: Typical evolution over time of BG particle concentration in the dispersion chamber at 12 ACH prior to the release of ENP

Considering that the detection size range of the particular instrument is of the order of the nanoscale then it can be concluded that HEPA filters were efficient enough at removing fine particles (< 2.5 μm in diameter) from the air introduced into the chamber. The indoor PNC reached a stable concentration of 650 particles/cm^3 at 12 ACH, one to two orders of magnitude less than the concentrations which could be measured in a typical indoor place (the particle concentration of an indoor environment ranges between 10^3 and 10^4 particles cm^{-3}).

3.2.1.2 Spatial air velocities under the operation of ventilation

As outlined in Chapter 2, the exposure levels to ENP in indoor environments are related to the air flow pattern. This pattern is determined by the location of the inlet and outlet air diffusers. Figure 3.1 indicates the locations of these diffusers for the Leeds chamber. Air in the dispersion chamber circulates between a top and bottom inlet and outlet diffuser located on the walls. King et al. (2013) measured the air velocities in the empty room corresponding to a 6 ACH ventilation rate by using a hot wire anemometer. The measurements were made on vertical lines at two locations as indicated in Figure 3.1. These measurements were compared by the authors to the results obtained by the application of two turbulence models (Reynolds stress model, RSM and k-ε re-normalisation group, RNG model) (Figure 3.3).

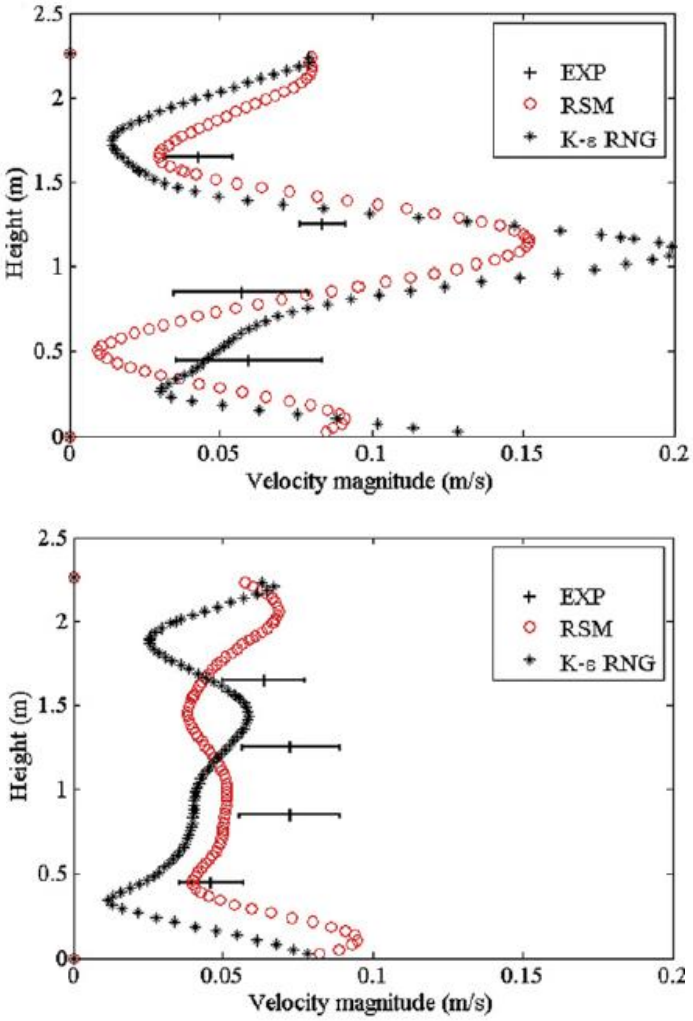

Figure 3.3: Anemometry comparison against k-ε RNG and Reynold stress model at (top) location 1, and (bottom) location 2 (King et al., 2013)

The results presented in Figure 3.3 clearly indicate spatial variability in the room airflow. The velocity at location 1 and at a height of 1.6 m from the floor (within the breathing zone) demonstrates higher values compared to those measured at location 2. According to King et al. (2013), this can be attributed to the impinging jet from the inlet diffuser to which location 1 is close. On the other hand, the low velocities in the region of location 2 correspond to slow recirculation of air. In conclusion, it is expected that the air inlet and outlet arrangement actually establishes two zones with different dilution rates. As indicated in Chapter 2, dilution is a major process in reducing the concentration levels of dispersed ENP in workplaces. Thus the employment of measurement devices with similar operational principles to each zone would give accurate estimations of the spatial ventilation efficiency profile during the decay period corresponding to various ventilation settings following an accidental prolonged release period of ENP, as will be investigated in Chapter 4.

3.2.2 Principal Particulate Instrumentation

3.2.2.1 Differential Mobility Spectrometer

The main piece of equipment used to measure the number based particle size distributions of airborne ENP within this study was a differential mobility spectrometer (DMS) which classifies particles in the size range $5 \leq d_p \leq 1000$ nm based on their mobility in an applied electric field. A photo of the DMS unit, with associated pump, is shown in Figure 3.4.

A series of grounded electrometer rings situated on the outside of an annular classifier allows simultaneous measurements of distinctly charged particles across multiple size classes. This makes the DMS a fast particulate spectrometer, with a response time of approximately 300 ms. This is very useful when the DMS is used for transient measurements of airborne ENPs that will occur in the dispersion tests.

Figure 3.4: Photograph showing the DMS unit and the associated pump (Cambustion, 2005)

The sampled poly-disperse aerosol is drawn into the instrument through the use of a vacuum pump, where instrument-software controlled dilution occurs. Particles > 1000 nm, which are greater than the maximum measurable particle size of the instrument, particles are removed from the inlet stream via a cyclone separator. The sample then passes through the three main components of the DMS; the aerosol charger, classification column and detection system (Biskos et al., 2005), as shown in Figure 3.5.

Initially, the sampled aerosol passes through a corona-wire uni-polar diffusion charger. The corona charger utilises a fine tungsten wire as an ion source. Through the application of a high positive voltage on the wire, ions are generated that flow into the aerosol flow region between the two electrodes on the charger (Biskos et al., 2005), and therefore the aerosol sample flow is exposed to the generated ions. The corona wire is prevented from becoming contaminated through a small grid surrounding the chamber which separates the sample from the corona wire, thus avoiding a subsequently unevenly charged sample. The main objective of the corona charger is to achieve the highest possible charge whilst minimising smaller particle losses due to diffusion (Reavell et al., 2002).

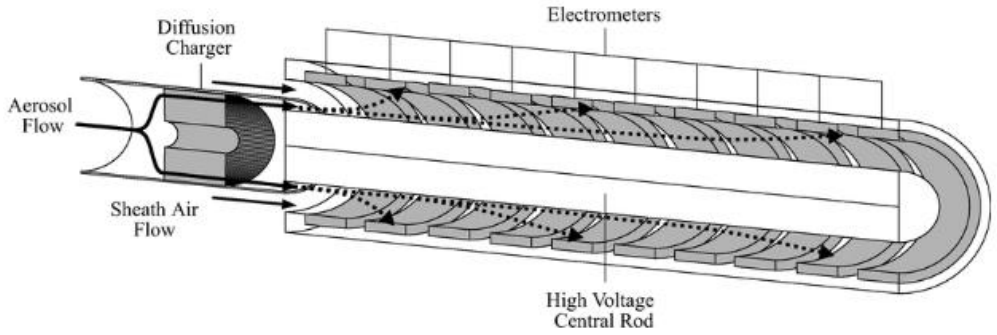

Figure 3.5: Schematic of the DMS classification column (Biskos et al., 2005)

This type of charger ensures a charging efficiency which is independent of particle composition (which makes it useful for studies on airborne ENPs sourced from different types of nanopowders), and is higher than that reported for bi-polar chargers (Biskos et al., 2005). In addition, the need for a radioactive charging source, such as those used in other particle instruments such as the scanning mobility particle sizer (SMPS), is eliminated by the use of a uni-polar charger.

The problems associated with the corona charger are losses of highly charged particles due to the strong electric field required to maintain the corona discharge (Agus, 2008). Additionally, multiple charging of the aerosol sample may occurs. The multiple charging causes particles of the same size to experience different electrostatic forces, resulting in particle collection in different locations on the classification column (Reavell et al., 2002; Biskos et al., 2005). However, through experimental calibration these problems are generally overcome.

The uni-polar charging at atmospheric pressure causes poor electrical mobility of larger particles (> 500 nm). To overcome this issue, the DMS is operated at a sub-atmospheric pressure of 250 mBar (Reavell et al., 2002; Biskos et al., 2005). As the pressure of the system

is decreased the electrical mobility increases. The increase is lower for larger particles and higher for smaller particles resulting in a greater gradient in the electrical mobility versus particle diameter function. As a result, the resolving power of the instrument is improved and the upper size limit is extended to 1 μm (Biskos et al., 2005). An additional advantage is that with decreasing pressure the charging efficiency increases.

After the aerosol charger the sampled aerosol is introduced into the classification column by a clean sheath air flow, where classification of particle size is taking place via electrical mobility. The charged particles enter the column, with the clean sheath air as shown in Figure 3.5. The air flow is adjusted so that the air flow in the column remains smooth and stratified (Biskos et al., 2005). Along the inner surface of the classification column, metal rings are connected to electrometers. A potential difference is applied between the two ends of the central rod. This produces a varying linear voltage along the axis, which in turn produces an electric field with a radial component. As a result, the charged particles are repelled outwards towards the electrometer rings, and the deposition of particles on these rings is dependent upon their electrical mobility (Biskos et al., 2005). An example of a particle trajectory within the classification column is illustrated in Figure 3.5.

In addition to the operating conditions, such as the reduced pressure described above, the number and width of the electrometer rings determine the resolution and range of the instrument. Also, according to Biskos et al. (2005), the sensitivity of the electrometers determines the minimum detectable PNC.

As particles deposit on specific electrometers they transfer their net charge and a current output is produced. Through the use of a transfer function of the instrument software, the calculation of the PNC and PSD is achieved via deconvolution of the electric current signal (Reavell et al. 2002; Biskos et al., 2005; Collings, 2003). By using this function it is possible to obtain a continuous PSD rather than a discrete binned PSD (Reavell et al., 2002). Electrically conductive silicon rubber is used for measurements taken within this study, in order to prevent the loss of naturally charged particles.

Initial calibration of the DMS was conducted by the instrument manufacturer, Cambustion. To check the accuracy of particle size measurements, certified aerosols containing particles of different diameters between 15 and 892 nm were sampled. During this calibration, Cambustion found the maximum error in detecting particle size was 8.8% (for particle size 892 nm) and the average error over all sizes tested was 4.0%. Internal instrument flow rates were also calibrated by Cambustion using an Aalborg GFC371 mass flow controller (DMS500 Certificate of Calibration, 2013).

As with any instrumentation used for analytical work, potential sources causing measurement error need to be considered. Briefly, the two main problems which occur when sampling with the DMS are due to instrument noise.

The first problem is associated with the instrument sensitivity, especially within the smallest diameter ranges. The electrical noise on the electrometers rings is relatively high during sampling when PNCs fall below the 'noise-floor' of the instrument. As a result, this electrical noise can produce positive and negative spikes in currents measured on the electrometer rings. One way to overcome this problem is to increase the averaging time of the measured data, as a decrease in noise can be approximated to $1/\sqrt{n}$, where *n* is the number of samples averaged across. As a result, improved signal to noise ratios across the entire size spectrum resulted from longer averaging times (Agus, 2008).

The second problem is associated with shifts in the base line during the zeroing procedure of the DMS due to instrument noise. During zeroing, a particular number of samples are logged by the instrument where a HEPA filter has been used to cover the internal sample inlet, with the number of samples logged based on the sample rate multiplied by 10. As described above, increasing the number of points logged during the zeroing procedure will result in the decrease of the noise by $1/\sqrt{n}$. If noise occurs during the zeroing significant shifts in the data baseline can occur. For high concentrations of particles, these shifts would not be important. However when sampling with lower concentrations of particles, these shifts can become problematic. Unfortunately these shifts cannot be corrected or minimised since the amount of zero data sampled is fixed (Agus, 2008).

As a result of these potential errors it became essential to check the entire data sets collected from the various measurement campaigns. This data checking procedure is described in more detail in Section 3.2.6.

3.2.2.2 Aerodynamic Particle Sizer Spectrometer

In this work in addition to measurements of particles over the nanoscale, measurements were also conducted at the microscale in order to assess the presence of larger airborne particles released during the injection process. As indicated in Chapter 2, large particles enhance the scavenging effect over small particles and subsequently affect their fate and behaviour in the air. Therefore, an aerodynamic particle sizer spectrometer (APS, TSI, model 3321) was employed in the present work for measurements in tests studying the dispersion characteristics of ENP in Chapter 5. The APS provides accurate count size distributions for particles with aerodynamic diameters from 0.5 to 20 μm. A photo of the APS unit is shown in Figure 3.6.

Figure 3.6: Photograph showing the APS unit (TSI, 2006)

The overall operation principle of APS is briefly described as follows: aerosol is drawn into the inlet and immediately split into a sample flow, through the inner nozzle, and a sheath flow, through the outer nozzle. As aerosol travels through the inner nozzle, the instrument is measuring the acceleration of aerosol particles in response to the accelerated flow. The aerodynamic size of a particle determines its acceleration rate (TSI, 2006). Therefore, large particles, accelerate more slowly due to high inertia.

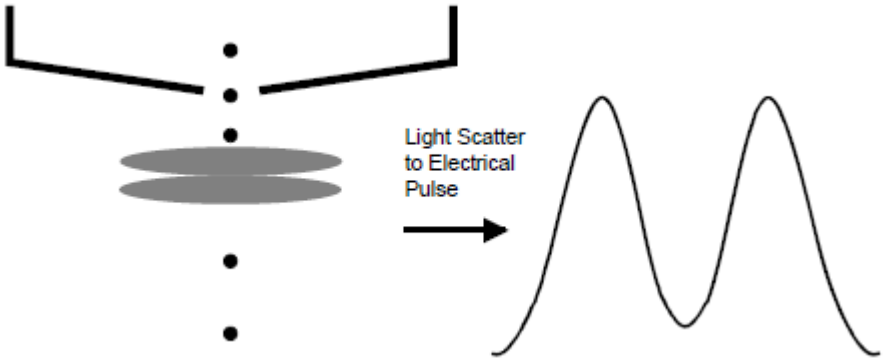

Figure 3.7: Double crested signal from particles passing through overlapping beams (TSI, 2006)

In contrast to the DMS, the produced size distributions are characterised by almost no background noise. This is due to the overlapping operation of two laser beams on which the instrument bases its detection ability. In more detail, when a particle passes through these beams, a single, continuous signal with two crests is produced (Figure 3.7). However, particles with diameters below the lower detection limit of the instrument produce a signal with one crest. Furthermore, in the sample aerosol there could be particles which produce more than two crests (coincidence error). None of the particles mentioned above are used in building size distribution calculations (TSI, 2006).

3.2.2.3 Condensation Particle Counter

The CPC (model 3775 by TSI) uses a light scattering technique to measure particles of diameter size up to 3000 nm. The particular instrument has a D_{50} of 4 nm and sampling aerosol with total flow rate 1.5 L/min. D_{50} is defined as the particle diameter at which 50 % of particles are detected. These types of counters measure individual particles through the quantity of light scattered as they pass through a focused beam of light.

Upon entering the CPC the aerosol is saturated with alcohol vapour (1-butanol) by passing over a heated bath, held at 35°C. The vapour-saturated aerosol then is introduced into a cold condenser (at 10°C) where cooling occurs. During the cooling process the alcohol vapour is condensed and the particles grow until they become sufficiently large (about 2 – 3 μm) to be optically counted. The calculation of PNC is made possible by separately counting the frequency of pulses of light scattered by individual particles as they pass through a light beam and scatter light onto a photo-detector (TSI, 2007).

3.2.2.4 Zeta sizer Nano

A Zetasizer Nano was employed in the present work for the particle size characterisation of samples of nanopowders suspended in water. The choice of a wet injection technique for nanoparticles (presented in Section 3.2.3.2) applied in dispersion experiments presented in Chapter 4 and 5, made it necessary to employ this particular device for the determination of particle size prior their injection. This particular device bases its operation on the Dynamic Light Scattering (DLS) method, which is suitable for measuring the size of particles in the sub-micron scale suspended within a liquid. According to Malvern (2013), the measurement range of the device has been estimated to be 0.3 nm – 10 μm. As the suspended particles are bombarded by the solvent molecules, Brownian motion causes a random movement which is related to the particle size. The larger the particles the smaller this motion will be compared to smaller particles which are kicked further by the solvent molecules and thus move more rapidly. The velocity of the Brownian motion is described by the translational diffusion coefficient (D) through which the device calculates the size of a particle (Malvern, 2013).

The coefficient D was estimated by measuring the rate at which the intensity of the scattered lights fluctuated. It is worth highlighting the difference between intensity, volume and number distribution measured by the light scattering method. Figure 3.8 describes the changes taking place in the size distributions as we move from the number to the volume and then to the intensity size distribution for a sample having two equal populations of spherical particles of diameter 5 nm and 50 nm. Considering that the populations between 5 nm and 50 nm are

equal, the number size distribution consists of two peaks of a 1:1 ratio. In the case of the volume distribution, the two peaks change to a 1:1000 ratio as the volume of a sphere is proportional to d_p^3. For further conversion to intensity the ratio will be 1:1000000 as according to Reyleigh theory, the intensity of a particle with size lower than the size of the wave length of the laser is proportional to d_p^6 (Malvern, 2013).

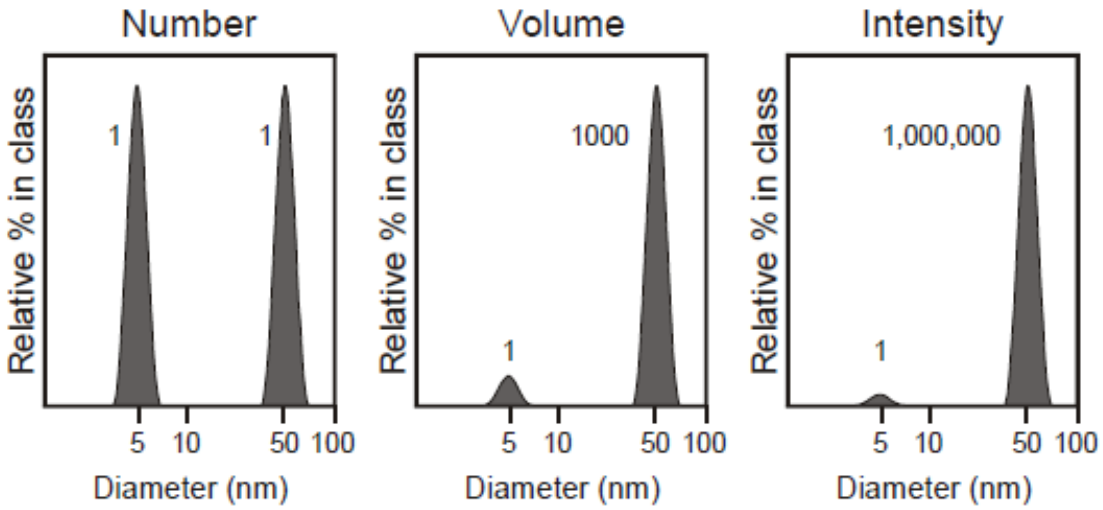

Figure 3.8: Number, volume and intensity distributions of a bimodal mixture of 5 nm and 50 nm (Malvern, 2013)

In conclusion, it is important to consider that the distribution obtained by the DLS method is based on the intensity which particles demonstrate in liquid suspension. All the other distributions are generated from this. This indicates firstly that this technique is extremely sensitive to the presence of larger particles in a sample. Secondly, it is proposed by the manufacturer to stop the conversion process on the obtained data at the volume distribution because small errors in gathering data for the correlation function will lead to very large errors in distribution by number. Therefore, in the present work, the DLS-derived PSDs of the liquid nano-dispersions will be presented in terms of volume fractions in Chapters 4 and 5. As the subsequent analysis on the aerosol produced by these liquids, through the atomization process described in Section 3.2.3.2, will be centred on the number based PSDs, any comparison between the particle size characteristics measured in the liquid and airborne state should be carefully considered.

3.2.3 Auxiliary equipment employed in the dispersion tests

3.2.3.1 Scanning Electron Microscope (SEM) and Transmission Electron Microscope (TEM)

An SEM was used in this study to assess the morphological characteristics of the particles composing the nanopowders used in the explosion tests presented in Chapter 6. However, while the SEM allows the efficient observation on the morphological characteristics in the powder bulk form, a TEM was also used in the present work for a more detailed analysis on the tiny precipitates collected from the surfaces of the dispersion chamber during the dispersion experiments presented in Chapter 5.

The SEM used was a Hitachi SU8230, high performance cold field emission (CFE) incorporating an Oxford Instruments Aztec Energy EDX system and an 80 mm X-Max SDD detector. The 8230 FE-SEM employed a novel cold field emission (CFE) gun for improved imaging and analytical performance. The newly designed Hitachi CFE gun complements the inherent high resolution and brightness of conventional CFE with increased probe current and beam stability (Hitachi, 2002). The samples were prepared for SEM analysis by fixing the nanopowders to an aluminium SEM stub using a carbon sticker. The samples were coated in approximately 5 nm of Iridium using an Agar Scientific high resolution sputter coater and were then inserted into the sample unit the SEM.

The TEM used was an FEI Tecnai TF20 of high resolution suitable for cryo single particles and semi-thick frozen cells (or sections up to 200 nm) electron microscopy and electron tomography. The TF20 was equipped with a Field Emission Gun (FEG) and +/-80° tilted computer controlled LiN cryostage. This microscope featured a TIETZ F415MP 4k x 4k multiport CCD camera with a 4-port readout and 15μm pixel size. Images were also recorded on a plain film camera (CNSI/EICN, 2008). 400 mesh Cu grids coated with holey carbon film (Agar Scientific) were attached to standard Al SEM stubs (Agar Scientific) using a spot of silver dag. Once the grids were attached, the stubs were placed inside the process chamber at various locations on the floor and the walls so particles could attach to the grids. After the experiments the grids were carefully removed from the stubs using tweezers and then transferred to the TEM for examination.

3.2.3.2 6-jet Collison nebulizer

A 6-jet Collison nebuliser (CN, BGI Inc., USA) was used in this work for the atomization of liquid suspensions of nanopowders and the subsequent introduction of the produced aerosol into the dispersion chamber. In the nebuliser, a gas was used to aspirate the liquid into a sonic

velocity gas jet, which leads to shearing of the liquid into droplets. Additionally, the walls of the jar worked as barriers on which the liquid/gas jet was impacted so that the larger fractions of the droplets were removed (Figure 3.9). In the present work, the nebuliser utilised a separate pump, pressure regulator and meter operating at a flow rate of 8 litres min^{-1} to deliver HEPA filtered air for the carrier gas. According to BGI (2002), the size distribution of particles ejected during the process was characterised by a mean mass diameter of 2.5 μm, or by a geometric mean diameter of 1 μm and a standard deviation of 1.8 μm. However, the eventual size distribution may have varied through evaporation and the experimental set up. In this study, the experimental setup of Chapters 4 and 5 included a heating section over the aerosol delivery pipe into the dispersion chamber in order to increase evaporation in the injected aerosol before release. More details are presented in the following chapters.

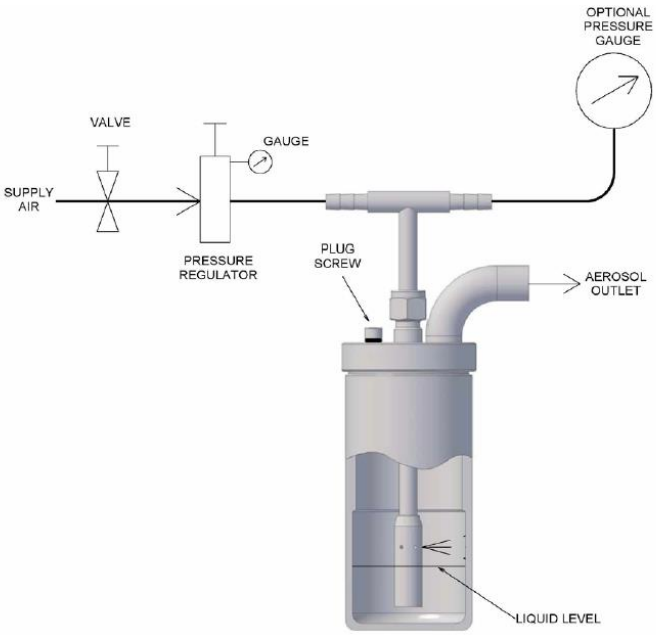

Figure 3.9: Schematic diagram of Collison nebuliser (BGI, 2002)

3.2.3.3 Ultra Sonicator

As described in the previous section, the nanopowder-water mixtures were introduced into the reservoir of a 6-jet Collison nebuliser for atomization. However, it was first required to process the sample in order to overcome the agglomeration problem indicated in Chapter 2. The purpose was to generate large fractions of particles with diameter <100 nm through aerosolization for subsequent assessment of their airborne characteristics. Thus, after an extensive review of previous studies, an ultra-sonicator was chosen for this purpose. The detailed process of sample preparation is presented in the next section.

The ultra-sonic processor used in this work was a UP 100H (Dr. Hielscher GmbH, Germany). The processor produced longitudinal mechanical vibrations by means of electric excitation with a frequency of 30 kHz (CmbH, 1994). The power output was adjusted in steps between 20 % and 100 % of the maximum output. A sonotrode fitted to the horn amplified the vibrations and transferred these to the liquid within which the horn was immersed during the process. The ultrasound produced cavitation in the liquid. The density of the acoustic power in the sample depended on the size of the sonotrode (Figure 3.10). The sonotrode of the particular device used in this work had a tip diameter of 7 mm and the acoustic power density provided to the sample was 130 W/cm^2.

Figure 3.10: Structure of the ultrasonic processor consisted of 1) the housing; 2) the horn and 3) the sonotrode (CmbH, 1994)

3.2.4 Sample Preparation

Samples of Aeroxide TiO_2 P25 nano-powder (average primary particle size 21 nm and specific surface area 50 ± 15 m^2/g) and Synthetic Amorphous SiO_2 (NM-200) (average primary particle size 14 ± 7 nm and specific surface area 189.2 m^2/g) were obtained and various dispersion methods were considered. As indicated in Chapter 2, agglomeration within nanopowders was very common and it was necessary to apply strong mechanical forces to break the bonds linking the particles. To this end, a method standardised by NIST (Taurozzi et al., 2012) for the preparation of nanoparticle dispersions of TiO_2 nanopowders was considered with some small modifications. The objective of this experimental work was to produce stabilised suspensions with large fractions of particles <100 nm in diameter. The experimental setup is illustrated in Figure 3.11.

Initially, weighed amounts of TiO_2 nanopowder, as proposed by National Institute of Standards and Technology (NIST), were suspended in 50 ml of Type I biological grade de-ionised water (≥18 MΩcm resistivity) within a 100 ml cylindrical glass beaker. The beaker was placed in a bath with chopped ice and water, and stabilised at the centre with clamps, as shown in Figure 3.11, and liquids were sonicated for 15 minutes. Through this method, TiO_2 nano-suspensions were produced with concentrations of 0.5, 1.0, 10, and 20 mg/mL and in triplicate for each concentration.

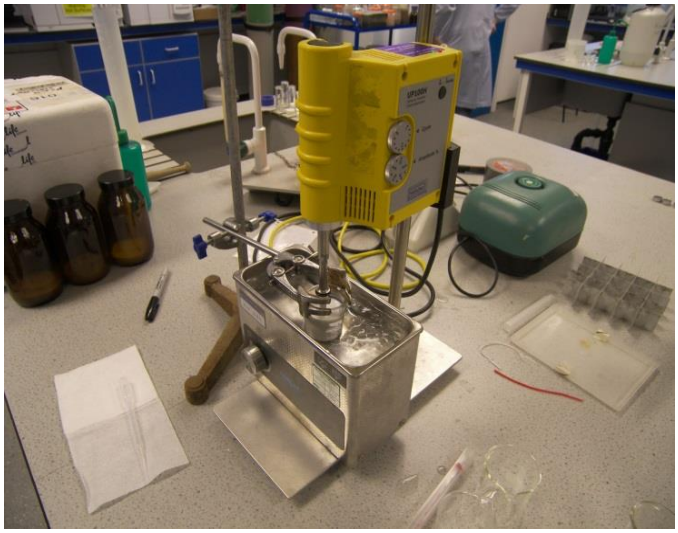

Figure 3.11: Experimental setup for the sonication of TiO_2 and SiO_2 nano-suspensions in purified water

Additional samples of the same powder concentration were sonicated for 30 minutes as a 0.7 cm diameter sonicator horn flat tip was used here, where the equipment protocol specified a diameter of 1.3 cm. However, a higher delivered power was used here (100 W) of a power of 50 W specified by the protocol.

Both sets of samples, once prepared, were immediately introduced in amber borosilicate glass containers to minimise their exposure to light (Taurozzi et al., 2012) and stored at ambient temperature for 24 hours. The next day, the samples were transferred to the Zetasizer for measurement of their PSD. The purpose of these tests was to evaluate the stability of dispersions with time against re-agglomeration, which according to the specified protocol has been validated up to 48 hours based on specific values of pH. Furthermore, these first comparisons between samples of the same concentration produced with different sonication times determined the ideal duration of sonication which ensured the higher fractions of particles with diameter ≤ 100 nm.

In the second set of experiments, a further comparison was conducted between samples of concentration 20 mg/ml and samples of increased concentration (30 mg/ml), both sonicated for the optimum time determined by the previous comparison and this time in a glass beaker of smaller volume (50 mL cf. 100 mL). The decision to increase the powder concentration was based on the investigation of the potential for further de-agglomeration through the reduction of the available space between the suspended particles. By reducing this available space, more particles then potentially come into contact with the tip of the sonotrode, therefore increasing the likelihood of achieving further de-agglomeration. Using the same logic, the smaller beaker was used. Similar to the first set of samples, all the samples here were produced in triplicate for each of the tested powder concentrations. Results of the PSDs obtained by the Zetasizer for both sets of experiments are presented and discussed in Chapter 4.

As indicated above, the specified process was first applied for TiO_2 samples and through this the optimum sonication time and powder concentrations were determined. The indication of these procedure characteristics established the final method of the sample preparation for the conduction of the experiments presented in Chapters 4 and 5. The same method was used to produce the SiO_2 suspensions for the dispersion tests presented in Chapter 5. Once produced, nano-suspensions were introduced into the reservoir of the nebuliser described in the previous section, which was subsequently utilised to atomise and inject the produced aerosol into the dispersion facility.

3.2.5 Dispersion Experiments

As mentioned in Section 3.2.1, one accidental scenario has been simulated and tested in Chapters 4 and 5: the continuous severe leakage of ENP corresponding to the tip or rupture of a tank, or the rupture of a pipe (aerosol injection). To this end, the suspensions produced through the method presented in the previous section were aerosolised through a 6-jet Collison nebuliser to represent the above accidental scenario. The injection time, after a number of tests with varying time, was determined to be 70 minutes. This particular length of the injection process was deduced from the required duration for the filling of the chamber with a sufficiently high aerosol concentration. This time was observed to be around 30 minutes, while in the following period the PNC was still increasing due to the injection. The rate of increase gradually plateaued due to the particle interaction counteracting the increase caused by the addition of fresh nanoparticles. The accumulated aerosol in the chamber's atmosphere obtained after the specified injection period was then subjected to decay through the application of various ventilation settings (3, 6, 9 and 12 ACH). Particle decay characteristics were monitored through a DMS and three distributed CPCs at various locations and results are presented in Chapter 4. Three replicate tests were conducted for each ventilation condition.

More details on the arrangement of the sampling instruments in the chamber's area are presented in Chapter 4.

A similar injection time was used in the experiments presented in Chapter 5. In contrast to the ventilation experiments, a prolonged period of study (5 hours) during which the accumulated aerosol concentration decayed under unventilated conditions, followed the end of injection. During both experimental periods, the near field source measurements of the PNC and PSD were conducted by a DMS, a CPC and an APS. In addition to aerosols produced by TiO_2 suspensions, experiments with SiO_2 suspensions in the nebuliser's reservoir were also conducted. Similarly to Chapter 4, three replicate tests were conducted for each of the tested materials and the arrangement of sampling devices is illustrated in Chapter 5. Finally, metallic stubs were placed at various locations on the floor and the walls of the chamber in order to collect deposited matter for subsequent TEM analysis.

3.2.6 Methods Processing of Data

In this section the techniques for processing the PSDs obtained by the dispersion experiments described in the previous section are presented. The PSDs measured by the DMS were modelled in order to study the evolution of the fitted component modes over time in Chapters 4 and 5 as well as to reveal the temporal size components within the PSD of the dust clouds before the initiation of the explosion tests in Chapter 6.

3.2.6.1 Modelling Particle Number Size Distributions

As particle size influences numerous impacts (Agus, 2008) it is important to find a way which will best describe the characteristics of PSDs. The following part of this section outlines the derivation of an equation which was used to describe the PSD of sampled particulates.

If *N(d)* is the number of particles in the interval *d* to *d* + *∂d*, where *d* is the particle diameter, the number distribution is given by;

$$\partial N = N(d)\partial d \qquad \text{Eq 3. 1}$$

Since the present work studies the dispersion of specific nanopowders, the diameters of the relevant airborne ENPs ranged over several orders of magnitude. Therefore, it became convenient to use a log format to describe the size intervals. In this work the Log_{10} format has been used. Therefore, the total PNC expressed in this format becomes;

$$\partial N = N(d)\partial Log_{10}d \qquad \text{Eq 3. 2}$$

As PSDs are seldom uniform in size, and indeed are composed of particles from a variety of different sources, it is effective to describe the distribution by distinct populations or 'modes' (Wehner and Wiedensohler, 2003). The most widely used function is the Log_{10}-normal distribution. According to Lingard et al. (2006), this enables the distribution to be described by a small number of parameters, the modal particle number concentration (mPNC) (or number fraction), count mean diameter (*CMD*) and geometric standard deviation (σ_g). Log_{10}-normal distributions are a group of distributions that have the same general shape, and are obtained from the normal function simply by using logarithmic values (Agus, 2008). They are symmetrical, with values more concentrated in the middle than in the tails. The basic normal distribution is described by the following equation;

$$f(x) = \frac{1}{\sqrt{2\pi\sigma^2}} e^{-(x-\mu*)^2/2\sigma^2} \qquad \text{Eq 3. 3}$$

where- $-\infty < x < \infty$

μ* - mean, and

σ - standard deviation.

Substituting in particulate variables for a mono-disperse population, this equation becomes (John, 2001);

$$\frac{\partial N}{\partial Log_{10} d} = \frac{N}{\sqrt{2\pi} Log_{10}\sigma_g} \exp\left[\frac{-(Log_{10} d - Log_{10} CMD)^2}{2(Log_{10}\sigma_g)^2}\right] \qquad \text{Eq 3. 4}$$

where: N - total number of particles (cm^{-3}),

d- particle diameter (nm),

σ_g - geometric standard deviation, and

CMD - count mean diameter (nm).

As mono-disperse aerosols consist of particles with a narrow range of diameters (typically 10 – 20% spread) they are only likely to be produced by laboratory controlled manufacture (Baron and Willeke, 2001). Therefore, measurements taken in aerosols originating from

nanopowders dispersion, as indicated in Chapter 2, are not likely to be mono-disperse, and Equation 3.4 needs to be expanded to reflect this. A typical PSD, consisting of *n* modes, is found to fit a sum of $\log_{10}$-normal distributions as shown below;

$$\frac{\partial N_{TOTAL}}{\partial Log_{10}d} = \frac{\partial N_{I}}{\partial Log_{10}d} + \frac{\partial N_{II}}{\partial Log_{10}d} + ... + \frac{\partial N_{n}}{\partial Log_{10}d} \qquad \text{Eq 3. 5}$$

Therefore if the equation can be solved for individual modal parameters, the evolution of size-segregated particle number size distributions can be accurately predicted and modelled.

Modelling Size Distributions with RMixDist

In this study, the modal parameters of mPNC, *CMD* and σ_g, were estimated through a modal fitting computer program called RMixdist. The particular program was developed by Macdonald and Green (1988) and analyses histograms as mixtures of statistical distributions by finding a set of overlapping component distributions that gives the best fit to the overall histogram. A 'mixture distribution' arises when sampling from within a heterogeneous sample with a different probability density function in each component (Du, 2002), such as those measured in nanotechnology workplace which are poly-disperse mixtures of particles arising from various sources. The distributions can be normal, log-normal, gamma or exponential distributions.

The RMixDist software uses an input text file along with an initial 'guess' of the modal parameters, which includes the number of modes present, approximate *CMD* and σ_g (Agus, 2008). During this study, a combination of previously reported modal parameters and estimates from inspecting the distributions were used in order to conduct the initial 'guesses'. RMixDist then uses the maximum-likelihood estimation method to provide a fit, and after a number of iterations outputs a modelled fit of the overall distribution and the modes within. This program has previously been used to describe urban roadside particle size distributions by Lingard et al. (2006), and a full description of its attributes are described by Leys et al. (2005).

The initial problem is deciding the number of modes which are required to accurately describe the PSD (Agus, 2008). Typically, in atmospheric studies, the size distribution of particles are characterized by size modes caused by aerodynamic processes. These modes according to Schneider (2011) are: nucleation mode (< 20 nm), Aitken mode (20 – 80 nm) which is the transition mode between nucleation and accumulation modes, accumulation mode (80 – 1000 nm), and coarse mode (> 1000 nm). Similar physical processes resulting in these distinct modes can be considered in the indoor studies related to emissions of ENP. It is probable that

the requirement for more than three modes, laying within the categories described above, is due to the transient nature of the released ENP as indicated in Chapter 2.

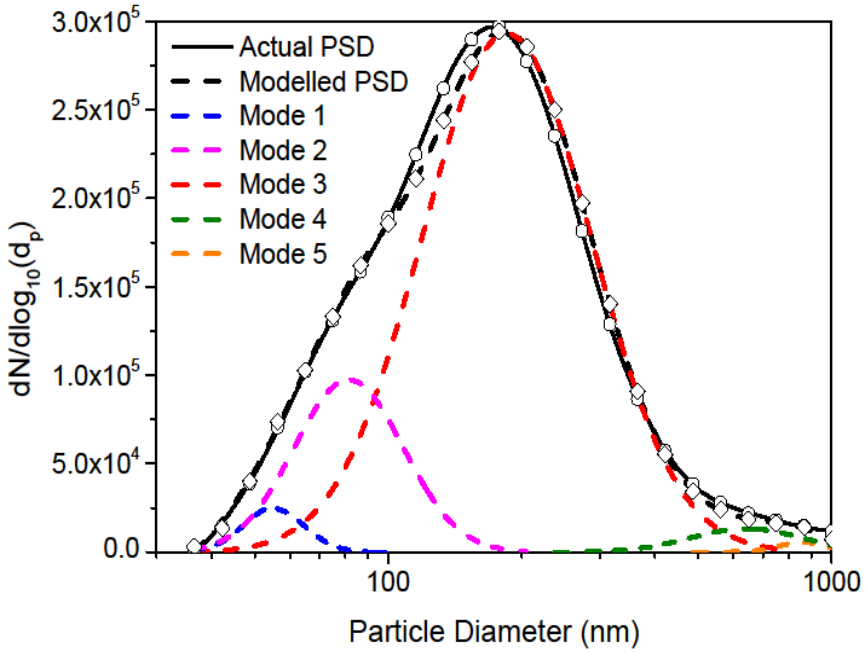

Figure 3.12: An averaged PSD of a typical TiO_2 dispersion test, indicating the modal parameters fitted by the RmixDist package

In this study, the PSD were initially fitted by three modes, with the number of modes fitted increased until the modelled PSD accurately described the experimental PSD. As a result, the PSDs measured within this study consist of five to eight modes depending upon the type of nanopowder of interest each time. An example campaign averaged PSD measured by the DMS of a 10 min interval during the injection of TiO_2 NPs into the dispersion chamber, fitted by RMixDist, is shown in Figure 3.12.

3.2.7 Data Quality Assurance

Time-consuming, data quality assurance is essential in any experimental process and should not be underestimated. Identification and removal of 'unusual' events from the data is demonstrated to ensure that only appropriate data is used in any subsequent analysis, therefore allowing that analysis to be unbiased, facilitating an accurate description of the evolution of the ENP airborne behaviour (Agus, 2008). These events, according to Agus (2008), are likely to be caused by periods where instruments have failed or are generating false readings. An improved understanding of any conclusions made on the dynamic processes governing changes of PSDs over time will be allowed by the removal of these points.

The experiments presented in Chapter 4 and 5 based their data obtaining procedure on in-parallel sampling of the DMS and CPCs. In this study the data quality was assessed by comparing measurements of one second DMS data from the individual measured diameters with data of the same resolution obtained by the CPC. In this way significant shifts within the DMS data which did not correspond to similar trends in the CPC data could be identified. On the occasions that these occurred, they were most likely due to instrument noise during periods of low PNCs, instrument zeroing or failure of the heating line to properly remove any humidity from the sampled particle's surface. The latter process could be attributed as the cause of many fluctuation events in the obtained DMS data during sampling from the dispersion chamber. Considering that the DMS model employed for this work was not equipped a with silica gel drier incorporated in the latest versions of the device, amplifiers were sensitive to humidity changes. Furthermore, it should be noted that the sampling of TiO_2 nanoparticles led to higher frequency of fluctuations than for SiO_2 nanoparticles. This was something which could not be explained and more technical analysis considering the different particle characteristics originating from different nanopowders should be considered in future work. The problem was addressed by cleaning the instrument on a regular basis and before each experiment, especially the classifier which accumulated deposits through diffusion which in turn caused corona discharges within the column.

Experimental Description	***Number of Minutes Sampled***	***% Removal of Total Data Collected***
Experiments in ventilated conditions with TiO_2 ENP (Chapter 4)	1545	5.5
Experiments in unventilated conditions with TiO_2 ENP (Chapter 5)	1110	4.3
Experiments in unventilated conditions with SiO_2 ENP (Chapter 5)	1110	1.2

Table 3.1: Percentage data removed from experimental campaigns after data quality assurance procedure

The overall data removal, as a result of these processes, is summarised in Table 3.1. The table was constructed according to the sampling hours corresponding to the different materials dispersed into the chamber, the different experiments and the number of replicate tests for each experimental condition. As mentioned above, the percentage removal of total data collected was estimated to be higher in the case of TiO_2 compared to SiO_2.

3.2.8 Comparison of particulate equipment

Since there is no standard instrument which is used to measure PNCs and PSDs, comparisons of the different instruments used for measurement are required to verify any collected data. This section will outline comparisons of particulate equipment which has been used in this study. Once the relationships between different particulate instrumentation have been obtained it becomes possible to compare particulate measurements and parameters found at different locations in the dispersion chamber. As will be shown in Chapter 4, the sampling set-up is based on distributed CPCs of the same model in order to estimate the evacuation characteristics under various ventilation settings following a continuous release of ENPs. Furthermore, the DMS used in this work, in Chapters 4 and 5, was sampling in parallel with a CPC at a specific location in the dispersion chamber. Therefore comparisons of the total PNC should be carried out between these two instruments since both the detection limits cover the entire nanoscale.

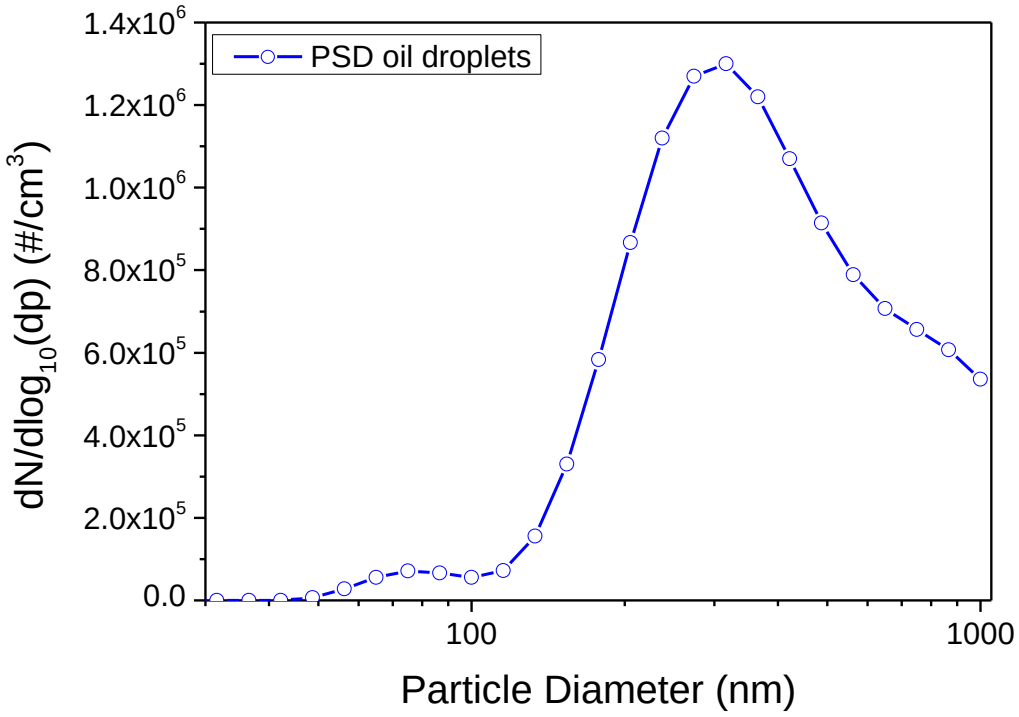

Figure 3.13: A typical average PSD of the oil droplets injected in the vessel for the comparison tests

According to Giechaskiel et al. (2009), one of the methods recommended for the calibration of CPCs is based on the comparison of the response of the CPC under calibration with that of a second one (reference CPC) which has been calibrated by the primary method. In this investigation, one CPC had been calibrated by the manufacturer by the primary method so that the other CPCs utilised in this work were calibrated against this. Among five CPCs (model

3775 by TSI) of the same model, after numbering the devices for functionality reasons and considering the operation status, three were chosen for use in the experiments, CPC#1, CPC#3 and CPC#4. CPC#4 was chosen to send for calibration to TSI and used as a reference device. Furthermore, as indicated in Section 3.2.2.1, the DMS was also sent and calibrated by the manufacturer. CPC#4 was installed at the same sampling location with the DMS for the experiments presented in Chapters 4 and 5. Therefore, comparisons in terms of total PNC were also conducted between these two calibrated instruments.

A simple experimental setup was used for the comparison tests. The explosion vessel presented in Section 3.3.1.1 was used as the confinement for the injection of oil particles generated by an aerosol seeding generator (PIVPart14 by PIVTec, Germany). The aerosol produced by the particular generator was polydisperse and before being introduced into the vessel passed through a silica gel drier section. Two dispersion tests were performed: one test involving the DMS, CPC#4 and CPC#3 and a second test for the DMS, CPC#4 and CPC#1. In both tests, the devices were sampling in parallel through common conductive silicone tubing from a port of the vessel. On this port, a stainless steel tube crossing the internal volume of the vessel was installed in order to deliver the aerosol from the centre and through silicone tubing to the sampling devices. Care was taken on the tubing length so that the CPCs sampled through tubing of same length, whereas the DMS sampled through a longer line. In this way the residence time of the sampled aerosol was similar for both CPCs and consequently similar particle diffusional losses were assumed. The longer length of tubing installed on DMS was roughly estimated due to the higher sampling flow rate compared to the CPCs. A typical PSD, as obtained by the DMS, of the oil droplets in the vessel produced by the aerosol seeding generator is presented in Figure 3.13 and represents an average of the obtained data over the 60 seconds period of injection applied for a typical test. As can been seen, the main peak diameter of the largest fraction of particles was located at 300 nm, while a secondary peak diameter of much lower PNC and less distinct characteristics, was established at 75 nm.

Total PNC validation based on 20 minutes of sampling (including the one minute injection period and following the 19 minute aerosol decay period) and at a time resolution of 1 second was performed for the DMS, CPC#4, CPC#3 and CPC#1 using the laboratory set up described above. The results of these validation comparisons can be seen in Figure 3.14. Regarding the CPCs inter-comparison tests, the above figures showed that CPC#4 and CPC#1 (Figure 3.14a) demonstrated very good linearity standards (slope 0.97641 and r^2=0.98883). A small shift of the linearity can be observed at a particle concentration threshold of $5x10^4$ particles/cm^3. According to TSI (2007), at concentrations between 0 and $5x10^4$ particles/cm^3 the device operates in single count mode. After this threshold, a photometric mode is established by

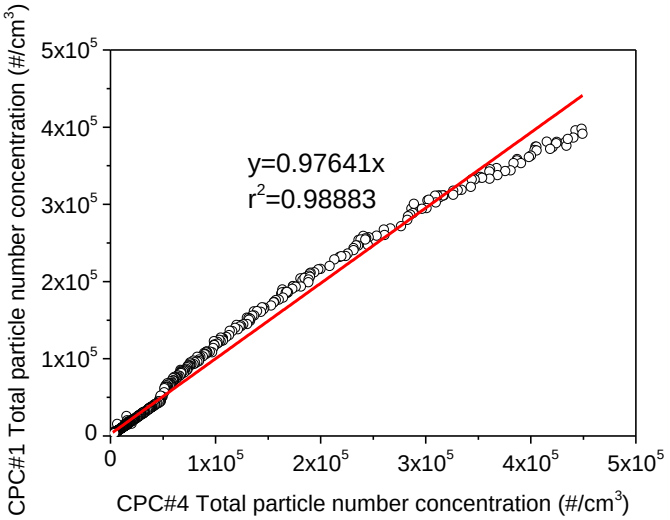

(a)

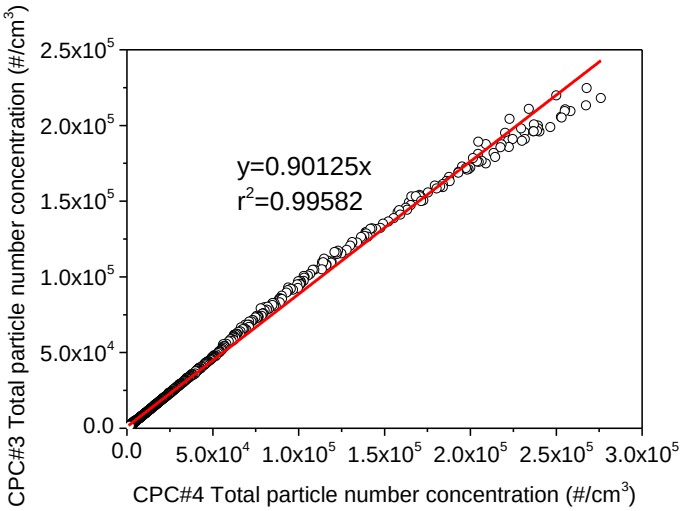

(b)

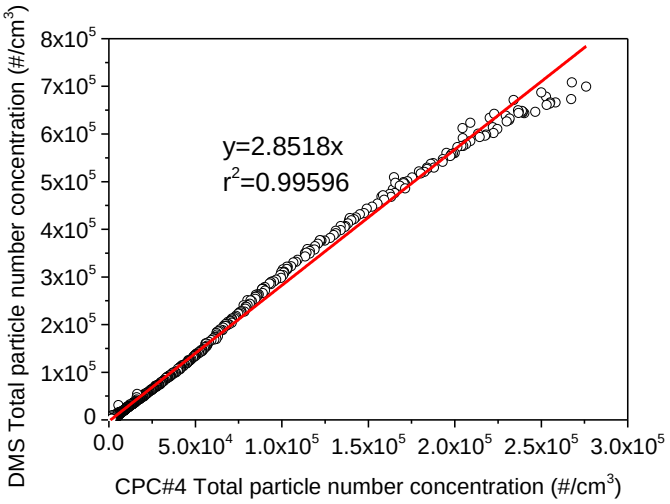

(c)

Figure 3.14: Comparisons of 20 min PNC for (a) CPC#4 and CPC#1, (b) CPC#4 and CPC#3 and (c) CPC#4 and DMS

employing continuous, live-time coincidence corrections in the single counting mode. Therefore, the shift observed may be attributed to this automatic change in the measurement process. CPC#3 also showed a good correlation to CPC#4 (slope 0.90125 and r^2=0.99586) although measured an approximately 10% lower number of particles than that of CPC#4. It can been seen that the deviation of response is established at the high PNC region which was reasonable by considering that CPC#3 was not calibrated (Figure 3.14b).

On the other hand, the comparison of PNC obtained by the two calibrated instruments, CPC#4 and DMS (as can been seen in Figure 3.14c), was described by the relationship y=2.8518x (DMS(y) and CPC#4(x)). This indicates that the DMS reads a greater proportion of particles compared to the CPC. Price et al. (2006), who conducted comparisons of a DMS and CPC also found a higher PNC reported in the response of the DMS. Indeed, the PNC measured by the DMS was a factor of 1.40 higher than that of the CPC. They indicated that the difference was most likely due to a larger fraction of nucleation mode particles resolved by the DMS compared to the CPC, and also possible differences in calibration.

In conclusion, comparisons indicate that reliable measurements from the particulate instruments used in this study can be obtained for both low and high number concentrations. In particular, the comparison conducted between the CPCs satisfies the standards on linearity proposed by Price et al. (2006): slope 0.9-1.1 and r^2>0.97. However, due to the high deviation observed between measurements of the specified CPC and DMS, it was decided to consider the measurements obtained in this work by each device individually and not to proceed to any comparison between parameters extracted from these (e.g. total particle decay rates), as will be shown in Chapter 4. Furthermore, the measurements obtained by the CPC, since it was sampling in parallel with the DMS in the experiments presented in Chapter 5, were used exclusively for the identification and removal of the unusual fluctuations in the DMS data. It should also be noted that the APS was not included in the validation tests presented here although its particle detection limits include the upper part of the nanoscale. This is due to the particular device being employed in the experimental work presented in Chapter 5 in order to provide measurements on the microscale.

3.3 Experimental Apparatus, Techniques and Procedures for the study of the Explosion Characteristics of ENP

In the present work, a fan stirred constant volume cylindrical vessel was used. This has a number of features that make it suitable for fundamental combustion studies: a) close to homogeneous, isotropic turbulence, b) small quantity of powder and fuel required and c) there are no problems associated with flame stabilisation compared with burners. In this study,

premixed flame propagation in hybrid mixtures were assessed at initial atmospheric pressure and temperature under low turbulence. The arrangement for the explosion study was based on central ignition to investigate the turbulent flame development during the early stages of combustion and before there is a significant increase in pressure. Deflagrations were studied by high speed Schlieren photography with simultaneous dynamic pressure recording. Further details on each component and experimental technique are discussed in the following sections.

3.3.1 Combustion Apparatus

The present work was conducted with existing apparatus at the University of Leeds. It comprised an optically assessed cylindrical combustion vessel which was equipped with an ignition system, pressure transducers and a Schlieren photographic system. Furthermore in this work, an injection system was designed for safe introduction of nanopowders into the explosion vessel.

3.3.1.1 Combustion Vessel

The bomb was previously used for studies of gaseous combustion and has been described by Hundy (1969), Andrews and Bradley (1972) and Lawes (1987). It comprised a cast steel cylinder of 305 mm diameter and 305 mm length and its working volume was 23.2 litres (Figure 3.15). Optical quality BK7 windows constructed by fused silica, 150 mm diameter and 39 mm thick, were fitted in each end. Four identical eight-bladed fans were fitted, equi-spaced around the central circumferential plane at 45° to the horizontal. For studies of turbulent combustion, they provided the required flow field. The fans generated isotropic turbulence within the field of view of the windows and the turbulence velocity was a linear function of fan speed. The vessel turbulence was fully characterised by Lawes (1987). All measurements were taken from within a central sphere of 150 mm diameter. The combustion bomb, including the access ports, was essentially the same as that used by previous workers.

Several access ports were present on the vessel. A $^1/_2$" BSP port, in the top of the bomb, was used to connect the bomb to the central fill and discharge valve (FDV) which linked the bomb with the gaseous fuel and air supply. A handheld pressure meter was used to monitor the initial mixture pressure, which was also connected to this port. More details on the pressure instrumentation are given in Section 3.3.1.2. To prevent exposure of the pressure meter to combustion pressures, which might result from accidental ignition, an additional isolating valve was fitted immediately adjacent to the port. This valve was equipped with a safety switch which intersected the ignition trigger when the valve was open, thus preventing accidental ignition.

Four 1" BSP ports were equi-spaced around the bomb. These ports were used as appropriate for ignition, the dynamic pressure transducer as well as for the installation of the injection system which is described in detail in Section 3.3.1.3. Two 1/8" Enots ports, located in the horizontal plane, were also used, with one of these being used for the exhaust and the other for powder suspension analysis with the DMS. In the latter case, samples were drawn from the centre of the vessel. When not in use, the ports were isolated with shut off valves in order to tolerate the produced explosion pressures.

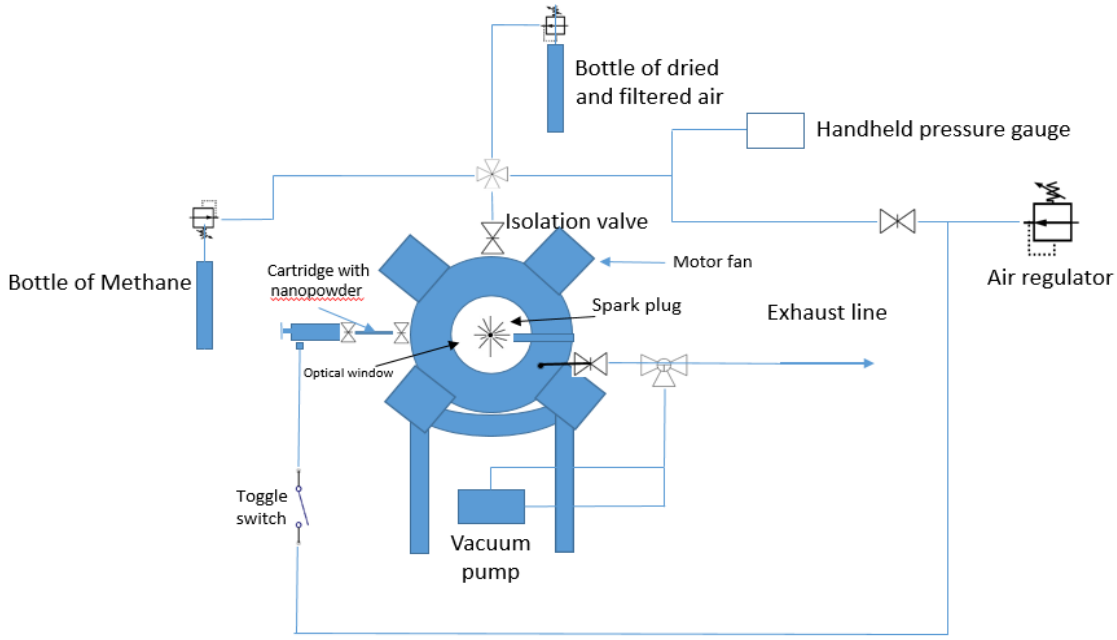

Figure 3.15: Schematic of Leeds explosion vessel

Isotropic turbulence at the centre of the vessel was produced by four individual 3-phase 1.5 kW fan motors and electronic motor controllers, Mitsubishi Freqrol Z024-S1.5K, which were installed by Drake. A heating system was also provided which was comprised by two heating elements, with a total installed power of 4.5 kW. The second heating element was mounted symmetrically opposite to the original heater, on the other end plate. Both heaters were controlled by a CAL Controls Ltd. Model 3200 electronic controller.

3.3.1.2 Auxiliary Systems

Ignition System

Two ignition systems were employed in the present work in order to evaluate the explosion phenomenology of the tested mixtures as a function of the nominal ignition energy. As indicated in the Section 2.4.7 of Chapter 2, it has been proven that the application of strong

ignitors in explosion tests of heterogeneous mixtures conducted in small and large volume vessels is capable of overdriving the explosion characteristics of the mixture in the case of the small volume vessel. It should be mentioned that the ignition of dust-air mixtures in the present work proved to be incombustible by these ignition techniques. More details about the process of the homogeneous (particle free) and heterogeneous mixture preparation are given in Section 3.3.1.4.

Central ignition was achieved via a standard 6.35 mm Minimag spark plug. It was mounted in the centre of the vessel using a stainless steel tube spark holder in which was mounted an insulated high voltage lead. The spark plug was connected to a variable energy ignition power supply unit. It consisted of three main units to control electrical breakdown and spark energy. The main spark unit used a bank of resistors to control the current by isolating or including these resistors within the circuit through a set of switches. The higher the series resistance of the circuit the lower the current through the spark plug, while reducing the series resistance increased the current. Optionally, the unit could be charged using a 600 V supply for an additional boost in ignition energy. Without the 600 V supply the system produced 300-400 mJ of nominal ignition energy whereas through the additional 600 V boost this nominal energy was increased up to 2 J. Due to the very low equivalence ratios and temperatures used throughout this work, the highest possible ignition energy was used at all times. This was considered acceptable as spark effects are not thought to impact the science being studied here. Bradley and Lung (1987) stated that the flame speed enhancement induced by a spark plug of 1 J energy has been observed at radii up to about 10 mm. Therefore, it is expected that in this work the effect of 2 J nominal ignition energy on the phenomenology of flame will be minor.

In order to increase the provided nominal ignition energy in the dust-air-methane and air-methane mixtures, electric matches were also used. An electric match is a device that uses an externally applied electric current to ignite a combustible compound (pyrogen). When a current is passed through the match conduction wires, a heating element coated by the pyrogen heats up causing its ignition. In this work, the conduction wires were de-insulated and cut to a length so that the head of the match could be installed onto a stainless steel rod at the centre of the explosion vessel. The rod was the conductive body for the delivery of the current to the match at the centre of the vessel. A power supply unit (PSU) was used to provide the required voltage (here, 6 V) and current for the initiation of the ignition of pyrogen. The matches applied in the present work were E-match pyrotechnic electric igniters supplied by Easypro (UK) having a heat of explosion (HOE) of 718 cal/gram. This specification was used to determine the ignition energy provided by the specific match through the calculation of the weight of pyrogen before and after the ignition. Calculations over three matches showed that

the energy corresponding to the calculated mass change of pyrogen was 67 ± 1 J. However, these calculations could be considered reliable only by assuming that pyrogen was combusted completely, although this assumption does not fully represent reality. Thus the above calculations include a high level of approximation.

Pressure Instrumentation

To record the pressure rise during flame propagation, a dynamic pressure transducer, Kistler 701A, was mounted flush with the inner surface at the bottom of the vessel. This transducer had a pressure operating range of 0-25 MPa and temperature of 123-513 K. The charge of the transducer was converted to a voltage (0-10 V) by a Kistler 5007 charge amplifier. An analogue to digital converter (ADC) Microlink 4000 digitised the voltages from the charge amplifier which were then interpreted on a PC, using LabView software. The transducer sampling frequency was set to a range of 50-100 KHz and the charge amplifier at 0.1-0.9 MPa/V, depending on initial pressure in order to capture the whole range of pressure rise. Initiation of pressure data collection was achieved through a triggering system which is described in Section 3.3.1.6.

Mixture initial pressure was measured with a Comark (C9555/SIL) manometer, designed to function between 0 to ± 2100 mbar. As this device was sensitive to sudden, large changes in pressure, it was isolated immediately prior to triggering an explosion by closing a ball valve in the line between the combustion vessel and the manometer. This transducer was used to measure the internal partial pressure of the combustible reactants during mixture preparation. A detailed description of the mixture preparation is given in Section 3.3.1.4.

3.3.1.3 Dust Injector

A commercially available Humphrey 6-D-6 stainless steel air cylinder was used for the piston-cylinder device on which was based the injection of nanopowders samples into the explosion vessel. The double acting model D-series requires high-pressure air to extend and retract the internal actuating piston. However, some additions and modifications were made in order to adapt the device for this particular application. Figure 3.16 shows the dust injector assembly and its components. The end of the piston was modified in order to fit a 3/8” threaded sleeve. Through this, the piston was connected with the remaining section of the system including two full-bore ball valves and a 15 mm diameter copper pipe (cartridge). Prior to loading with nanopowder, the pipe in the centre of the unit was separated from the push-fit connectors/ball valves.

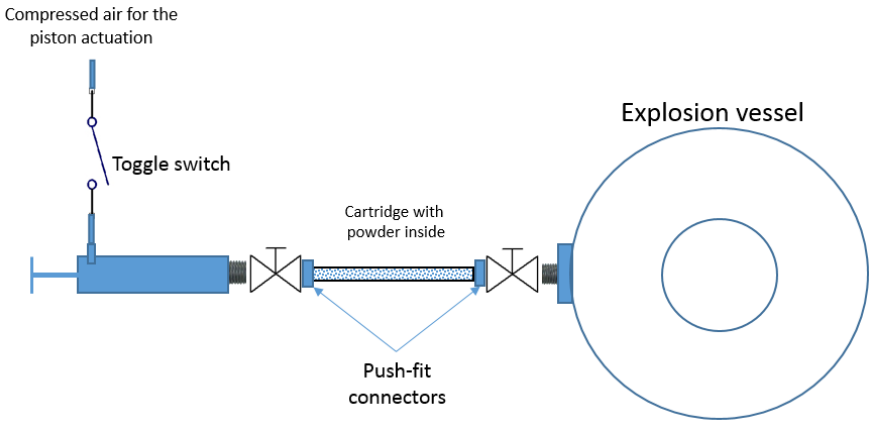

Figure 3.16: Schematic of the dust injector assembly

3.3.2 Mixture Preparation

As mentioned in Section 3.3.1.2, the experimental loadings of ENP in the vessel corresponding to the tested powder concentrations produced by the injection method herein, were not ignitable. This inability to ignite was likely a result of the employed ignition techniques, where these were not able to supply sufficient energy to initiate particle combustion. Since one of the objectives of the present PhD program was the study of the explosion potential of ENP, a hybrid blend of nanoparticles with an alkane (methane) and air were considered to meet this remit. A lean hybrid blend still provides the ability to study the effect of the tested nanoparticles on the combustion process while ensuring flammability.

The experimental procedure is described in full in the next section, however it should be noted here that in the case of tests related to hybrid mixtures, the preparation included some additional actions. Due to the large fractions of deposited dust on the walls and the vessel windows, it was necessary to frequently disassemble the bomb to remove these deposits after each experiment.

Additionally, after each explosion test, in order to ensure that the vessel was evacuated of a very large proportion of combustion residuals the bomb was first flushed with dry air from the laboratory compressed air system for 30 seconds. This also served to remove a large amount of the residual combustion heat. The flushing air was then switched off and the vessel evacuated down to a pressure of 50 mbar (a) using the vacuum pump connected to the explosion rig. To further enhance removal of combustion products, the vessel was then refilled to 1 bar (a) and evacuated back down to 50 mbar (a) for a second time.

Once the above cleaning processes was complete, the fuel components were added. The amount of fuel was first calculated using partial pressures and then introduced into the explosion vessel. After this, the vessel was filled with dry cylinder air to the required initial pressure (0.1 MPa). It should be noted that all the explosion tests were conducted at atmospheric pressure and room temperature. Simultaneously, the root mean square (rms) velocity induced by the fans was adjusted to the desired level for mixing purposes and subsequently for the conduction of turbulent explosions. The above procedure was followed for all of the explosion tests for the methane-air mixtures. Regarding the respective hybrid mixtures of the variable dust concentrations, the procedure employed was similar except for the quantity of dry cylinder air with which the vessel was filled to reach the required pressure prior to ignition. As air was introduced into the vessel with the nanopowder sample, the pressure increased and exceeded atmospheric prior to ignition. Thus, the vessel was filled with dry cylinder air up to 995 mbar (a) such that 5 mbar could be added by the piston to introduce the nanopowder and consequently to allow the ignition to take place under atmospheric pressure. This pressure addition caused by the piston of the applied injection system has been calculated using the manometer described in Section 3.3.1.2.

Two CB nanopowders, Printex XE2 and Corax N550 have been chosen for the study of the explosion characteristics of CB nanoparticles. More information on these materials are presented in the following section.

3.3.3 Experimental material

The term “carbon black” is used to describe materials consisting of carbon particles usually presented in spherical and colloidal size (Donnet, 1993). The most common manufacturing process for the CB ENP is based on the use of partial combustion or thermal decomposition of hydrocarbons (Kosinski et al., 2013). CB nanopowders are mainly utilised in the rubber industry as an additive in car tyres to ensure high resistance to abrasion, good road handling and ageing resistance (Orion, 2012). According to Turkevich et al. (2015), the nano-carbons are confirmed mainly to be in the St-1 explosion class, which in Chapter 2 has been determined to characterise weak explosions. In this study, Corax N550 and Printex XE2 (Orion Engineered Carbons, Germany) were selected for the generation of airborne CB nanoparticles. The CB nanopowders used in this work are specified by the manufacturers to have an extremely low volatiles content (< 0.5 %).

The characteristic diameter d_{50} of each powder, the BET (Brunauer-Emmet-Teller method) specific surface area and the equivalent BET diameter are described in Table 3.2. These measurements have been performed by Bouillard et al. (2010). As can been seen in Table 3.2,

the primary nanoparticles are forming large agglomerates of micrometric size. In addition, Printex XE2 is characterised by a larger specific surface area than Corax N550. Therefore, as outlined in Chapter 2, it is possible that difference will have an impact on their respective reactivity and physical properties. It should be also noted that, according to Bouillard et al. (2010), the Printex XE2 demonstrates lower apparent bulk density (0.15 g/m^3) than Corax N550 (0.38 g/m^3). This difference had a specific impact in the choice of the nominal dust concentrations injected into the vessel for the explosion tests, as will be shown in Section 3.3.6. Measurements conducted by the present work on the particle size characteristics of the original samples of each material utilised for the explosion experiments, are presented in Chapter 6.

Nanopowders	**BET specific surface area (m^2/g)**	**d_{BET} (µm)**	**d_{50} (nm)**
Corax N550	40	75	15
Printex XE2	950	3	10

Table 3.2: Main characteristics of the nanopowders (Bouillard et al., 2010)

3.3.4 Experimental Procedure for the hybrid mixture's explosion tests

Gaseous fuels were prepared using respective partial pressures directly, while the amount of dust was extracted by calculations of the nominal dust concentration based on the vessel's volume. The metered quantity of nanopowder was added to the pipe in the laboratory fume hood and the (closed) ball valves re-attached to the pipe. This served to prevent the escape of the powder into the laboratory on transferral to the combustion vessel. This assembly was then attached to the actuator unit and the combustion vessel. The desired gaseous mixture was then prepared and both ball valves opened. The toggle switch was then actuated, which allowed a burst of air at 7 bar initial pressure from the piston into the cartridge unit, which entrained the nanopowder and transported it into the combustion vessel. The ball valves were then closed manually prior to ignition of the dust/gas mixture to isolate the system from combustion pressures and products. Due to the need to study turbulent flames, fans were kept running at the desired ignition turbulence intensity (500 rotations per minute, RPM) during mixture preparation, powder introduction, ignition and the subsequent explosion event. Similar turbulence intensity was applied for the explosion tests conducted on homogeneous mixtures.

3.3.5 Schlieren Flame Photography

The growth rate of spherically expanded turbulent flames was studied using using high speed Schlieren cine photography. This technique allows for the visualisation of density gradients.

It is an effective method for flame imaging in combustion studies. The main advantage of this method is the simple setup configuration, providing a definable optical access on the flame surface at a certain isotherm and the ability to visualise the texture of the flame surface and hence observe the onset of flame cullularity (Kwon et al., 2002). A weakness related to this method according to Ormsby (2005) is that this technique gives a 2D projection of the 3D flame, therefore suffering from overlapping image effects.

The light source used was a 5 mW He-Ne laser model 106 1 diode laser, with a minimum possible beam diameter of 0.65 mm, producing light at 655 nm. As the light produced from this laser somewhat mimicked a point source, the initial concave lens traditionally incorporated into a Schlieren system was deemed unnecessary and was thus removed. The light was expanded over a distance of 1000 mm onto a plano-convex lens with a focal length of 1000 mm. This effected collimation of the beam, which then passed through the vessel windows onto a second, plano-convex lens with an identical focal length. This focussed the light beam down to a point at a distance of 1000 mm away from the second plano-convex lens. A 1 mm diameter pinhole was placed at this position to block light refracted by the density gradient around the flame edge. A variety of pinhole sizes were trialled (ranging from 0.5 mm to 1.5 mm) but the diameter used here was found to give the best compromise between flame structure detail and edge definition.

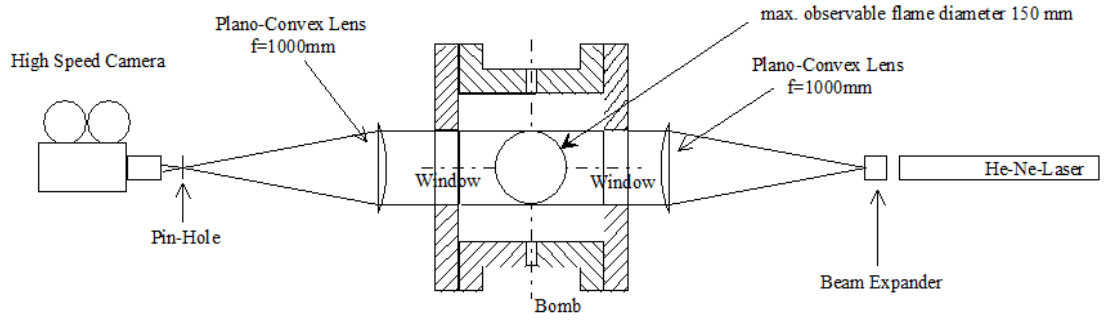

Figure 3.17: High speed Schlieren system

The arrangement of this technique applied in this work is shown in Figure 3.17. Schlieren images were captured using a Phantom V9.0 camera, recording at a rate of 3000 frames per second (FPS) at a resolution of 512 x 512 pixels. This produced greyscale images, with these being captured until the flame edge had reached the edge of the vessel windows.

3.3.6 Synchronisation System

It was necessary to ensure that the ignition system, high speed camera and pressure data acquisition system were triggered at a consistent point in time relevant to each other. To this end, a TGP110 pulse generator was used to generate the variety of signals required by these components. This pulse generator was triggered by a series circuit consisting of a 9 V power supply in series circuit with a push button circuit open/close switch. A second switch, actuated by the same push-button, was installed in series with the charge amplifier, which required a closed circuit trigger to reset the unit prior to data capture. On closing the push-button switch, the pulse generator produced a positive-going transistor-transistor logic (TTL) signal to trigger the pressure data acquisition system. It also produced a negative-going TTL signal to trigger the camera and a negative-going 15 V complementary metal-oxide semiconductor (CMOS) signal to trigger the ignition signal. Thus, each component could be triggered at the same moment in time, or with a delay between these if desired. A schematic of the ignition system whith its components used for synchronisation, is illustrated in Figure 3.18.

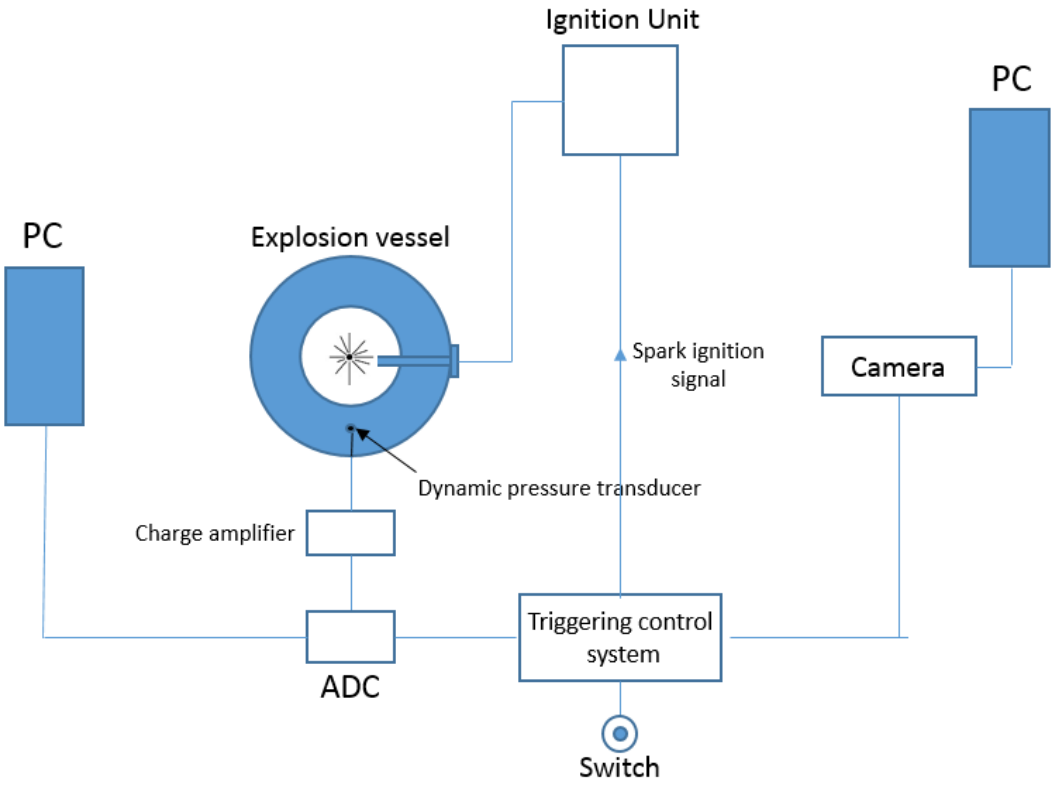

Figure 3.18: Schematic of the ignition system

3.3.7 Experimental process and repeatability

A summary of the explosion tests conducted in this work is presented in Table 3.3. This table contains the initial conditions (pressure, temperature and rms velocity), the amount of the flammable gas in terms of equivalence ratio for both methane-air and hybrid mixtures, and the amount of dust present in the hybrid mixtures in terms of nominal dust concentration. At least three explosions were performed for all turbulent tests carried out during the current study in order to improve statistical repeatability.

In the first course of experiments, the LFL of methane was indentified. Additionally, through these tests was identified the lowest equivalence ratio (φ) of methane-air mixtures where three ignitions of the mixture could be achieved. This course of experiments was completed with the application of pyrotechnic matches as ignition source in order to study the ignitability of mixtures of further reduced methane content.

In the second course of experiments, for the lowest φ estimated in the previous step, three nominal dust concentrations of the two different nanopowders (Printex XE2 and Corax N550) were introduced in the methane-air mixtures. When studying the influence of CB ENP on the explosion characteristics of pure methane-air, three replicate tests were conducted on each of the hybrid mixture of specific powder concentration. Additionally, interspersed in-between the tests on the hybrid mixtures, methane-air tests of the same φ were conducted. The final comparisons were conducted between the average flame speeds and explosion pressure measurements of the interspersed tests of methane-air and the average of the variable dust concentration hybrid mixtures.

The nominal dust concentrations used in the hybrid mixture tests were: a) 6, 25 and 75 g/m^3 of Corax N550, and, b) 6,25, 37.5 g/m^3 of Printex XE2. The observed differentiation between the highest concentration of the two materials is attributed to their different apparent densities, as outlined in Section 3.3.2. Therefore, to achieve the dispersion of 75 g/m^3 of Printex XE2, it was necessary to introduce into the catridge of the injector double the mass needed for 75 g/m^3 of Corax N550. In the subsequent explosion tests a such concentration of Printex XE2 caused the failure of the spark plug due to the deposition of particles on the spark electrodes. Therefore, the nominal concentration of the particular material was adjusted to 37.5 g/m^3 in order to ensure the fuctionality of the spark plug during the main explosion experiments.

A second course of experiments was conducted on hybrid mixtures of variable gas content below the LFL of methane. For these equivalence ratios the highest nominal dust concentrations among the three tested in the previous course were injected in order to study

the ignitability potential of mixtures below the LFL. Furthermore, similar tests were conducted using pyrotechnic matches as the ingition source rather than a spark plug. This was to evaluate the change of explosion characteristics of the same hybrid mixtures when the nominal ignition energy of the source is increased. Results of the above comparisons are presented and discussed in Chapter 6.

Ignition system	No	Fuel	φ
Spark plug	1	Methane-air	0.80
	2	Methane-air	0.75
	3	Methane-air	0.70
	4	Methane-air	0.69
	5	Methane-air	0.68
	6	Methane-air	0.67
	7	Methane-air	0.66
	8	Methane-air	0.65
	9	Methane-air-6 g/m^3 Corax N550	0.68
	10	Methane-air-25 g/m^3 Corax N550	
	11	Methane-air-75 g/m^3 Corax N550	
	12	Methane-air-6 g/m^3 Printex XE2	
	13	Methane-air-25 g/m^3 Printex XE2	
	14	Methane-air-37.5 g/m^3 Printex XE2	
	15	Methane-air-75 g/m^3 Corax N550	0.64
	16	Methane-air-75 g/m^3 Corax N550	0.60
	17	Methane-air-75 g/m^3 Corax N550	0.55
	18	Methane-air-37.5 g/m^3 Printex XE2	0.60
Pyr. match	19	Methane-air	0.60
	20	Methane-air	0.55
	21	Methane-air-75 g/m^3 Corax N550	0.55
	22	Methane-air-75 g/m^3 Corax N550	0.50

Table 3.3: Summary of the successful explosion tests conducted on methane-air and hybrid mixtures at atmospheric pressure and temperature and under 0.83 m/s of turbulent velocity

Finally, a third course of (no explosion) experiments was conducted in order to determine the particle size characteristics in the dust clouds explored in the explosion tests presented above. To this end, a steel pipe was inserted into one of the ports and extended to the centre of the vessel. To this pipe, the sampling line of the DMS described in Section 3.2.2.1, was fitted. Each of the specified powder quantities was introduced into the cartridge of the injector and

dispersed in the vessel where the DMS was sampling. At the same time, the rms velocity in the vessel was adjusted to the same level as was applied in the explosion experiments. Through these dispersion experiments, it was attempted to reproduce the dispersion state of the powder to its state before triggering the ignition in the explosion tests.

3.3.8 Data Processing Techniques

As illustrated in Table 3.3 of the previous section, a very large number of bomb tests were performed during the course of this study. These involved simultaneous pressure and image recording. A processing technique developed and applied by Mansour (2010) was employed in this work for the calculations of flame speeds based on Schlieren images. Results from these experiments and their analysis are presented in Chapter 6.

3.3.8.1 Image Processing Method

A number of MATLAB automated batch processing tools were utilised in the present work. The processing technique for the Schlieren images was initiated by conversion of original Schlieren cine movies acquired from Phantom V9.0 camera into separate 8-bit bitmap image files. This was followed by the subtraction of a pre-kernel image from each flame image to obtain a flame image without the intruding spark plug. Then the images were binarised to yield a white flame image, as can been seen in Figure 3.19, surrounded by a black background. Specifically, the white and black represent flame and unburned gas respectively. At this point it should be noted that in the case of the use of pyrotechnic matches as ignition units, flame image analysis through this MATLAB script was impossible because the initial ignition kernel of the pyrogen was big enough to eliminate optical access to the following flame development. Therefore, the analysis of the explosion characteristics in such cases was limited to the data obtained by the pressure transducer during the explosion event.

In order to determine the pixel size, an acetate sheet with a printed grid (with each cell measuring 10 mm by 10 mm) was placed in the collimated region of the laser light in the Schlieren system and a photograph taken. By expanding the resulting image, it was possible to count the number of pixels between gridlines. This was carried out both horizontally and vertically in several different regions if the grid to ensure consistency. The actual distance between the gridlines was then divided by the number of pixels present between these points to give the pixel size on mm/pixel. This value was transferred to Matlab, which then counted the number of white pixels in each image and thus deduced the flame area. This area was then used to calculate the radius of a circle with the same area, which therefore represented a mean

flame radius. Flame speeds were then determined by plotting flame radius versus time during the explosions.

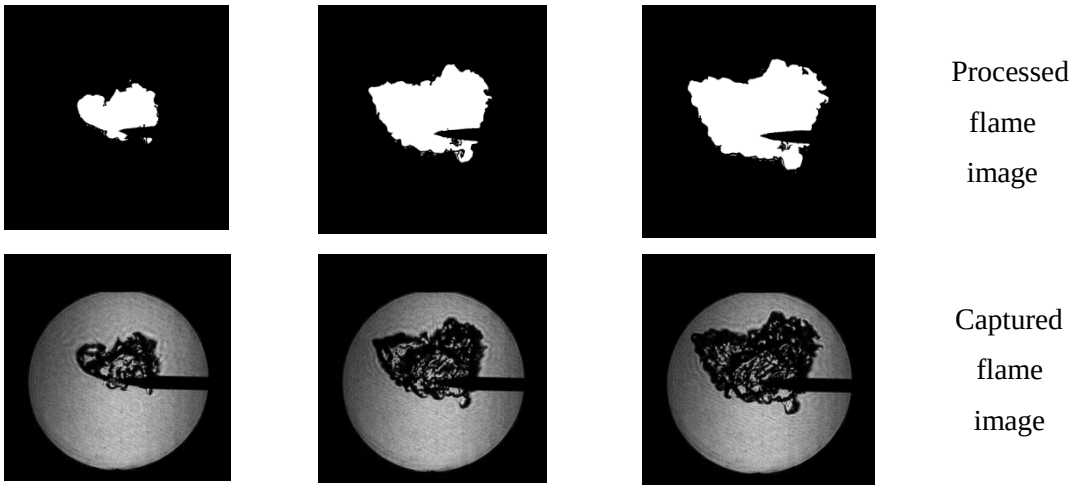

Figure 3.19: Sequences of Schlieren images of flames of a typical methane-Air turbulent explosion at φ=0.68

3.4 Summary

This chapter has described the experimental facilities used within this study for the conduction of the dispersion and explosion tests on specified nanopowders. Description of the main particulate instruments used to determine PNCs and PSDs were provided. The auxiliary equipment used to supply the experimental procedure was also described as well as the preparation of samples and mixtures. Additionally, this chapter included a presentation of the injection systems utilised for safe and effective introduction of the test materials into the dispersion and explosion facilities.

The data processing sections provided descriptions on the techniques applied in this work for the analysis of PSDs and images obtained from the dispersion and explosion tests, respectively. A description of the derivation of an equation used to obtain the PSD parameters was provided along with a description of the modelling program used for the approximation of these parameters. Furthermore, the principles underlying the MATLAB script used for the processing of Schlieren images along with the photographic system for the explosion image acquisition, were also presented. The data quality assurance and control techniques employed were also described. Finally, comparisons between the same and different particulate instrumentation indicated a good linear correlation.

The following chapters aim to provide an analytical view on the dispersion and explosion characteristics of various ENP. This will contribute to a deeper understanding of their airborne behaviour in an indoor environment under ventilated and unventilated conditions as well as their reactivity in the combustion of lean methane-air mixtures. By extension, this understanding can be related back to the health and safety risks, discussed in Chapter 2.

Chapter 4

4. Study of the decay characteristics of accidentally dispersed ENP under different ventilation rates in an indoor environment

4.1 Introduction

With increasing interest in the accidental release of ENP in indoor environments due to its reported effects on human health, increasing amounts of attention are being paid to the development of engineering controls to protect workers by removing hazardous conditions or placing a barrier between the worker and the hazard. One such case, was studied in the Leeds dispersion facility which provides a controllable and unpenetrated indoor environment appropriate for the conduction of dispersion tests of hazardous materials, such as ENP, and the subsequent study of their dispersion characteristics under calibrated ventilation settings.

Knowledge of the level of exposure under accidental scenarios is vital for the assessment and development of efficient mitigation strategies and therefore information is required on the spatial and temporal variation in PNCs established under various ventilation settings. This chapter presents the optimisation steps followed for the preparation of the final liquid nano-suspension which was utilised for the subsequent dispersion tests conducted herein as well as in Chapter 5. The liquid containing the suspended and processed nanopowder was aerosolised and injected into the Leeds dispersion facility with PNCs being measured by spatially distributed CPCs of the same model. The study period is divided into two stages: the injection stage of ENPs and the following aerosol decay stage under different ventilation rates. At the same time, the temporal variation of PSD obtained by the DMS, is also presented. The different modal groups present within the measured PSD of the accumulated aerosol after the prolonged injection period are characterised and the evolution with time of the modal PNCs during the following evacuation process is investigated. Finally, the evaluation of the spatial decay rates as well as of the size-resolved decay rates derived from the DMS measurements are presented along with the estimation of the spatial ventilation efficiency corresponding to each of the tested ventilation rates.

4.2 PSD measurements in TiO_2 nano-suspensions

The experimental configuration along with the auxiliary materials and equipment used in the tests presented in this section have been described extensively in Chapter 3. Current knowledge on the preparation of nano-suspensions indicates that careful specification of the

process is crucial for the de-agglomeration and stabilization of the resulting solutions. TiO_2 nanoparticles in their commercialized form are characterised by high surface energy which causes them to agglomerate in the synthesis and post-synthesis processes (Mandzy et al., 2005). The ultra-sonication process proposed by Taurozzi et al. (2012) (NIST) for the preparation of nanoparticle TiO_2 liquid dispersions is capable of transferring large quantities of energy into the suspension in order to break down the agglomerates into smaller aggregates. According to Taurozzi et al. (2012), 15 minutes of sonication over these samples yields aqueous monomodal nanoscale TiO_2 dispersions, characterised by a mean particle diameter (DLS derived) of 108-116 nm and stability in the sample based on a pH ranging between 3.7 and 4.9.

One of the objectives of the present work is the production of stabilised suspensions with large fractions of particles of diameter $\leq$ 100 nm. In order to achieve this, three sonication parameters were chosen to be studied: the pH, the sonication time and the powder concentration. While these parameters were already described by the specified protocol, it was decided, due to the different characteristics of the ultra-sonicator utilised in the present work, to apply some modifications to these (see Section 3.2.4).

4.2.1 PSD and pH measurements in TiO_2 nano-suspensions prepared in the previous day

Representative averaged DLS-derived PSD profiles of samples prepared on the day previous to the PSDs measurement, of variable TiO_2 powder concentration, sonicated for 15 and 30 minutes, are illustrated in Figure 4.1. As can been seen in Figure 4.1b, the suspensions sonicated for 15 min presented significant levels of μm particles except for the 10 mg/mL sample. The peak of these large agglomerates was detected at near 5.2 μm. The majority of particles in the nanometre range demonstrated diameters at around 122 nm, except for the 10 mg/mL sample which showed a main peak being centred at 111 nm. Furthermore, in all the samples, a secondary peak of large agglomerates was measured to be within the nanoscale and centred at near 400 nm.

The applied increase in the sonication time (30 min), resulted in samples presenting a further fragmentation within the nanoscale for both lowest and highest powder concentration samples (0.5 and 20 mg/mL). As shown in Figure 4.1a, both samples demonstrated a major fraction of particles centred at 123 nm and a minor fraction at 39 nm and 44 nm, for 20 and 0.5 mg/mL respectively. These small particles of diameters < 100 nm correspond to particle clusters which are described as primary aggregates and according to Taurozzi et al. (2012) are fused

crystallites resulting from the production process. Finally, it can be noted that samples with the lower powder concentration (0.5 and 1 mg/mL) exhibited peaks in the μm (3.9 - 5.1) range.

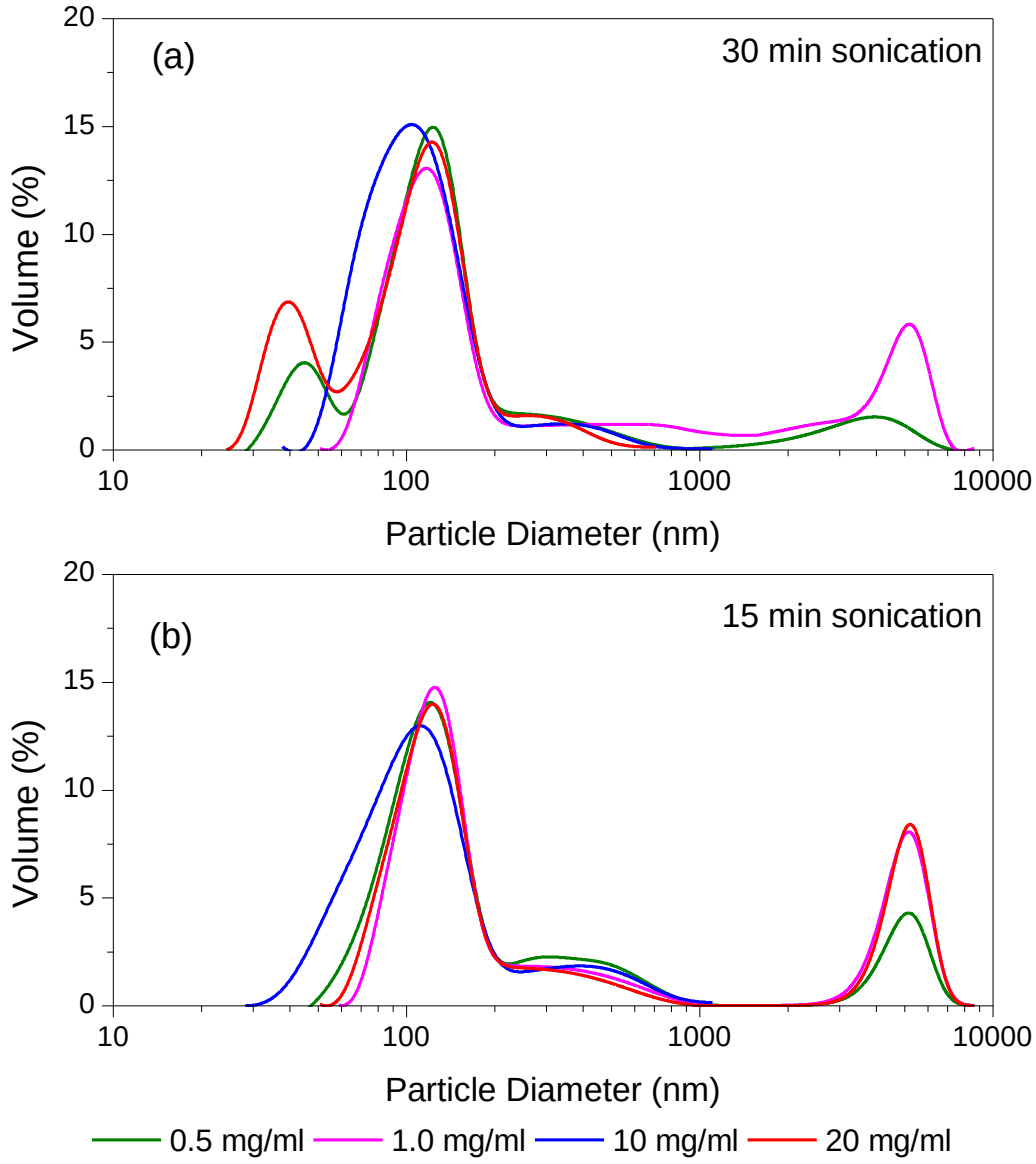

Figure 4.1: Comparison of the average PSDs measured for the previous day samples of variable powder concentration after sonication of a) 30 minutes, and b) 15 minutes

In conclusion, the above measurements indicated that the increased sonication time (30 minutes) resulted in the presence of larger fractions of smaller aggregates with size ≤ 100 nm in diameter than those observed in the samples sonicated for 15 minutes. At the same time, it was noted that the 15 minute sonication proposed by the NIST protocol was not enough to eliminate the particles' existence in the μm size. Additionally, the geometric characteristics of the measured PSD could not be described as monomodal. The 30 minute sonication, on the other hand, indicated the non-presence of μm particles in the 10 mg/mL and the 20 mg/mL

suspension, although this had to be validated in the samples prepared on the same day as the PSDs measurement, as will be shown in the following section. Therefore, considering the above findings, it was decided that for the same day samples, 30 minutes of sonication was the optimum duration for the achievement of an efficient de-agglomeration.

However, as outlined above, the pH factor was considered also in the present work to describe the stability of the produced nano-suspensions. According to Mandzy et al. (2005), one of the factors preventing de-agglomeration in a sonicated suspension is the pH. Taurozzi et al. (2012) indicated that the application of their preparation process produces TiO_2 nano-suspensions which exhibit pH values ranging between 3.7 and 4.9. To this end, in the present work, measurements of pH over the total number of samples prepared on the previous day, were conducted and presented in Table 4.1. As shown in the table, the lower in powder concentration sonicated samples demonstrated pH values out of the range proposed by NIST for stabilised TiO_2 nano-suspensions.

	pH value
Sample 1 (0.5 mg/mL)	5.53 ± 0.11
Sample 2 (1.0 mg/mL)	5.32 ± 0.19
Sample 3 (10 mg/mL)	4.50 ± 0.22
Sample 4 (20 mg/mL)	3.75 ± 0.27

Table 4.1: pH measurements in the samples prepared on the day previous to the PSDs measurement

All in all, the above experimental procedure indicated that 30 minutes sonication in samples of the highest dust concentration (10 mg/mL and 20 mg/mL) is able to produce stabilized nano-suspensions of high fractions in suspended ENPs. For this reason, following these specifications, samples were prepared on the same day as the PSDs measurement although within a beaker of lower volume (50 mL) than used in the previous experiments (100 mL). Additionally, as indicated above, samples of increased powder concentration were also prepared to evaluate any further de-agglomeration potential.

4.2.2 PSD measurements in TiO_2 nano-suspensions prepared in the current day

In the second course of experiments, samples were prepared at the same day as the PSDs measurement and were transferred immediately to the Zeta-sizer for PSD analysis. Initially, 10 and 20 mg/mL aqueous dispersions of TiO_2 were sonicated for 30 min in a glass beaker of 50 ml volume. Figure 4.2 illustrates the comparison between the averaged DLS-derived PSD measured in the samples after 30 minutes sonication. As shown in the figure, in contrast to the

respective samples of the previous day's preparation, the 10 mg/mL current day sample demonstrated a significant increase in the microscale component volume fraction. In the nanoscale, the further fragmentation within the ultrafine size range (< 100 nm) which was observed in the 20 mg/mL sample of the previous day can also be observed in the current day sample of both powder concentrations. However, the suspended particles of diameter ≤ 100 nm in the 20 mg/mL sample presented significantly higher volume fractions than the 10 mg/mL one. More specifically, the 20 mg/mL sample featured the main size peak at 36 nm, characterised by 10.5 % volume higher than that demonstrated by the secondary size peak (6 %) located at 120 nm. On the other hand, the 10 mg/mL sample presented also further fragmentation, although particles of diameter ≤ 100 nm were represented by a secondary size peak located at 36 nm with much lower volume than that of the main size peak located at 116 nm.

Since the previous comparison did not indicate the elimination of particles in the microscale, the next comparisons were chosen to be conducted between TiO_2 samples of 20 mg/mL and 30 mg/mL. At the same time, samples of 30 mg/mL concentration were also prepared without being sonicated in order to evaluate the contribution of the sonication process in the breakage of the large agglomerates.

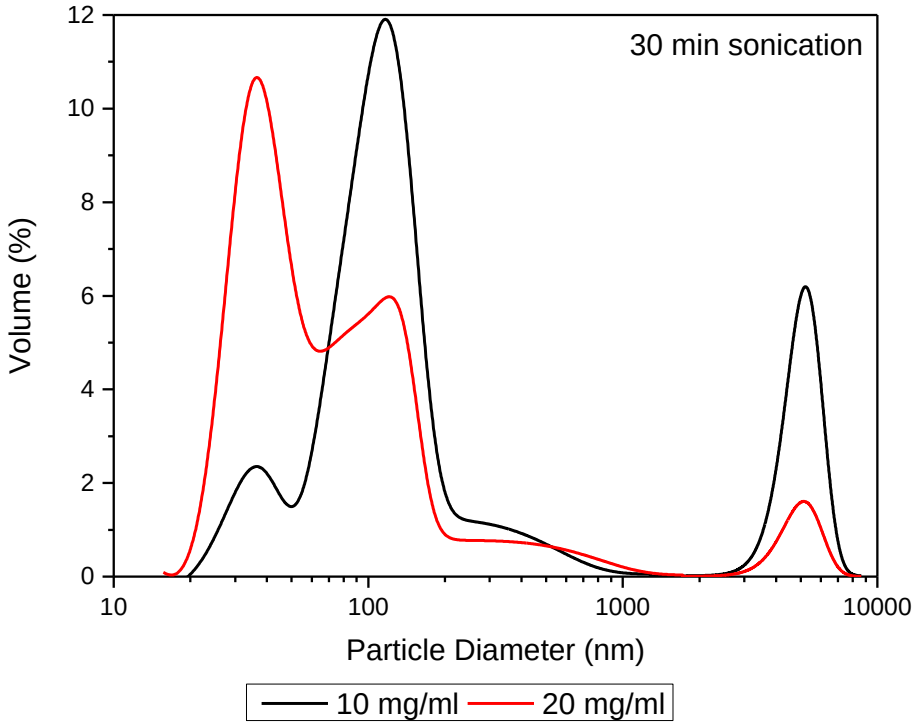

Figure 4.2: Comparison of the average PSD measured for the 10 and 20 mg/mL current day samples after 30 minutes of sonication

Figure 4.3 illustrates the comparison between the averaged PSDs measured in the 20 mg/mL and 30 mg/mL samples prepared in the same day after 30 minutes sonication. It could be noticed that both samples demonstrated fragmentation resulting in the establishment of peaks in the lowest size region with the 30 mg/mL samples presenting the highest volume fraction of particles ≤ 100 nm in diameter. More specifically, the 30 mg/mL suspension presented a peak centred at 28 nm of the highest volume fraction (11.5 %) while the secondary peak (112 nm) exhibited a volume approximately equal to 7.3 %. On the other hand, the 20 mg/mL suspension PSD, in contrast to the sample of the same powder concentration presented in the previous comparison, here demonstrated multiple peaks in the size region below 100 nm and the main peak to be located at 112 nm. Furthermore, for the particular sample the elimination of particles in the μm scale was not observed as it was for the 30 mg/mL. In conclusion, the increase in the powder concentration from 20 to 30 mg/mL benefited the presence of suspended particles of diameter quite close to the to the primary particle diameter in the powder form as specified by the manufacturer (21 nm) and at the same time led to the elimination of the microscale component fraction which was permanently observed in the samples of lower powder concentration.

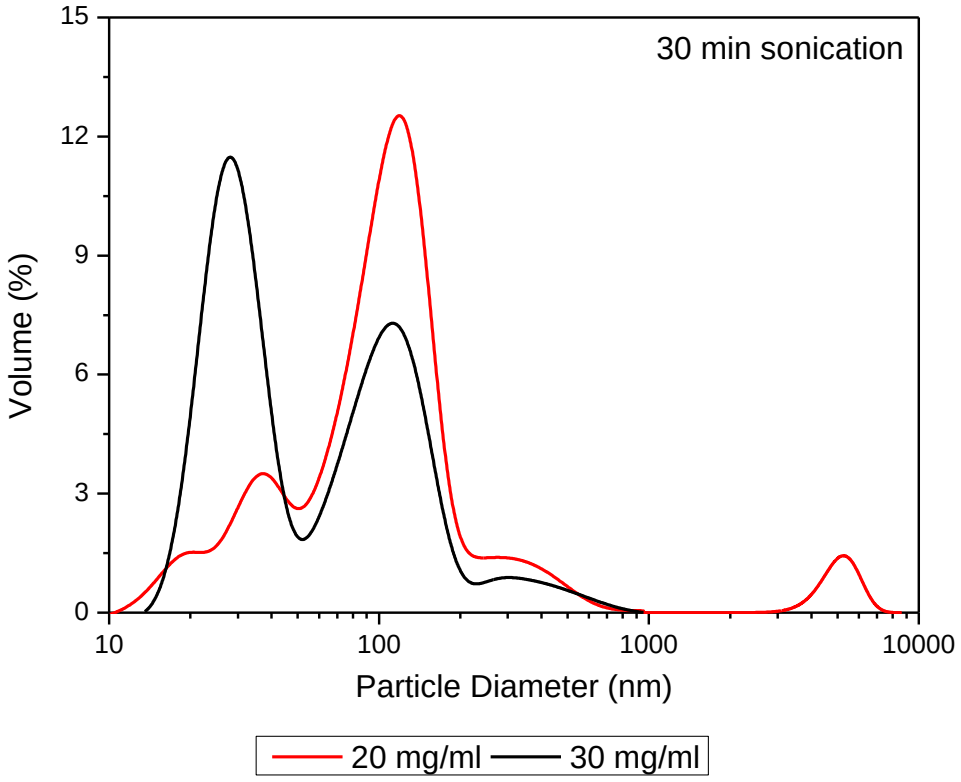

Figure 4.3: Comparison of the average PSD measured for the 20 mg/mL and 30 mg/mL current day samples after 30 minutes of sonication

As mentioned above, in order to evaluate the effect of the sonication process on the de-agglomeration of powder in the liquid, 30 mg/mL samples were prepared without being sonicated and compared to the sonicated one of same concentration. As can been seen in Figure 4.4, the starting suspension (prior to sonication) exhibited a broad polydisperse PSD predominantly in the (1-10) μm range with a major agglomerated fraction (80 % of the total particulate volume) centred at around 5.2 μm and a minor fraction of particles with a peak near 130 nm. The contribution of sonication in the fragmentation of the suspended powder is therefore clear, and this confirms the establishment of an efficient processing technique for the production of nano-suspensions appropriate for utilization in the subsequent risk assessment studies.

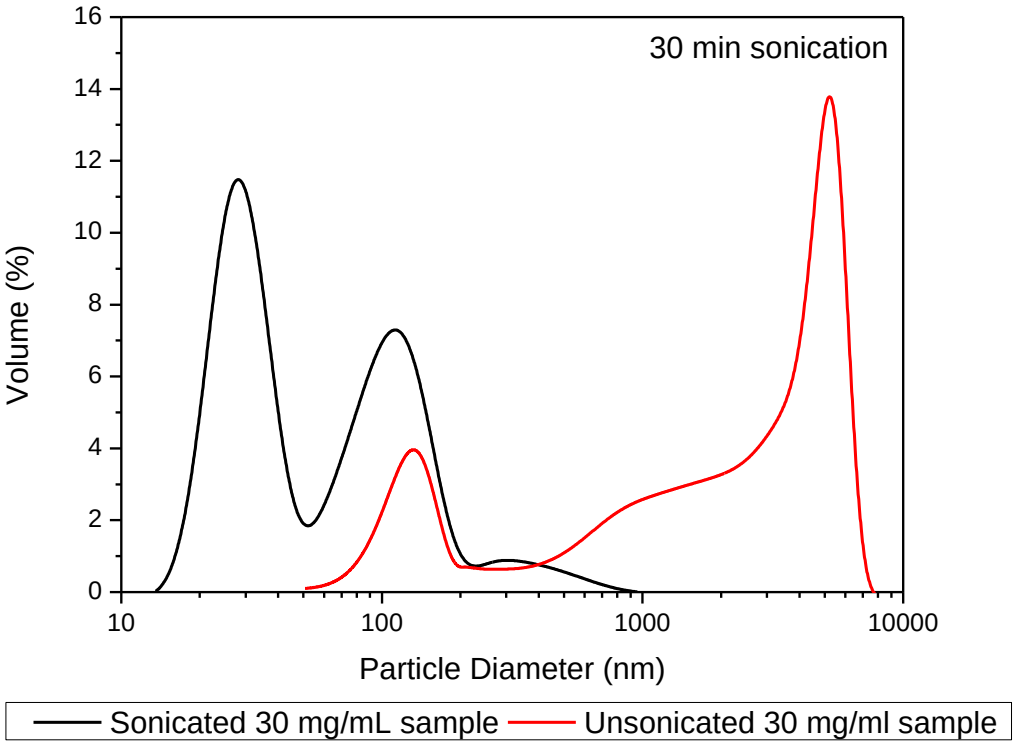

Figure 4.4: Comparison of the average PSD measured for the sonicated and un-sonicated 30 mg/mL samples

To this end, aqueous nano-TiO_2 dispersions were prepared according to the method indicated above and then were introduced into the 6-jet CN nebulizer's reservoir for atomization and subsequent injection into the Leeds dispersion facility which has been described in Chapter 3. It should be noted that the same method of preparation was applied for the TiO_2 and SiO_2 nano-suspensions of the same powder concentration (30 mg/mL) utilized in the dispersion tests presented in Chapter 5. Furthermore, the corresponding PSD to the SiO_2 nano-suspension analysis has been chosen to be presented in Chapter 5.

4.3 Description of the experimental set-up

The experimental facility used for the conduction of the dispersion experiments of ENPs here, as well as in Chapter 5, has been described in detail in Chapter 3. This section presents the applied experimental configuration of the particulate equipment for sampling from the chamber's atmosphere at specific locations and heights as well as the auxiliary equipment utilised for operation reasons.

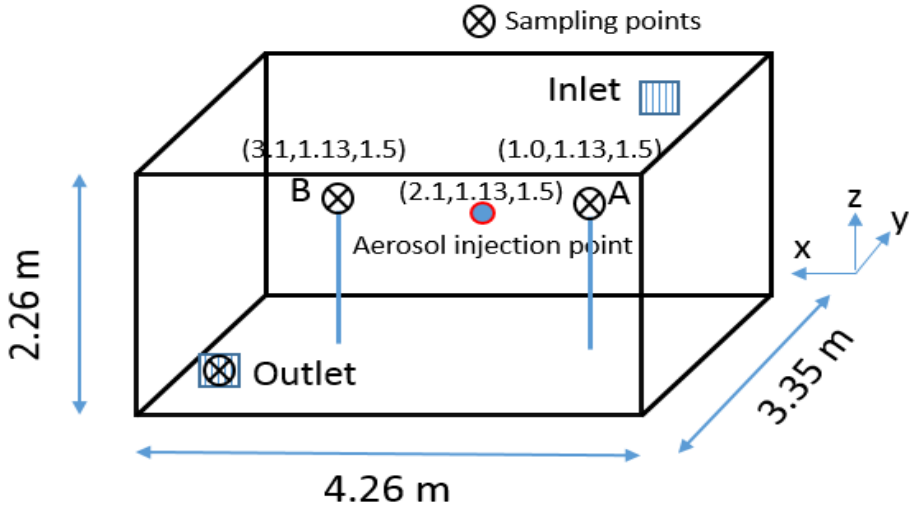

(a)

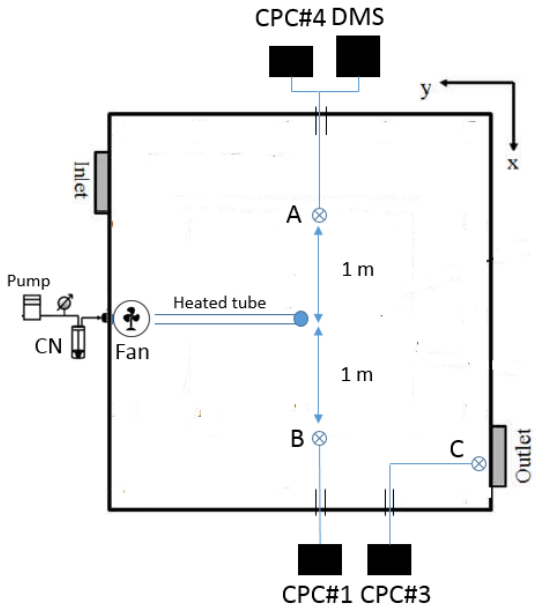

(b)

Figure 4.5: (a) elevation plan of dispersion chamber indicating the coordinates of source and sampling locations and (b) floor-plan of experiment

The setup consisted of three functional zones: dispersion area, air purification system and control devices. The indoor atmosphere was sampled through three ports, as illustrated in Figure 4.5b. Airborne matter in the nano-scale was tested using three condensation particle counters (CPC model 3775 by TSI Inc, USA) and a differential mobility spectrometer (DMS500 by Cambustion ltd, UK) employed both for the monitoring of the PNC and PSD respectively. The operation principles of these instruments have been described in Chapter 3. The instruments were synchronised through one computer and data was continuously stored in real time over the determined period of the experimental study. Sampling was conducted through silicone tubing by TSI (0.19" internal diameter) which reduce the build-up of static charge to minimise particle loss to the tubing wall.

As shown on the schematic in Figure 4.5, the sampling line of CPC#4 and DMS (parallel operation) was installed at position A, that of CPC#1 at position B, and that of CPC#3 at position C attached on the outlet diffuser. Figure 4.1a illustrates the coordinates of the sampling points and the source. Also shown on the figure, all the measurement devices sampling at positions A and B were installed at a height within the breathing zone (1.50 m above floor) adapted to chamber's height except to CPC#3 which was sampling at the middle of the outlet diffuser (0.55 m above the floor). The specified sampling strategy applied here was based on the velocity profile measurements conducted in the work of King et al. (2013) who conducted air velocity measurements at 6 ACH ventilation rate. According to those measurements (presented in Chapter 3), the velocity profile in the region of position A was generally higher due to the impinging jet from the inlet diffuser compared to the region of position B. Finally, CPC#3 was installed at position C for the measurement of the contaminant concentration at the exhaust diffuser during the evacuation of the room. These measurements, as will be shown in Section 4.4.4, were used as inputs for the estimation of the ventilation efficiency at the positions A and B.

Once the devices were scheduled to start the monitoring process at specific time, the 6-jet CN was filled with 50 ml of the sonicated TiO_2 nano-suspension. Once the 6-jet CN was tightened, it was attached on the inlet port used for the aerosol injection where a stainless steel tube of 1.13 meter length was fitted in order to deliver the produced aerosol at the centre of the chamber (Figure 4.5b). Additionally the tube was operated as a drying section by wrapping it in a heated tape at 50 ^{o}C to enhance the removal of humidity from the produced aerosol before its dispersion in the room. A fan at the bottom of the chamber and located behind the dispersion point was operating during the experimental process in order to establish good mixing conditions of the injected aerosol. According to the measurement obtained by a hand held anemometer, the induced velocity of air by the fan was 4 m/s.

The test chamber was initially subjected to a preliminary cleaning at 12 ACH for 20 min in order to reduce the background particle concentrations to a minimum level (< 1000 #/cm^3). Then the indoor environment was isolated through the shut-off dampers and TiO_2 nano-aerosol started to be injected continuously for 70 min. When injection process was completed, immediately the dampers were turned on and the ventilation system was activated. Four ventilation settings were tested in this study: 12, 9, 6 and 3 ACH. For each ventilation setting, instruments were sampling until the PNC dropped down to a plateau level where the dispersion chamber had reached its steady-state. Finally, three replicate runs for each ventilation rate were conducted for repeatability.

4.4 Ventilation strategies for the mitigation of accumulated TiO_2 aerosol after a simulated continuous leakage

Once TiO_2 samples of 30 mg/mL concentration were prepared, they were then introduced into the six-jet CN to be aerosolised and were injected continuously into the dispersion chamber. The evolution of PNC and PSD was being tracked in real time by the distributed particulate instrumentation during both injection and the following ventilation period.

4.4.1 Spatial PNC under different ventilation settings

This section provides the temporal and direct measurements of PNCs obtained by the two CPCs sampling on both sides of the injection point (source), as described schematically in Figure 4.5. As indicated in Chapter 2, measurement metrics along with the measurement principles are important issues in the exposure studies. Even if the best metric, related to possible health effects is yet not identified (Kuhlbusch et al., 2011), size-integrated measurements of PNCs obtained by devices of the same technology could be reliable indicators for the evaluation of the spatial variation of exposure within an indoor environment.

In addition, a crucial information for the exposure assessment is the knowledge of the aerosol behaviour during the first minutes of the release. Specifically, the mixing conditions provided by the fan utilised in the present work serve to understand the contribution of turbulence in the movement of the dispersed ENP from the source to the sampling points during the first minutes of release through the conduction of dispersion experiments with and without the fan.

4.4.1.1 PNC of the overall experimental periods

The averaged temporal variations of PNCs tracked by the CPCs sampling on both sides of the injection point, are shown in Figure 4.6. These measurements describe the overall experimental period divided into two stages: the injection and the cleaning stage of the

chamber through mechanical ventilation. Measurements obtained by CPC#3 are not included as the particular device was sampling at a height not representative of an exposure scenario, for the reasons described in Section 4.2.

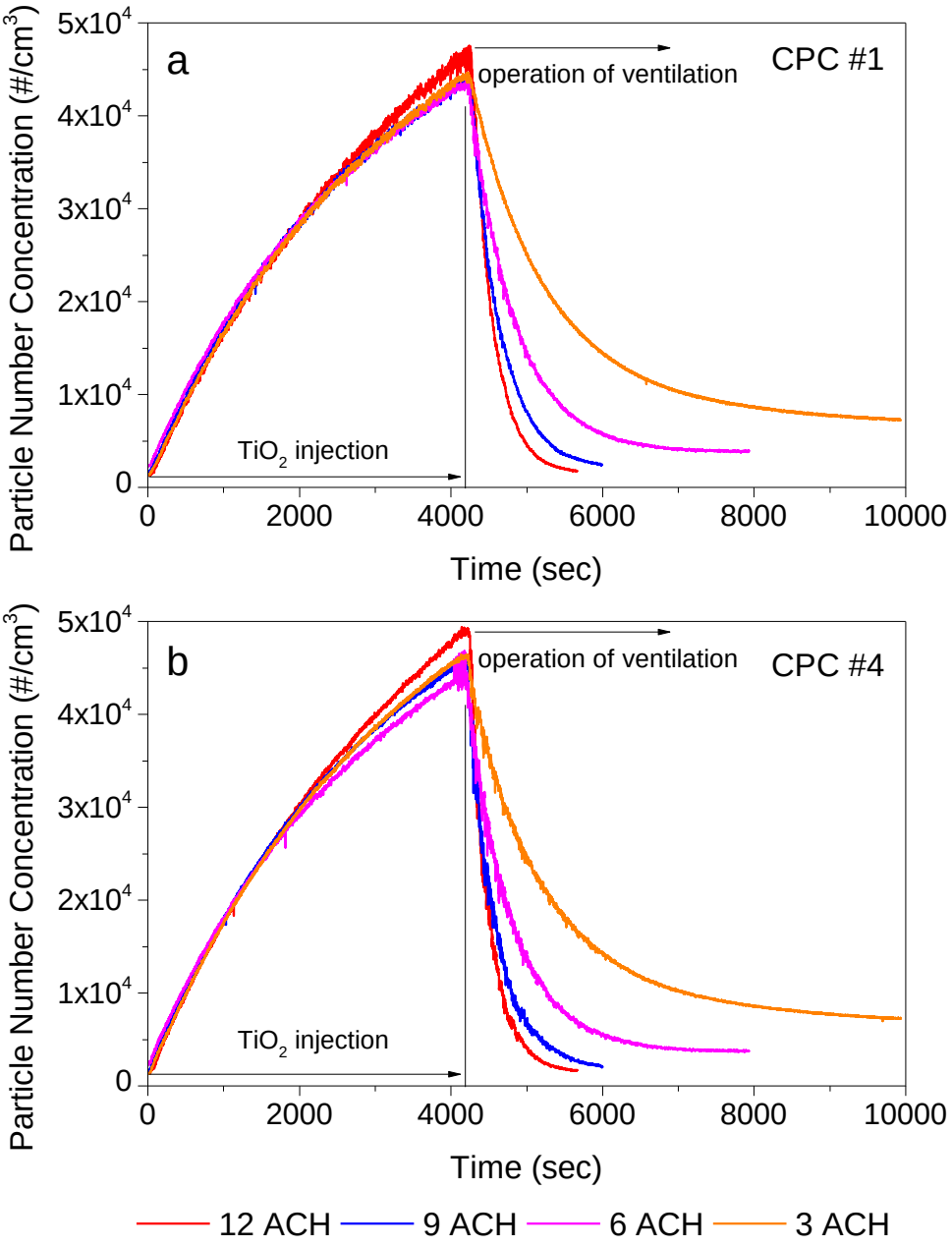

Figure 4.6: Temporal variation of the average PNCs in the dispersion chamber during the overall experimental period as measured by a) CPC#1 and b) CPC#4

As shown in Figures 4.6a and b, once the nanoparticles were emitted into the dispersion facility they spread throughout the room within a few seconds. More details about this important stage of the injection process will be given in the next section. At a first glance, in the beginning of injection stage PNC is described by a rapid increase with time due to the emission event. As the chamber's atmosphere was filled with more ENP the PNC growth rate

was levelled out to some limiting value. This is an indication of the action of inter-particle mechanisms benefited by the increase of PNC resulting in losses of ENPs and in the consequent balancing to the ongoing increase of PNC. The mechanisms counterbalancing the ENP emission rates are not the focus of the current chapter, although an analytical study of these will be presented in Chapter 5.

The following period, after the shut-off from the nebuliser, was described by an exponential decline of the PNCs. As outlined in Chapter 2, dilution due to ventilation is a major process in reducing the concentration levels of dispersed ENP in workplaces. In this study, ventilation rates ranged from 3 up to 12 ACH. Therefore, as was expected, at the highest ventilation rate (12 ACH) the induced dilution resulted in the faster decay of the PNCs in the chamber. These losses, according to Howard-Reed et al. (2003), while being relatively easy to quantify and of equal importance to all particle sizes of nanoscale for a given space and number of air change rate, are however influenced by inter-particle mechanisms. These mechanisms are dependent on several factors including particle size, shape, and concentration and room surface characteristics. The role of these particle mechanisms will become more apparent as the results are presented in the next sections.

Also, in Figure 4.6, it is interesting to notice the leftover particles suspended in the air at the end of the ventilation process, varying with the number of the applied air change rates. As indicated in Section 4.2, the end of cleaning process was considered the time when the PNC curve became asymptotic to the horizontal axis of time where no more extraction of particulates could be achieved by the ventilation system according to the measurement devices. For the highest ventilation rates (12 ACH and 9 ACH), the chamber was evacuated down to levels of PNC close to the initial background particle concentrations before the start of injection. Contrary to this, as can been seen in Figure 4.6, for the lower ventilation rates (6 ACH and 3 ACH) at the end of the decay process PNC relatively higher than the background PNC were measured by both measurement devices. Considering that even at low PNC, ENP could be harmful for human health, then a proper design of the ventilation system at a nanotechnology workplace should cautiously consider and integrate low values of air change rate. Finally, regarding the time required for the chamber to reach a steady state, it is interesting to notice that for the highest ventilation rates, 12 ACH and 9 ACH, this time was 24 and 30 minutes, respectively. On the other hand, for 6 ACH and 3 ACH this time was regulated at 60 and 95 minutes, respectively.

4.4.1.2 PNC during the first minutes of leakage

As described briefly in the previous section, once the TiO_2 nanoparticles had been released into the room, they spread throughout its volume within a few seconds. Figure 4.7 illustrates the averaged evolution of PNC with time over 12 injection tests (three replicates per ventilation setting) during the first five minutes of the leakage as recorded by the two CPCs. These tests, as indicated in Section 4.2, were conducted under the mixing conditions induced by the fan located behind the injection source. Since the release of ENP took place under unventilated conditions and mixing induced by the fan, then particular conclusions on the aerosol motion could be extracted for the first minutes of a hypothetic worst case accidental scenario.

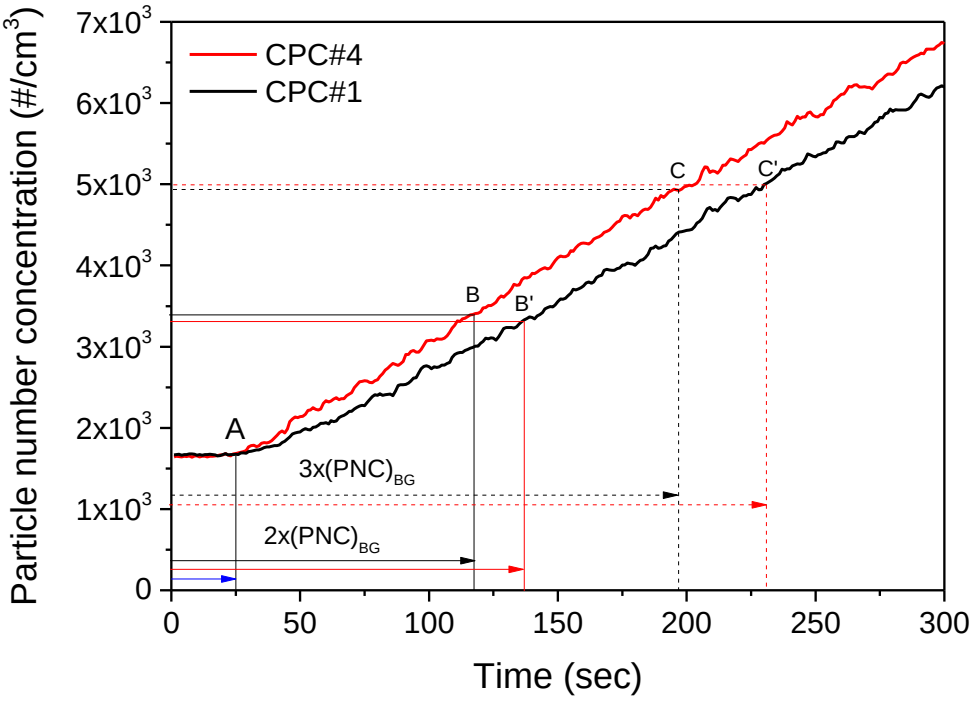

Figure 4.7: Temporal variation of the PNC in the dispersion chamber during the first 5 minutes of leakage as measured by CPC#1 and CPC#4 with the fan on

The point "0" in Figure 4.7 represents the moment when the nebuliser was switched on. Point "A" represents the first response to the elevation of PNC due to the leakage from both CPCs. As can been seen in the graph, this elevation was simultaneously recorded by both measurement devices. This is an indication that the fresh aerosol spread homogeneously in the relatively free of particle environment once it was released from the injection point. The travelling characteristics of the first released aerosol from the source to the sampling points located on both sides and equally distanced from the source were described by quite short times. More specifically, the emitted nano-aerosol cloud needed exactly 25 s to cover the 1

meter (4 cm/s) distance between the source and the sampling points. Furthermore, the time required for PNC to become double (points “B” and “B”’), was 120 s and 137 s, and triple (points “C” and “C”’), 195 s and 230 s, for CPC#4 and CPC#1 respectively.

According to Hinds (1982), the aerosol cloud is defined as the region of high PNC with a definite boundary in a much larger region of clean air. The aerosol bulk motion could be considered only when it is characterised by high mass concentration. A typical example given by Hinds (1982), is the densest smoke which has a density 8.3 % greater than that of clean air, and this difference is a cause of bulk motion. For the case investigated here, the aerosol motion characteristics at such low PNC during the first minutes of leakage could be explained only by the mixing conditions induced by the fan.

In order to evaluate the contribution of the fan operation in the motion of the first released aerosol, three replicate injection tests were conducted by using the same set-up with the fan off. The average variation of the PNC with time during the first five minutes of ENP release is presented in Figure 4.8. As was expected, after approximately 175 s (0.57 cm/s) from the start of injection, the first elevations of the PNC due to the release process were recorded almost simultaneously from both measurements devices. These initial temporal elevations were followed by bursts of concentrations, especially in the case of CPC#1, where the measured PNC temporally changed up to one order of magnitude.

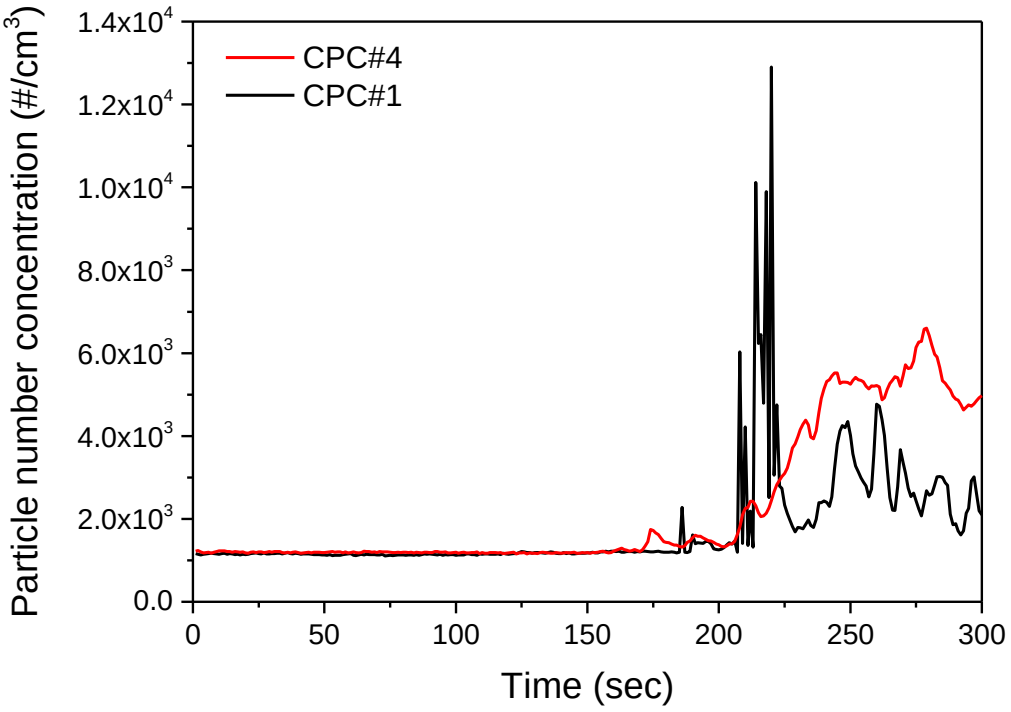

Figure 4.8: Temporal variation of the PNC in the dispersion chamber during the first 5 minutes of leakage as measured by CPC#1 and CPC#4 with the fan off

Following Yang et al. (2012), similar observations were conducted by the authors in the study on PNC distribution of aerosol emitted in a real nano-TiO_2 plant during regular production activities. Their results indicated that the dispersive forces on the aerosol particles from a discharging port had a profound influence on the flight of the suspended particles. Therefore, it is understood that in real-life conditions, the exposure to accidentally released ENP is expected to be homogeneously distributed in atmosphere due to their travelling characteristics enhanced by the mixing conditions established at a workplace.

In conclusion, the above results suggested that in a real life scenario a ENP accidental release due to the isotropic spread of the plume accelerated by turbulence could be detected by a single measurement device, in a well-mixed environment. This information could be utilized for the design of protective systems in nanotechnology workplaces based on particle sensors energising an alarm when abrupt elevation of PNC are detected at least one order of magnitude higher than the background PNC.

4.4.2 Number based PSD and modal parameter fitting

In order to accurately characterise the modes constituting the actual PSDs, the Rmixdist package, which has been described in Chapter 3, was utilised for the estimation of the following modal parameters: mPNC, *CMD* and σ_g. These estimations were used to illustrate the temporal characteristics of the aerosol before the start of the ventilation system, as well as, to describe the evolution of the mPNC with time during ventilation. The results of this analysis are presented in the following two sections.

4.4.2.1 Average PSD and modal fitting analysis on the accumulated aerosol at the end of injection

As indicated in the introduction, the present work aimed to focus on the decay characteristics under various ventilation settings of the dispersed TiO_2 aerosol accumulated in the air of the dispersion chamber after 70 minutes of continuous injection. Therefore, it was important to evaluate first the particle size characteristics of the dispersed aerosol before the start of the ventilation mechanism. To this end, the averaged number based PSD measurements over the last 10 minute period obtained by the DMS are presented in Figure 4.9a. The standard deviations are also included to illustrate the variability between the overall numbers of the injection tests. Furthermore, in Figure 4.9b are illustrated the modal groups present within the actual averaged PSD using Log_{10}-normal distributions as estimated by the Rmixdist program (described in Chapter 3).

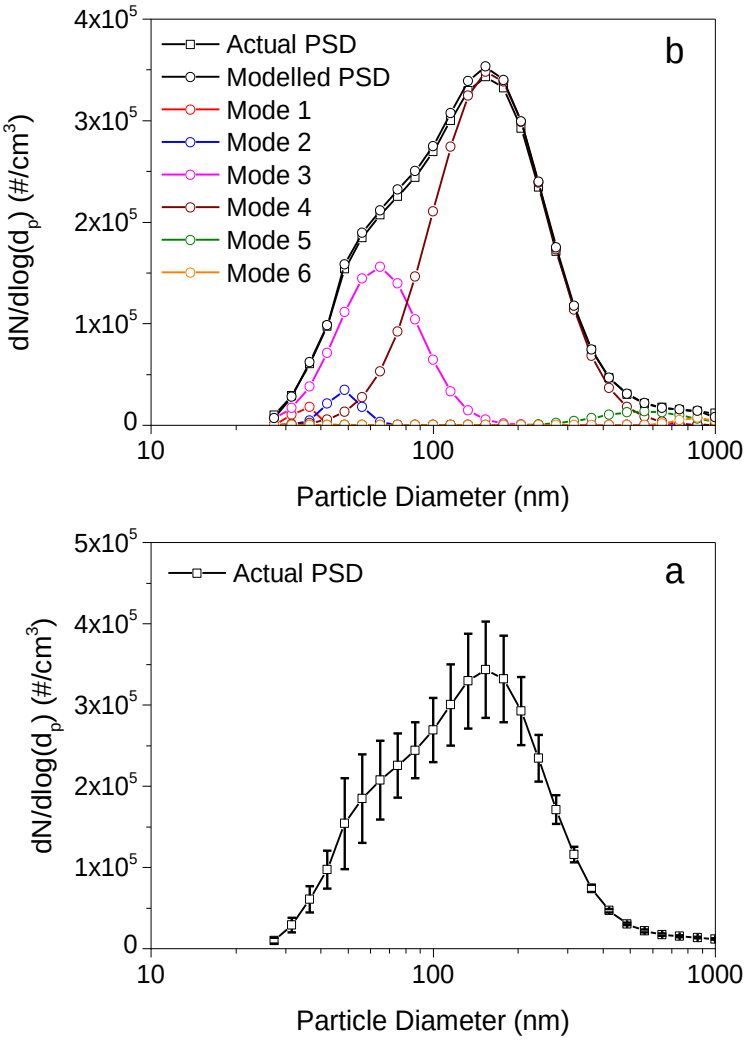

Figure 4.9: a) Averaged PSD obtained by the DMS over the last 10 minute period of injection and b) modelled PSD along with the modes present within the actual PSD as estimated by the Rmixdist program

As shown in Figure 4.9a, the accumulated aerosol at the end of the continuous injection is characterised by a wide multimodal PSD with a distinct peak concentration at 154 nm, while a satisfactory deviation can be observed. Additionally, it could be noticed that the total PNC measured by the DMS ($2.39 \cdot 10^5$ #/cm^3) is significantly higher compared with the averaged peak PNC ($0.45 \cdot 10^5$ #/cm^3) measured by the CPC presented in Section 4.4.1.1. This difference between the two devices has been indicated and quantified by the inter-comparison tests presented in Chapter 3. However, for different sampled aerosol (oil droplets), the tests in Chapter 3 indicated that DMS measured 2.851 times higher PNC than the CPC. Therefore, it could be concluded that this difference in particle measurements is not constant and varied by the aerosol type. Furthermore, it should be considered that these two measurement devices have different operation principles and also possible differences in calibration. Due to this

disagreement, the measurements obtained by the two devices in this work have been studied separately as will be shown in the next sections.

The Rmixdist fitting results suggested that the actual PSD can be de-convoluted into 6 modes with *CMD*s of 34 nm, 48 nm, 64 nm, 158 nm, 555 nm and 860 nm, while the average percentage contribution of each mode to total PNC was 0.74%, 2.07%, 23.2%, 71.5%, 2.05% and 0.46%, respectively. By comparing the particle size characteristics between the airborne and the liquid state (described in Section 4.2) of the TiO_2 nanopowder, then important conclusions could be derived. As indicated in the PSD analysis conducted on the nano-suspension, the peak volume concentration was located at 28 nm and the secondary peak at 112 nm. Results presented in this section showed that the peak mode (Mode 4) concentration of the dispersed aerosol was located at 158 nm and the secondary mode (Mode 3) in concentration at 64 nm. However, the DLS-derived PSD was based on size-resolved volume fractions and the transition to number based distributions involves the multiplication of the values with a factor equal to 10^3 since the volume of a sphere with diameter d is proportional to d^3. Therefore, it could be concluded that the TiO_2 particles in the aerosol generated by the nebulisation of the specified suspension were agglomerated significantly and shifted toward to larger sizes. Additionally, it should be considered that the average PSD illustrated in Figure 4.9 represents an aerosol which had been sampled at 1 meter from the source and which had already been subjected in particle dynamic processes (further analysed and quantified in Chapter 5) resulting in the change of its geometrical characteristics over time.

As outlined in Chapter 2, nanoparticles demonstrate low inertia combined with high-diffusion, therefore are more likely to follow the surrounding flow. At the same time nanoparticles present low potential to escape from the flow and deposit on a surface due to gravitational forces. Additionally, their toxicological impacts are enhanced by this diffusional behaviour since ENPs enter into the human body and deposit at different parts of the inhalation system according to their shape and size. To this end, the nano-toxicology field has significantly focused on the study of ultrafine ENP due to their high penetration efficiency (Biskos, 2012). Therefore, a well-designed and efficient ventilation system should remove ultrafine ENPs as efficiently as for fine particles. The evolution of the modal PNC grouped into fine (diameter > 100 nm) and ultrafine (diameter ≤ 100 nm) during the decay period over the measured PSD of the aerosol evacuated by the specified ventilation rates, is presented in the next section. This section provides a deep insight into the selective removal ability performed by the ventilation system over these two size groups of particles.

4.4.2.2 Evolution of the modal PNC under the different ventilation rates

As discussed in Chapter 3, describing the modal groups present within the PSD using Log_{10}-normal distributions helps to more accurately characterise the modes and represent accurately the evolution of parameters such as the modal PNC (mPNC). Additionally, based on the specified particle size grouping, the evaluation of the selective removal behaviour of the tested ventilation rates on the dispersed ENP was achieved.

As the modal fitting was time-consuming, the measured PSDs obtained by the DMS during the decay periods corresponding to the different ventilation rates, were averaged over determined time intervals according to the time length required from each ventilation to establish in the chamber a steady state. Therefore, intervals of 2.5 min, 5 min, 10 min and 10 min were considered to divide the total decay periods corresponding to 12, 9, 6 and 3 ACH respectively. Over these specified intervals the measured PSD were averaged and introduced into the Rmixdist fitting program for the calculation of mPNC. The evolution with time of the average normalised mPNC for the different ventilation rates, is presented in Figure 4.10.

As shown in Figure 4.10, at the higher ventilation rates (12 ACH and 9 ACH) the maximum and the fastest particle removal of both particle size categories was achieved. Specifically, ultrafine PNC was decreased down to almost zero by the ventilation system in 12 and 35 minutes, as estimated from the 12 ACH and 9 ACH tests, respectively. On the other hand, fine particles required 20 and 35 minutes to reach the same state, at 12 and 9 ACH, respectively. Therefore, results suggest that at the highest ventilation rate (12 ACH) very fast evacuation of the dispersed ENP was achieved, with ultrafine particles being removed faster than the fine ones. However, by reducing the number of ventilation rate from 12 ACH to 9 ACH, a significant increase of the evacuation time in the chamber was demonstrated. At the same time, in contrast to 12 ACH tests, the times required by both particle size groups to be totally removed from the air of the chamber became equal, an indication that the removal ability of ventilation on the ultrafine particles started to be degraded. However, at 9 ACH, similar to the 12 ACH tests, the total elimination of the PNC of both size groups at the end of the cleaning process was accomplished.

For the lower ventilation rates, 6 ACH and 3 ACH, the removal efficiency presented a significant weakness in removing the suspended ENP compared with the higher ones. Specifically, as shown in Figure 4.10, the transition to these low ventilation rates resulted in difficulties of the ventilation system in the removal of ultrafine particles. Indicative of this trend is that at 3 ACH, 30 min after the activation of the ventilation system, the population of

ultrafine ENP had dropped down to 60 % of their initial peak concentration. At the same time, fine particles had reached the 30 % of their initial peak concentration.

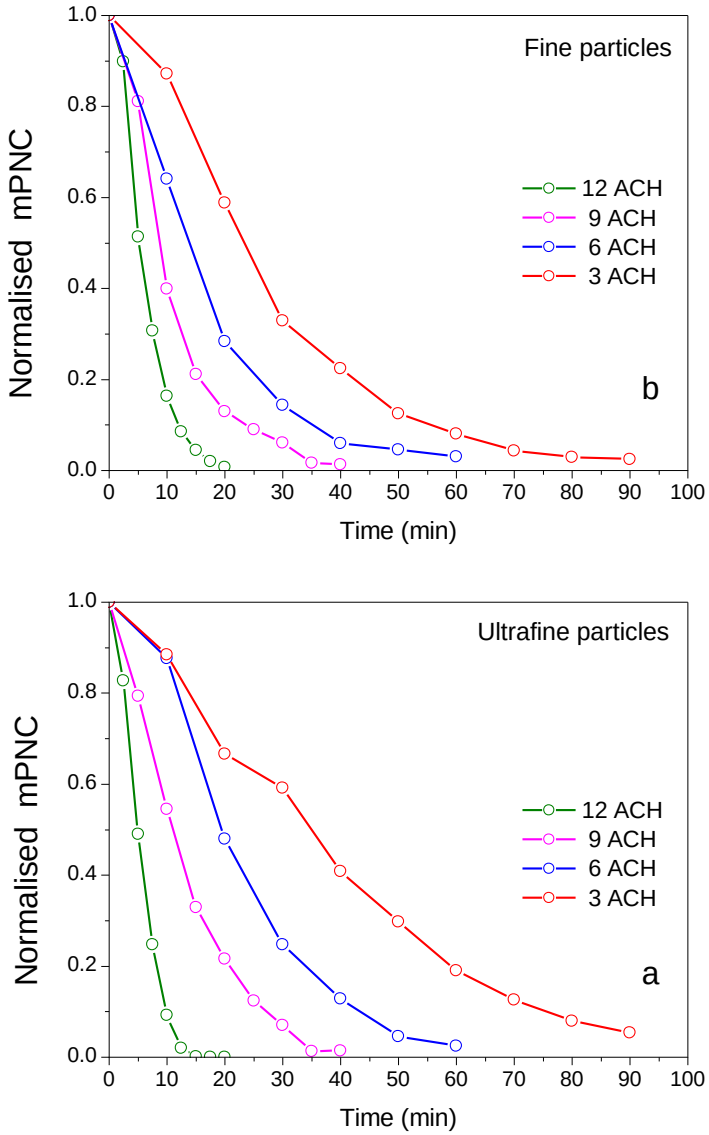

Figure 4.10: Evolution with time of the normalised modal PNC under the different ventilation rates for a) ultrafine, and, b) fine TiO_2 ENP

Furthermore, at the lower ventilation rates, it is interesting to notice the high PNC of leftover particles at the end of the cleaning process. Similar observations were made on the measurements obtained by the distributed CPCs presented in Section 4.1.1.1. However, the size-resolved analysis provided by the DMS reveals information related to the particle size characteristics of these leftover particles. Therefore, at 6 ACH, it can be seen that the populations of leftover particles in the chamber are equally distributed over the fine (Figure 4.10b) and ultrafine (Figure 4.10a) size range. However, at the lowest ventilation rate (3 ACH), the leftover ENP in the chamber were dominated by ultrafine particles.

Considering that ultrafine ENP are hazardous even at low PNC, then exposure to these could be assumed as significant even when the chamber has been ventilated until its steady state. In conclusion, it is obvious that these small particles due to their strong diffusion characteristics, are capable in small fractions to escape from a low strength ventilation flow field, such as established at 3 ACH, and to remain suspended in the air maintaining exposure at relatively high levels even after a complete evacuation.

Therefore, is important to investigate further the decay period corresponding to the different ventilation rates by the introduction into the analysis of a parameter extensively used in the indoor particle studies: the particle decay rate. The particular parameter integrates all these particle mechanisms resulting in the change of PSDs by altering their characteristics with time. To this end, the measurements obtained by the DMS over the decay periods corresponding to the different ventilation rates were utilised in the calculation of the size-resolved particle decay rate. At the same time, the determination of the spatial decay rate based on the measured total PNC obtained by the distributed CPCs was also conducted. The results from these estimations are presented in the following section.

4.4.3 Particle decay rates under the different ventilation rates

The decay of an initial aerosol with concentration C_0 described by Nazaroff et al. (1993) as:

$$C(t) = C_0 \exp(-\beta t) \qquad \text{Eq. 4. 1}$$

where β is the particle decay rate (h^{-1}) and t is the elapsed time. The factor β of equation, as indicated in the previous section, integrates all the particle loss or formation mechanisms contributing in the life time of the dispersed aerosol e.g. coagulation, deposition, ventilation, resuspension etc. By considering that β integrates the air change rate and deposition losses in a ventilated room or container, Howard-Reed et al. (2003) modified the above equation as:

$$\ln\left(\frac{C_t}{C_0}\right) = -(\alpha + k)t \qquad \text{Eq. 4. 2}$$

where k is the particle deposition rate (h^{-1}), α is the air change rate (air changes per hour, h^{-1}) and C_t is the PNC measured at time t; Eq. 4.2 suggests to transform the measured data of PNC (C_t) to natural logarithms and carry out a linear regression analysis over time. Then the negative slope of the best fitted line is the particle decay rate β which represents the losses due to deposition and ventilation. However, in the present chapter, the estimated particle decay

rates were used for conclusions without quantifying the mechanisms which they represent. By applying the discrete form of Eq. 4.2, the estimation of the size resolved particle decay rates can be obtained from the PNCs corresponding to the size bins of the DMS. In addition, the application of the general form of Eq. 4.2 can be used for the estimation of the total particle decay rates based on the size integrated measurements of PNC obtained by the distributed CPCs.

As described above, the transformation of the acquired data into natural logarithms, as has been shown in other works (Howard-Reed et al., 2003; Rim et al., 2012; Gao et al., 2013), should demonstrate a linear pattern and the slope of the linear fit represents the value of the particle decay rate. However, this methodology was not applicable in the case investigated here. Previous studies following the particular methodology were related to episodic releases of particles originating from housekeeping activities and the applied ventilation rates were low. Since the applied ventilation rates in the present work were significantly higher compared to those used in the reviewed works, a lack of linearity was observed for the transformed data. Therefore, simple exponential fits were applied to the original data obtained for each size channel of the DMS, while significantly improved fits were observed on the data obtained by the distributed CPCs through a bi-exponential function representing more than one loss mechanisms.

4.4.3.1 Size-resolved particle decay rates

By averaging the particle decay rates, individually estimated for each size bin of the DMS, over larger size bins, then the average particle decay rates were obtained and are presented in the bar plot of Figure 4.11. The standard deviations are included (as error bars) to illustrate the variability between the replicate runs conducted for each ventilation rate. Considering that the test chamber has been calibrated for the studied air change rates and that the introduced air into the chamber is almost particle free, as outlined in Chapter 3, it is expected that the measured decay rates would be equal or greater to the number of ACH. Also, high standard deviations were observed in the smallest size bin and this could be attributed mainly to the high noise levels of the DMS electrometers corresponding to the size channels within the particular bin.

As shown in Figure 4.11a, for the highest ventilation rate (12 ACH) the total number of the size bins presented decay rates substantially higher than the actual particle ventilation sink (12 h^{-1}), an indication of the action of a secondary mechanism on the particle loss process. Lai et al. (2002) concluded that particle deposition indoors is an important mechanism when the indoor air speed increases. Therefore, in the work presented here, due to the strong induced

air flow fields in the chamber at the highest ventilation rate it is possible that deposition was promoted resulting in higher decay rates than the established ventilation sink. For the lowest size bin representing the ultrafine particles (5-100 nm), the measured decay rate was observed to be significantly higher than the ventilation particle sink. Ultrafine particle deposition under strong air fields has been studied by Gong (2009) in vehicles and the author found experimentally that the deposition rates of these particles were increased when the in-cabin air velocity was increased with the highest increases to be occurred for smaller particles.

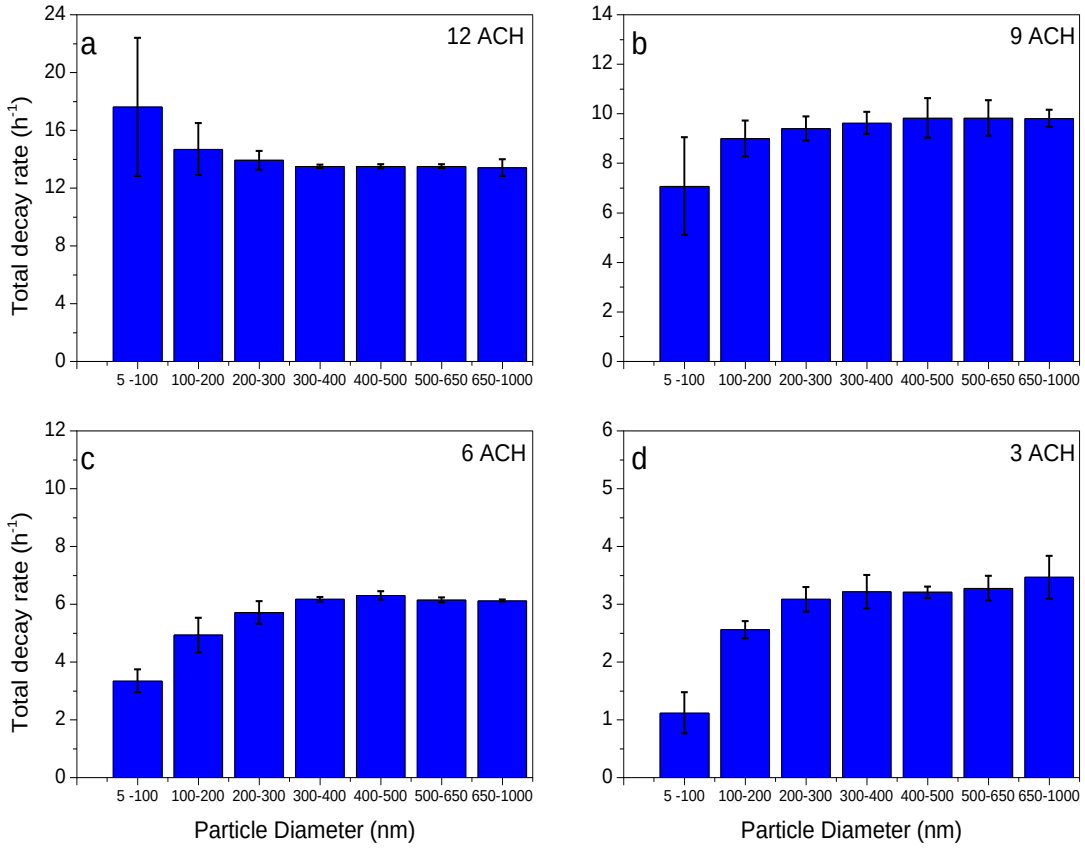

Figure 4.11: Average particle decay rates (h^{-1}) estimated from the measurements obtained by the DMS for ventilation rate a) 12 ACH, b) 9 ACH, c) 6 ACH, and, d) 3 ACH (error bars: standard deviation ± 2σ)

When the ventilation rate was decreased from 12 ACH to 9 ACH, the majority of size bins demonstrated decay rates relatively higher than the corresponding ventilation sink (9 h^{-1}), except for the ultrafine particles' bin (Figure 4.11b). Considerably strong air flow velocities induced by the specified number of air changes may have resulted in the resuspension of deposited particles into the air. Resuspension of particles could also be considered at 12 ACH, however, the fast evacuation induced at such a high ventilation power may result in the fast removal of the re-suspended particles and consequently their detection by the DMS was impossible.

Resuspension of deposited layers of particles into air is a particle formation process caused by the exposure of surfaces to occasional bursts of turbulent eddies. Longer exposure times result in greater probabilities for re-entrainment of particles into air. Hinds (1982) called this process "erosion" and described this as re-entrainment of particles from the top boundary of the layer as individual particles or small clusters. Therefore, in this work, these small clusters were considered as responsible for the drop of smaller particles' particle decay rate below the established ventilation sink.

On the other hand, for the lower ventilation rates, as can been seen in Figures 4.11c and d, more size bins were introduced into the group of those which presented decay rates below the established ventilation sinks. This group of bins affected by the decrease of the ventilation rate includes the size bin, which as indicated in Section 4.4.2.1, contains the mode of the highest particle population (100 – 200 nm). It is also interesting to notice that at 6 ACH ventilation rate, more bins demonstrated decay rates below the expected than those which occurred at 3 ACH tests. Therefore, by considering that for the 6 ACH test the particulate mass extraction should be higher than this for 3 ACH, important conclusions could be derived related to the combined effects induced by the action of particle mechanisms.

As mentioned in Section 4.2, the injected aerosol, before being introduced at the centre of chamber, passed through a heating section comprised of a 1.13 m length steel tube wrapped in a heating tape. Initially, the fresh aerosol was heated through this section before its introduction into the chamber. Afterwards, the dispersed aerosol in the chamber was continuously heated by the heat emitted from the heating tape throughout the injection period. When the nebuliser was switched off, the following activation of the ventilation system introduced filtered air into the chamber of atmospheric temperature. Therefore, in the beginning of ventilation the existing air in the chamber was mixed with the inlet cool air, and according to Friedlander (1977), this mixing process of the different temperature gases may result in the growth of particles through condensation. Additionally, condensation by mixing implemented by small particles (nuclei) that function as sites for new particle formation (Friedlander, 1977). Therefore, this process may lead to the flux of clusters into the lower size bins of the DMS. As a result, this flux of mass affected the measurements of DMS over the smaller size bins and by extension reduced the particle decay rates corresponding to the particular bins.

Considering the above, then various conclusions could be derived to explain the larger number of bins demonstrating decay rates below the established ventilation sink at 6 ACH than these at 3 ACH. It is possible that air velocity at 6 ACH was still strong enough to benefit

resuspension of small deposited particles in the air. Therefore a possible contribution of both resuspension and condensation, resulted in the re-appearance of new airborne particles which affected more size bins than those observed at 3 ACH. For 3 ACH, only the action of condensation could be considered since the induced flow field in the chamber by ventilation was too weak to benefit resuspension.

4.4.3.2 Spatial and size integrated particle decay rates

The average spatial particle decay rates derived from the measurements of PNC obtained by CPC#1 and CPC#4 at the different ventilation rates, are presented in Table 4.2. As indicated earlier, a bi-exponential function was applied on the acquired data and through a limited number of initial parameters and iterations, good fits were achieved ($R^2 \geq 0.99$). The graphical representations of these fits on the data are presented in Appendix A. Since two values of decay rates were determined by the fitting process, two mechanisms were considered to decay the dispersed aerosol during ventilation: mechanism (1) and mechanism (2). Mechanism (1) was described by the highest decay rate value, and therefore was considered to correspond to the mechanical ventilation sink. On the other hand, mechanism (2) of the lowest decay rate value was considered to represent the sum of all those particle mechanisms contributing to the maintenance or the loss of airborne particles during the ventilation period.

Ventilation rate	**12 ACH**		**9 ACH**		**6 ACH**		**3 ACH**	
mechanism→	*(1)*	*(2)*	*(1)*	*(2)*	*(1)*	*(2)*	*(1)*	*(2)*
CPC#1	-12.81	1.087	-9	0.50	-6.08	0.022	-3.7	-0.177
CPC#4	-14.25	-2.42	-10.72	-1.36	-6.22	-0.08	-4.10	-0.288

Table 4.2: Average spatial decay rates (h^{-1}) derived from the bi-exponential fits on the data obtained by CPC#1 and CPC#4.

At a first glance, the decay rates corresponding to the ventilation sink at the location where CPC#4 was sampling, demonstrated in general higher values than those at the location of CPC#1. This could be attributed to the relative distance between the sampling points and the inlet air diffuser. The sampling point close to the inlet diffuser was subjected to higher dilution rates than the one located far from this. As a result the PNC dropped faster resulting in higher decay rates. Furthermore, considering that the particle decay rate is represented normally by negative values, it is interesting to notice that decay rate corresponding to mechanism (2) at the sampling location of CPC#1 demonstrated positive values in all the tests except for 3 ACH. The physical meaning behind these positive values is that mechanism (2) at the location of CPC#1 was preserving instead of removing suspended ENPs during the ventilation period. In

addition, as can been seen in Table 4.2, CPC#4 demonstrated decay rates corresponding to mechanism (1) relatively higher than expected in the 12, 9, 3 ACH tests. In contrast, at 6 ACH this difference between the measured and the expected value is the smallest. This observed weakness at 6 ACH is consistent with the trend observed in the size-resolved decay rates obtained by the DMS at the same ventilation rate, as presented in Section 4.4.3.1.

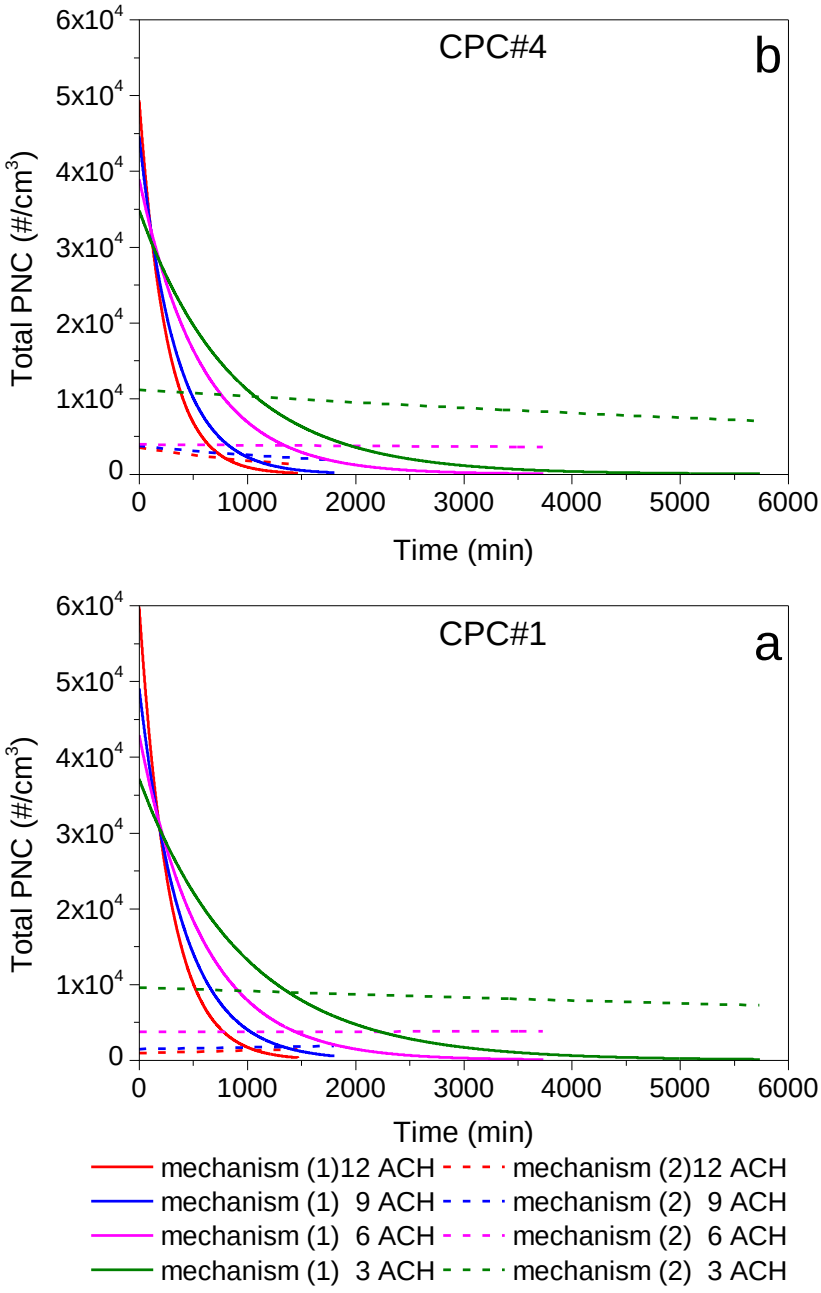

Figure 4.12: Modelled total PNC representing each one of the terms of the bi-exponential function utilized for fitting on the data obtained by the a) CPC#1 and b) CPC#4

Since values of decay rates alone are limited to provide only quantitative information, in the same graph, Figure 4.12 shows the evolution of PNC with time, corresponding to each

mechanism and to each ventilation rate. Mechanism (1) demonstrated to have the dominant role in removing suspended ENP from the air of the chamber in all the tested ventilation conditions independent of the sampling location. However, by decreasing the ventilation power, the strength of the particular mechanism was noticed to gradually become weak, while, at the same time, this decrease had the opposite effect on mechanism (2), whose strength showed to benefit.

Specifically, as shown in Figure 4.12a, in the region where CPC#1 was sampling, at the high ventilation rates (12 and 9 ACH), the PNC corresponding to mechanism (2) was evolving constantly with time at very low levels. On the other hand, the same mechanism in the region where CPC#4 was sampling, resulted in relatively higher initial PNC in the beginning of ventilation followed by a gradual linear decrease with time. These different trends of the PNCs between the two sampling locations could be attributed to the different air flow ventilation characteristics established in the chamber during ventilation. As indicated in Chapter 3, the air velocity profile estimated by King et al. (2013) in the Leeds dispersion chamber, showed that at the sampling height applied here, the air velocity at the region of CPC#4 was generally higher than that observed at the region of CPC#1 due to the impinging jet from the inlet diffuser. Therefore, it is possible that resuspension occurred in the region of CPC#4, which resulted in the high initial PNC of mechanism (2) and in the subsequent gradual decrease due to the high dilution induced by the closely located air inlet in this region.

At 6 ACH and 3 ACH, mechanism (2), for both sampling locations, was shown to be gradually enhanced by the decrease of ventilation power, while mechanism (1) showed a gradual loss of its contribution in the removal of the dispersed ENPs. Furthermore, it could be noticed that the evolution of PNC corresponding to mechanism (2) was described by a slightly declining profile indicating the maintenance of relatively high concentrations of ENP throughout the evacuation process up to the end. Similarly to the assumptions conducted in the previous section, it is possible that the decrease in the number of ACH to benefit the increase of the life time of suspended particles. Post-formation mechanisms of airborne particles such as condensation and resuspension may have acted against the particle removal induced by the ventilation system. On the other hand, particle losses due to coagulation, deposition etc., could also be considered. However, as will be shown in Chapter 5, these mechanisms are very slow at low PNC. Therefore, considering that all the above particle mechanisms were slow, then a counterbalance between their opposite actions may have resulted in the maintenance of suspended ENPs throughout the ventilation process. Given that ENP could be hazardous for public health even at low concentrations, then the particular ventilation rates should be

specifically considered in the design process for the development of mechanical ventilation systems in future nanotechnology workplaces.

4.4.4 Ventilation efficiency

The concept of ventilation efficiency provides a useful tool for the evaluation of the performance of ventilation systems in an indoor environment. Chung and Hsu (2001) considered this parameter as an indicator of the mixing characteristics of incoming air with air already present inside an indoor environment. Furthermore, ventilation efficiency may also be used for the characterisation of the indoor contaminant distribution resulting from the interaction of the supplied air with internal pollutant sources. In the present work, we used the definition of ventilation efficiency introduced by Sandberg (1981). Using values of the steady-state conditions, the relative ventilation efficiency at a given point in an indoor exposure zone may be defined as:

$$E = \frac{C_e - C_s}{C_i - C_s} \qquad \text{Eq. 4. 3}$$

where E is the relative ventilation efficiency at the sampling points, C_e is the contaminant concentration in the exhaust diffuser, C_s is the contaminant concentration in the supply diffuser and C_i is the contaminant concentration in the indoor sampling points. In the present study, the C_i was represented by the PNC measurements obtained by CPC#1 and CPC#4, while the C_e was represented by CPC#3 which was sampling at the outlet diffuser during the tests. Regarding the C_s quantity, separate tests of 10 minutes duration and under the studied ventilation rates were conducted by installing the sampling line of CPC#4 on the supply diffuser. These measurements were averaged over the specified measurement periods and introduced as constant inputs into Eq. 4.3 applied for each tested ventilation rate.

4.4.4.1 Spatial variation of ventilation efficiency under the different ventilation rates

The average spatial variation of the ventilation efficiency corresponding to the different ventilation rates have been investigated and presented in Figure 4.13. Two coloured bordered bars has been used to represent the ventilation efficiency calculated for the two different locations where the measurement devices were sampling. The standard deviation is included to describe the variation between the replicate runs conducted per ventilation rate. The results indicate that at high ventilation rates, the sampling point (CPC#4) close to the inlet diffuser exhibited the highest ventilation efficiency compared to the point where CPC#1 was sampling. However, by decreasing the ventilation power, the relative difference between the ventilation

efficiency of the two sampling points was observed to gradually decrease. Finally, at 3 ACH the two values became almost equal. It is clear that the sampling point close to the air inlet demonstrated higher sensitivity to the decrease of the ventilation power compared to this being located far from the inlet diffuser. This relationship between the ventilation efficiency and the location within an indoor environment with particles suspended in its atmosphere has been reported in a previous study conducted by Bouilly et al. (2005). According to the authors, the tested ventilation rates (0.5 and 1 ACH) in a cubic chamber (2.5 m x 2.5 m x 2.5 m) after the dispersion of particles of 0.3 – 15 μm aerodynamic diameter indicated that the influence of the inlet/outlet locations were stronger for the small particles (0.3 – 5 μm).

This interaction between sampling location and inlet diffuser indicates an important aspect in the design of the ventilation systems for nanotechnology workplaces. Therefore, a case by case study of the ventilation system might be undertaken before the actual system construction in order to ensure a homogenously distributed spatial ventilation efficiency through a proper arrangement of inlet/outlet diffusers. Furthermore, since the dispersion chamber used in the present work provides alternative inlet/outlet locations on the ceiling, then future work based on the application of ventilation strategies described by the utilization of different arrangements of inlet/outlet diffusers would contribute in drawing further conclusions in the study of ventilation efficiency against accidentally emitted ENPs in indoor environments.

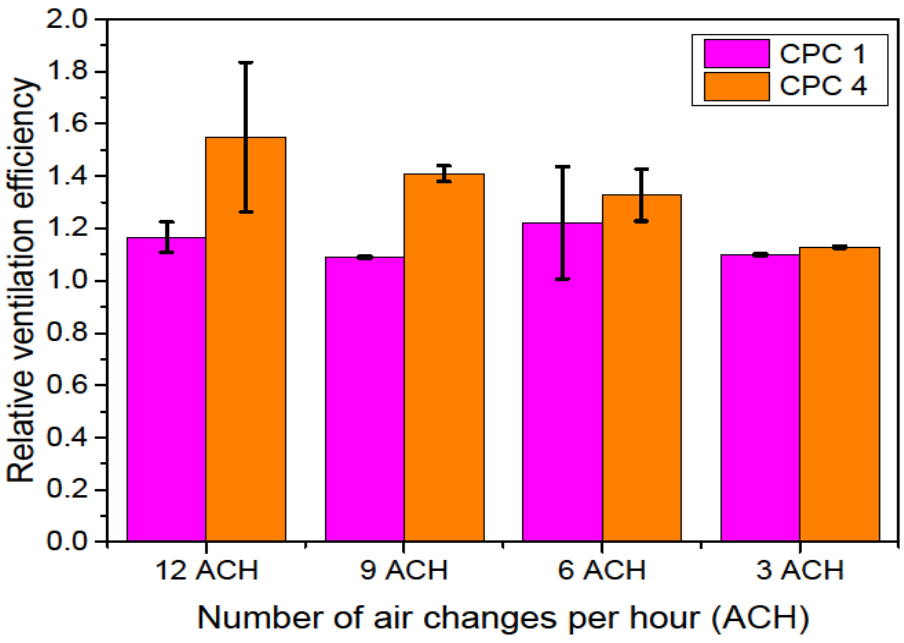

Figure 4.13: The ventilation efficiency of different sampling locations under the different studied ventilation conditions

4.5 Summary

This chapter has presented the volume-based PSDs of nano-TiO_2 suspensions produced for the determination of the optimum liquid mixture which was subsequently used for injection into the Leeds dispersion facility. The continuous release of TiO_2 ENP in a practically particle-free environment was simulated through a 6-jet CN followed by the ventilation period which lasted until a steady-state was established in the chamber. At the same time, a fan located behind the injection source was mixing the dispersed aerosol mimicking the turbulent conditions established in a workplace. The influence of four different ventilation rates (12, 9, 6, 3 ACH) separately tested on the aerosol decay characteristics was investigated and the overall experimental period was monitored by measurement devices spatially distributed within the dispersion room. More specifically, the temporal variation of PNC and PSD was recorded by two CPCs sampling at one meter on both sides of the injection point, and one DMS sampling in parallel with one of the CPCs, respectively. The above devices were spatially distributed in the dispersion room, all sampling within the breathing zone while the sampling line of a third CPC was attached on the outlet diffuser. All the above measurements were utilized for the estimation of the spatial decay rate, the size-resolved decay rate and the spatial ventilation efficiency corresponding to the tested ventilation rates.

- The DLS-derived PSD analysis in sonicated nano-TiO_2 suspensions indicated the establishment of a successful technique for processing nanopowder liquid dispersions in order to achieve efficient de-agglomeration of the stored particles. This technique introduced a considerably modified experimental preparatory process compared to that proposed by NIST. The optimization of sonication parameters such as sonication time and powder concentration indicated that the 30 mg/mL TiO_2 samples after their sonication for 30 minutes exhibited a large fractions of particles <100 nm in diameter. At the same time, the presence of particles in the microscale was eliminated. To this end, 30 mg/mL TiO_2 suspensions were produced by applying the particular method, and introduced into the reservoir of a nebulizer for the conduction of dispersion tests in the Leeds dispersion facility.
- TiO_2 nano-aerosol was injected into the dispersion chamber for a prolonged period (70 minutes) followed by the application of the specified ventilation rates. The spatially measured PNC, indicated an exponential increase of concentration during the injection stage, tending to a plateau at the end. The following decay period was described by an exponential decrease of the PNCs reaching a steady-state which indicated the termination of the ventilation system. However, relatively high PNC of leftover particles were detected after the completion of the evacuation process at the lowest ventilation rates (6 ACH and 3 ACH).

- Regarding the first minutes of the simulated accidental release, under the mixing conditions induced by the fan, the spatial measurements of PNC indicated that the exposure to the first released ENP started 25 seconds after the beginning of injection. In a different course of injection experiments without the application of the fan, it was shown that in stagnant air conditions the plume of ENPs expanded slowly reaching the sampling points on each side of the source in approximately 175 s after the start of injection. For the following period, bursts in PNCs were observed, described by increases of one order of magnitude higher than the background particle levels. It was concluded that in real life conditions it is expected that in the case of an accidental release, ENP are going to be homogeneously spread rapidly to all the directions. Therefore, the installation of a single particle sensor would be able to detect elevations of PNC out of the range of the background particle levels and provide prior warning to personnel to evacuate the workplace.
- The measurements obtained by the DMS confirmed the presence of ultrafine particles generated by the injection technique applied in the present work. The modal fitting analysis on the averaged PSDs over the last 10 minute interval of injection indicated fractions of 26 % and 74 % corresponding to ultrafine and fine particles respectively. The evolution of the modal PNC of the above particle size groups during the following ventilation period showed that at the highest ventilation rate (12 ACH) ultrafine particles were removed faster from the air of the chamber than fine particles. At 9 ACH particles of both size groups were removed in equal times by ventilation. Also, for the high ventilation rates it was noticed that the air cleaning process completed with suspended leftover particles levels close to the initial background particle levels of the chamber. However, by reducing the ventilation rate down to 6 ACH and 3 ACH, the ventilation system presented a removal difficulty especially over ultrafine particles. At the same time, relatively high concentrations of leftover particles were detected by the DMS. The modal analysis on the measured PSD indicated that at 6 ACH these leftover particles were distributed equally in number concentration into fine and ultrafine size groups. At 3 ACH, the leftover ultrafine particles' population was shown to be higher than that of the fine ones.
- The size-resolved decay rates derived by the DMS measurements showed that at the highest ventilation rate (12 ACH) the total number of size bins presented decay rates over the established particle ventilation sink (12 h^{-1}). However, by decreasing the ventilation rate, the decay rates of the smaller size bins started demonstrating lower values than expected. This trend suggested the presence of particle formation processes, such as resuspension and condensation, influencing the smaller size bins. Specifically, at 9 ACH

tests, resuspension of very small particles was considered due to local turbulent effects induced by the strong ventilation flow field. On the other hand, at 3 ACH, due to the extended residence time of the aerosol in the dispersion chamber, condensation by mixing was assumed to affect the particle decay rates of the smaller size bins. In this case, mixing of the existing air in the chamber with the introduced cooler air was considered as responsible for this influence. However, the number of the affected size bins was observed in the case of the 6 ACH tests to be the largest. This led to the conclusion that the particular ventilation setting was a threshold between resuspension and condensation, therefore resulted in the maximum post-formation of airborne particles and consequently in more affected size bins.

- The spatial decay rates, based on the measurements obtained by the diametrically distributed CPCs, were derived by a bi-exponential function indicating the combination of two mechanisms' action on the decay of the dispersed aerosol. The first was considered to represent the ventilation sink, and the second all these particle mechanisms leading to formation and loss. The modelled PNCs corresponding to each term of the function, were plotted together in the same graph and the evolutions of these two mechanisms for each CPC were illustrated. At the high ventilation rates (12 ACH and 9 ACH), the suspended ENP were shown to be removed exclusively by the ventilation sink. However, by decreasing the ventilation rate (6 ACH and 3 ACH) the strength of the mechanism corresponding to ventilation was shown to decrease, and at the same time the contribution of the second mechanism to be enhanced. However, the second mechanism was described by an evolution of PNC which indicated the maintenance rather than the removal of particles at both sampling locations.
- Results of the spatial ventilation efficiency derived from the measurements obtained from the distributed CPCs indicated that at the high ventilation rates (12 ACH and 9 ACH) the sampling point close to the inlet diffuser performed higher ventilation efficiency than that performed by the sampling point located far from the inlet diffuser. By decreasing the ventilation rate, it was noticed that this difference was gradually decreased until 3 ACH where ventilation efficiencies of the two sampling points became almost equal. It was concluded that the relative location of the sampling points from the inlet diffuser influenced the spatial distribution of the ventilation efficiency. Therefore, in order to ensure homogeneous ventilation efficiency independent of location in an indoor environment, further studies should be conducted through ventilation experiments under different arrangements of inlet/outlet diffuser.

Within this chapter a number of size-dependent particle mechanisms have been inferred to explain the decay behavior of ENP accidentally released in an indoor environment under

different ventilation rates. In the following chapter, a number of these particle loss mechanisms are investigated, such as coagulation and deposition, developing during the injection of TiO_2 and SiO_2 ENP and the following decay period under unventilated conditions within the same experimental facility.

Chapter 5

5. Study of Particle Interactions during and following an ENP continuous accidental release

5.1 Introduction

Whilst Chapter 4 investigated the technical and organisational strategies to lower the accidental risk arising from a continuous leakage of ENP in an indoor environment, in this chapter the fundamental understanding of agglomeration, deposition and dispersion will be discussed. The purpose of this work is to provide experimental and modelling tools to assess the risks associated with the worst accidental scenario: continuous leakage followed by a prolonged period in a sealed and unventilated environment. As indicated in Chapter 2, accidentally released ENP in nanotechnology workplaces, from the source to the receptor, undergo aerosol processes which alter the size distributions and accordingly the exposure levels to ENP of different sizes. Therefore, it is of great importance to simulate the release of ENP in potential accidental situations under defined boundary conditions to allow the quantitative analysis of these aerosol processes.

Nano-TiO_2 and nano-SiO_2 liquid dispersions were prepared through sonication using the optimised parameters (powder concentration and sonication time) indicated in Chapter 4. Whilst particle size characterisation in the nano-TiO_2 liquid dispersions has already been presented in Chapter 4, by following the same measurement technique the volume based PSD of sonicated and un-sonicated SiO_2 samples was determined and is presented here. Once the samples of both materials had been sonicated, they were introduced into the reservoir of the 6-jet CN and injected into the Leeds dispersion facility for the time determined by the evacuation experiments presented in Chapter 4. The results of continuously monitoring of the PSDs, in the dispersed aerosols, over the nano and microscale, by a DMS and an APS, respectively, are presented. The overall measurement period is divided into two stages: the injection stage and a prolonged stage following the end of injection. Furthermore, similarly to Chapter 4, Rmixdist is used to distinguish the different modal groups within the measured size distributions, thus highlighting the interactions between different modal groups.

An indoor aerosol model is used to investigate the differential effect of coagulation and deposition on the changes of PNC with time for both experimental periods. More specifically, the modelled coagulation sinks and the total particle loss sinks based on the experimental measurements are used to estimate the deposition sinks. Additionally, the modelled source

rates provide estimates for modelling purposes relating to the injection stage. These processes are represented in an equation predicting the time-dependent changes in PNCs of specific diameter particles within what is considered to be a well-mixed chamber. These estimated changes in PNC are then compared with the experimental measurements and will serve to highlight the importance of the different physical experimental processes in the change of exposure during and after the simulated accidental release.

5.2 Description of the experimental set-up and procedure

The instrumentation arrangement applied for this work is illustrated in Figure 5.1. In addition, in the same figure are illustrated the coordinates of the one sampling point located close to the source. Similar to Chapter 4, the size distributions of the nanoparticles were measured at a 1 metre distance from the source using the DMS, which was installed to sample in parallel with the CPC. However, as indicated in Chapter 3, the inter-comparison tests between these two measurement devices indicated a higher PNC in the response of the DMS. Therefore, since the present work was based on size resolved measurements, the data obtained by the CPC were exclusively used to identify significant shifts within the DMS data. Due to the long-term nature of the experiments, the continuous sampling resulted in an accumulation of deposited particles on the electrometers of the DMS and consequently in temporal fluctuations of the data. These fluctuations had to be removed in order to accurately study the particle interactions over time of the dispersed ENP.

In this work, due to the high interest in the generation of μm particles by the applied dispersion technique and the subsequent influence of these large particles on particles of the nanoscale, an APS was also utilised for the airborne particle characterisation within the μm range. The particular device extracted a sample flow in parallel with the above measurement devices and its operational principles were described in Chapter 3. Finally, metallic stubs were placed at various locations on the floor and the walls of the chamber in order to collect deposited matter for subsequent TEM analysis.

As indicated above, the near-field to the source measurements of PSD were considered to represent an accidental scenario described by the rupture of a pipe supplying airborne ENPs and the subsequent leakage of these in an indoor environment. Similar to the ventilation experiment presented in Chapter 4, the simulated continuous leakage of ENPs lasted 70 minutes. The following period was described as 5 hours of allowing the decay of the dispersed aerosol under unventilated conditions. This prolonged period was chosen to represent the worst case scenario after an accidental release of ENP: the failure of the ventilation system.

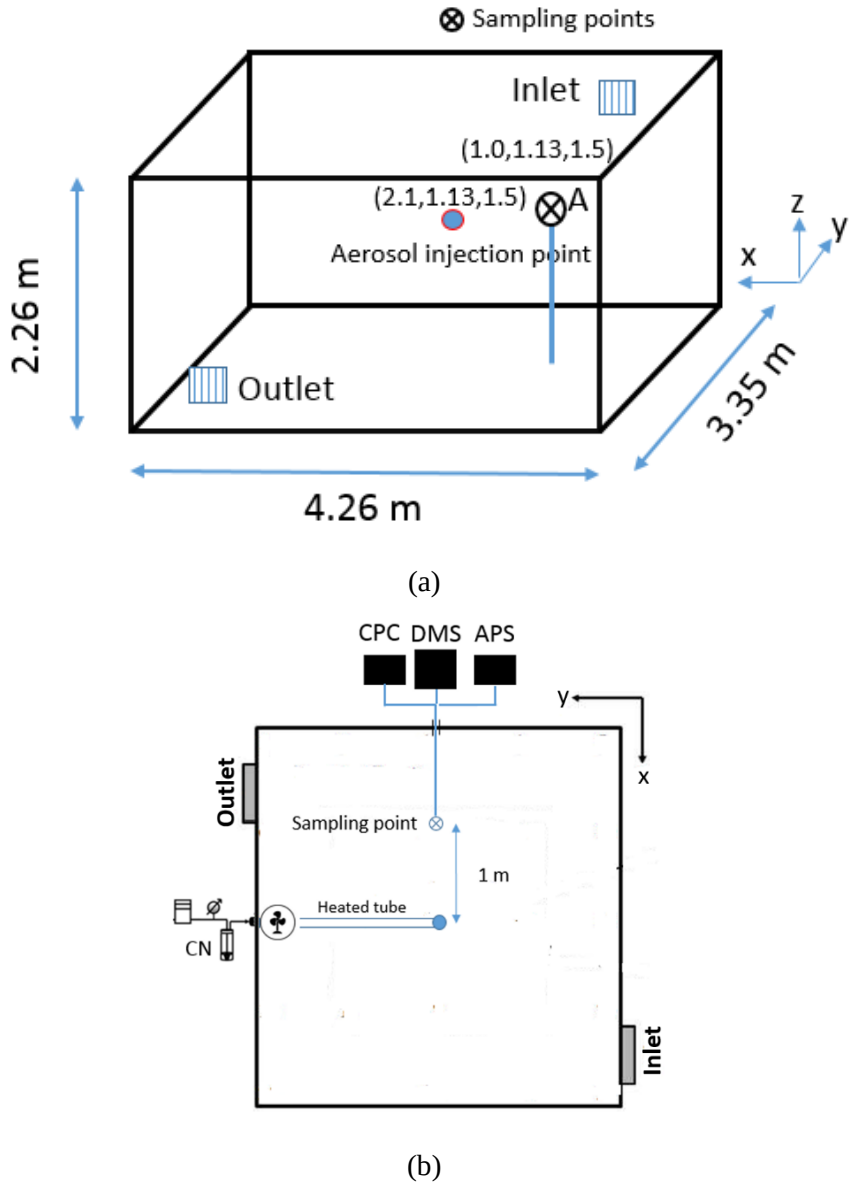

Figure 5.1: (a) Main test chamber dimensions, with air inlet and outlet locations; (b) floor plan of the main chamber indicating the location of the experimental measurement devices

To this end, in the low background particle concentration air environment of the dispersion chamber, TiO_2 and SiO_2 aerosol generated by the 6-jet CN, were injected continuously for 70 minutes into the well-mixed chamber followed by a 5 hour period with the accumulated dispersed aerosol decaying under unventilated conditions. This particular experimental process was repeated three times for each tested material. Table 5.1 gives an overall description of the experimental structure and materials utilised in the process. The temporal evolution of PNC and PSD of the dispersed aerosols was recorded by two computers, one connected to the DMS and the second to the APS and CPC. Both computers were synchronised in order to collect data simultaneously.

	Experimental periods	
Material	**Leakage**	**Prolonged period following the end of leakage (unventilated conditions)**
Aeroxide TiO_2 P25	70 min continuous injection	5 h decay period
Synthetic Amorphous SiO_2 (NM-200)	70 min continuous injection	5 h decay period

Table 5.1: Experimental periods and materials utilised for the dispersion tests

For the dispersion experiments presented here, TiO_2 and SiO_2 nano-suspensions of the same concentration were prepared using the modified experimental preparatory process presented in Chapter 4. Once the samples were sonicated, they were then introduced into the reservoir of the 6-jet CN for their subsequent injection into the dispersion chamber. However, before the presentation of results relating to the dispersion events, the particle size characterisation conducted over SiO_2 nano-suspensions is demonstrated in the following section. It should be noted that the particle size characterisation on the TiO_2 nano-suspension was presented in Chapter 4.

5.3 Characterisation of SiO_2 suspension through the DLS method

Chapter 4 presented the optimisation process followed for the preparation of TiO_2 nano-suspensions characterised by a large fraction of particles with a diameter ≤ 100 nm. Through specific steps, the protocol proposed by Taurozzi et al. (2012) (NIST), was modified in order to achieve the highest potential de-agglomeration of the suspended powder. Finally, this particular optimisation process indicated that the sonication of a 30 mg/mL TiO_2 sample for 30 minutes was sufficient to de-agglomerate the suspended powder and to eliminate the presence of particles in the μm range.

To this end, similar to TiO_2, three samples of 1.5 g SiO_2 nanopowder were suspended in water (30 mg/mL) and then sonicated for 30 minutes. Immediately after this, the sonicated samples were transferred to the zeta-sizer for PSD analysis. At the same time, three un-sonicated samples of the same powder concentration were also prepared for a PSD analysis in order to be used as reference samples for assessment of the effect of the ultra-sonication process on the de-agglomeration of suspended particles in the liquid phase. The experimental set-up, as well as the auxiliary equipment utilised for conducting the above tests, were described in Chapter 3.

The averaged data points of the DLS-derived PSD over the three sonicated samples and the three un-sonicated ones are presented in Figure 5.2. As shown, the non-sonicated samples exhibited a broad polydisperse and multimodal PSD predominantly described by the presence of particles in the (1-10) μm range. The samples typically had a major fraction of agglomerates centred at around 5.2 μm and a minor fraction of particles centred around 668 nm. Fragmentation occurred in suspension after undergoing sonication resulting in a multimodal distribution. Specifically, the suspended material presents high dispersity with the majority of the volume distribution located within the nano-range, having a peak at 295 nm, and a small volume of particles located in the micrometre range (peak at 4.74 μm).

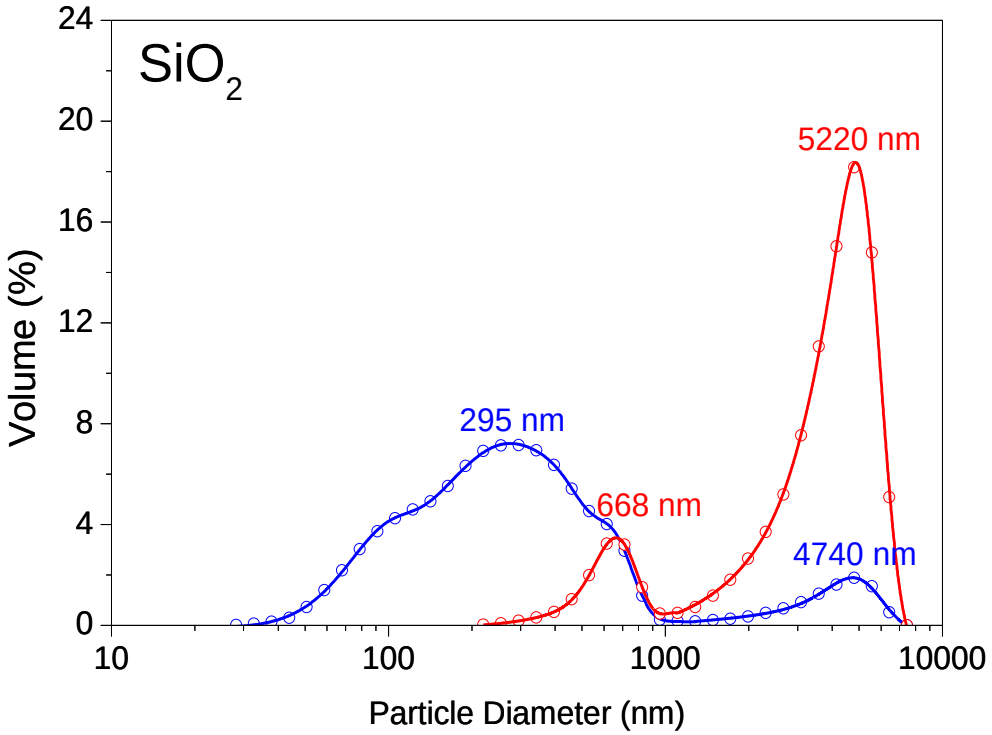

Figure 5.2: Averaged volume based PSD derived by the DLS method, over three sonicated and three un-sonicated SiO_2 suspensions of the same powder concentration (open dots: experimental data; line: log-normal fitting and main peak positions)

Through a comparison of the results presented here with the work conducted by the Joint Research Centre (JRC) (2013) on the same material, an adequate agreement can been seen relating to the polydispersity characteristics of the measured PSDs. These authors sonicated 6.82 mg/mL suspensions of the specified powder for 20 minutes with 40 % pulsed operation mode of the ultra-sonicator. Their results indicated a lower mean hydrodynamic size of particles (207.8 nm ± 11.9), across five replicate samples, than that measured in the work presented here (331.52 nm ± 21.83). It is obvious that this difference is attributed to the different characteristics between the two preparation methods. However, these authors reported high polydispersity and the presence of large agglomerates of several μm size.

Additionally, according to these authors, due to the wide size-distribution and the presence of these large agglomerates, the intensity signal weighed towards the bigger particles. Therefore, it is possible through the DLS method that the smaller particles may not be resolved well and the true sizes could be smaller than those indicated by the DLS method.

In conclusion, similar to TiO_2 (presented in Chapter 4), sonication proved to be efficient for the fragmentation of the suspended SiO_2 powder in water. The PSD obtained from the SiO_2 sonicated samples demonstrated a wider distribution over the nanoscale with less distinct characteristics compared to those demonstrated by the TiO_2 case. Furthermore, in contrast to TiO_2, it may be observed that there is no evidence of the primary particle size (14 ± 7 nm). However, as described in the previous paragraph, the high polydispersity presented by the sonicated SiO_2 samples possibly influenced the resolution of the particular measurement technique resulting in overestimated sizes of the smaller particles. In addition, a small fraction of μm particles was observed in the SiO_2 sonicated suspensions, which was not seen in the case of TiO_2.

5.4 Evolution of PSD with time in the chamber

Immediately after the TiO_2 and SiO_2 suspensions were prepared, they were introduced into the 6-jet CN's reservoir and injected continuously in the dispersion chamber for the specified length of time. This stage was followed by a 5 hour decay period of the accumulated dispersed aerosol under unventilated conditions. As indicated in Section 5.2, three replicate runs were conducted for each tested material and the obtained measurements were averaged over all of the runs. The evolution of the average PSD profiles with time measured in the nanoscale by the DMS, are presented in the following sections as contour plots and as plots of the data using the normalised and size-resolved PNC ($dN/d\log d_p$). Additionally, the evolution throughout the total experimental period of the average size-resolved normalised PNC obtained by the APS is provided.

5.4.1 Concentration Contour Plots

The number based average PSDs of TiO_2 and SiO_2 for all replicate tests of each case and over the total experimental period are shown as contour plots in Figures 5.3a and 5.3b respectively. The x- and y- axis show the time and the particle diameter respectively. The number concentrations are indicated by the colour spectrum. The superimposed lines follow changes in the colour spectrum in order to indicate the regions where physical processes are likely to be affecting changes in PNC after the end of injection. The information provided by the specific contour plots are not sufficient to reveal particular geometric characteristics of the

PSDs. However they could be used to evaluate the decay characteristics of the dispersed aerosols as a function of PNC and particle diameter during the 5 hours following the end of injection.

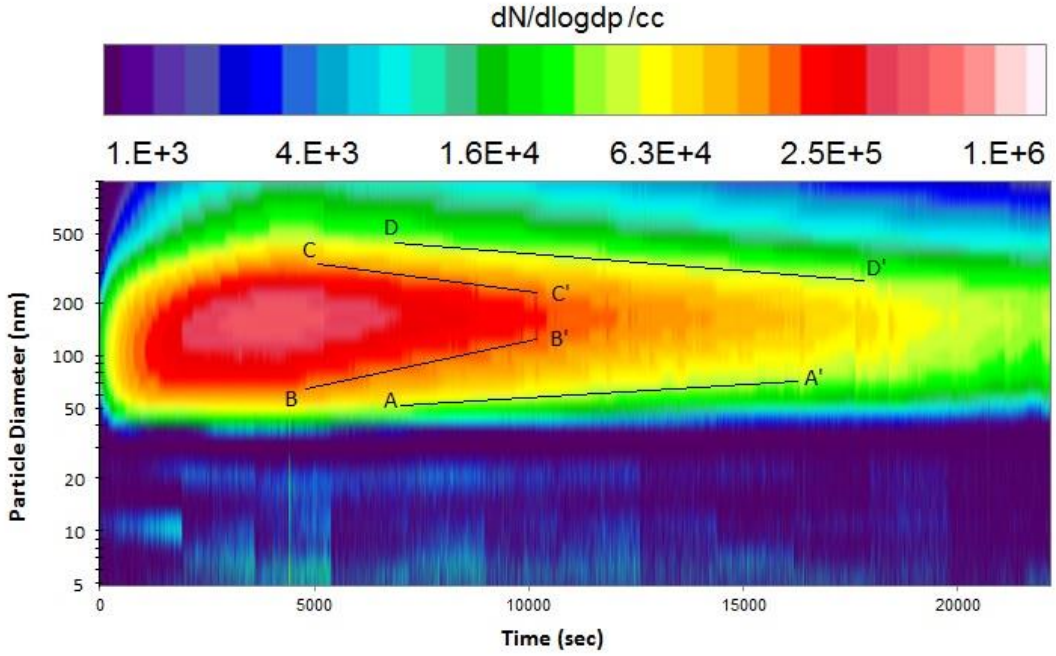

(a)

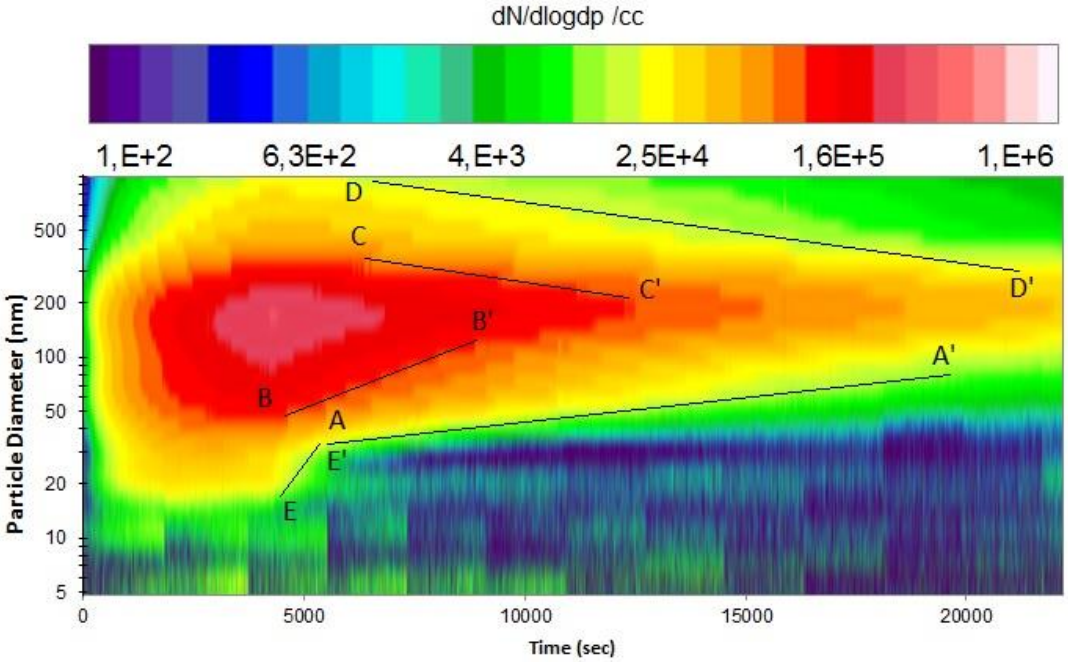

(b)

Figure 5.3: Contour plots of the average PSDs measured over the entire experimental period of (a) TiO_2 and (b) SiO_2 dispersion (70 min continuous injection and 5 h after the injection)

After the end of injection, a region of high PNC (indicated by the red colour) was established in the size spectrum 50 – 300 nm, for both materials. Particles in this region presented strong decay characteristics indicating the action of a loss mechanism benefited by the high PNC. The slope of the lines BB' and CC' reveal the strong contribution of such a mechanism over the particle loss rates. Additionally, a region of low PNC described by the yellow colour demonstrated moderate decays over time (lines AA' and DD'). Due to the wide range of this region in the size spectrum it is reasonable to consider the combination of more than one size-dependent particle loss mechanism. Finally, in the case of the SiO_2 dispersion experiment, an additional line (EE') was drawn to describe a large decay of very small particles (< 20 nm in diameter) immediately after the end of injection. This could be attributed to the presence of high PNC of larger particles dominating over the smaller particles and leading to their elimination through agglomeration.

5.4.2 Evolution of PSD with time in the nanoscale

The total experimental period, 70 minute injection and the following 5 hours, was divided into 10 minute intervals. The real time size distributions monitored by the DMS were averaged over these intervals in order to provide an overall picture of the evolution of the main modes. Furthermore, the results obtained through this process were averaged over three replicate runs conducted for each material and they are presented separately in the following two sections. Each data point in the graphs presented below represents the channel specific number concentration averaged over the specified time intervals and for all the replicate runs conducted for each tested material. The y-axis of these graphs is a relative number concentration. The error bars for all the curves on each graph are omitted for clarity. The standard error of the mean for each process was varied with the channel size. Specifically, the standard error represented typically 5-25 % and 4-15 % of the channel mean number concentration value, for TiO_2 and SiO_2 dispersion tests respectively.

5.4.2.1 TiO_2 Aerosol

Figure 5.4 presents the evolution of the average PSD over time, based on the 10 minute intervals of the injection stage (Figure 5.4a) and of the following 5 hour period (Figure 5.4b) during which aerosol was allowed to disperse under sealed conditions. As can be seen, during the first 20 minutes of the injection a single peak of diameter ~100 nm was observed. The subsequent averaged PSDs during the injection stage each show a slow but stable shift of the central particle mode diameter to larger sizes, reaching 164 nm at the end of the injection process. The rapid increase in concentration of that mode during the first 20 minutes of the release is due to the time required for the volume of the chamber to be filled with sufficiently

high PNC. After that period, substantial coagulation may occur driven by the high PNC which has already become well mixed into the total space of the test chamber leading to shifts in the peak diameter.

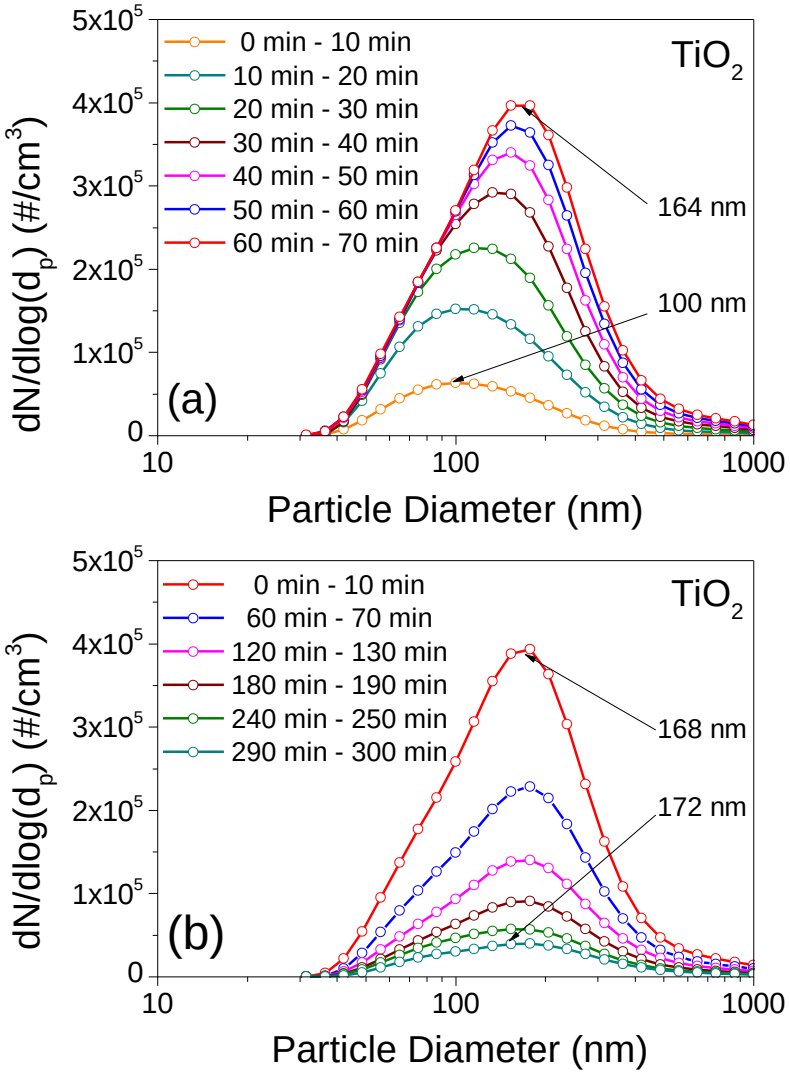

Figure 5.4: Evolution with time of the averaged PSDs in a) consecutive 10 min intervals during the 70 min continuous injection period and b) the first 10 min intervals of each hour following the end of injection of TiO_2 aerosol up to the last 10 min interval of the study period

During the 5 hours following the end of injection, the PNC decays with time. As can been seen in Figure 5.4b, the PNC decreased to almost one half of the initial PNC within the first hour, indicative of the action of a strong particle loss mechanism or a combination of mechanisms. Since no ventilation was used in combination with the adiabatic walls of the dispersion chamber, it could be considered that the simultaneous action of coagulation and deposition may have resulted in this strong decrease of PNC. Furthermore, the co-existence of the above mechanisms could also explain the relatively stagnant location of the main mode to the same diameter throughout the overall study period.

An important conclusion which may be derived from the results presented here is that the applied injection technique results in the generation of large fractions of particles in the nanoscale. According to the CN droplet number output provided by BGI (2002), for the given back pressure provided by the pump (20 psi), the method is expected to generate aerosol consisting of droplets with 1 μm count median diameter (CMD). Considering the size range (100 – 164 nm) demonstrated by the main peak diameter during injection (Figure 5.4a), an efficient injection technique for the production of solid ENPs has been established. Furthermore, the particle size characteristics described by the PSD in the airborne state come into a satisfactory agreement with those demonstrated in the liquid phase. The DLS-derived PSD of the TiO_2 nano-suspension (Chapter 4) indicated the main peak diameter of the suspended particles at 28 nm and a secondary one at 122 nm. Therefore, the peak diameter (at 100 nm) of the fresh dispersed ENP observed during the first 10 minute interval of injection, indicates an adequate agreement between the liquid and the airborne measurement technique. At the same time, this comparison reveals the strong agglomeration governing the aerosol particles once they were released from the nebuliser's outlet.

5.4.2.2 SiO_2 Aerosol

Figure 5.5 shows the evolution of SiO_2 aerosol over the specified time intervals of the two experimental periods. As shown in Figure 5.5a, in the first 10 min of the release three peaks were found to be within the nano-scale, specifically at 24 nm, 86 nm, and 178 nm. The second peak was observed to have the highest number concentrations (main peak diameter). As the injection stage proceeded, the main peak diameter was stabilized at 168 nm while the smaller modes started to merge, forming a size distribution with more distinct characteristics. Similar to TiO_2, agglomeration resulted in shifts in the modal characteristics during the injection phase. However, it is clear that in the case of SiO_2 there is a strong presence of what would usually be classified as nucleation mode particles, as indicated also in the contour plot presented in Section 5.4.1. These were not observed for TiO_2 and their presence may have resulted in different agglomeration rates when the chamber was filled with a sufficient PNC of large particles.

On the other hand, as shown in Figure 5.5b, for the SiO_2 decay period a gradual shift of the dominant mode to larger diameters can be seen throughout the whole study period of the 5 hours. At the same time, it can been seen that the PSD was gradually narrowing with the decrease of PNC. While the main mode was located at 177 nm at the start of the decay process, it continuously increased up to 198 nm at the end of the final 10 minute interval. The drop in PNC within the first hour of the decay process was smaller than that observed for TiO_2. This could be attributed to the different relative importance between coagulation and deposition,

resulting in the maintenance of more airborne nano-particulates compared to the TiO_2 tests. This subsequently led to more interactions between particles resulting in the observed small shifts of the main mode toward to larger sizes. It is interesting to note the rapid loss of particles with diameter < 100 nm within the first hour of the decay period. This could be attributed to high coagulation rates developed for these small particles after the termination of a constant supply of fresh ENP by the source.

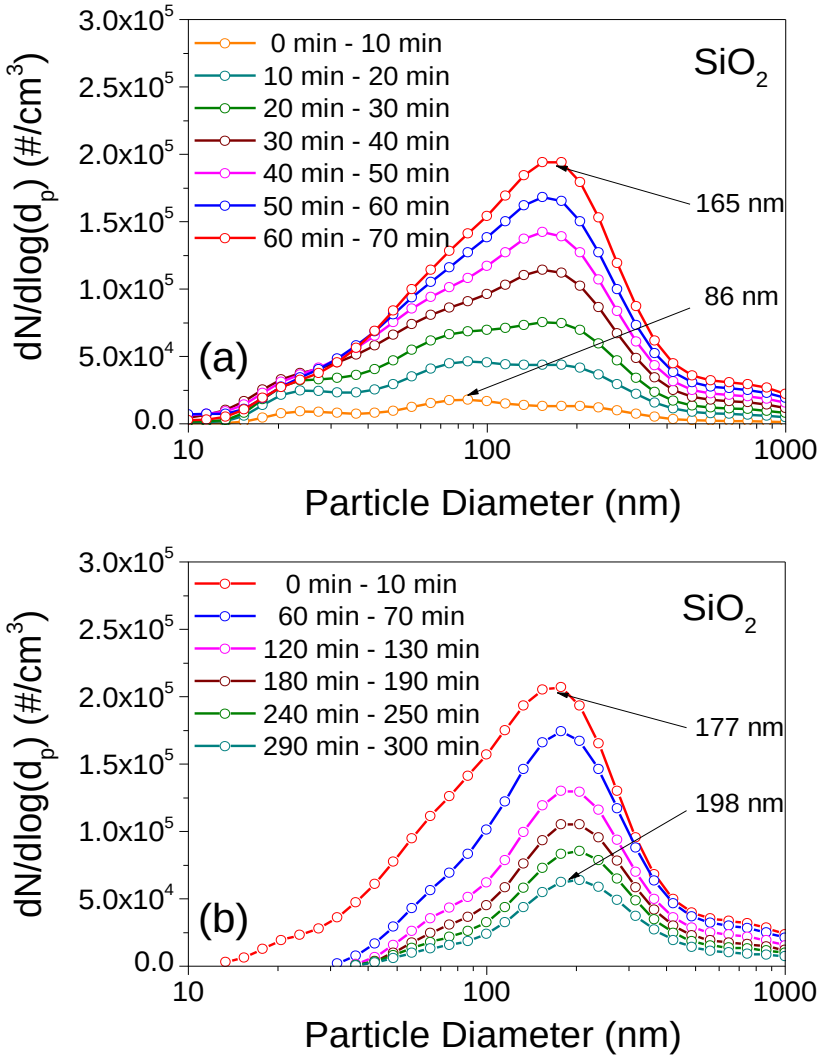

Figure 5.5: Evolution with time of the averaged PSDs in a) consecutive 10 min intervals during the 70 min continuous injection period and b) the first 10 min intervals of each hour following the end of injection of SiO_2 aerosol up to the last 10 min interval of the study period

The comparison of the particle size characteristics presented here with those in the liquid phase (Section 5.3), confirms the polydispersity detected by both measurement techniques. In addition, the DLS-derived PSD showed that the main peak diameter in the liquid phase was located at 295 nm. However, as discussed in Section 5.3, the true diameter of the smallest SiO_2 particles may not be resolved well by the DLS technique. This was attributed to the presence

of large agglomerates that resulted in an intensity signal weighing towards the bigger agglomerates.

5.4.3 Evolution of PSD with time in the microscale for both study cases

Similar to the graphs illustrating the data obtained by the DMS in the previous sections, the data points obtained by the APS, represent the channel-specific number concentration averaged over the specified time intervals and for all replicate tests conducted for each material tested. Also, the error bars for all the curves in the following graphs are omitted for clarity. The standard error of the mean for each process estimated in the APS data was lower than that of the DMS data. Specifically, the standard error typically represented 4-9% and 3-6.5% of the channel mean number concentration value, for TiO_2 and SiO_2 dispersion tests respectively. This difference between the two measurement devices is normal and attributed to the fact that the two instruments use different principles to measure particle size, with the DMS being more vulnerable to variability due to its electrometers.

In Figures 5.6a and c and 5.6b and d, the evolution of the average PSDs based on the measurements of APS for TiO_2 and SiO_2 respectively, is illustrated. Particle growth, which was observed in the measurements obtained by the DMS, is also indicated here. During the injection phase, distributions are described initially by a single peak located in the fine range of diameters, 626 nm and 670 nm, for TiO_2 and SiO_2 respectively, moving towards larger sizes and reaching the 640 nm and 700 nm diameters of the size spectrum, respectively, at the end of the study period. Additionally, the presence of large particles (>1 μm) can be observed, for both suspended materials, following an increasing trend during injection. In particular, for the case of TiO_2, the emitted concentrations of micro-particles at the end of the injection period were approximately four times higher compared to those emitted in the SiO_2 dispersion test.

In general, the total PNC in the produced aerosols by the injection technique applied herein, was higher in the TiO_2 aerosol than in the SiO_2 one. The particular trend was also observed in the measured PSDs obtained by the DMS over the two tested materials (Sections 5.4.2.1 and 5.4.2.2). This difference is attributed to the different levels of the sufficiently suspended mass of each tested material in the liquid. Specifically, it was observed that the sonicated TiO_2 nano-suspension presented an opaque white appearance, an indication of homogeneity. On the other hand, the sonicated SiO_2 nano-suspension presented a transparent appearance, whereas a slight sedimentation was observed at the bottom of the nebulizer's reservoir after the end of injection. This was an indication of loss of the suspended powder mass which consequently resulted in a lower load of particles in the produced aerosol compared to that produced by the TiO_2 nano-suspension.

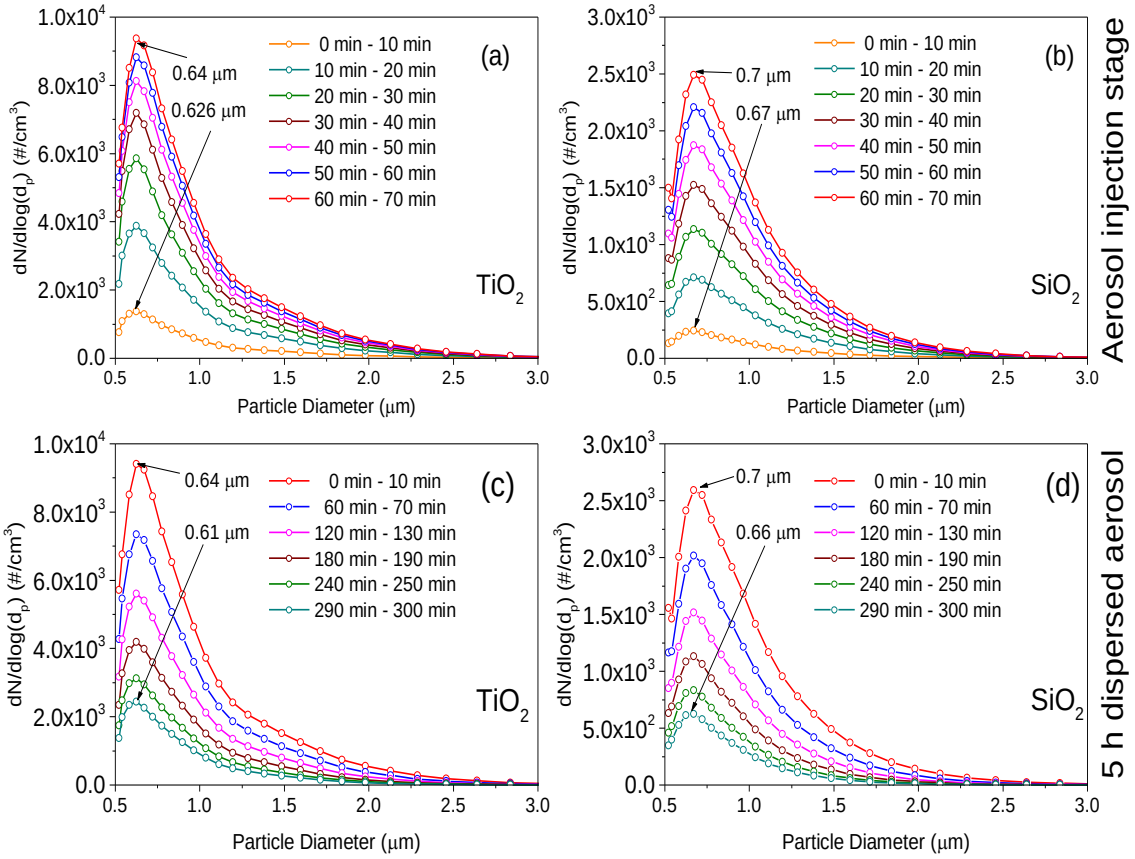

Figure 5.6: Evolution over time of the averaged PSD measured by the APS over the consecutive 10 min intervals during the 70 min continuous injection (a and b) and the first 10 min intervals of the consecutive hour following the end of injection up to the last 10 min interval of the study period (c and d), for TiO_2 and SiO_2 dispersion tests

Also, it should be noted that the particle concentrations detected in the overlapped size channels between DMS and APS, at the end of injection stage of both materials, demonstrated one order of magnitude between their measurements. This difference may be to do with the fact that the two instruments, as indicated in Chapter 3, use different principles to measure particle size, hence resulting in different PNC. Similar observations were made by Pfefferkorn et al. (2010) who utilized in their study an APS and an Engine Exhaust Particle Sizer (EEPS) to study the exposure to airborne nanoscale particles originating from friction stir welding of aluminum. The EEPS operation principles are similar to these of the DMS used in this work.

Regarding the following 5 hour period, the total PNCs were shown to gradually decrease over the total size spectrum covered by the APS. In parallel, the main peak slightly shifted toward smaller sizes throughout the study period, from 640 nm to 610 nm and 700 nm to 660 nm, for TiO_2 and SiO_2 respectively. This observed particle size reduction is possibly related to a drying process which the suspended particles undergo during the 5 hour period following the end of injection. These slight indications of condensation-evaporation observed in the APS

measurements could also be considered in the DMS measurements regarding the larger size channels of the instrument. However, as the DMS sampled the aerosols through its heated line at a constant high temperature 120 ºC, removal of any potential moisture from the particles' surface can be assumed.

5.4.4 Results of Modal Parameter Fitting

As with previous results presented in Chapter 4, the modal fitting program Rmixdist was used within this study to estimate the mPNCs, *CMD*s and σ_g of the modes within the measured PSD by the DMS. The fundamentals of the particular R-package were described extensively in Chapter 3. Among the two different dispersed materials, the number of fitted modes required to accurately model the measured size distributions varied due to changes in emission profiles and subsequent aerosol transport processes acting over the dispersed ENPs from the source to the sampling point.

5.4.4.1 Variation in Fitted Modal Count Median Diameter (*CMD*)

The averaged PSDs, measured by the DMS, over the same time intervals applied in the previous sections, were analysed through the Rmixdist package and for all replicate tests conducted for each tested material. The average results obtained from the above process are presented in the following two sections, corresponding to each tested material. Full details on the fitted modal parameters can be found in Appendix B.

Variation in CMD for TiO_2 Aerosol

The average *CMD*s resulting from Rmixdist fitting of the size distributions measured by the DMS are shown in Figure 5.7, for TiO_2. The injection stage of TiO_2, shown in Figure 5.7a, indicates a continued presence of what would usually be classified as Aitken (25 – 100 nm) and accumulation (> 100 nm) mode particles. At the end of the second 10 min interval of injection a rapid shift of all the modes was observed. This shift was stronger for particles in the upper region of the nanoscale. Indicative of this, is the 300 nm net increase of the diameter of Mode 4 during this time. The results support the theory that agglomeration was occurring after the chamber was filled and mixed with a sufficiently high PNC of large particles. The shifts of the modal diameters towards larger sizes continued until the 30th minute of injection while in the remaining time up to the end of the process, the majority of the modes maintained a constant *CMD* except for Modes 3 and 4. Mode 3, the main mode, increased its diameter during this period from 168 nm to 185 nm and the *CMD* of Mode 4 increased from 594 nm to 620 nm. However, the radical changes in the modal diameter shifts observed during the injection stage were not continued in the measurements in the following 5 h period (Figure

5.7b). *CMD*s remained relatively stable throughout this period, except for some temporal fluctuations. Agglomeration was revealed only for Mode 4, whose *CMD* increased by 20 nm by the end reaching a diameter of 640 nm.

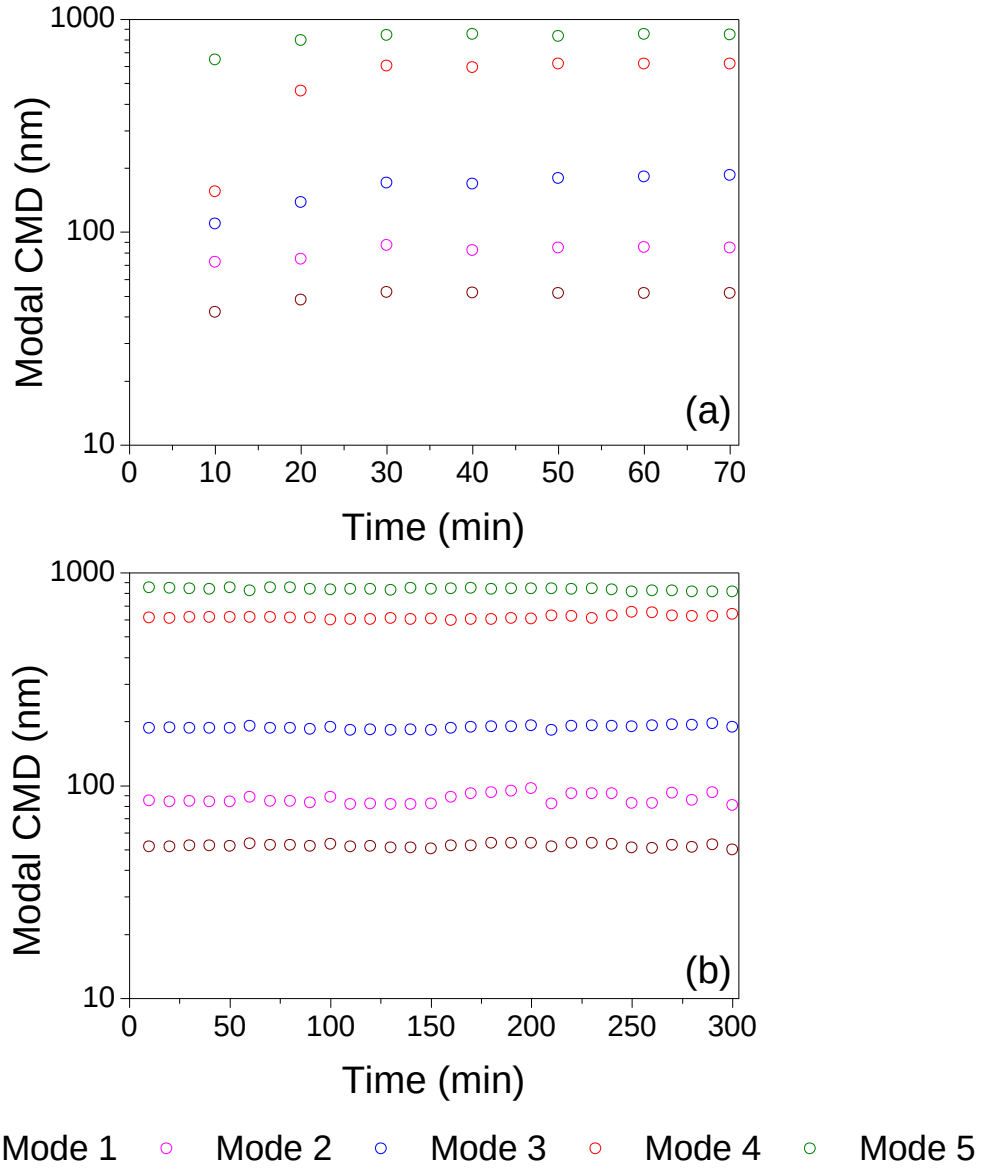

Figure 5.7: Variations in the average modal diameter for the TiO_2 test (a) during injection and (b) in the following 5 h period

Variation in CMD for SiO_2 Aerosol

Regarding the SiO_2 modal analysis (see Figure 5.8) the variations in the average *CMD*s showed a different development compared to TiO_2, for both experimental periods. The number of modes selected in the fitting procedure to adequately describe the averaged PSDs was seven as opposed to five used in the TiO_2 modal analysis. The injection stage (Figure 5.8a) indicates the presence of Modes 1 and 2 whose diameters lie within what is usually classified as

nucleation size range (0 – 25 nm). These modes represent relatively stable diameter characteristics with time for the entire duration of the injection. The medium diameter size modes (Mode 3 and 4) remained constant during the first 20 min of injection. Similar behaviour by the larger particles (Mode 5 and 6) was also seen during this period. The exception was Mode 7 which showed growth in diameters from 786 nm to 859 nm at the end of this period. For the following intervals up to the end of injection all the modal diameters lying in the Aitken and accumulation region, gradually increased. Significant increase in *CMD* was seen for the largest modes (Mode 6 and 7), while it can be noted that particles of Mode 4 due to their continuous growth after the 50th minute transferred into the accumulation region.

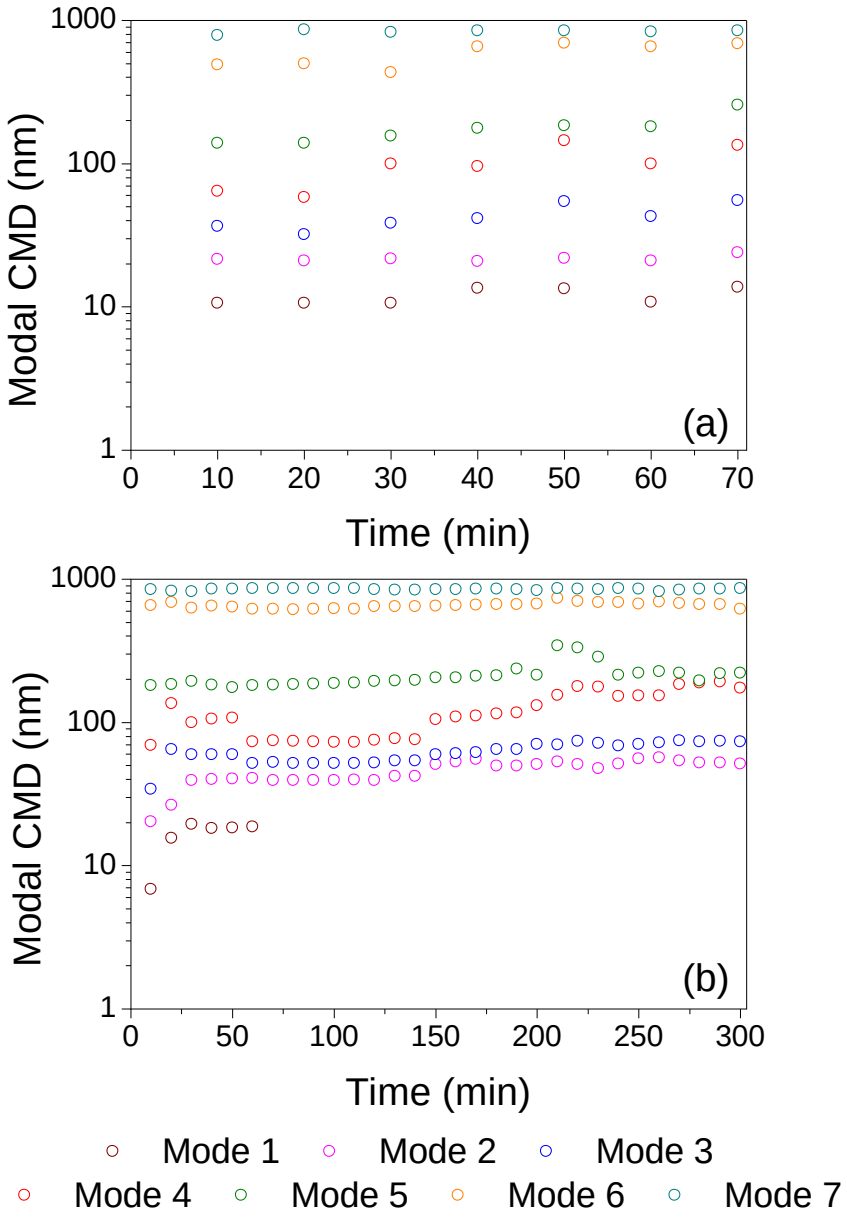

Figure 5.8: Variations in the average modal diameter for the SiO_2 test (a) during injection and (b) in the following 5 h period

In the 5 h period after the injection, as shown in Figure 5.8b, the growth process continued for the majority of the modes throughout the entire duration of the specific study period. This is contrary to the behaviour of TiO_2 nanoparticles. Mode 1 and 2 increased in diameter significantly during the first 30 min with Mode 2 stabilising within the Aitken region at the end of this period. Finally, the presence of modes in the nucleation region ended after the first hour and this is also be confirmed by the relevant measured PSD presented in Section 5.4.2.2. In the middle of the 5 hour period, due to continued growth processes, Mode 4 rose from the Aitken to the accumulation region. Mode 5, with the highest particle population, proceeded incrementally throughout the testing period starting from a *CMD* of 180 nm, and reaching 220 nm at the end of the study period. The largest diameter modes (Mode 6 and 7), at the largest size channels of DMS, showed a stable evolution without remarkable changes of their size, similar to the TiO_2 case.

5.4.4.2 Variation in Fitted Modal Fractions

By considering that agglomeration is a number-reducing (mass-conserving) process that shifts PSDs toward larger sizes, and grouping the Rmixdist fitted *CMD*s into nucleation (0-25 nm), Aitken (25-100 nm) and accumulation (>100 nm) modes, the influence of agglomeration can be seen on the particulate modal fractions over the two experimental periods, for the two tested materials. The total number of particles modelled was calculated per mode, and using appropriate size groups, was summed and then divided by the overall modelled number concentration. By applying this process for the determined time intervals and averaging the results obtained for all the replicate tests conducted for each tested material, the variation of the average modal fractions can be performed.

Variation in Modal Fractions for TiO_2 aerosol

During the injection period of TiO_2, as shown in Figure 5.9a, the dominance of the accumulation mode particle population against the Aitken population shows variations over time. As indicated in the measured PSDs presented in Section 5.4.2.1, the aerosolization of the TiO_2 nano-suspension did not generate airborne particles of sizes in the nucleation region. In the first 30 min, the two modes were observed to move away from each other. This could be an indication of agglomeration which potentially decreased the Aitken mode number concentration by collision and aggregation with larger particles of the accumulation region. In the following 10 min period, this effect was in some manner counterbalanced and resulted in a temporal convergence between the two modes. In the remaining time until the end of injection the two modes proceeded constantly with minor relative changes which could be attributed to a balance established in the system, possibly between agglomeration and

deposition, with the latter affecting mainly particles of the larger size region where the gravitational and diffusional particle motions are combined. The same balance is shown to be present throughout the 5 h period after injection. More specifically, from Figure 5.9b it can be seen that the two modes exhibited temporal fluctuations without any significant change in their modal fractions up to the end of the study period.

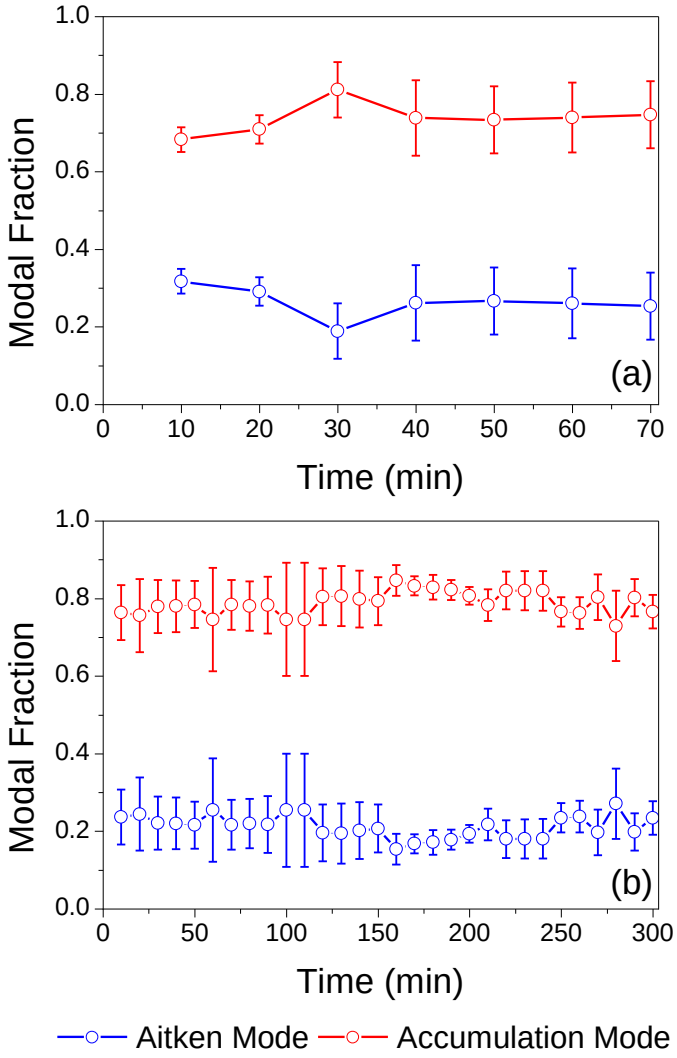

Figure 5.9: Variation in the average modal fractions during the (a) injection and (b) 5 h period after injection for TiO_2 dispersion tests respectively (open dots: data ± 2σ)

Variation in Modal Fractions for SiO_2 aerosol

Different evolution patterns of the modal fractions of SiO_2 nanoparticles can been seen in Figure 5.10 for the two experimental periods compared to the TiO_2 dispersion test. In the first 30 min of injection (Figure 5.10a), Aitken and accumulation modal fractions were constantly converging towards each other. At the same time, nucleation mode particles illustrated a stable presence over time. Contrary to the TiO_2 dispersion tests, agglomeration appeared to not affect

the particle concentrations in the nucleation and Aitken size regions. This could possibly indicate the presence of a second mechanism counterbalancing the agglomeration effect. For the period up to the end of injection, it can been seen that Aitken and accumulation modes were gradually moving away from each other, an indication of coagulation as observed also in the TiO_2 injection stage. However, during the last 10 min period of the injection, the two modes appear to converge for a second time in the study period. This trend could be attributed to high coagulation rates demonstrated this period between Aitken and nucleation mode particles. Through this process, it was possible the coagulation taking place simultaneously between accumulation and Aitken mode particles to be counterbalanced. As a result, the population of Aitken mode particles was temporally benefited by this process resulting in the observed convergence. In parallel, for the period following the 30th minute the fraction of nucleation mode particles constantly decreased up to the end of the study period. This is an indication of the strong coagulation exhibited by these particles with the larger particles from the Aitken and the accumulation region.

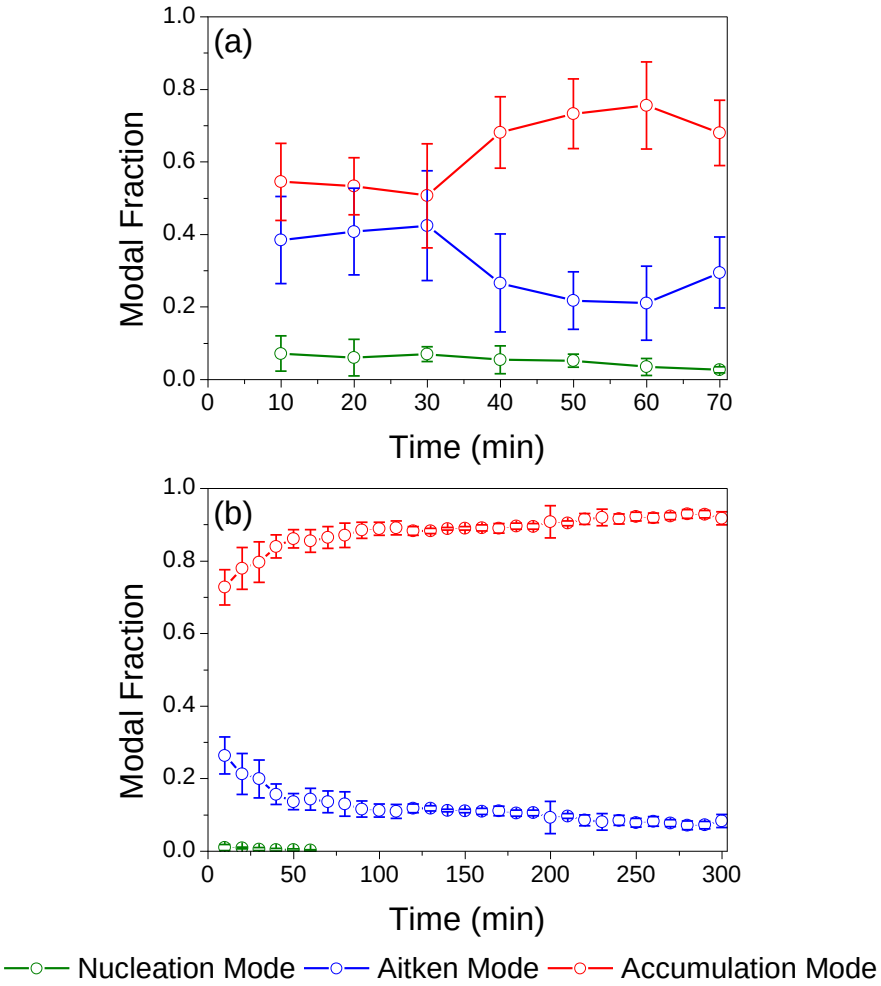

Figure 5.10: Variation in the average modal fractions during the (a) injection and (b) 5 h period after injection for SiO_2 dispersion tests respectively (open dots: data ± 2σ)

The observed differences between the variations in modal fractions during the first minutes of the injection stage of TiO_2 and SiO_2 aerosols, could be attributed to the different emission profiles presented in Sections 5.4.2.1 and 5.4.2.2 respectively. For TiO_2, in the first 30 minutes of injection, a single peak diameter with distinct characteristics, showed abrupt increases in concentration with time, with simultaneous shift in its size. On the other hand, during the same time, the SiO_2 aerosol size distribution presented a variety of peaks with concentrations almost equal. Therefore, for TiO_2 aerosols, the peak diameter had an apparent domination since the early stage of injection. Following Hinds (1982), agglomeration is benefited when the large absorbing surface of the bigger particles is combined with the rapid diffusion characteristics presented by smaller particles. It is then obvious that in the case of TiO_2 aerosol the high surface area and increased agglomeration subsequently led to the divergence between the modal fractions of Aitken and accumulation mode particles during the first minutes of injection.

Finally, in Figure 5.10b, the evolution of the average modal number fractions over the 5 h following the end of injection is demonstrated by the end of the presence of the nucleation mode particles at the end of the 1st hour, and simultaneously the gradual distancing between accumulation and Aitken mode particles. It is possible that after the elimination of the nucleation mode particles, agglomeration was induced mainly for the Aitken mode particles throughout this period, resulting in the decrease of their modal fraction with time in comparison to the accumulation mode ones. In parallel, this continuous agglomeration assumed as the cause of the divergence between the two different size groups, can explain the gradual shift of the main mode toward larger sizes observed in the measured PSDs in Section 5.4.2.2.

5.4.5 Modelling Coagulation/Deposition Sinks and Source Rates

It is clear from the discussion above that the action of various mechanisms during the two experimental stages (injection and the following decay period) substantially changed the PSDs of the measured dispersed aerosols. The results so far indicate that for the two tested materials, the influence of agglomeration over the evolution of their PSDs was described by different time scales. Furthermore, the decay profile of their PNC after the end of injection showed different characteristics, reflecting a change in the relative importance of these mechanisms between materials.

Two main processes are assumed in this work to contribute to these phenomena. Firstly the intensity of the agglomeration effect can be explained using the concept of a coagulation sink. Additionally, a coagulation sink can describe how rapidly nm-sized particles are removed

through coagulation, as indicated by an increase in the larger particle concentrations. Secondly, the deposition of the dispersed nanoparticles onto the surfaces of the test room provides a competitive process for the loss of airborne particles. The balance between these two competing processes will affect the resulting size distributions and consequently any toxicological impact related to the particle size characteristics.

5.4.5.1 Modelling theory

For a completely (and instantly) mixed room, the time dependent change of PNC with diameter d_i, $N(d_i,t)$, in the room can be described by (Schneider et al., 2011):

$$\frac{\Delta N(d_i,t)}{\Delta t} = \frac{S(d_i,t)}{V} + \left(\frac{\Delta N(d_i,t)}{\Delta t}\right)_{coag} + \left(\frac{\Delta N(d_i,t)}{\Delta t}\right)_{loss} \qquad \text{Eq. 5. 1}$$

where $S(d_i,t)$ is the source rate (particles/s) of the dispersed nanoparticles with diameter d_i in the room and V is the volume of the room. The subscripts "*coag*" and "*loss*" refer to changes due to coagulation and surface deposition-ventilation respectively. Since the experiments were conducted under sealed conditions then the last term of the right hand part of the above equation refers exclusively to deposition.

Eq. 5.1 was applied in this work in order to estimate the changes in PNC during the determined time interval Δt which were then compared with the relevant experimental measurement. The injection stage was divided into 14 time intervals (5 min each) while the 5 h period after injection into 30 (10 min each). Since the DMS measurements are based on discrete particle size bins, the equation can be applied separately for each bin with the same specific sequence of calculations followed in order to enable comparison between the modelled and experimental data.

Total Particle Loss Sink for the Calculation of Deposition Sink

As indicated in Chapter 4, the size dependent particle decay rate (β_{d_i}) integrates all the particle loss (coagulation, deposition, ventilation etc.) and formation (coagulation, condensation, resuspension etc.) mechanisms. The equation describing the particular factors has already been introduced in Chapter 4. Considering that in the present work, these factors represent coagulation and deposition, the plots of the size resolved logarithmic values of $N(d_i,t)$ versus time obtained by the DMS during the decay period, enables the calculation of the total particle losses through the gradient of the best fitted line. In Eq. 5.1, the total particle losses are represented by the sum of the two terms on the right hand side. As a consequence, given the

values of the total particle losses, and subtracting the losses corresponding to coagulation, then an estimation of the losses due to deposition can be obtained. The calculation method followed for the coagulation losses is presented in the following section.

Coagulation Sink

Since the DMS measurements are based on discrete particle size bins a discrete equation modelling coagulation losses is used (Kulmala et al., 2001; Mönkkönen et al., 2004) for the calculation of the change in PNC of diameter d_i, with time due to coagulation:

$$\frac{\partial N_{d_i}}{\partial t} = J_{d_i} - CoagS \cdot N_{d_i} \qquad \text{Eq. 5. 2}$$

where - N_{d_i} - number concentration particles of size d_i (cm^{-3})

J_{d_i} - formation rate of size d_i particles based on coagulation losses ($cm^{-3}s^{-1}$), and

$CoagS$ - coagulation sink (s^{-1})

In order to calculate the coagulation losses the coagulation sinks have been modelled. In this work coagulation was determined by both self-coagulation and coagulation scavenging. The coagulation sink in a discrete form is expressed as (Kulmala et al., 2001):

$$CoagS = \sum_j K_{i,j} N_{d_j} \qquad \text{Eq. 5. 3}$$

where - $K_{i,j}$ - coagulation coefficient between particles d_i and d_j, $j \geq i$, ($cm^{-3}\ s^{-1}$), and

N_{d_j} - number concentration particles of size d_j (cm^{-3}).

Since the coagulation losses in the present work are based on self-coagulation and coagulation scavenging, $j \geq i$. The formation rate of particles d_i based on the coagulation losses (J_{d_i}), on the right hand side of Eq. 5.2, in a discrete form is given by the equation (Schneider, 2011):

$$J_{d_i} = \frac{1}{2} \sum_j^{i-j} K_{i-j,j} N_{d_{i-j}} N_{d_j} \qquad \text{Eq. 5. 4}$$

where $K_{i-j,j}$ - coagulation coefficient between particles d_{i-j} and d_j, $j < i$, ($cm^{-3}\ s^{-1}$), and

$N_{d_{i-j}}$ - number concentration particles of size d_{i-j} (cm^{-3}).

The coagulation coefficient is found using the following equations (Kulmala et al., 2001):

$$K_{i,j} = \pi(D_i + D_j)(d_i + d_j)\cdot \left(\frac{d_i + d_j}{d_i + d_j + 2(g_i^2 + g_j^2)^{1/2}} + \frac{8(D_i + D_j)}{(c_i^2 + c_j^2)^{1/2}(d_i + d_j)} \right)^{-1} \quad \text{Eq. 5. 5}$$

Where D_i and D_j are the particle diffusion coefficients ($cm^2\ s^{-1}$) for particles d_i and d_j respectively, given by the equation:

$$D_i = \frac{kT}{3\pi\mu d_i}\left(\frac{5 + 4Kn_i + 6Kn_i^2 + 18Kn_i^3}{5 - Kn_i + (8+\pi)Kn_i^2} \right) \quad \text{Eq. 5. 6}$$

$$g_i = \frac{1}{3d_i\ell_i}\left[(d_i + \ell_i)^3 - (d_i^2 + \ell_i^2)^{3/2} \right] - d_i \quad \text{Eq. 5. 7}$$

$$Kn_i = \frac{2\lambda_{air}}{d_i} \quad \text{Eq. 5. 8}$$

$$\ell_i = \frac{8D_i}{\pi \bar{c}_i} \quad \text{Eq. 5. 9}$$

$$\bar{c}_i = \left(\frac{8kT}{\pi m_i} \right)^{1/2} \quad \text{Eq. 5. 10}$$

where: m_i = mass of particle d_i (kg)

The constants assumed in Eq. 5.5 to 5.10 are:

T = 25 °C or 298 K

ρ = 1,0 g cm^{-3}

λ_{air} = 0.0686 μm (mean free path of the air molecules at 25 °C)

μ = 1.83 x 10^4 g $cm^{-1}\ s^{-1}$ (the viscosity of the air at 25 °C)

k=1.38 × 10^{-23} J/K (Boltzmann's constant)

K_n= Knudsen number

Using Eq. 5.3 to 5.10, the coagulation sinks and formation rates based on the coagulation losses, for individual particles of a given size during the two experimental stages, have been calculated based on the time intervals Δt determined for the application of Eq. 5.1. It has to be noted that the coagulation coefficient $K_{i\text{-}j,j}$, as well as, D_j and $D_{i\text{-}j}$ were found in a similar way. Once the size resolved coagulation sinks and formation rates based on coagulation losses were obtained, then through the Eq. 5.2, the estimation of the particle losses due to coagulation over the specified time intervals was conducted.

The sinks were based on coagulation to particles ≤ 2.5 μm, including the overall nanoscale according to the detection size range of the DMS and the upper limit of APS where micron-particles were able to be detected. It should be noted that the particles in the micron-scale were considered to contribute to coagulation as scavengers over the particles of the nanoscale excluding self-coagulation (homogeneous coagulation). Additionally, for both experimental periods, due to the lower limit on the DMS (4.87 nm), stable clusters smaller than 4.87 nm are too small to be measured.

Source Rate

Regarding the first term of the right hand side of Eq. 5.1, source rates $S(d_i,t)$ were calculated from the formula by Wallace et al. (2004):

$$S(d_i,t) = \frac{V\beta_{d_i}(N(d_i,t) - N_{d_i(0)})}{1-\exp(-\beta_{d_i}t)} \qquad \text{Eq. 5. 11}$$

where $N_{d_i(0)}$ is the initial PNC of particles d_i in the testing room of volume V before the start of injection process and t is the elapsed time (s). Considering that the quantities $S(d_i,t)$ and β_{d_i} are functions of particle size then the above equation refers to a particular aerosol size. By extension this implies that any mechanism which resulted in changes of the particle size (e.g. coagulation) taking place between the source point and the instrument's sampling point, was ignored. Source rates of particles of a given size have been calculated based on the 1 second DMS scans and values averaged over the Δt time intervals determined from Eq. 5.1. For the decay period the source rate term in Eq. 5.1 was set to zero.

5.4.5.2 Modelling Results

By grouping and summing the modelled and experimental measurements of the changes in PNC over nucleation (0 – 25 nm), Aitken (25 – 100 nm) and accumulation (> 100 nm) size regions, comparisons of their evolution during each experimental period were obtained. As indicated above, the model was applied to the averaged PSDs over the determined time intervals and for all the replicate runs conducted for each tested material.

TiO_2 – Injection Stage

As observed in the measured PSDs presented in Section 5.4.2.1, in the case of TiO_2 dispersion tests, airborne particles in the nucleation mode region were not detected. Therefore, the model herein was applied over Aitken and accumulation mode particles. Figures 5.11a and b, for time steps of 300 sec (5 min), show the average modelled changes in PNC and are compared to the measurements obtained during the experimental process corresponding to the injection part, for Aitken and accumulation size groups, respectively. The differential effects of coagulation and deposition enable the identification of the importance of each mechanism on the PNC modification from the dispersion point to the sampling point (1 m distance).

For Aitken mode particles during the first 15 min of injection, coagulation and deposition co-existed at very low levels (Figure 5.11a). After this period, when the chamber was filled with more particles, then substantial coagulation resulted in the domination by this mechanism until the end of the process. Therefore, the abrupt shifts of the *CMD*s in the accumulation size region at the 20th minute of injection (Section 5.4.4.1) are attributed to this domination. On the other hand, accumulation mode particles were characterised by higher deposition rates, and as particle concentrations increased with time, both mechanisms increased their contribution to the particle loss rate with deposition dominating over coagulation (Figure 5.11b). However, at the end of the study period both mechanisms became equal.

Since the model results have been summed over the specified size regions, the heterogeneous coagulation attributed to μm particles over accumulation mode and Aitken mode particles, was estimated to be very low for both experimental periods. Furthermore, similar observations were noted for the SiO_2 counterpart in the model results which are presented in the following sections.

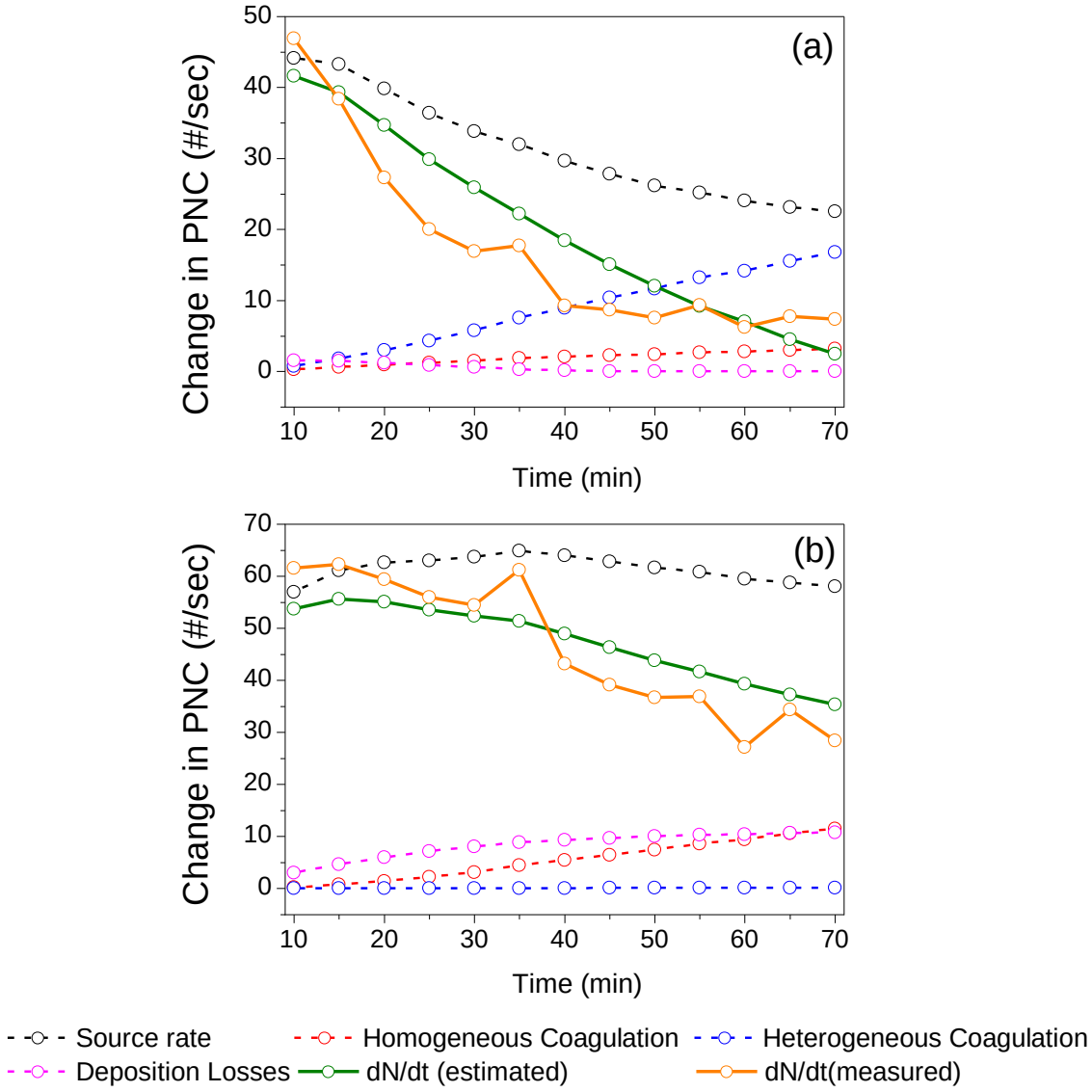

Figure 5.11: Evolution over time of the average change in PNC (estimated and measured) of TiO_2 aerosol due to coagulation and deposition for (a) Aitken and (b) accumulation mode particles during the injection stage

TiO_2 – 5 hours following the end of injection

Figures 5.12a and b present the average evolution of the modelled and measured change in PNC demonstrated by the determined size groups during the 5 hour period following the end of injection in the sealed well mixed and unventilated chamber. Results for Aitken mode particles indicate the importance of coagulation during the first 150 min and the increase in deposition as particle concentrations decreased with time (Figure 5.12a). Following this, coagulation was counterbalanced by deposition, with deposition presenting a slight domination against coagulation during the last minutes of the process when the particle concentrations have fallen to low levels. Considering the accumulation mode particles, deposition continues to dominate the particle removal process and linearly decreased with

time as the particle concentrations decrease (Figure 5.12b). Coagulation, despite its initial significant contribution at the beginning of the process, exponentially decreased to the point where concentrations were so low that no substantial coagulation could occur.

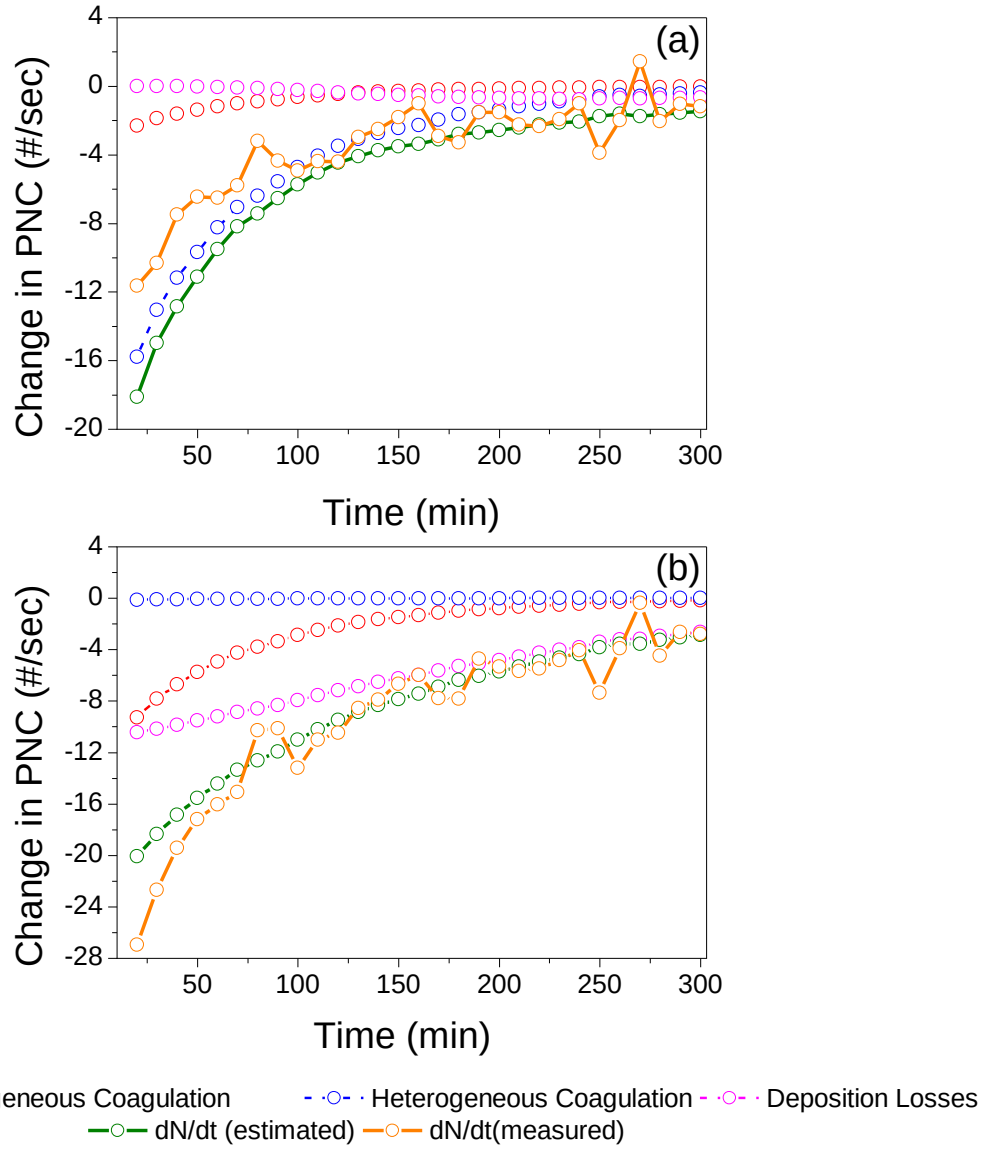

Figure 5.12: Evolution over time of the average change in PNC (estimated and measured) of TiO_2 aerosol due to coagulation and deposition for (a) Aitken and (b) accumulation mode particles during the 5 hours following the end of injection

Comparisons of the findings of Rim et al. (2012) with the resulting from the present study suggest a good agreement on the relative intensity between coagulation and deposition, however limited only for ultrafine particles (<100 nm). The particular work studied the temporal changes in the actual size distributions following an episodic release resulted in high ultrafine PNC in a ventilated 140 m^2 test house. Particles were generated indoors by various sources related to household activities (combustion due to cooking and use of consumer products that release ultrafine particles). They modelled the source rates and the coagulation

sinks through the same equations used in the present work. Furthermore, they modelled deposition through the use of an equation proposed by Lai (2000). They found that at high PNC the temporal changes in number concentrations were due to coagulation effects. As PNC decayed the effect of deposition gradually increased in its relative importance compared to coagulation.

SiO_2 – Injection Stage

For the SiO_2 dispersion experiments, the relative importance between coagulation and deposition for the smaller particles, showed differences compared to TiO_2 during the injection stage. In the first minutes of injection both nucleation and Aitken mode particle losses were dominated by deposition (see Figures 5.13a and b, respectively). Contrary to TiO_2, deposition losses demonstrated an increasing trend reaching a maximum at the 20^{th} minute, while coagulation was almost linearly increasing. Following this period, as PNC in the chamber reached higher levels, coagulation became dominant and determined the losses up to the end of injection.

This difference between the model estimation on the deposition of smaller particles of the two tested materials during the early stage of injection can explain the evolution of the relevant modal fractions presented in Sections 5.4.4.2, for TiO_2 and SiO_2. As was shown, the modal fractions corresponding to the two tested materials during the first minutes of injection demonstrated opposite evolutions. Specifically, opposed to the convergence presented by the modal fractions between the Aitken and accumulation TiO_2 particles, the SiO_2 relevant modes showed a divergence during the same period. The explanation given for this difference was based on the higher surface area provided by the TiO_2 accumulation mode particles than this of the SiO_2 counterparts, during the specified period. This difference was considered to benefit higher agglomeration in the TiO_2 dispersed aerosol than in SiO_2 one, as the rapidly diffused TiO_2 smaller particles had higher possibilities than the SiO_2 ones to be absorbed due to the provided surface area. The weak agglomeration effects over the small SiO_2 particles (Aitken and nucleation), seem to have allowed the development of deposition over these. Therefore, it could be concluded that the model correctly predicted the domination of deposition against coagulation over the SiO_2 smaller particles during the specified period of injection.

On the other hand, as shown Figure 5.13c, accumulation mode particles were increasingly removed by deposition throughout the injection process. In parallel, homogeneous coagulation was also increasing, although in contrast to the TiO_2 case, at the end of the process an equivalence between the two removal mechanisms was not seen. This difference between the model estimations on the two tested materials can be explained through the theory developed

by Hinds (1982) for the coagulation taking place in polydisperse aerosols. Specifically, when a polydisperse PSD is characterised by a sufficient width then it tends to become narrower

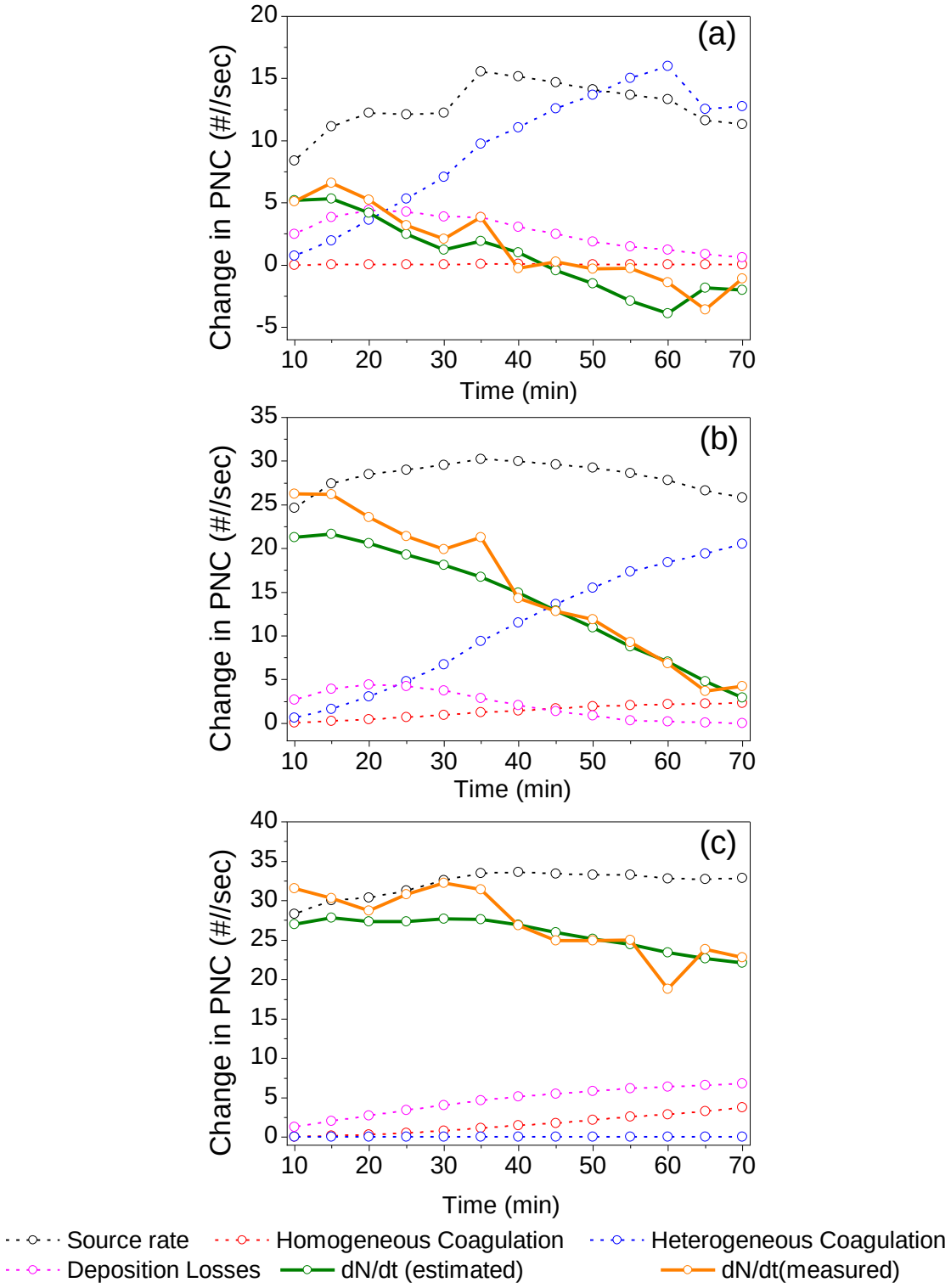

Figure 5.13: Evolution over time of the average change in PNC (estimated and measured) of SiO_2 aerosol due to coagulation and deposition for (a) nucleation, (b) Aitken and (c) accumulation mode particles during the injection stage

with time due to the strong coagulation of the smallest particles with the largest ones. The apparent result of the particular process, is the reduction of the PNC of small particles, and at the same time, the slight increase in the number of the larger particles.

Considering the above, the measured PSDs of SiO_2 (Sections 5.4.2.2) during the injection stage demonstrated significantly wider size distribution characteristics than these of the TiO_2 aerosol (Section 5.4.2.1). Therefore, in the case of SiO_2, it can be concluded that the losses due to homogeneous coagulation in the accumulation region were counterbalanced by the formation process of particles based on the process described in the previous paragraph. Therefore, the model prediction on the different intensity of the particular mechanism over the large particles of the two tested materials, seems to be quite reasonable.

SiO_2 – 5 hours following the end of injection

For the 5 h period after injection the model tracked the fast decay of the nucleation mode particles measured by the DMS in the first 20 minutes (Figure 5.14a). This rapid decay according to the model was attributed mainly to heterogeneous coagulation. However, for the remaining period, the model indicated the presence of nucleation mode particles of very low concentrations, while the measurement device had stopped detecting particle airborne concentrations in this size range. Aitken mode particles, similar to TiO_2 counterparts, showed changes in PNC due to heterogeneous coagulation (Figure 5.14b). For both nucleation and Aitken mode particles, deposition losses during this period were low, except for minor contributions estimated at the very low PNC, when the relative importance of both coagulation and deposition became almost equal. Accumulation mode particles, as in the case of TiO_2, reduced mainly by deposition which linearly decreased over time with the decrease of the PNC (Figure 5.13c). However, it can be seen that the measured changes in PNC attributed to homogeneous coagulation are weaker for SiO_2 accumulation mode particles compared to the TiO_2 counterparts, as shown in Figure 5.12b. The reasons for this different intensity of the particular mechanism over the large particles of the two tested materials, have been described in the previous section.

The weaker homogeneous coagulation losses of SiO_2 accumulation mode particles compared to the TiO_2 counterparts, can describe the reasons of the lower decrease in the total PNC of SiO_2 aerosol than this of TiO_2 one observed during the first hour followed the end of injection (Sections 5.4.2.1 and 5.4.2.2). Homogeneous coagulation in the accumulation size range could be considered as a mechanism that results in the decrease of PNC without shifting the modes toward larger diameter sizes. This can be attributed to the fact that large particles have a higher mass and, therefore, are subjected to relatively larger gravitational forces than smaller

particles, resulting in settling and finally their disappearance from the air. For these large particles, during their settling process to the floor of the testing room, it is possible that the

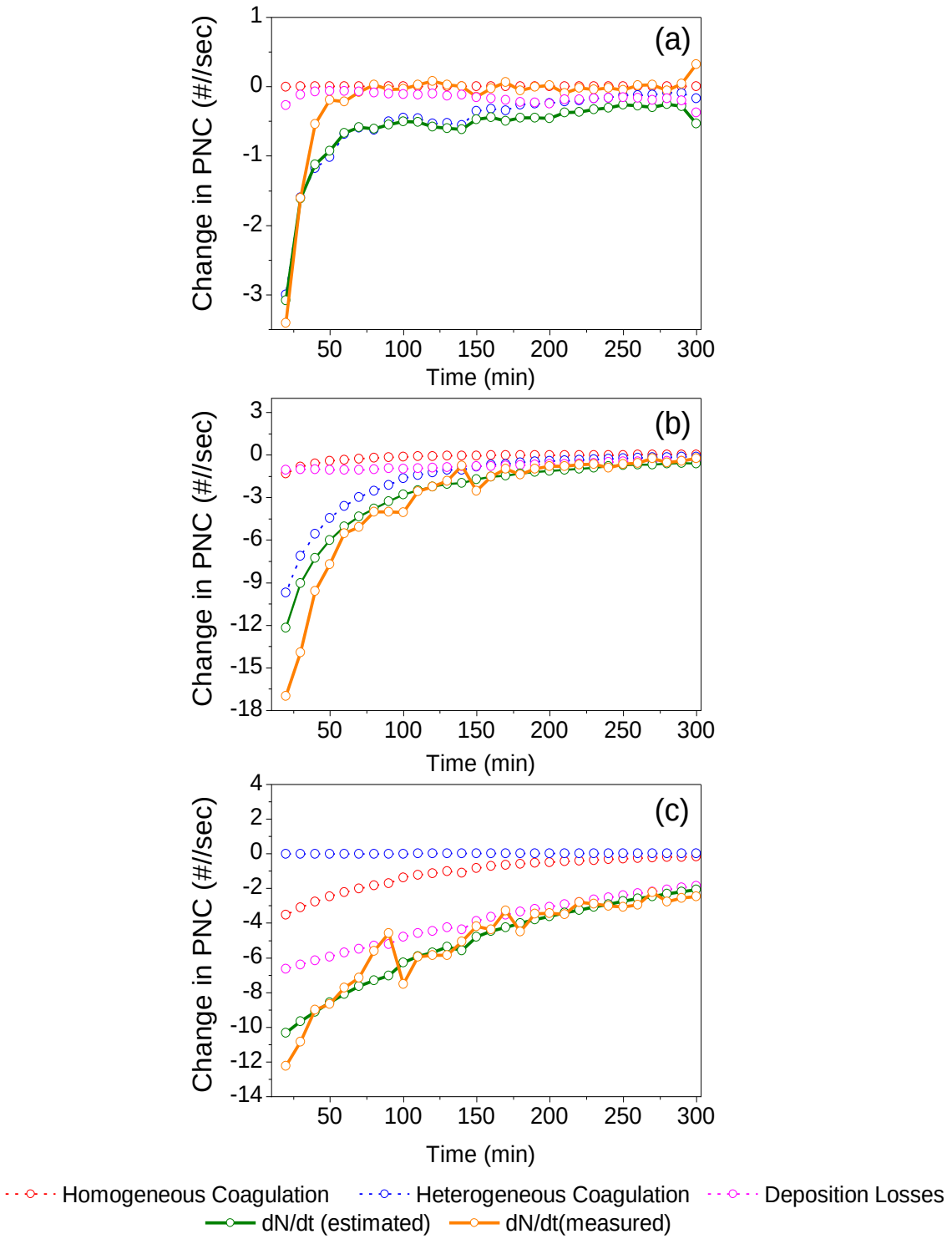

Figure 5.14: Evolution over time of the average change in PNC (estimated and measured) of SiO_2 aerosol, due to coagulation and deposition for (a) nucleation and (b) Aitken and (c) accumulation mode particles during the 5 hours following the end of injection

smaller particles became attached to them, and finally were removed through this process. Therefore, the scavenging process can be considered as a mechanism which indirectly contributes to the decrease of the aerosol PNC. It is reasonable then to consider that the model correctly predicted this different intensity of the particular mechanism between the two materials. As shown in the measured PSDs, SiO_2 aerosol demonstrated a more moderate decay of the PNC compared to TiO_2, during the first hour following the end of injection. Thus, all the above suggests that so far, the predictions of the model are consistent with the experimental observations.

Cumulative results in the nanoscale

In Figure 5.15, by summing the average results presented in the previous sections over the specified size groups, then the comparison between the total PNC changes, measured and estimated by the equations, for both materials, for the whole size spectrum of DMS, can been seen. The analytical model is not capable of capturing the fluctuations of PNC that may result for example from localized turbulent flows, although the temporal changes of mean PNC are captured well, indicating that an acceptable explanation of the particle mechanisms has been found.

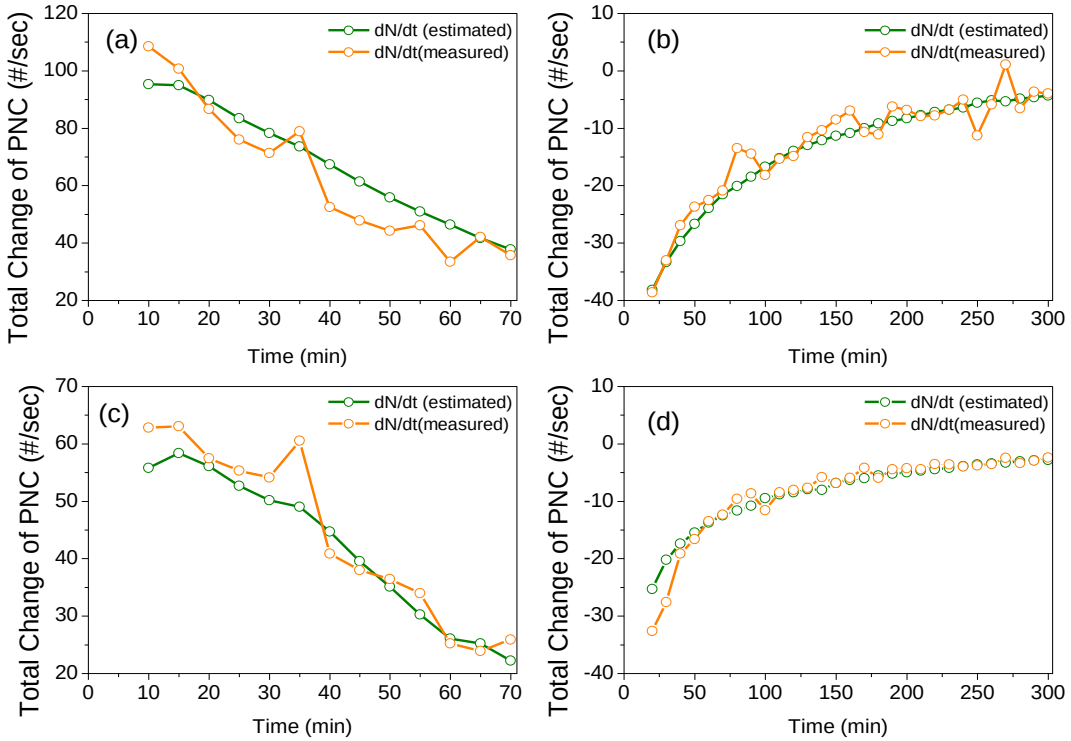

Figure 5.15: Aggregate model and experimental results of (a and c) the injection stage and (b and d) the 5 hours following the end of injection for (a and b) TiO_2 and (c and d) SiO_2 respectively. Results refer to the whole size spectrum of the DMS (4.87-1000 nm)

5.4.6 TEM images of the deposited matter

As indicated in Section 5.2, metallic stubs were placed at various locations on the floor and the walls of the chamber in order to collect deposited matter for subsequent TEM analysis. Therefore, complementary information related to the formation characteristics of the deposited particles could be obtained by the TEM images in Figure 5.16. More TEM images describing the deposited matter of both materials are contained in Appendix C.

As can been seen in Figure 5.16, primary particles were not detected on the metal stubs for both materials. TiO_2 samples revealed the presence of large spherical shaped formations composed by multiple primary NP and the majority of sizes within the micro-scale (Figure 5.16a). Additionally, in some cases these large spherical particles were observed to be attached to smaller particles forming chainlike agglomerates (Figure 5.16a). All the above suggests that significant agglomeration was taking place in the sealed chamber, which along with deposition of the larger particles resulted in the reductions in PNC over time. Additionally, images confirm the scavenging process induced by the larger particles over the smaller ones, validating the strong hetererogeneous coagulation indicated by the aerosol dynamic model.

On the other hand, as shown in Figure 5.16b, the average size range of the deposited matter collected during the SiO_2 dispersion experiments was lower compared to the TiO_2 samples whereas the morphology of the deposited agglomerates presented a more rod-shaped structure. Aggregates of small sizes were observed which in many cases reached 50 nm. This could be aligned with the deposition losses of Aitken and nucleation mode particles estimated by the model for the early stage of injection.

A more analytical observation on the TEM images reveals that TiO_2 agglomerates presented a compact structure characterized by a spherical shape within which the primary particles appear to be held together by strong bonds. On the other hand, the SiO_2 agglomerates are shown to consist of primary particles which coalesced to each other with loose bonds. When particles are in close proximity, surface forces come to play an important role in particle interactions. According to Bergström (1997), among the various interactions between the surfaces of particles, Van der Waal's force is a determinant factor in the promotion of particle coalescence. The magnitude of the particular factor is represented by the Hamaker constant. A high value of the Hamaker constant illustrates a Van der Waal force of high strength (Bergström, 1997). Since the specified constant is different from material to material, it is anticipated that different coalescence rates are developed between the primary particles of the same material. According to Bergström (1997), for TiO_2 and SiO_2 particles, their Hamaker constants in air medium have been estimated to be $15.3*10^{-20}$ J and $6.5*10^{-20}$ J, respectively.

Therefore, the more strongly bonded structure presented by the TiO_2 deposited agglomerates compared to the SiO_2 ones, seems to be reasonable.

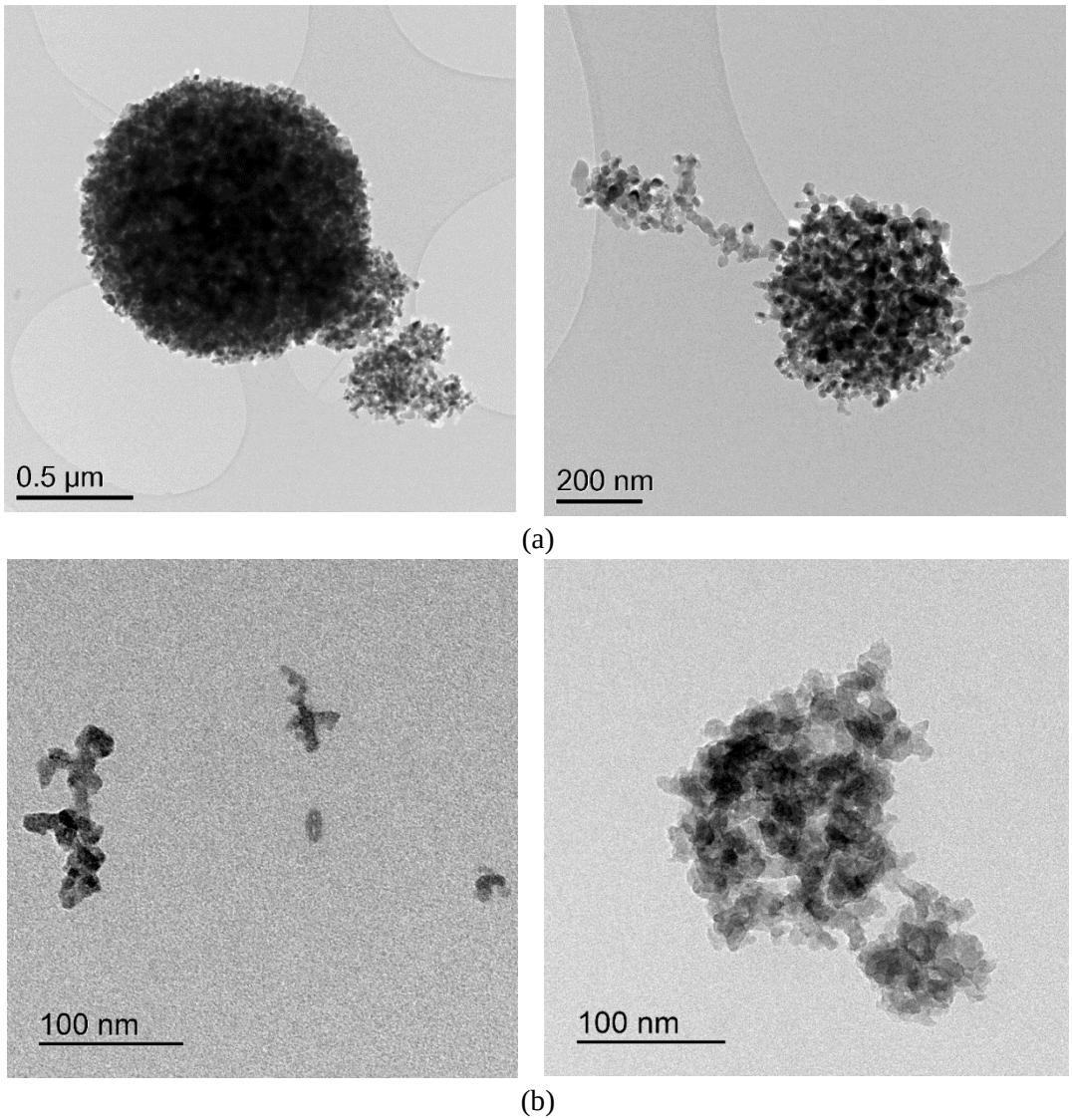

Figure 5.16: (a) TiO_2 and (b) SiO_2 agglomerates deposited on the floor and the walls of the exposure chamber as captured by TEM

In terms of risk assessment, regarding the airborne state of the illustrated in the TEM images deposited matter, the potential inhalation of an SiO_2 nano-agglomerate may present higher impacts on human health than a TiO_2 particle. In the case of inhalation, there are higher possibilities for a SiO_2 particle to de-agglomerate than a TiO_2, due to, the indicated by the images, weak bonds between the SiO_2 coalesced primary particles. Following Maynard and Kuempel (2005), the formation of smaller particles through de-agglomeration when an inhaled particle has reached the lungs can catalyze inflammatory responses.

The weak bond impacts could be also considered even when an SiO_2 agglomerate is deposited on a surface. In the case of the action of a turbulent air stream, it is possible for the agglomerate

to break into smaller clusters. These smaller clusters, by extension, have high potential for re-entrainment into the air with their consequent transition into the airborne state resulting in the increase of exposure of humans in indoor environments. This process is the so called ‘resuspension’ and has been described by Hinds (1982). Indications of resuspension of ENP were given the experimental work presented in Chapter 4. Therefore, a post-accidental scenario described by the resuspension of deposited ENP can be applicable and strongly dependent to the type of particle.

5.5 Summary

This chapter investigated dynamic aerosol processes describing the evolution of specific ENP size distributions during and a following prolonged period of a massive release of ENP in a sealed indoor environment and under unventilated conditions.

- The optimized sonication process in TiO_2 nano-suspensions, described in Chapter 4, was also applied herein for the preparation of SiO_2 nano-suspensions of the same powder concentration. Results, similar to the TiO_2 (Chapter 4), indicated sufficient de-agglomeration of μm-particles and simultaneously an increase of the volume fractions of particles in the nanoscale.
- Aerosol size distributions were measured over the entire nanoscale and the first channels of micron-scale by the DMS and APS respectively. The DMS results indicated shifts toward larger sizes of the geometric mean diameter for both materials during the injection stage. In the 5 hours period following the end of injection, the monitored PSDs showed stable geometric characteristics with fast decreasing PNCs with time for TiO_2 ENPs. In contrast, the PSDs of SiO_2 were decreasing moderately with the main peak shifting gradually toward larger sizes up to the end of the study period. In contrast to the fact that the two different aerosols were originated from liquids of the same powder concentration, the TiO_2 aerosol showed significantly higher PNC than the SiO_2. This difference was attributed to the loss of powder mass through sedimentation, as observed in the SiO_2 nano-suspensions at the bottom of the nebulizer’s reservoir after the end of experiments. The measurements over the micron-scale indicated the presence of small fractions of suspended large particles in the testing room. Similar to the trends observed in the measurements of DMS, the relative concentrations of TiO_2 μm-particles were almost three time higher than those measured for SiO_2.
- The modal fitting results indicated the shift of the modal diameters towards larger sizes. Based on the concept of agglomeration, the intensity and time length of agglomeration was noticed to be different between the two tested materials. In the TiO_2 tests, agglomeration

was shown to have a temporal but strong influence in the PSDs during the first minutes of the release. In contrast, in the SiO_2 tests, agglomeration acted constantly throughout both experimental periods gradually changing the PSDs characteristics over time. Additionally, different size grouped modal fraction evolution was noticed for the two tested materials during the early stage of their injection. This difference was attributed to the different emission profiles of the two tested materials which was considered to determine the agglomeration level during the specified period. In more detail, the apparent domination of the TiO_2 peak diameter, in contrast to the multiple SiO_2 peaks, resulted in the increase of the large absorbing surface of the bigger particles. As a result, this increase led to the increase of the agglomeration over the smaller TiO_2 particles.

- A simple aerosol processing model was used to demonstrate the dynamic aerosol processes for evolution of the PNC changes during and following the accidental release. The advantage of this model lies in the fact that the estimation of loss rates due to coagulation and deposition with a single particle spectrometer sampling at a distance from the source point could be achieved. We managed to determine with good accuracy the processes resulting in the changes of the PNC from the source to the receptor point. In general the modelling results suggest that for ultrafine particles (<100 nm) heterogeneous coagulation was the main particle loss mechanism which was increasing as the PNC increased in the chamber. On the other hand, larger particles (≥ 100 nm) were predicted to be mainly dominated by deposition losses. The above observations were common for both tested materials.
- The SiO_2 ultrafine particles during the early stage of release, according to the model, presented significant deposition losses which were not observed in the case of TiO_2. As indicated in previous paragraph, the evolution of the size grouped modal fraction showed that the agglomeration induced over the small SiO_2 particles during the early stage of injection, was weaker than that over the TiO_2 one. As a result, this weakness benefited the diffusional deposition, which according to Hinds (1982) is a process which is enhanced by the decrease of the particle size. Therefore, the model correctly perceived this difference on the intensity of the particular mechanisms over the small particles of the two tested materials. Additionally, the model at high PNC estimated a higher homogeneous coagulation intensity over the TiO_2 accumulation mode particles than this over the SiO_2 counterparts. This particular estimation led to the conclusion that the large particles generated through homogeneous coagulation operated as scavengers of smaller particles. These particle-scavengers due to their large size were subjected in considerable gravitational forces leading to their settling. In turn the small, suspended in air, nano-agglomerates were considered to reach the surfaces of the room attached to these particle-scavengers. To this end, since the TiO_2 aerosol was estimated by the model to have a

stronger presence of scavenger particles compared to the SiO_2, it was expected to present a strong decrease of PNC once the injection stopped. Indeed, the evolution of the measured PSDs of TiO_2 indicated a significantly higher drop of PNC within the first hour following the end of injection than that of SiO_2 at the same time.

- The TEM images obtained on the samples from the walls and the floor of the dispersion chamber demonstrated large TiO_2 agglomerates with average sizes ranging between the nano and micron scale and in some cases smaller particles being attached on them. Additionally, the TEM images illustrated very small deposited SiO_2 particles (< 100 nm) which were not be seen in the TiO_2 samples. All the above was consistent with the intensity of the loss mechanisms estimated by the model. Finally, according to the images, the coalescence of the primary TiO_2 particles within the agglomerated formations of each material, were shown to be described by stronger bonds than the SiO_2 ones. The particular structural difference was attributed to the higher van der Waal forces between TiO_2 particles in proximity than those of the SiO_2 ones. Due to the above, it was concluded that since the weak bonds increase the de-agglomeration potential, then it is expected for SiO_2 agglomerates to present higher exposure risks than the TiO_2 ones, either in accidental or post-accidental scenarios.

Within this chapter, the rapid coagulation at sufficient levels of PNC of continuously released ENP in a well-mixed confined environment has been inferred. In particular, different coagulation rates were estimated for the two tested materials. Considering that coagulation increases the particle diameter and subsequently decreases the specific surface area, according to Chapter 2, the explosion reactivity of a dust cloud consisting of ENP is expected to be reduced. Therefore, considering all the above, different explosion characteristics are expected to be demonstrated by dust clouds generated by different materials. The explosion characteristics of a dust cloud generated by the massive and instantaneous dispersion of specific carbon black nanopowders in a cylindrical explosion vessel filled with low amounts of a flammable gas (methane) and under mechanical turbulence is to be investigated in the following chapter and linked to the average particle size in the cloud immediately before the start of ignition.

Chapter 6

6. Influence of ENP on the explosion characteristics of lean methane-air mixtures

6.1 Introduction

Incidents which combine confined, suspended, dust particles in the air with an ignition source may result in explosions of similar severity to those of gas explosions. Experiments concerning μm primary sized dusts with flammable gas have been experimentally proven to cause explosions of greater severity in combination than separately. According to recent reports (Chapter 2), the explosion severity in dust clouds of ENP increases sharply with decreasing average airborne particle size. Furthermore, turbulence has been recognised to have a primary role in the explosion behaviour of fuel-air mixtures as well as in dust-fuel-air mixtures. All the above have led to concerns due to the increasing use of powdered ENM in various applications leading to an increased risk of accidental nanotechnology emissions in the workplace (Chapter 2). The case of particles suspended in a flammable gas which are then exposed to an accidental electrostatic spark is a worst case scenario in the process industry.

Knowledge of the change in the explosion severity of lean turbulent, fuel-air mixtures after the addition of ENP is vital for the completion of risk assessments related to processes taking place in nanotechnology production environments. Furthermore, various applications involving airborne nanoparticles (e.g. soot) suspended in flammable gases (e.g. automotive applications that use natural gas) result in situations where the risk of accidental explosions exist. To this end, this Chapter presents measurements of the explosion pressure history and of flame speed derived from high speed Schlieren cine photographs to characterise the explosion severity in lean and extra-lean methane-air mixture turbulent explosions conducted in the Leeds 23 litre explosion vessel (for more information of methodology see Chapter 3). Two types of carbon black (CB) nanopowders were dispersed in methane-air for the formation of hybrid mixtures with variable dust concentration. The influence of CB ENP on explosion severity is investigated by comparison with results obtained for pure methane-air explosions. In addition, the explosion potential of hybrid mixtures of specific dust concentration and with methane below its LFL, is investigated. Also, the influence of ignition energy on the explosion pressure characteristics of a hybrid mixture with methane below its LFL, is studied. Explosion tests have been conducted under specific conditions and triggered by two devices of different nominal ignition energy (low and moderate). The PSD in the variable dust concentration clouds formed for the conduction of the explosion experiments, was measured by the DMS.

The estimation of the particle size characteristics were linked to the explosion severity demonstrated by the relevant hybrid mixtures. Furthermore, the SEM method was used to determine the particle size and morphology characteristics of the two tested materials in their powder form.

6.2 Material characteristics

In order to extract conclusions on the influence of variations in particle size on explosion severity, it was necessary to quantify particle size and size distribution. This was conducted in the bulk powder as well as in the airborne state of the tested powders, by SEM micrographs and DMS measurements, respectively. Additionally, Schlieren images obtained from two typical dispersion tests of the highest nominal dust concentration of each tested material, are also provided. The results from the experiments using the methodology in Chapter 3 are presented below.

6.2.1 SEM images

The SEM images obtained in the present work for the bulk form of the two tested powders are presented in Figure 6.1. The figure shows that both materials are described by a wide distribution of particle sizes with large agglomerates of several μm size. These μm agglomerates consist of primary particles with sizes ranging between 35-80 nm and 40-60 nm, for Corax N550 and Printex XE2, respectively, lending validity to the nanoparticle size range as described in Chapter 3. As mentioned in Chapter 3, BET specific surface area measurements indicated that Printex XE2 nanoparticles have a much larger specific surface area (950 $m^2 g^{-1}$) than Corax N550 (40 $m^2 g^{-1}$). Considering the role of the specific surface area in the reactivity of dust clouds (described in Chapter 2), it would be expected that a cloud of dispersed Printex XE2 would have a more violent explosion than Corax N550 when mixed with flammable gas. Results of this study are presented in Section 6.4 with images at several magnifications in Appendix D.

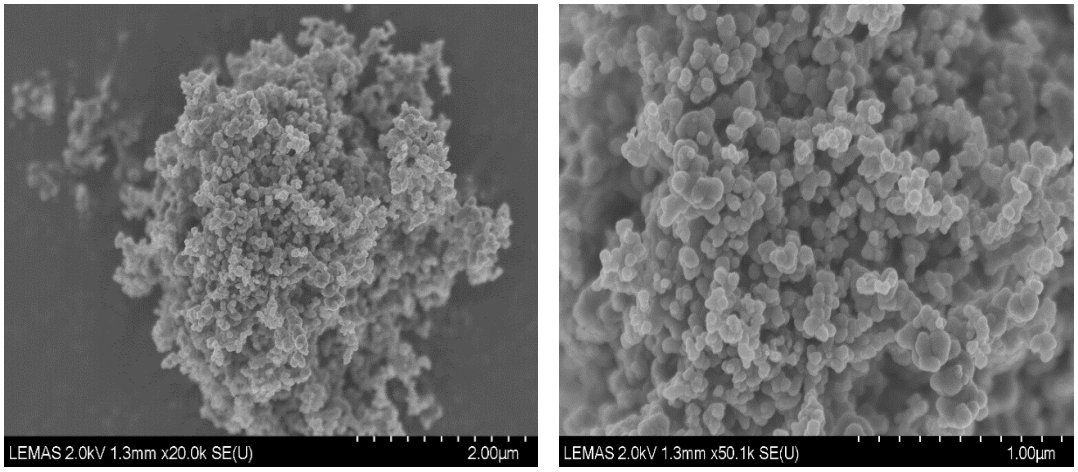

(a) Corax N550

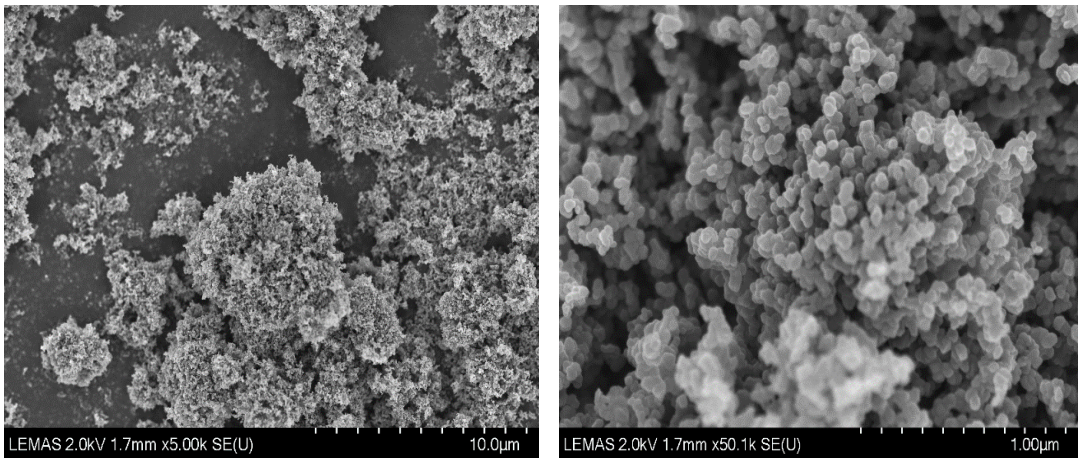

(b) Printex XE2

Figure 6.1: SEM images of (a) Corax N550 and (b) Printex XE2 nanopowders

6.2.2 Particle Size Distributions obtained by DMS

This section discusses results from real time measurements of the PSD in the dust clouds originating from the dispersion of the powder concentrations applied in the explosion tests presented in Section 6.4. As described in Chapter 3, the sampling line of the DMS was attached on a steel pipe fitted on one of the ports provided by the explosion vessel. The length of the pipe was extended on the inside of the vessel up to the centre of its volume where the spark plug was located (ignition point). The same turbulence levels which were used in the explosion experiments presented in Section 6.4, were also applied here. Three replicate dispersion tests for each nominal dust concentration were conducted resulting in PSDs and their modal parameter fitting results. As in the previous chapters, the Rmixdist fitting program (described in Chapter 3) has been used for the estimation of the modal particle number concentrations (mPNCs) of the modes present in the measured PSDs. By grouping particles into two categories, ultrafine ($\leq$ 100 nm) and fine ($>$ 100 nm), the influence of the nominal dust concentration on the specified groups of particles can been seen.

6.2.2.1 Corax N550 dispersion tests

The particle size characterisation over the total PNC of the dispersed powder concentrations, is presented in Figure 6.2. The averaged PSD over the three runs as well as the PSD measured for each run, are illustrated in Figure 6.2a-c. In Figure 6.2d the average modal fractions of the fitting modes are grouped according to the specified size categories.

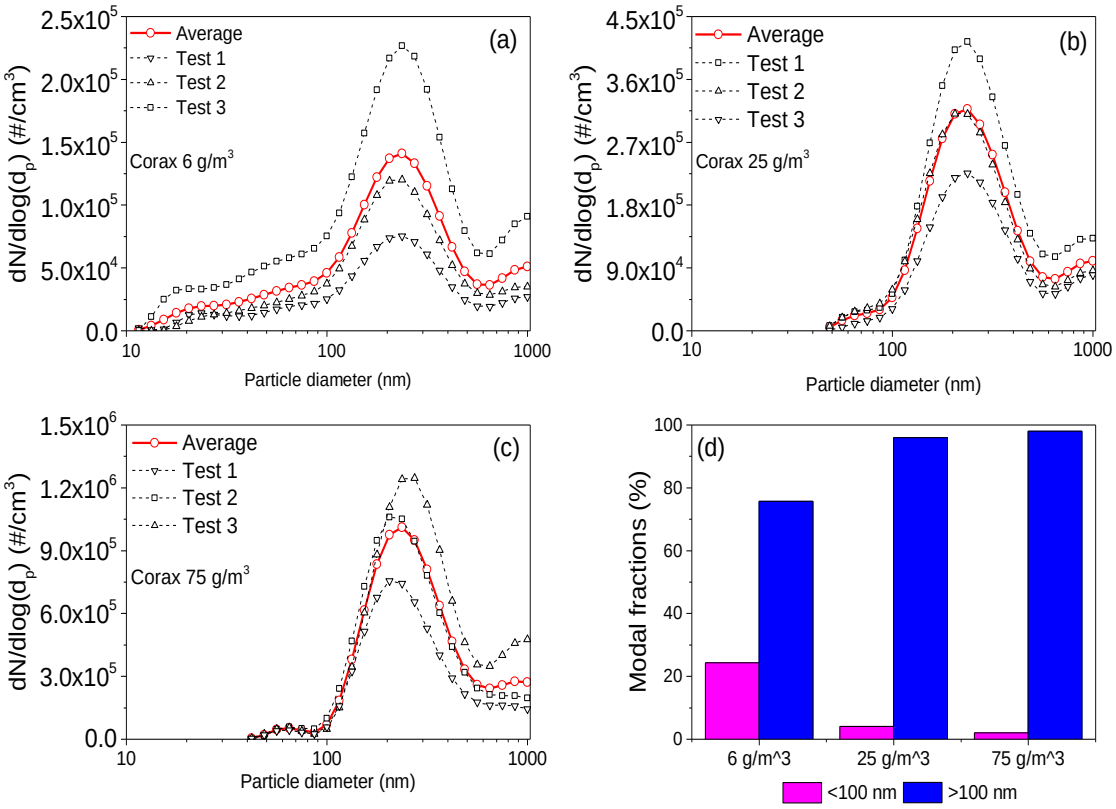

Figure 6.2: PSDs measured by DMS for (a) 6 g/m^3, (b) 25 g/m^3, and (c) 75 g/m^3 of Corax N550 and (d) average modal fitting fractions of the measured PSDs grouped into fine and ultrafine nanoparticles averaged over three replicate runs per dust concentration

Figure 6.2 shows that the measured PSDs for Corax N550 have broad multimodal characteristics with a main peak diameter being at 237 nm, independent of the powder concentration. This diameter is larger than the size of the primary particle (35-80 nm) indicated in the SEM micrographs (Section 6.2.1); which suggests a fraction of the microscale agglomerates that existed prior to injection was de-agglomerated into a size within the nanoscale during injection. Reasons for this may include the blast induced by the injection piston movement and/or interaction with the gaseous mixture through jet and turbulent shear forces. For the lower powder concentration tests, the measured PSDs revealed the presence of a higher fraction of ultrafine particles than observed for the higher powder concentrations. Additionally, it can been seen that all the PSDs of the different powder concentrations present

a rise over the largest size channels of DMS. This is an indication of a peak located very close to the nanoscale. However, micrometric PSD measurements was not possible in this work, therefore the accurate location of this peak was unable to be determined. Finally, the modal fraction, estimated by Rmixdist, confirms the negative association between the population of ultrafine particles and the increase of the nominal dust concentration (Figure 6.2d).

6.2.2.2 Printex XE2 dispersion tests

For the Printex XE2 dispersion tests, as can been seen in Figures 6.3a-c, the particle number concentrations (PNC) in the vessel were, in general, higher than those measured in the case of Corax N550. This difference in PNCs between the two tested materials for the same nominal dust concentrations (6 and 25 g/m^3) clouds, is attributed to their different apparent bulk density. As indicated in Chapter 3, Printex XE2 demonstrates lower apparent bulk density (0.15 g/m^3) than Corax N550 (0.38 g/m^3). Therefore, for the same nominal dust concentrations, higher quantities of Printex XE2 powder were utilised in the dust injector's cartridge than those for Corax N550.

Similar to the results from testing Corax N550, the general shape of the distribution function is broad and multimodal (Figure 6.3a-c). However, contrary to these tests, the main peak diameter is an inverse function of the powder concentration, this is evidence by a peak at 237 nm for 6 g/m^3 and another at 205 nm for 37.5 g/m^3. This further fragmentation could be attributed to the increase of the particle surface area of this material which might increase the importance of particle/gas shear interactions. This was not observed in the case of using Corax N550 because the resulting PNC were lower than those occurring in the Printex XE2 dispersion tests, as indicated above. The resulting effective surface provided by the suspended Corax N550 particles was consequently lower than that of Printex XE2.

In contrast to the Corax N550 dispersion tests, the size distributions over the larger size channels of DMS show a gradual decline as the mass of tested material is increased. This trend indicates that a peak in the microscale was gradually distanced from the nanoscale by increasing the mass of the tested material. Therefore, larger μm particles could be considered in the Printex XE2 clouds compared to the Corax N550 ones. In the present work, μm agglomerates were unavoidable but in future work it may be possible to enhance agglomeration breakup through improved dispersion nozzle design. Figure 6.3d shows that the fraction corresponding to ultrafine particles was found to have a lower percentage than Corax N550 at the lowest nominal dust concentration (6 g/m^3), although by increasing the powder content their percentage was shown to increase slightly compared to the dominant fine one, which was not seen in the case of Corax N550.

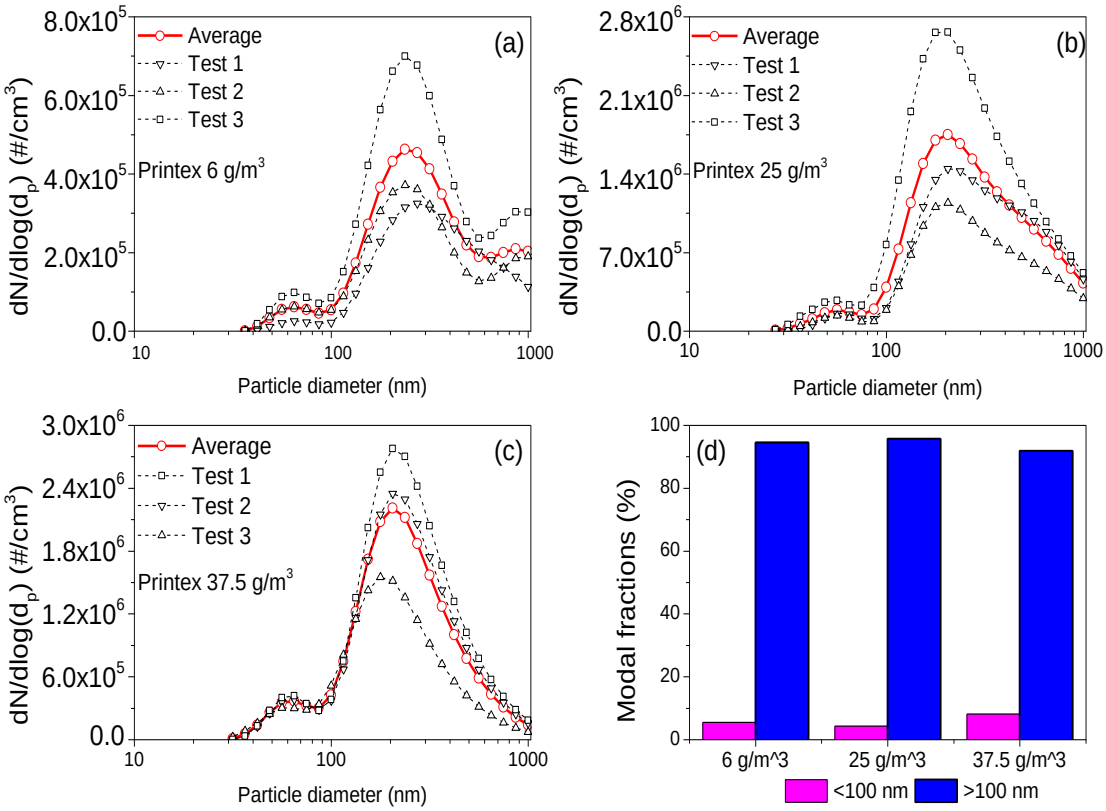

Figure 6.3: PSDs measured by DMS for (a) 6 g/m^3, (b) 25 g/m^3, and (c) 37.5 g/m^3 of Printex XE2 and (d) the average modal fitting fractions of the measured PSDs grouped into fine and ultrafine nanoparticles averaged over three replicate runs per dust concentration

6.2.3 Schlieren images

As indicated in Section 6.2.2, the μm particles suspended in the Corax N550 dust clouds were shown to be smaller compared to those in the Printex XE2 one. Two Schlieren images, randomly selected immediately after the dispersion of materials, were chosen from dispersion tests conducted on 25 g/m^3 of Corax N550 and Printex XE2 samples, and are presented in Figure 6.4. It can been seen that the image corresponding to Printex XE2 shows a significant increase in the concentration of black dots compared to the image corresponding to Corax N550. Assuming that these are large agglomerates, it is clear that the density of the Printex XE2 μm particles in the air of the vessel immediately after their injection was higher than that of Corax N550. Therefore, the particular observation through the visualisation method provided by the Schlieren system confirms the accuracy of the DMS measurements.

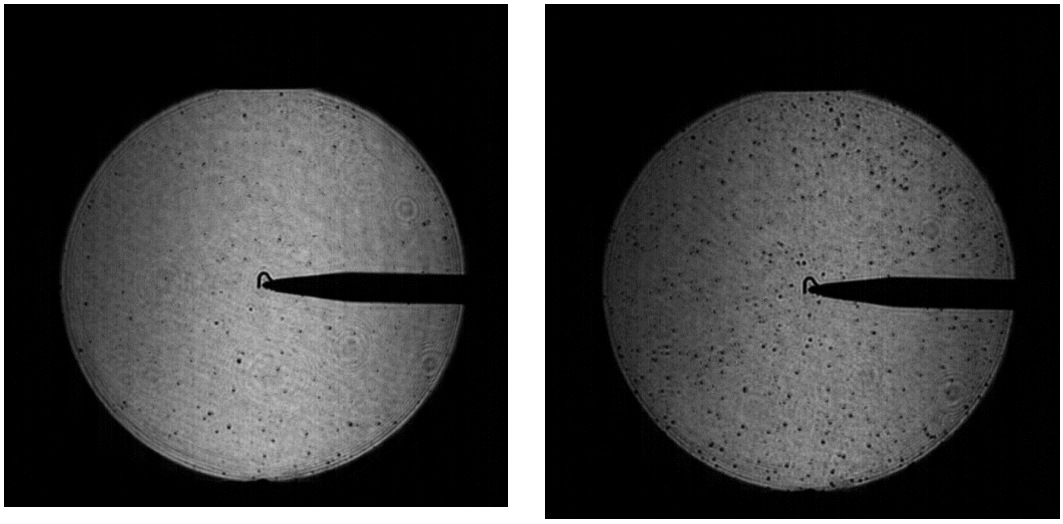

Figure 6.4: Schlieren images of dispersed powders in the explosion vessel obtained for 25 g/m^3 Corax N550 (left); 25g/m^3 Printex XE2 (right)

6.3 Explosions tests in methane/air mixtures and identification of flammability limits

This section presents results from explosion tests of lean methane-air mixtures. It provides benchmark data for the explosion tests on the hybrid mixtures produced by the mix of the specified gas and the nominal dust concentrations utilised in the dispersion experiments in the previous section. Although methane-air mixtures have been studied extensively, there is little data and no comparative photographs at the conditions required as a basis for this work. For this reason, this section is a necessary pre-requisite to Section 6.4, where a comparison of the explosion characteristics between methane-air mixtures and their equivalent hybrid mixtures of variable nominal dust concentration are presented.

6.3.1 Burning rates and LFL of methane-air mixtures

Methane-air mixtures of 0.68 equivalence ratio were ignited through the spark plug and under an rms velocity (u') of 0.83 m/s; the same rms velocity that has been used uniformly throughout the work in this chapter. Laminar explosion tests were conducted on the same mixture for comparison. Figures 6.5a-b show the averaged pressure and flame speed development versus time, over three repeats for the laminar and turbulent lean mixtures. The standard deviation for each measurement is illustrated with error bars representing the variability of the measured data over repeated tests. In Figure 6.5a, it is clear that the burning rate is greater for the turbulent mixture than the laminar one. Furthermore, the turbulent explosion experiments were found to have approximately 40 % higher maximum explosion pressure than the laminar ones.

Regarding the evolution of the flame speed, as illustrated in Figure 6.5b, the profile of the data shows there is a decrease during the first 5 ms followed by an increase corresponding to the normal development of flame. This is because there is a short transition period following spark ignition in which the initial high energy provided by the spark dissipates to be subsequently superseded by chemical reaction. This evidence is in line with research by Gillespie et al. (2000). Immediately after this spark plug effect, the flame increased for both mixtures. During the normal development of flame, the turbulent mixture has a significantly higher flame acceleration than for the laminar mixture.

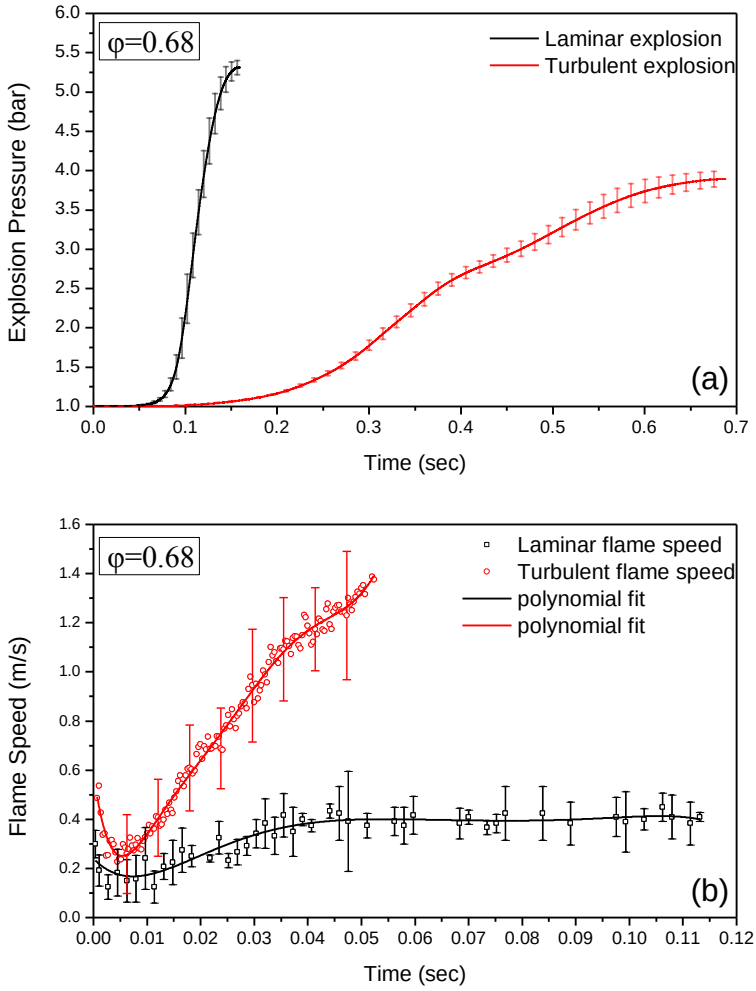

Figure 6.5: Comparison between the variation with time in the (a) average explosion pressure and (b) average flame speed of turbulent (u'=0.83 m/s) and laminar methane-air mixtures. Symbols are experimental data (Error bars indicate ±2 standard deviations, solid curve: polynomial fit)

Figure 6.6 presents a sequence of Schlieren images as obtained from two typical tests corresponding to a laminar and a turbulent explosion test at the studied conditions. It is not within the remit of the present work to conduct analysis on the morphological characteristics of the flame structure, although it is interesting to note there is a change of the flame surface

resulting from changes in flow conditions. Laminar flames were noticed to be spherical and smooth while the turbulent flames were wrinkled with a high surface area. Since the surface of the flame is the area from which the energy is released, a larger surface area leads to an increase in the total rate of energy release (Lemkowitz and Pasman, 2014). Turbulence induced explosion severity is valid not only in gas explosions but also in dust and mist explosions.

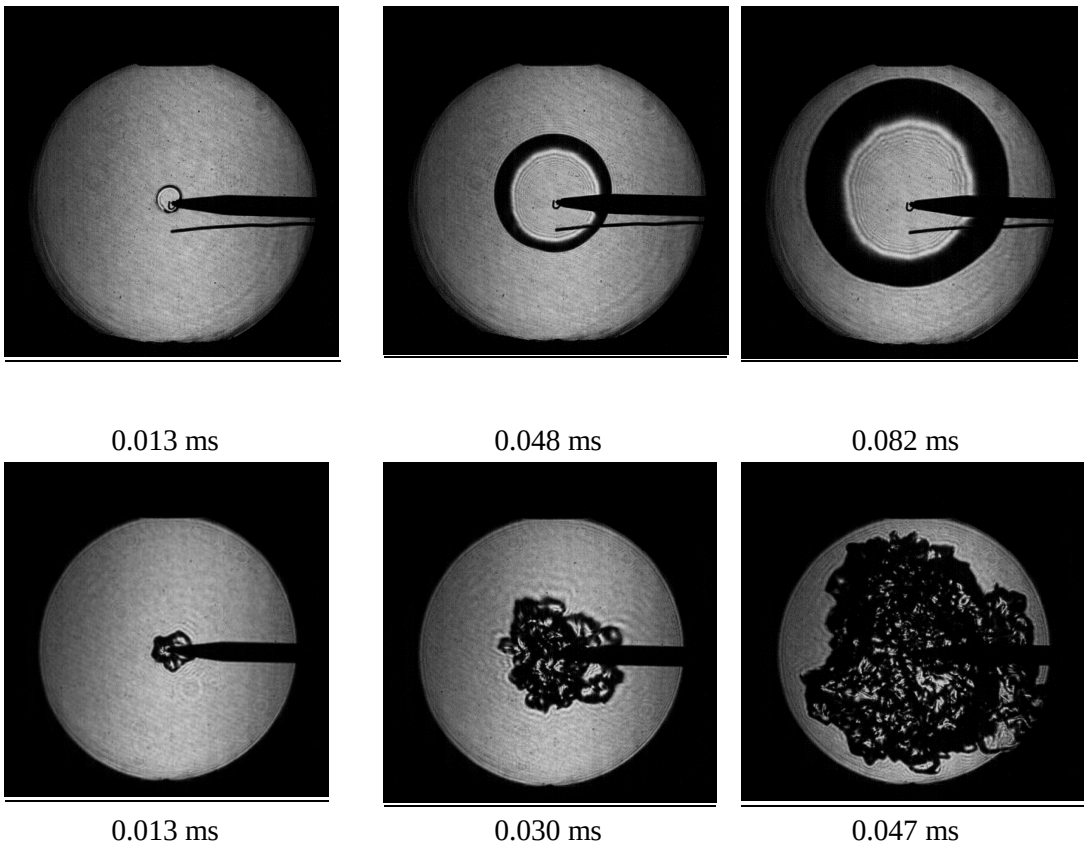

Figure 6.6: Schlieren images of selected (top) laminar and (bottom) turbulent flames of methane-air mixtures at φ=0.68 and u'=0.83 m/s

The explosion experiments with the hybrid mixtures in Section 6.4 utilised ignition energies between 2 J and 60 J, provided by spark-plug and electric pyrotechnic matches, respectively. Therefore explosion tests were undertaken, with the different ignition sources, on mixtures of pure methane-air at specific equivalence ratios (φ) under the specified rms velocity and in atmospheric pressure and temperature. The purpose of the particular experiments was the identification of methane LFL and the investigation of its ignitability at φ < LFL when ignition is provided by the stronger ignitor (pyrotechnic match). Details on the experimental process have been given in Chapter 3.

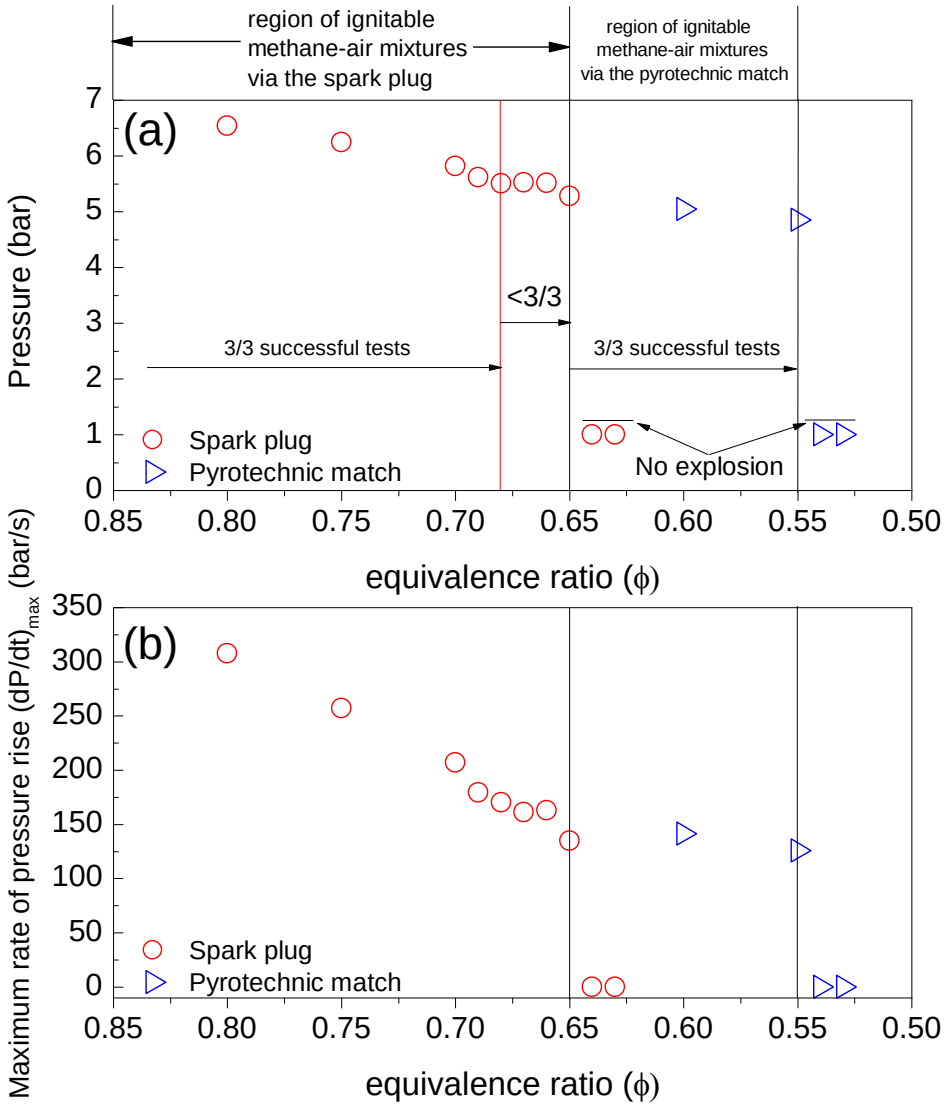

Figure 6.7: Variation in (a) Maximum explosion pressure and (b) maximum rate of pressure rise, Averaged over three repeated tests per condition, of methane-air mixtures for the identification of the LFL of methane. Note that the x-axis has been plotted in reverse order to illustrate the sequence of the experiment

Shown in Figure 6.7a and b are the variations of the averaged maximum explosion pressure (P_{max}) and the maximum rate of pressure rise (dP/dt_{max}) over three repeats conducted for each condition, with the change of equivalence ratio. Also, the graph has been divided into sections corresponding to regions where the mixtures were ignitable via the spark plug and the pyrotechnic match. Furthermore, it should be stressed that the average standard deviation of the pressure data over the total number of tests was ±1.63 % and ±5.57 % for P_{max}, and ±11.6 % and ±18.4 % for dP/dt_{max}, for mixtures ignited by the spark plug and the pyrotechnic matches, respectively. Figure 6.7 shows that both the explosion parameters increased with increasing equivalence ratio towards stoichiometric, but that there is a minimum equivalence ratio of 0.65 below which combustion could not be initiated. Hence, the lower flammability

limit (LFL) of methane-air under the conditions applied in the present work, was found to be 0.65. Additionally, the pyrotechnic matches ignited methane-air mixtures with lower equivalence ratio due to higher utilised ignition energy. As can been seen, the ignitability of methane-air mixtures was extended down to 0.55 equivalence ratio by the utilisation of the pyrotechnic matches (Figure 6.6).

6.3.2 Ignition behaviour of the electric pyrotechnic matches in methane-air mixture

Before presenting the comparison between the explosion characteristics of methane-air and their equivalent hybrid mixtures, it is worthwhile to examine the behaviour of a pyrotechnic match during its ignition. The purpose of this section is to introduce the ignition characteristics of the particular ignitor which, as will be shown in Section 6.5.2, affected the explosion regime of a hybrid mixture with suspended ENP when ignited by the two different energy ignition systems applied in this work.

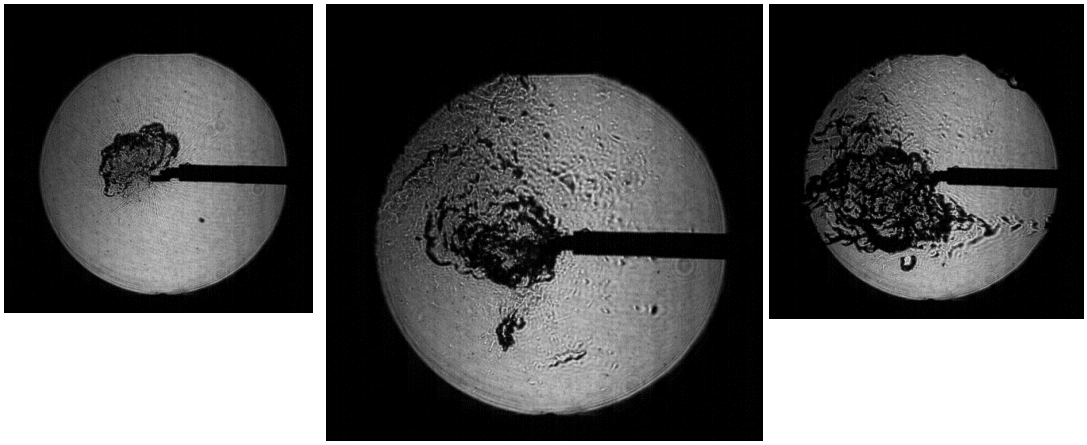

0.00138 ms 0.00586 ms 0.0238 ms

Figure 6.8: Schlieren photographs of the ignition process in a methane-air mixture (φ=0.55) using a pyrotechnic ignitor: framing speed 2900/s

Figure 6.8 shows a sequence of Schlieren photographs illustrating the early stage of the match ignition as well as in a methane-air mixture at φ=0.55. At 0.00138 ms after the triggering of the match, a jet-like volumetric ignition developed. Long streaks probably produced by the passage of hot fragments emitted by the tip of the match can be identified in the image. As indicated in Chapter 3, the Schlieren technique allows for the visualisation of density gradients. The streaks may illustrate the degradation of the heating energy as these emitted fragments travel throughout the vessel. Therefore, it can be concluded that the fragments produced by the ignition of the match are characterised by high heating energy. The amount of this heating energy could not be quantified in this research. However, these emitted fragments could potentially initiate the flame at various points inside the vessel. This particular

mechanism is obviously different from the conventional single-point ignition induced by a spark plug.

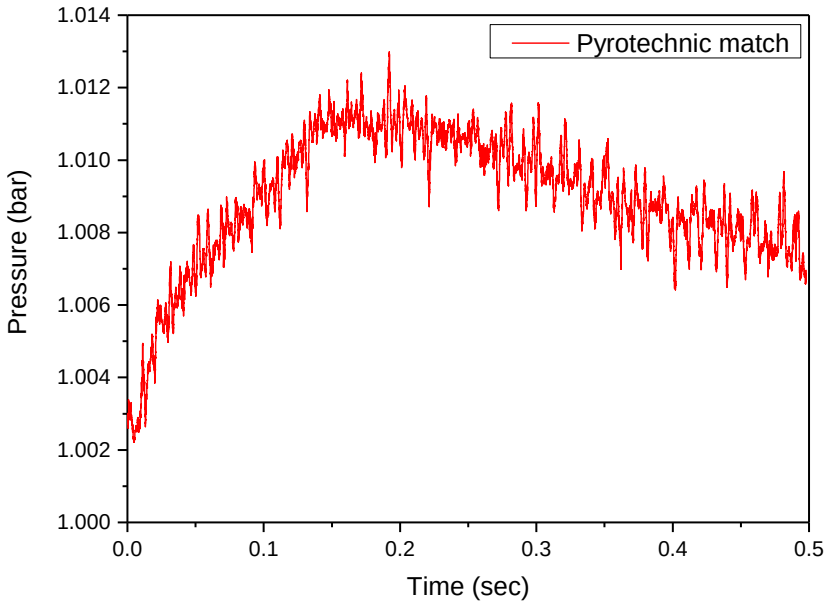

Figure 6.9: Overpressure produced by a pyrotechnic match inside the 23-L explosion vessel with no fuel (device property of University of Leeds)

In order to investigate the potential effect of the excessive ignition energy (by the transition from the spark plug to the pyrotechnic match) on the explosion kinetics of a methane-air mixture, the explosion pressure history of a pyrotechnic match ignited with no fuel in the Leeds explosion vessel was recorded. As shown in Figure 6.9, the net increase of pressure in the vessel due to the match ignition was approximately 8 mbar. Following Cashdollar (1993), the application of a Sobbe ignitor of 5 kJ nominal energy can produce a pressure rise of 540 mbar in a 20-L explosion vessel in the absence of an ignitable mixture. According to the author, this pressure rise corresponds to a flame volume of around 35 % of that of the chamber. Considering the nominal ignition energy of the pyrotechnic match used here (67 J), it is expected that the volume of ignition would be approximately 0.5 % of the volume of the explosion vessel. Therefore, it can be considered that the effect of the excessive ignition energy provided by the pyrotechnic match on the explosion kinetics of the homogeneous mixture are minor. The results presented in Section 6.3.1 confirms this statement with results showing the explosion pressure parameters of methane-air mixture were normally reduced with the equivalence ratio despite the transition from the spark plug to the pyrotechnic match.

6.4 Influence of CB ENP insertion on methane explosion severity

As indicated in the previous section, the repeatable ignition in methane-air mixtures under specific starting conditions was guaranteed at φ=0.68. Below this limit, it is not certain that

the mixture will ignite. For this reason $\phi = 0.68$ was chosen as the datum condition into which was introduced specified nominal concentrations of dust from the two tested materials for ignition attempts with the spark plug. As indicated in Chapter 3, the process was described by explosion tests in methane-air mixtures under the specified conditions, followed by an explosion test on the same mixture with added CB nanopowder. Since three nominal dust concentrations of each material were tested, the results of the 18 interspersed methane-air mixtures were averaged and compared with the average results obtained from the tests performed on the produced hybrid mixtures of variable dust concentration.

6.4.1 Maximum pressure and maximum rate of pressure rise measurements

6.4.1.1 Corax N550

In Figure 6.10 the comparisons between the average explosion pressure characteristics of methane-air mixture and these of the equivalent hybrid mixtures of variable dust concentration are presented. Each hybrid mixture case (see x-axis) is represented by two bordered bars, one corresponding to the average explosion parameters of pure methane-air (blue coloured bar) and the second to the average explosion parameters measured in the respective hybrid mixture (magenta coloured bar). The standard deviation for each point is included to illustrate the variability between the data obtained from the replicates.

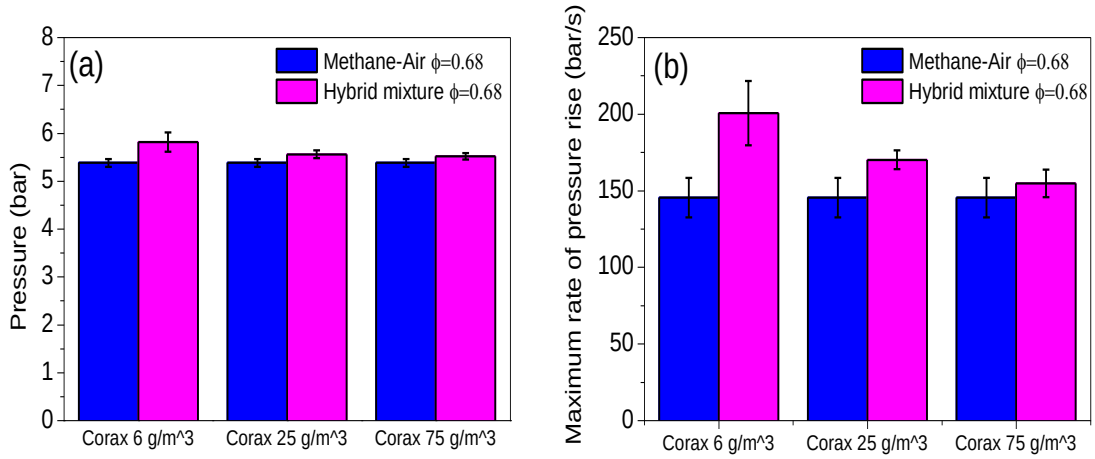

Figure 6.10: Comparison of (a) maximum pressure (Pmax) and (b) maximum rate of pressure rise (dP/dt_{max}), between methane-air mixtures and their respective Corax N550 hybrid mixtures of variable dust concentration (error bars: data $\pm 2\sigma$)

In general, it appears that the insertion of Corax N550 ENPs into methane did not significantly modify the maximum explosion pressure of the gas-air mixture (Figure 6.10a). However, significant changes can be observed in the maximum rate of pressure rise as a function of the powder concentration in the mixture (Figure 6.10b). The highest influence on the explosion

parameters can be observed at the lowest dust concentration (6 g/m^3) hybrid mixture. More specifically, the dP/dt_{max} was significantly increased, by around 33.3 %, after the addition of 6 g/m^3 Corax N550. By increasing dust concentration, it was showed that the burning rate gradually decreased until the highest dust concentration (75 g/m^3), where the parameter became slightly higher than that demonstrated by the pure methane-air mixture.

6.4.1.2 Printex XE2

As can been seen in Figure 6.11, similar to Corax N550, the addition of Printex XE2 ENPs in methane-air mixtures resulted in slight increases in the maximum explosion pressure independent of the nominal concentration of the powder. Regarding the maximum rate of pressure rise, it is shown that methane burning rate was significantly increased by the presence of Printex XE2 ENPs. However, in contrast to Corax N550, it could be noticed that the level of increase of dP/dt_{max}, was almost the same over the different dust concentrations of the particular material. The average increase of dP/dt_{max} due to the insertion of the variable Printex XE2 was estimated to be approximately 16 %.

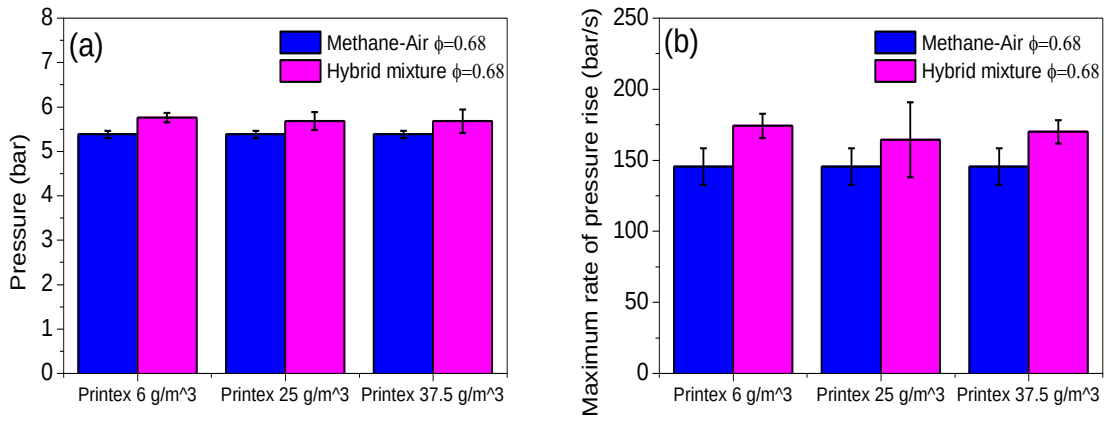

Figure 6.11: Comparison of (a) maximum pressure (Pmax) and (b) maximum rate of pressure rise (dP/dt_{max}), between methane-air mixtures and their respective Printex XE2 hybrid mixtures of variable dust concentration(error bars: data ±2σ)

Comparing the findings here with those of Torrado (2016) suggests a disagreement between the results. In the former case, the authors dispersed very low concentrations of Corax N550 and Printex XE2 (0.5 and 2.5 g/m^3) in a wide range of equivalence ratios of methane-air mixtures to study the influence of the carbon black ENPs on the explosion severity of the gas mixtures. The authors' experiments were conducted in a 20-L sphere. However, in contrast to the vessel utilised here, the former facility did not provide fans for the establishment of a constant rms velocity. Hence, in order to control the initial turbulence, the ignition delay time of the high-pressure based injection system, applied for the injection of the powdered material, was adjusted. Furthermore, they used an ignition system utilising higher energy (100 J) than

those of the two ignition systems applied in this work. The findings of Torrado (2016) indicated a negative effect of both nanopowders in the explosion severity of the homogeneous mixtures especially at the highest rms velocity (3.40 m/s). Finally, it has to be noted that Torrado (2016) did not conduct particle size characterisation in the dispersed clouds.

6.4.2 Flame speeds measurements for both case studies

The average Schlieren derived flame speeds (=dr_{sch}/dt) are plotted against time of methane-air and the respective hybrid mixtures of variable dust concentration in Figure 6.12. The data displayed in the graphs represent the polynomial fits on the average original data of flame speed as extracted by the Schlieren images obtained from the flame development demonstrated by each mixture. The original data has been omitted for the purpose of clarity, although its standard deviations are included to illustrate the variability between the three replicates.

As shown in Figure 6.12a, the ignition of the hybrid mixture suspended with Corax N550 ENPs originating from the lowest powder concentration (6 g/m^3) was described by the fastest flame propagation among the total number of the tested hybrid mixtures. Increasing concentrations of Corax N550 into methane-air mixtures produces more modest increases in flame speed than for the lowest dust concentration. Also, it is interesting to note that the increase in the flame speed induced by the addition of 25 g/m^3 Corax N550 was higher than that induced by the addition of 75 g/m^3 of the same material. The explosion severity, as illustrated by the measurements of the flame speed, agree with the estimations of the subsequent explosion severity of the same mixtures as described by the explosion pressure measurements presented in Section 6.4.1. Therefore, it seems to be confirmation of sorts between the different measurement techniques of the explosion violence.

The addition of Printex XE2, as can been seen in Figure 6.12b, resulted in higher flame speeds than the particle-free mixture. However, in comparison to Corax N550, the induced increase of the flame speed by the suspended ENPs was lower. This difference could be attributed to the different particle size characteristics in the dust clouds produced by the dispersion of each material. As indicated in Sections 6.2.2 and 6.2.3, the suspended μm particles in the Printex XE2 dust clouds were noticed to have larger size diameter and more intense presence compared to the Corax N550. According to Lemkowitz and Pasman (2014), the combustion of μm size particles is a process which occurs heterogeneously. This process involves many sequential stages, where one of the factors influencing this process is the particle size (larger particles need more time to be exposed to heat to be totally burnt compared to the smaller ones). Therefore, it is possible that the heat released from the flame front was not sufficiently

energetic to ignite fast the surrounding coarser fractions of Printex XE2. As a result the flame growth in the Printex XE2 cloud was slower than by the Corax N550 flame.

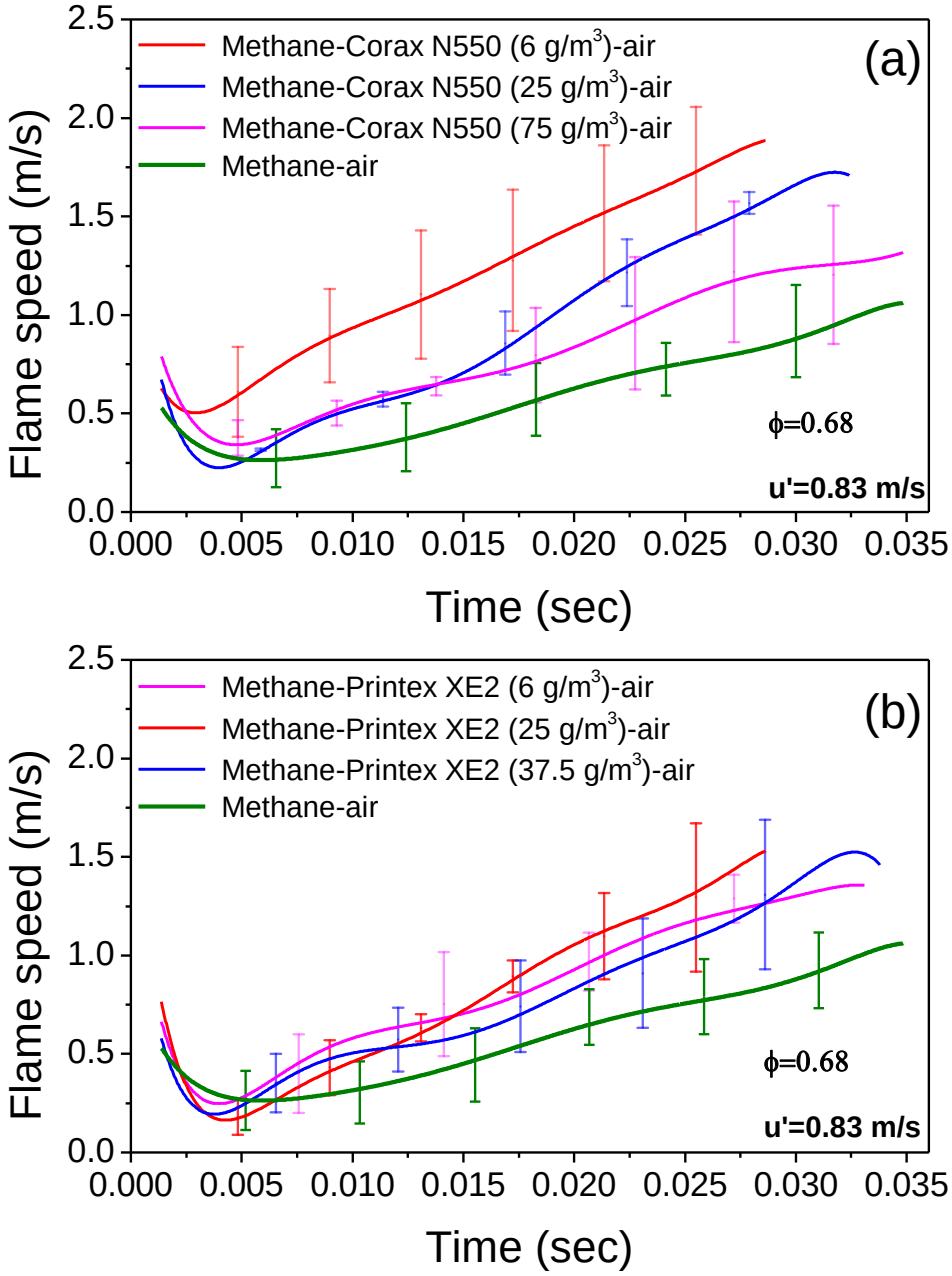

Figure 6.12: Variation in the average Schlieren flame speed with time on (a) methane-Corax N550-air and (b) methane-Printex XE2 mixtures of variable dust concentration (error bars: data ± 2σ, line: polynomial fit)

One interesting outcome in this section, as well as in the previous one, relates to the lowest dust concentration of Corax N550 (6 g/m^3) which demonstrated the highest explosion violence among the tested hybrid mixtures. In parallel, the particle size characterisation presented in Section 6.2.2 indicated that the highest fraction of ultrafine particles was released by the

dispersion of the lowest dust concentration of Corax N550. Therefore, it seems that there is a possible link between the dust cloud particle size characteristics and its explosion severity.

A theoretical approach on the flame speed in a burning dust cloud by Moussa et al. (2015) provides conclusions which support the experimental measurements presented here. Their results indicated that the calculated flame speed due to radiation in the nanoscale was approximately one order of magnitude higher than this in the microscale. Furthermore, the numerical simulations conducted by Liberman et al. (2015), for the gas and solid phase of the ignition in a dust cloud, supports the connection between the particle size and explosion violence indicated from the results here. Their simulations considered both the solid and gas phase of a dust cloud consisting of a hydrogen gaseous mixture suspended with fine particles. According to the authors, it was shown that the radiative preheating of the mixture ahead of the flame was dependent to the spatial distribution of the dispersed particles. As the authors concluded, the consequence of the radiative preheating can be the increase of flame propagation.

6.5 Ignition of hybrid mixtures with methane below its LFL

As indicated in Section 6.3.1, the methane-air mixtures with the spark plug providing ignition, were shown to be experimentally ignitable down to φ=0.65. Through the application of the electric pyrotechnic matches, due to the higher energy provided, ignition of methane was feasible down to φ=0.55. In this section the explosion potentials of extra lean methane-air mixtures below the LFL of gas with added specific dust concentrations are investigated. Additionally, the effect of the application of two different ignition systems (spark plug and pyrotechnic match) on the explosion pressure characteristics of the same hybrid mixture of very low methane content, is presented. The experiments here, similar to those presented above, were conducted under the same conditions.

It has to be noted that the explosion pressure data was preferentially chosen for presentation in this section. Flame speed measurements were also conducted and are presented in Appendix E. As indicated in Chapter 3, flame image analysis through the MATLAB script was impossible in the case of the ignition provided by pyrotechnic matches. The reason is that the initial ignition kernel of the pyrogen was big enough to eliminate optical access to the subsequent flame development. Finally, it has to be noted that the calculation of the flame speed at φ=0.55 of the two successful tests was not conducted. Due to an incorrect estimation, the high speed camera system was not adjusted properly to track the entire development of the very slow flame kernel at this low equivalence ratio. Therefore, this fragmentary capture of the explosion process led to the inability to calculate the photographic-derived flame speed.

6.5.1 Explosion pressure measurements in hybrid mixture with variable φ < LFL

For the tests presented here, the highest nominal dust concentrations of each tested material (75 g/m^3 Corax N550 and 37.5 g/m^3 Printex XE2) were dispersed in methane-air mixtures of specific equivalence ratio (< methane LFL). The results obtained from this experimental process are presented in Figure 6.13.

In Figure 6.13 the explosion pressure parameters of various hybrid mixtures in a double y-axis graph are illustrated. The standard deviations are also illustrated for replicates ignited at least twice. Due to the very low content of methane, it was difficult for some mixtures to be ignited. It has to be noted that Printex XE2 was tested in methane gas mixtures of φ=0.55, however, the hybrid mixture was impossible to ignite with the spark plug.

It is interesting to observe that the explosion parameter affected most by the decrease of equivalence ratio is dP/dt_{max}. The results also indicate that the addition of Corax N550 in the gas mixture resulted in the combustion of mixture at φ=0.55 when the spark plug was used for ignition. However, as indicated above, the ignition of the gas at the same equivalence ratio was impossible to achieve for Printex XE2. As indicated in the previous section, the slower flame growth observed in the Printex XE2 hybrid mixture compared to Corax N550, was attributed to the most intense presence of μm particles in the Printex XE2 cloud as a result of their slow combustion. The long time needed for the large particles to be burned compared to the small ones, combined with the reduced content of methane, resulted in the observed non-ignition of Printex XE2 hybrid mixtures at φ=0.55.

Another interesting feature in Figure 6.13 is the high standard deviation estimated between the replicates at φ=0.60 for the Corax N550 hybrid mixture. This indicates that the severity of explosion at very low equivalence ratios could be very violent and unpredictable in a hybrid mixture with suspended ENP. It is possible that as the methane content is reduced then the explosion phenomenology of mixture relies more on the particle combustion process than on the gas. At the same time, as outlined in Chapter 2, the particle size characteristics in a dust cloud under turbulence effects are rapidly changing due to the vorticity induced by turbulence. Therefore, the size characteristics of the suspended particles, especially of those in motion around the spark plug at the moment it is triggered, are not stable. As a consequence, a possible large fraction of ultrafine particles close to the spark plug, where the strong heating energy is released, can result in a deflagration strong enough to quickly ignite the unburned mixture ahead.

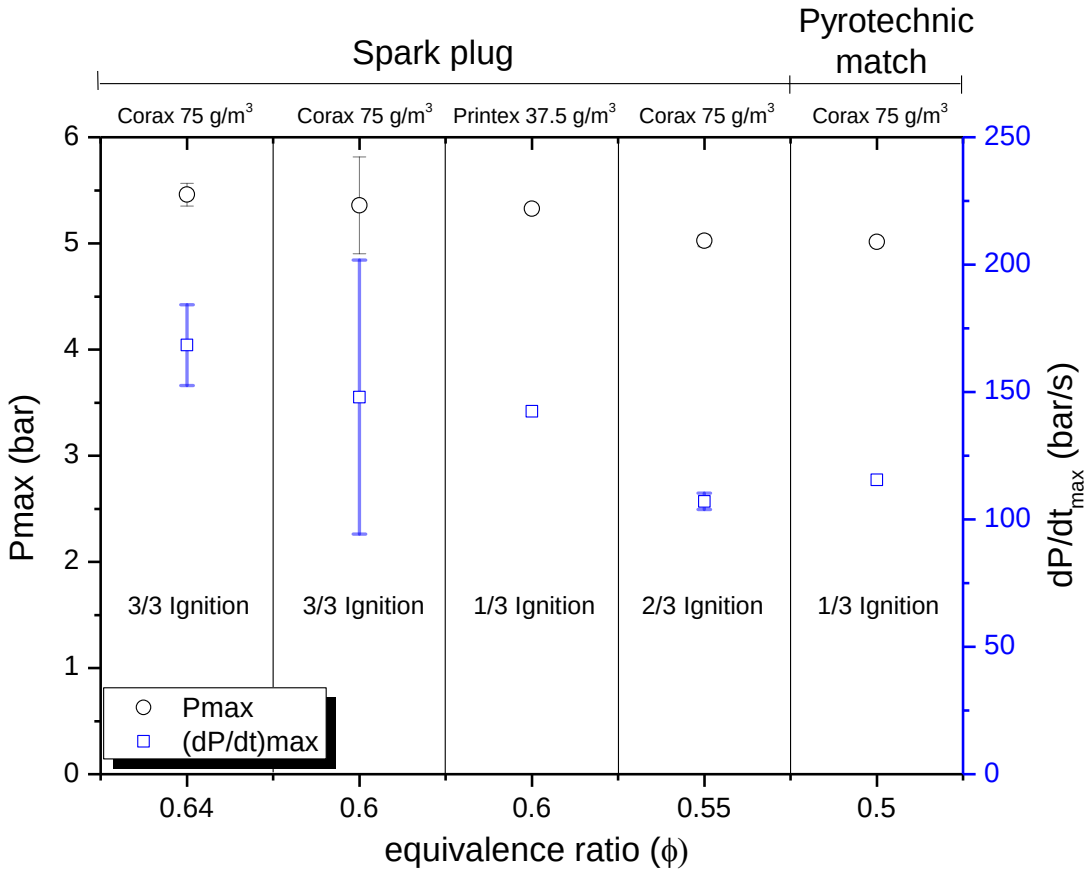

Figure 6.13: The average explosion pressure characteristics of hybrid mixtures below the flammability limit of methane

Regarding the application of pyrotechnic match, as can been seen in Figure 6.13, one successful ignition was conducted at φ=0.50 when 75 g/m^3 Corax N550 was added to the gas mixture. Therefore, it is clear that the application of a moderately higher ignition energy than that utilised by the spark plug, led to the ignition of a hybrid mixture with extremely low content in the flammable gas. According to Billinge (1979), in the industrial ignition incidents, a medium energy ignition by friction (approximately 1 kJ) can be caused by 25 kg of powder falling 4 m. This suggests that the ignition energy utilised by the pyrotechnic match (67 J) is significantly lower than that which describes a medium energy ignition. Therefore, the pyrotechnic match simulates ignitions which are very likely to occur in the real world.

Finally it has to be noted that Kosinski et al. (2013) attempted to ignite hybrid mixtures of propane and CB nanoparticles below the gas flammability limit, however they reported that this was impossible. These authors, conducted explosion experiments on the specified hybrid mixtures in a 20 L explosion vessel which they tried to ignite through 1 kJ chemical igniter. The applied turbulence in their vessel was adjusted by the ignition delay time after the injection process, however, this method did not provide them with a quantified measurement of the established turbulence at the moment of ignition.

6.5.2 Influence of different ignition systems on the explosion characteristics of a hybrid mixture with φ< LFL

The same hybrid mixtures consisting of very low methane content (φ=0.55) and 75 g/m^3 Corax N550, were ignited through the spark plug and pyrotechnic match. The explosion pressure histories obtained from the particular tests, are presented in Figure 6.14. The replicates corresponding to each condition are presented individually. This is due to the strong deviation observed between the replicates conducted with the pyrotechnic matches as the ignition source. Additionally, two successful ignitions were achieved through the use of the spark plug instead of three performed by the use of the pyrotechnic match. The table in Figure 6.14 contains the average results of the explosion pressure parameters.

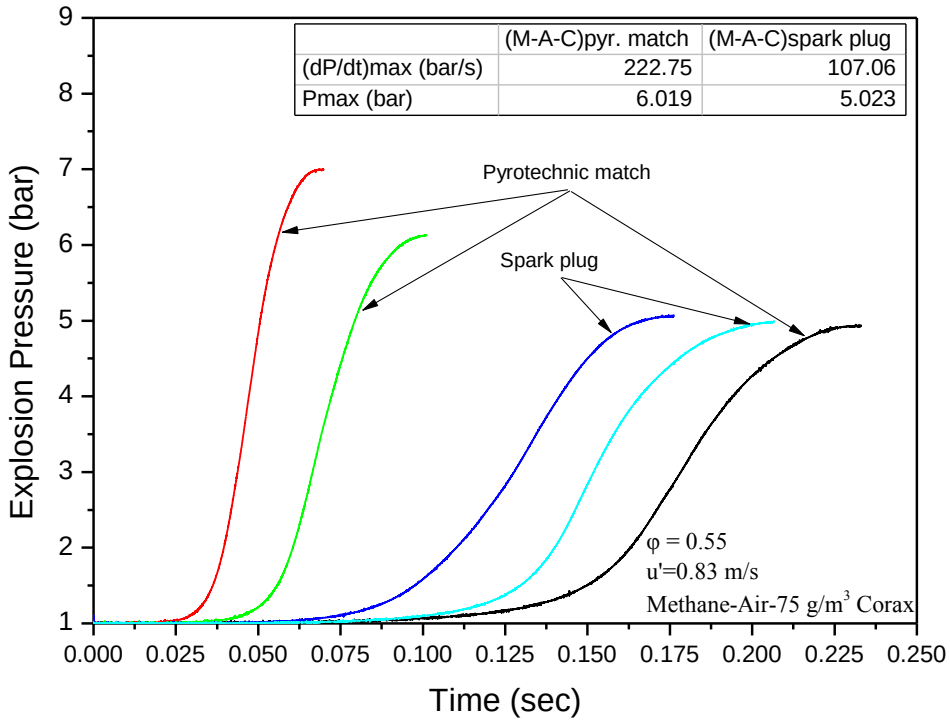

Figure 6.14: Pressure versus time for the same hybrid mixture (methane-air-75 g/m^3 Corax N550, φ=0.55) ignited by the spark plug and pyrotechnic matches

Figure 6.14 shows a significant increase in the explosion parameters resulting from by the transition from the spark plug to the pyrotechnic match. More specifically, the average dP/dt_{max} of the same mixture was increased by more than 100 % by the use of the pyrotechnic matches, while a remarkable increase can be observed also in P_{max} (20 %) (See table in Figure 6.14). Considering the findings from the sections above, this significant increase in the explosion parameters of mixture induced by the pyrotechnic match could be explained by the ignition behaviour of the pyrotechnic matches combined with the particle size characteristics spatially varying within the dust cloud at the moment of ignition.

As described in Section 6.3.2, hot fragments are emitted from the tip of the match immediately after its triggering. These fragments were considered to carry heating energy which through their high mobility may have caused a start of ignition of the dust cloud at various points away from the source. At the same time, as discussed in the previous section, the size characteristics of particles spatially distributed in a turbulent environment are changing rapidly with time due to vorticity. This process is more intense for the small particles which have the tendency to follow the stream lines established in the turbulent environment. In parallel, the small particles have the tendency to be easily ignited, transfusing the radiative preheating to the dust cloud which results in the increase of the flame velocity and consequently of the explosion violence, as mentioned in Section 6.4.2. Therefore, the observed increase in the explosion parameters of a hybrid mixture induced by the application of the pyrotechnic match could be attributed both to the spatial characteristics of ENPs in the dust cloud and the multi-point ignition effect demonstrated by the particular ignition system. As a consequence, there is strong deviation between the replicate tests, as can been seen in Figure 6.14.

A study similar to the present work was conducted by Di Benedetto et al. (2011), although with different powdered materials. These authors dispersed nicotinic acid powder, of μm primary particle size, in lean methane-air mixtures within a 20-L spherical vessel. Turbulence was adjusted by the ignition delay time based on a pressurized powder injection system. The conducted explosion tests were based on ignition provided by: an electric spark and chemical igniters of 500, 1000 and 10000 J energy; the nominal dust concentrations dispersed in the vessel were 30 and 60 g/m^3, near to the lean limit of the specified dust. Furthermore, the equivalence ratio of methane (φ=0.68) was higher than that applied in the mixtures tested here. For turbulence induced by an ignition delay time of 60 ms, these authors found that the transition from a spark plug to a chemical igniter resulted in an increase of dP/dt_{max} ranging between 10 % and 34 %, for the 500 J and 10000 J igniters, respectively. However, in contrast to dP/dt_{max}, the maximum pressure remained approximately constant which was not observed in the present work.

6.6 Summary

In this chapter the changes in the explosion severity of lean-methane-air mixtures occurring after the addition of specific masses of two CB nanopowders were quantified. Each explosion test was conducted in the Leeds explosion vessel under constant rms velocity. Two ignition systems of different nominal ignition energy (low and moderate) were tested for the ignition of the homogeneous and heterogeneous mixtures. Particle size characterisation was conducted via the DMS for the dust clouds produced by the dispersion of the same masses of powder used for the production of the hybrid mixtures in the explosion experiments. Additionally,

SEM images were obtained for the dust samples of the original powders used in the explosion tests. The explosion severity in this work was described by the measurements of pressure history as well as by the Schlieren photography-derived flame speeds. The flammability limits of methane were identified and the explosion potential of hybrid mixtures with methane content below its LFL, were studied. Finally, the effect of excessive ignition energy on the explosion kinetics was evaluated in the same hybrid mixtures of methane content below its LFL.

- SEM images of the tested materials indicated a strong agglomeration state in their bulk form through the observation of particles with several μm size. Images of greater magnification revealed the range of the average primary particle size in Corax N550 was 35-80 nm and in Printex XE2, 40-60 nm. In the dust clouds formed by the nominal dust concentrations utilised in the explosion experiments, the number based PSDs measured over the nanoscale were characterised by multiple peaks with the main peak diameter between 205-237 nm for both materials. The results obtained from the modal fitting analysis on the measured PSDs indicated that in the Corax N550 dust clouds, the fraction of ultrafine particles demonstrated a negative correlation with the mass of dispersed material. For Printex XE2, the population of ultrafine particles was higher at the greatest dust concentration. At the same time, the size distributions over the last size channels of nanoscale revealed the presence of a peak in the microscale for both dispersed materials which for Corax N550 was shown to be located closer to the nanoscale than for Printex XE2. Schlieren images obtained from dispersion tests of each material confirmed the higher density of suspended μm particles in the Printex XE2 cloud than those observed in the Corax N550 one.
- In this work, the explosion tests in lean methane-air mixtures provided the benchmark data for the experiments involving hybrid mixtures with suspended ENP. For the specific rms velocity and the lowest nominal ignition energy provided by the spark plug used in this work, the explosion violence was significantly higher for the turbulent methane-air mixture than for the laminar one. In addition, the experimental process on methane-air mixtures indicated the LFL of methane for the given conditions. Furthermore, through the same experimental process the equivalence ratio of gas-air mixture for the introduction of the various nominal dust concentrations originated from the each tested material was identified.
- The addition of CB ENP in methane-air mixtures at φ=0.68 resulted in generally higher burning rates than those demonstrated by the respective pure methane-air mixture. Among the tested dust concentrations the lowest one of Corax N550 formed a hybrid mixture which demonstrated 33 % higher dP/dt_{max} than that demonstrated by the

respective pure methane-air mixture. By using the concept of thermal exchanges by radiation in the hybrid mixtures, explosion violence was correlated to the fraction of suspended ultrafine ENP. This concept was confirmed by the experimental measurements of the PSD which indicated the largest fraction of ultrafine ENPs at the lowest Corax N550 dust concentration.

- The Schlieren photography-derived flame speed method also indicated and confirmed the above trend. The agreement between the two different methods employed for the estimation of the explosion severity indicated that severity at the very early stage of explosion could be used to foreshadow the following explosion. Therefore, optical measurement techniques could be an important evaluation tool of the explosion severity in the conduction of future risk assessments on the explosion potential of ENPs.
- A very important finding of this work, is the successful conduction of explosions in hybrid mixtures below the methane LFL (φ=0.65) identified within this work. Hybrid mixtures with suspended ENPs were successfully ignited through the spark plug at φ=0.55 and φ=0.60, for Corax N550 and Printex XE2, respectively. A hybrid mixture of further reduced methane content (φ=0.50), was ignited through the application of the pyrotechnic match. This has potentially high impacts in future applications involving ENPs with flammable gases.
- Another interesting finding was that the addition of Corax N550 formed a hybrid mixture ignitable at φ=0.55, while the Printex XE2 one was ignitable at φ=0.60. This was attributed to the presence of larger μm agglomerates in the Printex XE2 dust clouds than those with Corax N550, as indicated from the measured PSDs and from the obtained Schlieren images. It has been reported in the current literature that as the size of the particle increases then the time needed for complete combustion is increased at the same time the particle becomes less sensitive to combustion. Therefore, in the case of the Printex XE2 hybrid mixture, the coarser particles suspended close to the spark plug were not exposed to sufficiently high heating energy to be ignited and subsequently ignite the unburned mixture ahead. In conclusion, as the average particle size in a hybrid mixture suspended with ENPs decreases then the possibility of an accidental explosion to significantly increase even at equivalence ratios significantly lower than the LFL of the gas.
- Finally, the two ignitors in this work were used to investigate the impact of excessive ignition energy on the explosion kinetics of a hybrid mixture of very low methane content. The results indicated that the explosion severity in the mixture ignited by the pyrotechnic match were significantly higher than those in the same mixture ignited by the spark plug. The comparison with current literature showed that the observed

modification in the explosion severity of the mixture could partially be attributed to the excessive ignition energy provided by the stronger ignitor. However, the observed changes in the explosion parameters due to the increase of ignition energy were significantly higher than those reported in the literature. In addition, high deviation in the explosion data obtained from the replicate tests were observed. By tracking the ignition behavior of the pyrotechnic match through the Schlieren system, emitted fragments from the tip of the match travelled throughout the vessel's volume carrying heating energy to various locations. Consequently, this ignition behavior was considered to increase the possibility for the initiation of the flame at locations where the particle size characteristics benefit thermal exchanges based on radiation thus resulting in violent flame propagation. Therefore, the studies on the explosion characteristics of ENP should carefully consider the data obtained on mixtures (dust-air or dust-gas-air) ignited through volumetric ignition systems such as pyrotechnic matches and chemical ignitors. The reason is that the induced deviation in the obtained data can possibly lead to overestimation of the average measured explosion characteristics.

Chapter 7

7. Final Discussion and Conclusions

7.1 Research summary

A better understanding of the dispersion and explosion potential of ENP allows the development of appropriate models and tools for analysis and management of accidental risks related to the production, transportation and use of nanostructured materials. Up until recently very little attention has been given to the study of accidental risks, such as fire, explosion and massive release of ENPs. The majority of previous studies were confined to the evaluation of exposure in workplaces or in the environment. Accidental release scenarios and identification of the explosivity and dispersion parameters are an important area that requires attention. With this knowledge more effective risk management responses, not only to present accidental scenarios, but also to clean up the environment in post-accidental scenarios will be possible. The research described in this thesis, successfully developed methods for the release of hazardous ENPs originating from specific nanopowders into specially designed facilities simulating accidental situations. This enabled the subsequent study of their airborne behaviour as well as of their explosion characteristics within an explosive atmosphere (flammable gas), under controlled conditions. Furthermore, the present work provides experimental and modelling tools to access risks associated with accidental scenarios, and proposes organizational strategies to lower accidental risk through the conduction of ventilation tests.

Chapter 2 introduced the theory describing the dispersion and explosion behaviour of airborne ENP, as well as the relevant contribution of various studies on the particular topic. Chapter 3 presented the dispersion and explosion facilities, the main instrumentation, and the auxiliary equipment utilised to fulfil the research objectives. The dispersion characteristics of specific ENPs were studied in Chapters 4 and 5. Specifically, Chapter 4 presented the modifications applied to an existing preparation protocol for the production of nano-suspensions. The volume-based PSDs of the resulting nano-suspensions were provided for each modification step. TiO_2 nano-suspensions produced according to the modified protocol, were injected continuously into the Leeds dispersion facility for a determined time, followed by decay periods induced by different ventilation rates. The evolutions of PNC and PSD measured by spatially distributed instrumentation, were presented. The impact of the different ventilation strategies on the PNC's decay was analysed through the estimation of the size-resolved and size integrated particle decay rates. Additionally, the spatial ventilation efficiencies corresponding to the different ventilation rates, were presented. In Chapter 5, TiO_2 and SiO_2

nano-suspensions, were produced according to the modified protocol, and injected continuously for the same time applied in the experiments presented in Chapter 4. However, the end of injection was followed by a prolonged period when the dispersed aerosols were allowed to decay under unventilated conditions. The evolution of nanoscale and micron-scale measurements of the PSDs obtained during the entire experimental period at one point near to the source, were presented along with their modes estimated by the Log_{10}-normal fitting program. In addition, an indoor aerosol model was applied for the estimation of changes in the PNC which were compared with these derived from the experimental measurements. Finally, Chapter 6 presented the particle size characterisation conducted in the powder form as well as in the dust clouds generated from the dispersion of two types of CB nanopowders (Corax N550 and Printex XE2) in the Leeds explosion facility. These clouds were mixed with methane of low content to form hybrid mixtures, and the influence of CB nanoparticles on the explosion severity was investigated by comparison with the results obtained for pure methane explosions. Additionally, the influence of CB nanoparticles on the ignitability of methane-air mixtures of equivalence ratio below the flammability limit of methane, were discussed and presented.

7.2 Conclusions

- This work has demonstrated that it is feasible to de-agglomerate TiO_2 and SiO_2 nanopowders for the subsequent study of ENP dispersion characteristics (**Objective 1**), by introducing a considerably modified experimental preparatory process (**Chapter 4**). Specifically, the ultra-sonication of an agglomerated cohesive nanopowder in water was shown to be sufficient to de-agglomerate the stored nanoparticles and to enable the production of nano-suspensions characterised by large fractions of particles with diameter ≤ 100 nm (**Section 4.2.2**). At the same time, this method results in the significant reduction of particles in the micron-scale. The particular modified method was successfully applied to the production of the nano-suspensions utilised in the dispersion experiments presented in **Chapters 4** and **5**.
- The aerosolization of the nano-suspensions through a 6-jet Collison nebuliser was proven to be an effective technique for aerosol production of high PNC in ENP (**Objective 1**), as indicated by the measured PSDs (**Sections 4.4.2** and **5.4.2)**. In addition, the particular technique allowed for the safe introduction of the aerosol into the atmosphere (in our case the dispersion facility). This injection technique combined with the preparatory process developed, will enable other researchers to conduct detailed, size-controlled, studies related to toxicology, and human/environmental exposure of various types of ENP.

- Release of ENP under turbulent conditions, which can be typically anticipated in real life situations, was measured and shown to spread spatially homogeneously from the source (**Objective 1**). In **Section 4.4.1.2**, for the freshly emitted aerosol under the operation of a fan, it was estimated that its spatial motion was described by 4 cm/s velocity homogeneously developed from the source to the sampling points. On the other hand, the motion of the aerosol plume without the use of the fan, was described by a velocity equal to 0.5 cm/s. Therefore, the installation of a single particle sensor close to a real production line in a nanotechnology workplace, will be able to rapidly track an accidental ENP release and thus provide a sufficiently early warning allowing time for the evacuation of the area before the exposure reaches dangerous levels.
- The study of ventilation strategies for cleaning an environment filled with dispersed ENP (**Chapter 4**) indicated that reducing the ventilation power resulted in the increase of leftover particles in the air of the chamber, when the cleaning process had been completed. Specifically, the modal parameter fitting applied to the measured PSDs corresponding to the decay period, showed that the gradual decrease of the ventilation strength led to an increased number of leftover particles at the end of evacuation (**Section 4.4.2.2**), and to an increased ratio of ultrafine particles over the fine ones. Therefore, considering that ENP (especially the ultrafine ones) could be hazardous for human health even at low PNC, ventilation rates within low ranges of ACH (3-6 ACH) should be carefully considered in the design process of ventilation systems at nanotechnology workplace (**Objective 2**). In addition, this work indicated that the 12 ACH ventilation rate was the most effective, accomplishing the total removal of both particle size groups at the end of the cleaning process.
- The spatial ventilation efficiency (**Section 4.4.4**) as a function of ventilation rate and distance from the inlet diffuser, indicated that at high ventilation rates, optimal ventilation (i.e. higher ventilation efficiency at a specific location) occurs closer to the inlet diffuser. However, by decreasing the ventilation rate, ventilation efficiency close to the inlet diffuser was shown to be decreased, whereas the ventilation efficiency further away remained constant. Finally, at the lowest tested level of ventilation rate, spatial ventilation efficiency was shown to be independent of the distance to the inlet diffuser. Therefore, in order to ensure a homogeneous ventilation efficiency, the arrangement of inlet/outlet diffusers should be carefully designed (**Objective 2**).
- The level of exposure during an accidental release of ENP was shown to depend on the emission profile of the material under release (**Objective 1**). The modal fitting analysis of the measured PSDs (**Section 5.4.4**) indicated shifts of the modes towards larger sizes (agglomeration) for both materials over time at a certain point under a

continuous release rate. Abrupt growth of the TiO_2 modal diameters, was recorded during the first minutes of the release. In contrast, the SiO_2 modal diameter growth, induced by agglomeration, presented a moderate evolution throughout the release period. Therefore, in the case of an accidental release, given a typical individual human intake fraction (0.47 $m^3 h^{-1}$) and the fact that agglomeration results in reduced particle numbers, exposure levels will be influenced by the size growth rate of ENP. As a consequence, according to the above, exposure to accidentally released ENP is expected to be different for different ENM.

- The TEM images of deposited matter (**Section 5.4.6)** indicated that risks posed by ENP sourced from different materials may have different impacts on human health, either during accidental or post-accidental conditions (**Objective 1**). Specifically, the deposited SiO_2 agglomerates, as indicated by the images, presented weak bonds between their coalesced primary particles. In contrast, the TiO_2 deposited agglomerates were described by primary particles strongly bonded together. Therefore, it is reasonable to consider that an SiO_2 agglomerate may present higher possibilities to de-agglomerate than an TiO_2 one. As a result, through de-agglomeration, the formation of smaller particles when an inhaled SiO_2 agglomerate has reached the lung, could catalyse inflammatory responses. In addition, the de-agglomeration potential of an SiO_2 agglomerate could be considered even when the particle is deposited on a surface. In the case of the action of a turbulent air stream, it is possible for the loose agglomerate to break into smaller clusters. These clusters, by extension, have high potentials for re-entrainment into the air with their consequent transition into the airborne state, resulting in the increase of exposure of humans in indoor environments.
- This work established a simple aerosol model (**Chapter 5**) which was shown to be effective for predicting the changes in PNC with time induced by two important particle mechanisms: coagulation and deposition (**Objective 1**). In addition, the particular model is an easy to use tool, since in the calculation process it is not essential to have knowledge of the characteristics of the primary aerosol released at the source. Furthermore, since this model was successfully applied to two different types of ENP, it is likely that it can be applied over a wider range of materials. By grouping particles into specific size categories, the model estimated that the weak agglomeration illustrated by the SiO_2 ultrafine particles during the early stage of injection (**Section 5.4.4**) was due to the dominance of deposition. Additionally, the model provided a satisfactory explanation for the abrupt decrease of TiO_2 PNC after the end of injection (**Section 5.4.2.1**) which was not seen with the SiO_2. Specifically, the model indicated stronger homogeneous coagulation between TiO_2 fine particles

than SiO_2 ones when PNC were high. Due to this enhanced homogeneous coagulation in the TiO_2 aerosol, the strong scavenging effect of the larger particles over the smaller ones was considered the reason for the high decrease of the total PNC. The above were confirmed by the deposited matter's size characteristics revealed in the TEM images (**Section 5.4.6**). Images illustrated large TiO_2 agglomerates with average size ranging between the nano and micron scale. In several cases, these large agglomerates were shown with smaller particles being attached to them (scavenging process). However, in contrast, SiO_2 deposited particles were characterized by agglomerates of smaller size than the TiO_2, while in some cases they were observed as very small particles of diameter < 100 nm.

- The work presented in **Chapter 6** demonstrated that the fraction of ultrafine ENP within a hybrid mixture is able to determine the severity of its explosion triggered by an accidental electrostatic spark (**Objective 3**). Specifically, it indicated that the addition of various amounts of two types of CB nanopowder in a lean methane-air mixture, resulted in more severe turbulent explosions than of the gas alone. Interestingly, it was shown that among the hybrid mixtures of variable dust concentration, the mixture of the highest fraction of ultrafine particles produced the severest explosion **(Section 6.4).** At the same time, the particular mixture was that of the lowest dust concentration. Considering the findings of **Chapter 5** which indicated that coagulation is increased by the increase of PNC, the presence of the highest fraction of ultrafine particles at the lowest dust concentration was reasonable. The above indicate that the accidental release of a relatively minor amount of ENP combined with a low amount of a flammable gas and an electrostatic spark, can result in a severe explosion with consequences for humans and installations higher than those of a higher amount.
- **Chapter 6** also showed the application of an optical technique (Schlieren system) for the determination of flame speed, and that this can be an appropriate methodology that will enable researchers to conduct accurate studies on the explosion characteristics of ENP (**Objective 3**). Specifically, the Schlieren-derived flame speed measurements identified the severest explosion for the same mixture as that indicated by the traditional method based on the explosion measurements **(Section 6.4)**. Therefore, the former can be used for direct measurements of the flame velocity with higher accuracy than that of the indirect measurement method based on the explosion pressure data.
- In **Chapter 6** it was also shown that a hybrid mixture can be ignitable through an accidental electrostatic spark at an equivalence ratio (φ) well below the LFL of the

gas (**Objective 3**). Specifically, between two dust clouds formed by different nanopowders, the cloud with the lowest presence of μm particles demonstrated the highest extension below the LFL of the gas **(Section 6.5)**. This was attributed to the difficulty of sufficient μm particles to be ignited by the provided ignition energy. Therefore, it can be concluded that as the mean particle size decreases, a hybrid mixture of an extremely low content of gas, could be ignitable. This finding can be applicable not only in the field related to the risk assessment of ENP but also in the study of risks posed by technological applications involving airborne nanoparticles (e.g. soot particles) suspended in flammable gases (e.g. automotive applications that used natural gas).

- Finally, through the application of an ignitor utilising higher energy, it was demonstrated that the ignition behaviour of different ignition systems, can influence the measured explosion parameters of a hybrid mixture (**Objective 3**). The explosion tests conducted on the same hybrid mixture with the gas below its LFL **(Section 6.5.2)**, indicated that the multi-point ignition induced by the strong ignitor resulted in significantly higher explosion violence than that induced by the spark plug. This difference was attributed to the rapid change of the particle size characteristics within a turbulent dust cloud combined with the possibilities presented by the multi-point ignition to initiate the explosion at points where large fractions of ultrafine particles existed. As a result, it demonstrated high deviation in the data obtained from the replicate tests conducted through the strong ignitor. Therefore, for any application of strong ignitors in the study of ENP explosion characteristics, a high level of uncertainty should be considered as likely in the obtained data - this was not seen in the case of using ignitors such as the spark plug.

7.3 Opportunities for Future work

As indicated in **Chapter 4**, the spatial ventilation efficiency in the chamber was found to be strongly dependent on the relative location from the inlet diffuser. Therefore, given the potential provided by the Leeds dispersion facility, future work could be based on the study of the different flow recirculation scales induced by different arrangements of inlet/outlet diffusers. An ideal air flow stream path could ensure a homogeneously established ventilation efficiency and integrate the functionality of the ventilation system.

Chapter 5 also offers many perspectives for future work. Since effective techniques were established for the de-agglomeration of nanopowders and for their subsequent injection into the dispersion facility, the addition of more materials in the experimental process would

support further the validation of the aerosol model applied herein. In addition, accidental scenarios involving dry dispersion techniques, such as the free falling of nanopowder, could be tested and expand the knowledge on emissions induced by different accidental conditions.

Finally, opportunities for future work are provided by the work presented in **Chapter 6**. Firstly, the data of this work could provide a basis from which explosions arising from large scale accidental release can be assessed. This could be achieved through the application of appropriate methods of scaling the data to large industrial and commercial plants focusing particularly on the risks posed by accidental releases of ENP. In addition, as indicated in the results presented in **Chapter 6**, the presence of large suspended μm particles was unavoidable in the explosion tests. Therefore, the addition of a specially designed dispersion nozzle in the current injection system could enhance the de-agglomeration of the tested powders. This subsequently will result in the generation of clouds characterised by large fraction of primary aggregates for the conduction of enhanced explosion studies focusing on the combustion phenomenology of ENP.

APPENDIX A

Bi-exponential fitting on data obtained by CPC#1 and CPC#4 during the tested ventilation rates

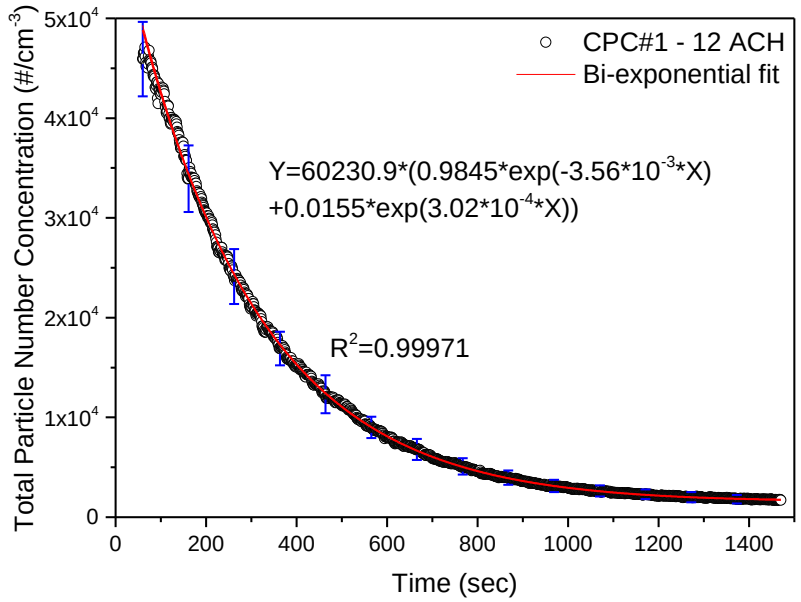

(a)

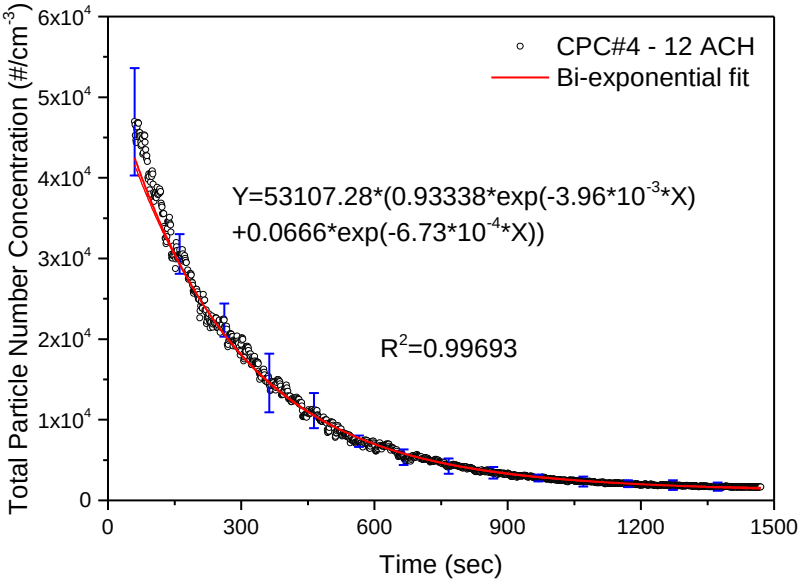

(b)

Figure 1: Bi-exponential fitting on data obtained by (a) CPC#1 and (b) CPC#4 at 12 ACH

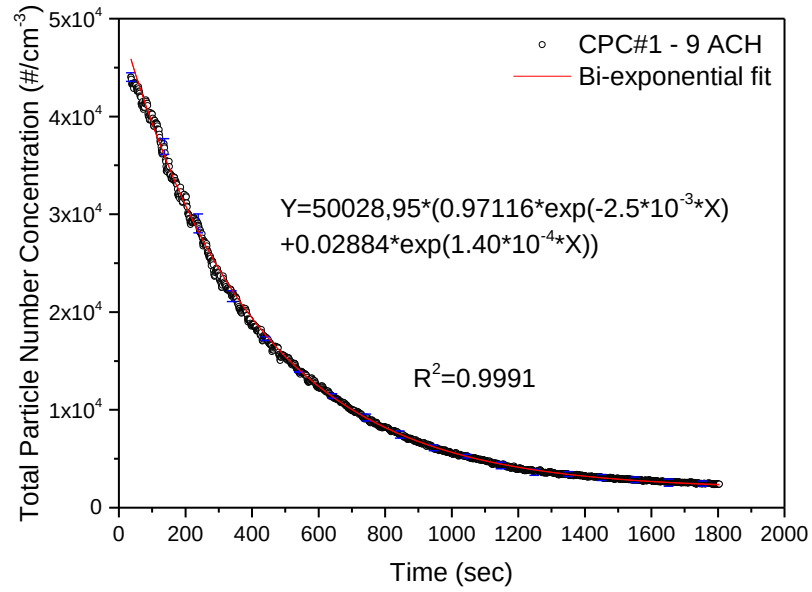

(a)

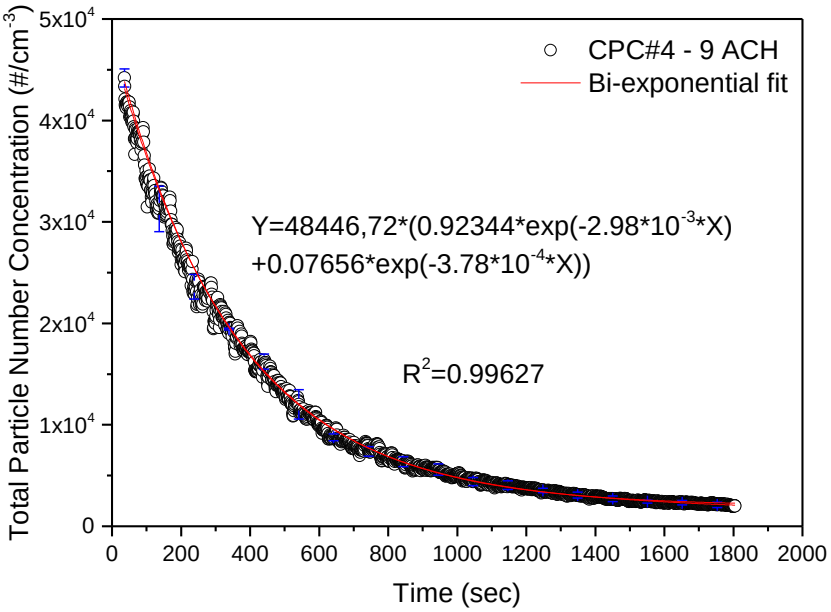

(b)

Figure 2: Bi-exponential fitting on data obtained by (a) CPC#1 and (b) CPC#4 at 9 ACH

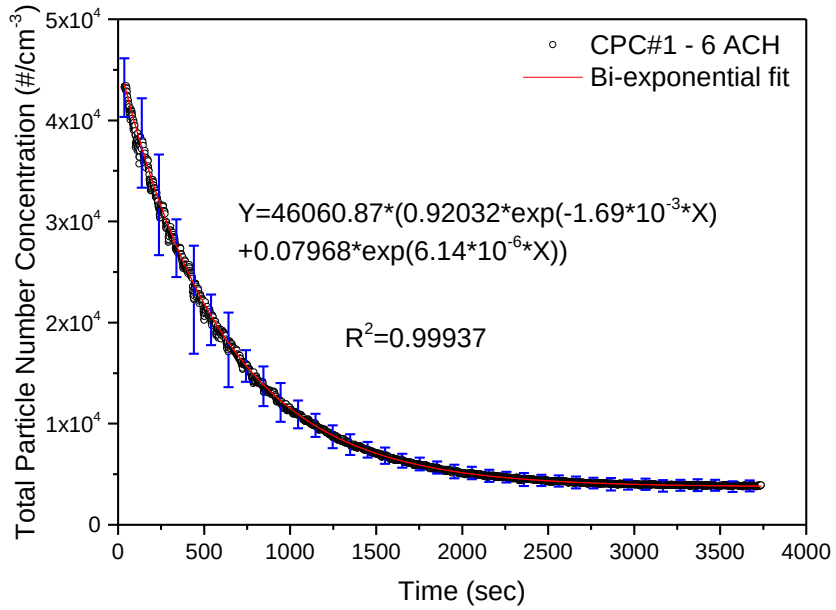

(a)

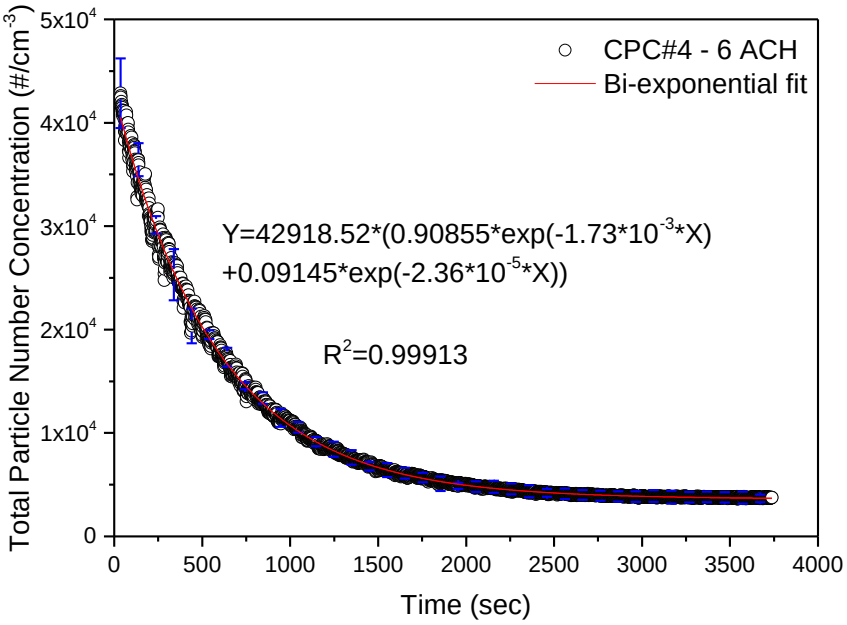

(b)

Figure 3: Bi-exponential fitting on data obtained by (a) CPC#1 and (b) CPC#4 at 6 ACH

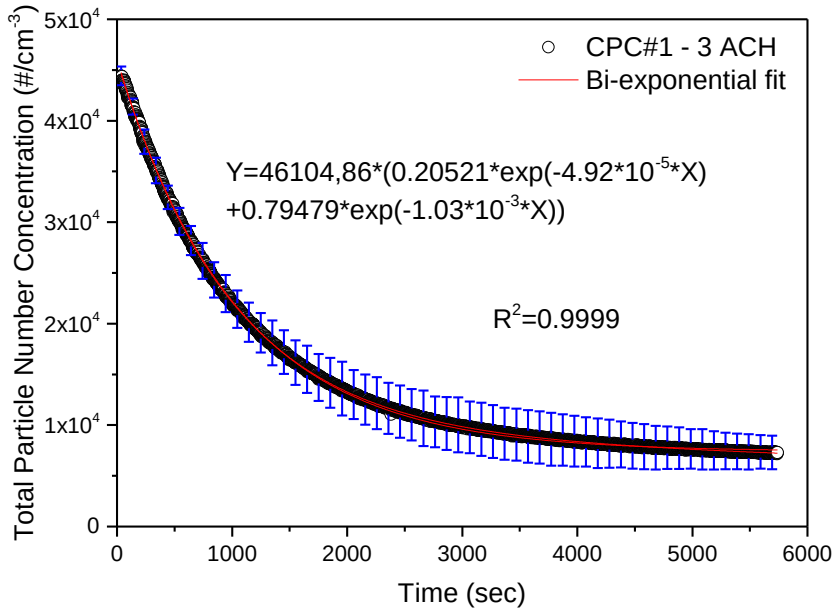

(a)

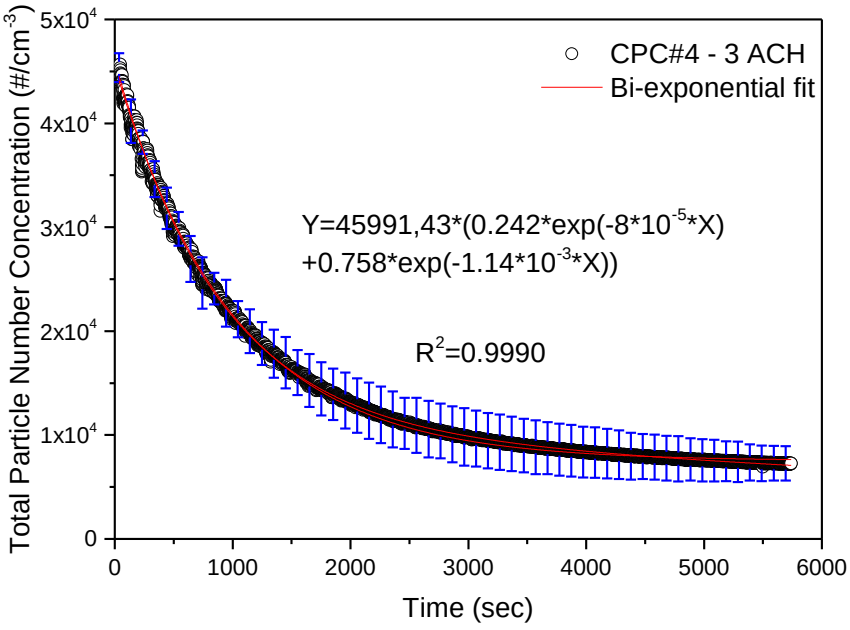

(b)

Figure 4: Bi-exponential fitting on data obtained by (a) CPC#1 and (b) CPC#4 at 3 ACH

APPENDIX B

Rmixdist Fitted Modelled Modal Parameters

Mode 1			Mode 2			Mode 3			Mode 4			Mode 5		
Weight, p	CMD, m	S.D., s	Weight, p	CMD, m	S.D., s	Weight, p	CMD, m	S.D., s	Weight, p	CMD, m	S.D., s	Weight, p	CMD, m	S.D., s
0.010077	42.17259	1.135121221	0.217795	72.56188	1.307224	0.282811	109.4093	1.538853	0.680512	154.9545	1.58127	0.012338	645.8126	1.328897
0.015779633	48.04679	1.092606056	0.193955	74.6346	1.283877	0.514452	138.2771	1.450484	0.254779	461.7313	1.432614	0.004606	797.5136	1.150749
0.024095333	52.12644	1.169808932	0.262705	86.76925	1.348146	0.663127	170.5268	1.533781	0.017398	604.5741	1.339779	0.002922	843.4476	1.140068
0.023596333	51.80268	1.157208155	0.231105	82.05285	1.336176	0.717546	168.6383	1.548899	0.016611	594.8756	1.304211	0.004365	849.866	1.164799
0.018785	51.64191	1.157923024	0.238127	84.65289	1.361471	0.707957	178.7545	1.523852	0.022456	619.879	1.339999	0.002952	833.8853	1.097956
0.017922667	51.5909	1.156984599	0.231403	84.98131	1.363637	0.713533	182.5853	1.526648	0.022656	618.7983	1.329584	0.003671	851.8462	1.137877
0.018251667	51.76685	1.156748805	0.226342	84.56613	1.36502	0.719226	185.2095	1.527047	0.024869	619.4981	1.340388	0.003314	845.4324	1.112084

Table 1: Rmixdist fitted parameters for modes 1 to 5 from fitting of TiO_2 dispersion test data averaged in consecutive 10 min intervals during the 70 min continuous injection period.

Mode 1			Mode 2			Mode 3			Mode 4			Mode 5		
Weight, p	CMD, m	S.D., s	Weight, p	CMD, m	S.D., s	Weight, p	CMD, m	S.D., s	Weight, p	CMD, m	S.D., s	Weight, p	CMD, m	S.D., s
0.023427	55.97576	1.17842	0.171621	84.33348	1.335919	0.76637	196.336	1.538757	0.03377	615.1769	1.326844	0.004812	849.1805	1.131202
0.022061	55.71857	1.178176	0.167101	83.946	1.335734	0.771111	197.2423	1.545397	0.035109	613.762	1.331435	0.004618	849.1805	1.125667
0.02304	56.4937	1.175791	0.154918	83.75293	1.323214	0.781609	197.697	1.555428	0.038016	632.4119	1.348187	0.002417	820.3515	1.043758
0.022516	56.36377	1.174981	0.149678	83.17638	1.322041	0.787496	197.2423	1.560116	0.037891	632.4119	1.347119	0.002419	810.9611	1.013512
0.021714	56.1048	1.174762	0.145739	82.79422	1.322056	0.791224	197.2423	1.563436	0.036789	619.4411	1.330516	0.004535	847.2274	1.11797
0.021942	56.62393	1.174059	0.141626	83.17638	1.317164	0.793383	196.7886	1.564372	0.040365	632.4119	1.347659	0.002683	824.1381	1.056574
0.021587	56.36377	1.174871	0.143653	83.17638	1.320049	0.792272	195.8845	1.562752	0.037516	618.0164	1.329872	0.004972	849.1805	1.123001
0.02212	56.23413	1.17598	0.149426	82.98508	1.322513	0.785678	194.9845	1.562068	0.037773	616.595	1.330761	0.005003	849.1805	1.123828
0.02043	55.84702	1.171899	0.14421	82.22426	1.320657	0.79175	191.4256	1.559517	0.04111	622.3003	1.352882	0.00251	807.235	1.002767
0.020864	55.71857	1.17303	0.144839	82.03515	1.319064	0.789056	191.4256	1.558845	0.042733	610.942	1.356863	0.002508	809.0959	1.01386
0.020287	55.46257	1.171494	0.142989	81.28305	1.316619	0.790763	190.5461	1.561781	0.043432	606.7363	1.360411	0.002529	814.7043	1.033451
0.02023	55.46257	1.167777	0.13455	80.16781	1.307254	0.80094	189.2344	1.57152	0.04181	602.5596	1.362762	0.00247	814.7043	1.032001
0.021147	53.45644	1.167293	0.125065	78.34296	1.29006	0.81408	186.2087	1.588803	0.037026	605.3409	1.353848	0.002682	829.8508	1.078127
0.021758	53.21083	1.182116	0.138615	78.88601	1.308639	0.801266	186.2087	1.591732	0.034085	597.0353	1.339708	0.004275	841.3951	1.122122
0.020857	52.36004	1.187107	0.158339	79.25013	1.325623	0.784105	183.6538	1.594263	0.034499	608.135	1.357532	0.002201	812.8305	1.022068
0.023801	52.84453	1.177118	0.162043	78.88601	1.311354	0.781059	181.5516	1.609385	0.029336	605.3409	1.330087	0.003761	843.3348	1.117789
0.02563	52.96634	1.170954	0.167115	78.88601	1.304638	0.774549	182.81	1.617559	0.028678	610.942	1.321752	0.004028	845.2788	1.120263
0.02598	55.33501	1.168181	0.1806	80.35261	1.313772	0.75731	184.5015	1.610683	0.0337	616.595	1.346697	0.00242	824.1381	1.061916
0.025356	55.08077	1.167374	0.182421	80.16781	1.314771	0.756964	184.9269	1.615177	0.031243	605.3409	1.329597	0.004016	839.46	1.116195
0.026551	55.20774	1.166595	0.181246	79.79947	1.31066	0.758171	184.0772	1.620616	0.030735	608.135	1.334197	0.003297	835.603	1.101666
0.027884	55.46257	1.169769	0.18781	80.7235	1.314861	0.749851	187.9317	1.618863	0.031799	620.869	1.338967	0.002656	829.8508	1.075177
0.027875	55.46257	1.171521	0.191129	81.09611	1.318803	0.745832	189.2344	1.616367	0.032778	626.6139	1.342703	0.002386	816.5824	1.036502
0.028056	55.46257	1.174898	0.196757	81.84648	1.3266	0.740045	193.1968	1.613021	0.032707	635.3309	1.340232	0.002435	818.4648	1.03717
0.029656	53.45644	1.187217	0.189223	80.7235	1.326295	0.74686	194.536	1.61566	0.031842	641.2096	1.33598	0.002419	818.4648	1.038771
0.027899	52.84453	1.193191	0.192019	80.7235	1.338875	0.743853	195.4339	1.609941	0.033711	642.6877	1.340078	0.002517	818.4648	1.038221
0.02629	51.76068	1.205424	0.2049	80.53784	1.361978	0.73074	196.336	1.601032	0.03547	641.2096	1.345117	0.0026	818.4648	1.034999
0.022935	50.00345	1.218176	0.232581	80.35261	1.394826	0.70497	198.1527	1.59621	0.036867	636.7955	1.348528	0.002647	818.4648	1.036907
0.021845	49.54502	1.216186	0.225287	79.06786	1.392836	0.71255	197.697	1.598306	0.037634	635.3309	1.348652	0.002684	814.7043	1.028442
0.03585	52.11947	1.249396	0.213615	81.65824	1.386437	0.707237	198.1527	1.591109	0.040379	623.7348	1.357688	0.002919	805.3784	1.000034
0.017805	46.77351	1.183475	0.224199	77.09035	1.400238	0.715367	196.7886	1.596537	0.039857	633.8697	1.349401	0.002773	809.0959	1.010478

Table 2: Rmixdist fitted parameters for modes 1 to 5 from fitting of TiO_2 dispersion test data averaged in consecutive 10 min intervals during the 5 hours period following the end of injection

Mode 1			Mode 2			Mode 3			Mode 4			Mode 5			Mode 6			Mode 7		
Weight, p	CMD, m	S.D., s	Weight, p	CMD, m	S.D., s	Weight, p	CMD, m	S.D., s	Weight, p	CMD, m	S.D., s	Weight, p	CMD, m	S.D., s	Weight, p	CMD, m	S.D., s	Weight, p	CMD, m	S.D., s
0.025252	10.62738	1.150581	0.045682	21.57639	1.194855	0.141156	36.57791	1.39726	0.15798	64.38612	1.368673	0.46061	139.198	1.553285	0.156794	491.6185	1.435625	0.018787	786.5906	1.222551
0.015329	10.64572	1.142324	0.044576	20.90825	1.213552	0.12787	32.08903	1.381744	0.163866	58.22539	1.38928	0.468928	138.9806	1.605231	0.160872	498.9678	1.420588	0.008309	859.0226	1.149507
0.01238	10.62217	1.137669	0.057327	21.71085	1.29021	0.119617	38.31847	1.503593	0.472513	99.94968	1.777429	0.129558	156.5687	1.58399	0.186222	433.1738	1.476857	0.007838	827.0034	1.123423
0.01078	13.57072	1.201639	0.042903	20.81173	1.318044	0.176145	41.39769	1.553317	0.339909	95.87488	1.620282	0.384931	176.862	1.521012	0.0397	653.3849	1.358385	0.005488	844.3591	1.086769
0.006914	13.37882	1.190327	0.044256	21.87831	1.370882	0.216202	54.28054	1.713534	0.568134	145.2063	1.984156	0.126511	183.9319	1.40682	0.03397	696.7186	1.324005	0.003894	845.7017	1.077861
0.00595	10.79758	1.190112	0.028806	20.98887	1.281332	0.157801	42.81815	1.546203	0.356104	99.50703	1.570873	0.395144	180.6479	1.512916	0.050481	652.4773	1.373642	0.005714	830.7557	1.070815
0.008589	13.69597	1.213265	0.035468	23.85761	1.31588	0.193799	55.19547	1.520943	0.462923	134.6729	1.661302	0.155829	257.6188	1.510241	0.039906	689.1713	1.333458	0.006263	845.4637	1.090378

Table 3: Rmixdist fitted parameters for modes 1 to 7 from fitting of SiO_2 dispersion test data averaged in consecutive 10 min intervals during the 70 min continuous injection period

Mode 1			Mode 2			Mode 3			Mode 4			Mode 5			Mode 6			Mode 7		
Weight, p	CMD, m	S.D., s	Weight, p	CMD, m	S.D., s	Weight, p	CMD, m	S.D., s	Weight, p	CMD, m	S.D., s	Weight, p	CMD, m	S.D., s	Weight, p	CMD, m	S.D., s	Weight, p	CMD, m	S.D., s
0.0034983	6.820243	1.312756	0.014125	20.26987	1.209292	0.047055	34.17162	1.381078	0.228992	69.24818	1.529933	0.494929	181.0074	1.536405	0.044077	652.8548	1.325412	0.0094976	849.7321	1.106305
0.0075765	15.57526	1.203067	0.014167	26.39564	1.24784	0.183251	64.76943	1.552353	0.319032	135.8565	1.697316	0.306983	184.9623	1.481423	0.049689	687.7973	1.350235	0.0053933	825.6644	1.043551
0.007475	19.47602	1.243158	0.018484	39.49154	1.217231	0.119925	59.83313	1.342777	0.24584	99.83635	1.419804	0.583962	193.2872	1.616528	0.057002	630.2339	1.356272	0.009779	821.1008	1.123926
0.0059145	18.24205	1.246875	0.010804	39.99579	1.169485	0.120518	59.84059	1.351877	0.229965	105.6457	1.38817	0.603866	182.6224	1.687648	0.061247	650.4047	1.361421	0.0098297	854.4955	1.118759
0.0051415	18.30304	1.223488	0.011082	40.53764	1.164896	0.102033	59.80395	1.323157	0.311161	107.3819	1.397102	0.792907	174.5827	1.643085	0.066954	641.3337	1.373543	0.0107473	853.9614	1.11314
0.003278	18.70861	1.168818	0.011248	40.6611	1.119879	0.038137	51.94558	1.232172	0.105932	73.4326	1.321265	0.772201	180.8771	1.604309	0.066652	618.1223	1.358757	0.0163583	863.66	1.154601
			0.004983	39.50978	1.112935	0.033402	52.45274	1.217836	0.097159	74.54974	1.311623	0.776872	182.8316	1.592877	0.072469	618.9159	1.371083	0.0151147	862.3352	1.147987
			0.002503	39.35549	1.053953	0.027904	51.72329	1.206925	0.099727	73.69561	1.30547	0.77951	184.9585	1.583437	0.074526	615.5673	1.372187	0.0158307	861.0074	1.149688
			0.00255	39.35508	1.02518	0.02357	51.96212	1.182624	0.090994	73.34097	1.289618	0.792026	186.2407	1.578652	0.075527	618.7635	1.369866	0.015334	861.6645	1.147137
			0.002349	39.49141	1.029977	0.019561	51.64603	1.179069	0.091268	73.00568	1.293486	0.795733	187.0891	1.579599	0.076453	621.1539	1.369201	0.0154193	862.9892	1.146069
			0.00221	39.62875	1.034743	0.016947	51.80908	1.169925	0.091725	73.01623	1.29501	0.795799	188.8246	1.574436	0.078131	620.6801	1.369572	0.015925	862.9892	1.146588
			0.002723	39.35501	1.009467	0.017589	52.24359	1.171765	0.099115	75.19991	1.304666	0.790653	193.6754	1.562001	0.079157	642.6834	1.36323	0.012578	847.4166	1.11186
			0.001947	42.16013	1.040404	0.023226	53.97523	1.193652	0.093014	77.20009	1.303678	0.789996	194.8572	1.55744	0.079859	642.7511	1.365164	0.0126057	843.6192	1.103891
			0.002026	42.2637	1.033475	0.022155	54.06129	1.183902	0.087658	76.04389	1.293464	0.796085	196.5423	1.54945	0.08019	643.5592	1.364203	0.012562	842.4141	1.099194
			0.02114	51.0505	1.206174	0.042586	59.78411	1.225714	0.154534	104.8467	1.373142	0.703366	204.8892	1.555205	0.081172	649.0006	1.370197	0.0112883	846.196	1.098215
			0.024527	53.08844	1.225237	0.042032	60.61581	1.230928	0.175304	109.2312	1.371985	0.684637	206.0162	1.569324	0.078948	657.4107	1.367438	0.010899	844.2884	1.090774
			0.029722	55.20774	1.25268	0.042749	61.61428	1.240503	0.204799	111.5294	1.368528	0.656109	210.929	1.586857	0.073672	659.4428	1.356912	0.0127637	857.0786	1.118615
			0.01289	49.55837	1.128849	0.045606	64.71853	1.254426	0.201575	114.5654	1.363201	0.658647	211.2822	1.591692	0.074042	664.0344	1.357791	0.0115363	855.1406	1.113149
			0.012237	49.54867	1.156725	0.044308	64.96114	1.254878	0.270154	116.9791	1.381591	0.596331	236.7703	1.604753	0.069297	666.7357	1.346533	0.0117517	847.7375	1.09242
			0.016346	51.02211	1.148021	0.057006	70.18372	1.29634	0.195001	130.9553	1.430936	0.648882	214.159	1.565215	0.078119	668.9042	1.365304	0.010095	836.4758	1.076729
			0.019232	53.27216	1.230137	0.059039	70.06034	1.290745	0.424007	154.3682	1.451199	0.442844	341.9237	1.550574	0.052802	734.2183	1.296904	0.0084893	860.3853	1.090222
			0.014112	50.81968	1.217465	0.074794	73.8069	1.322454	0.441377	178.339	1.509799	0.40905	332.3698	1.567463	0.055938	701.666	1.315917	0.0094303	851.7301	1.080554
			0.011169	47.75157	1.190565	0.066377	71.76672	1.317221	0.447313	176.356	1.533195	0.396933	284.802	1.490157	0.072091	687.0027	1.33663	0.0098393	847.4249	1.070542
			0.009552	51.27919	1.161552	0.056505	68.80586	1.300991	0.226777	152.6968	1.391735	0.671424	214.3169	1.603996	0.064283	687.5548	1.326064	0.012901	860.5918	1.110829
			0.020392	55.64938	1.199478	0.043434	70.45385	1.239582	0.455837	153.2413	1.454298	0.604238	220.7465	1.62635	0.071654	673.3672	1.348128	0.012656	857.7569	1.114518
			0.0229	56.82901	1.210377	0.044556	72.40448	1.244938	0.461451	153.1095	1.453085	0.593781	226.9695	1.623414	0.076473	693.5774	1.363575	0.0064003	817.8907	1.025158
			0.018209	53.82926	1.210388	0.063907	74.47438	1.308895	0.458032	184.6436	1.524952	0.573263	221.6174	1.620511	0.073725	674.4783	1.359206	0.0100253	843.6328	1.082763
			0.014931	52.10177	1.195345	0.060512	73.29681	1.302991	0.481852	188.209	1.512585	0.544359	194.6837	1.612753	0.071829	665.1527	1.356357	0.0129577	851.3281	1.108349
			0.014974	52.40016	1.202163	0.06151	73.9245	1.308826	0.499021	191.912	1.507395	0.522042	219.9171	1.625624	0.067151	668.7796	1.345872	0.0143003	854.0648	1.110393
			0.008735	51.24509	1.242096	0.076609	73.30747	1.336331	0.552345	174.4737	1.489384	0.685045	221.9043	1.503498	0.072115	620.6252	1.365026	0.0203982	863.66	1.156516

Table 4: Rmixdist fitted parameters for modes 1 to 7 from fitting of SiO_2 dispersion test data averaged in consecutive 10 min intervals during the 5 hours period following the end of injection.

APPENDIX C

TEM Images of TiO_2 and SiO_2 Deposited Matter

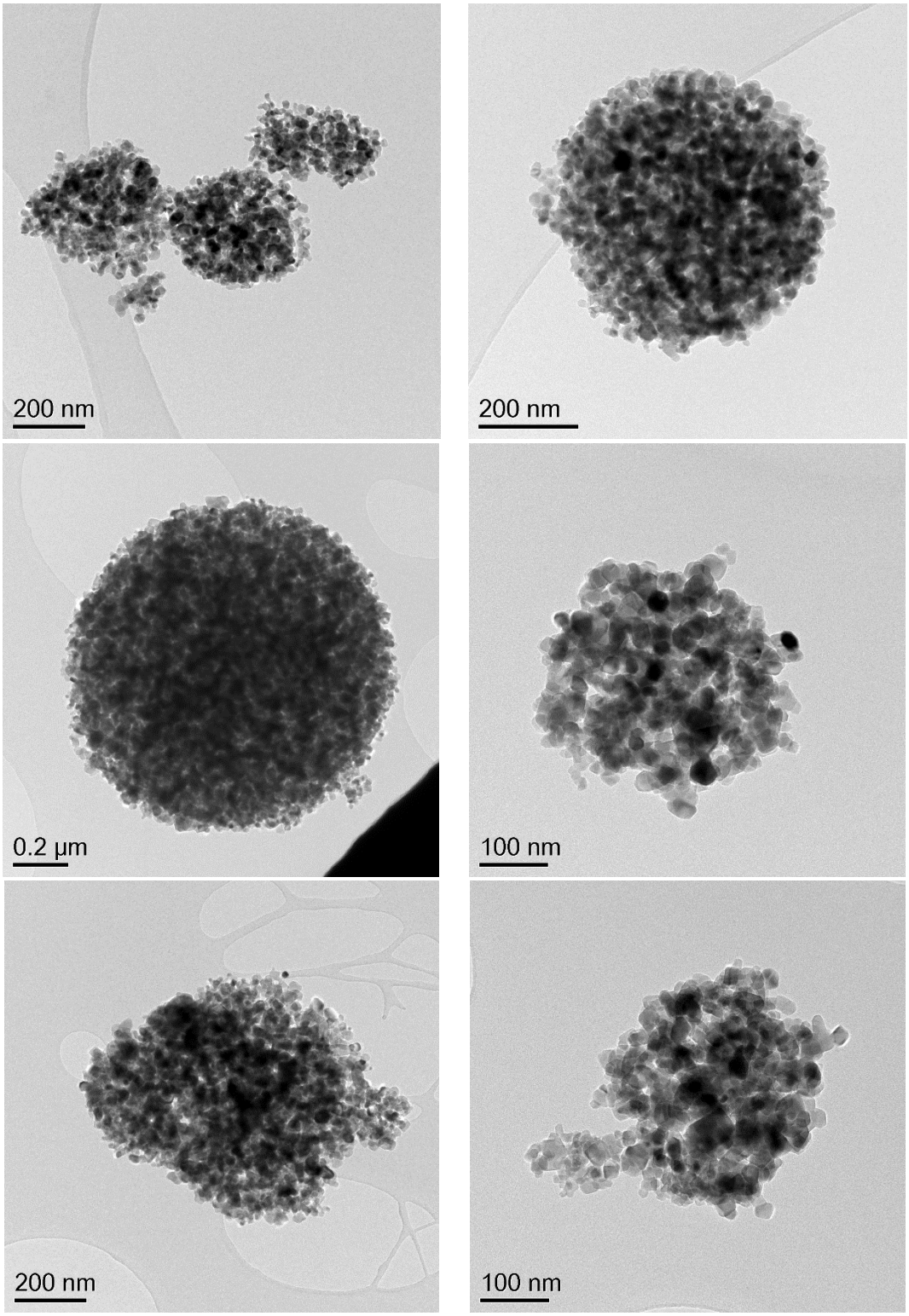

Figure 1: TEM images of TiO_2 deposited matter collected from the floor and the walls of the dispersion chamber.

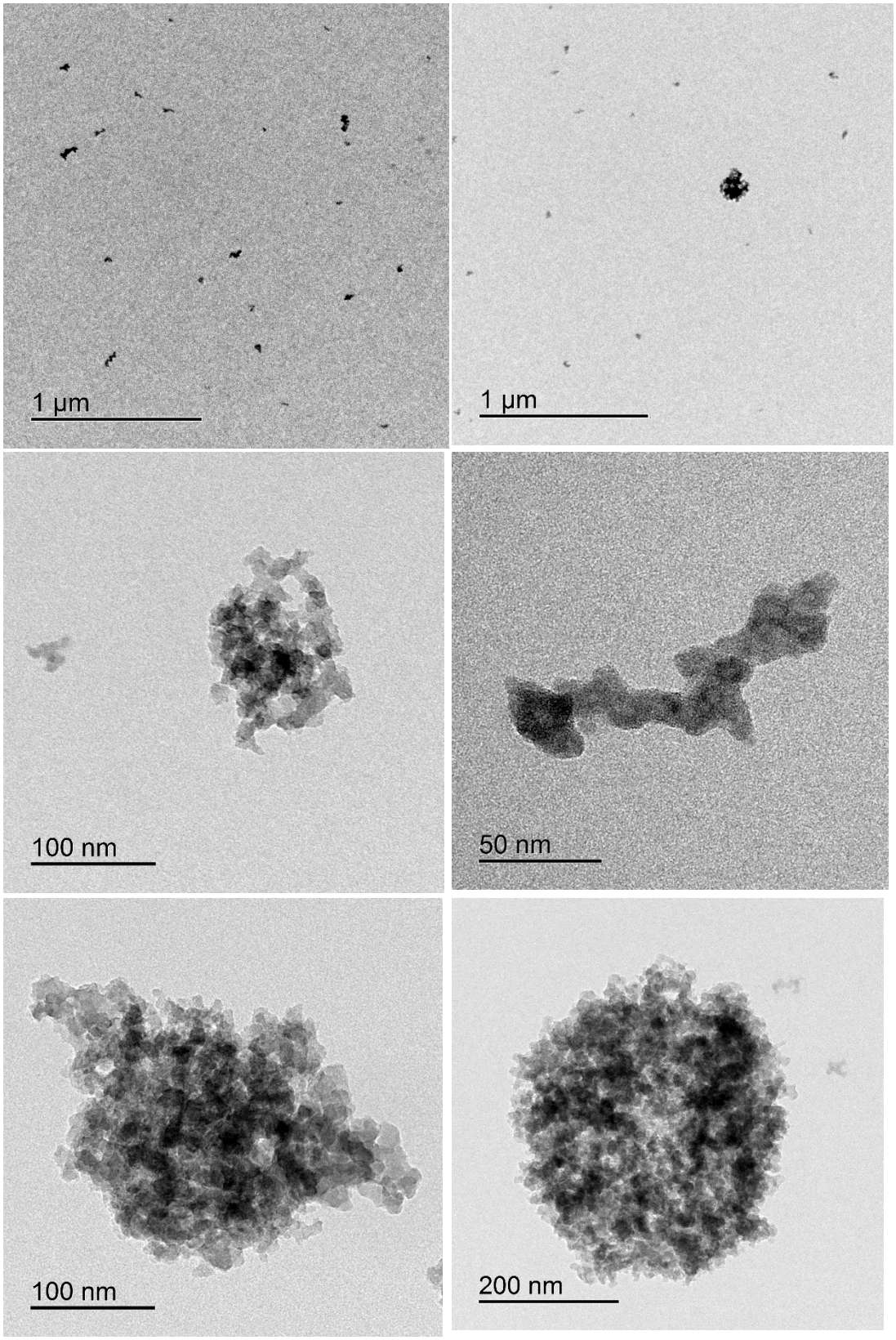

Figure 2: TEM images of SiO_2 deposited matter collected from the floor and the walls of the dispersion chambe

APPENDIX D

SEM images of CB nanopowders

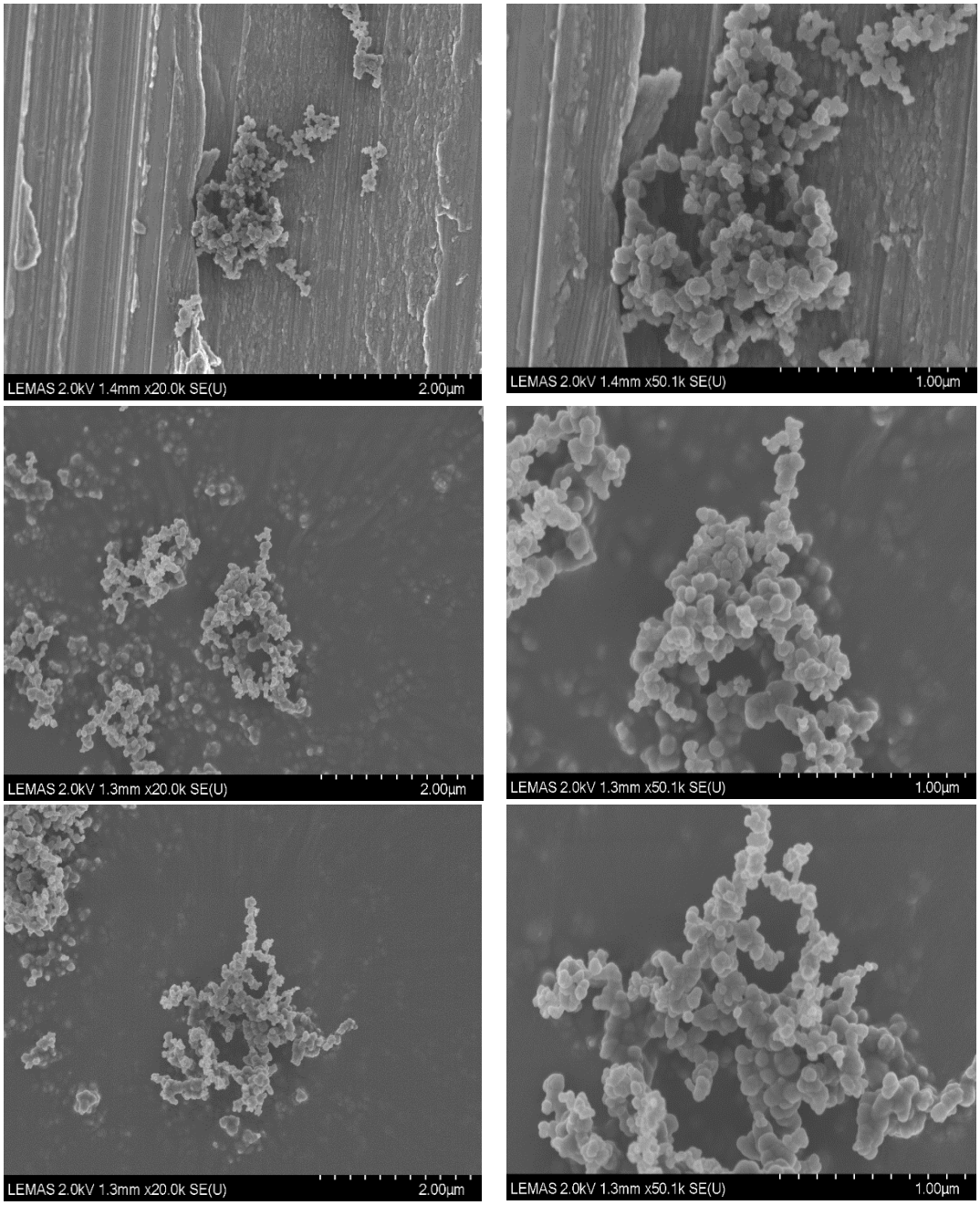

Figure 1: SEM images on Corax N550 nanopowder.

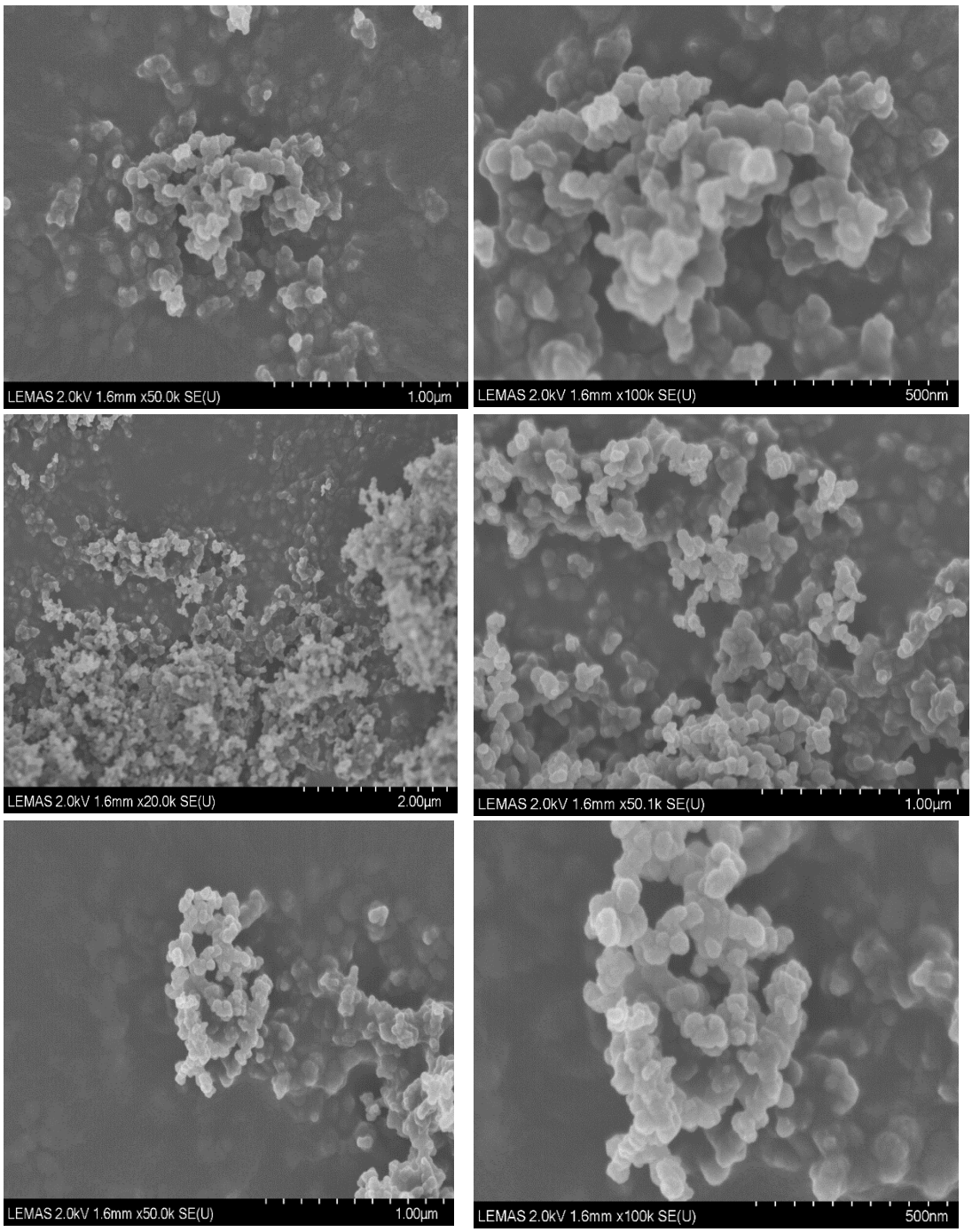

Figure 2: SEM images on Printex XE2 nanopowder.

APPENDIX E

Flame speed measurements of hybrid mixtures with φ < LFL

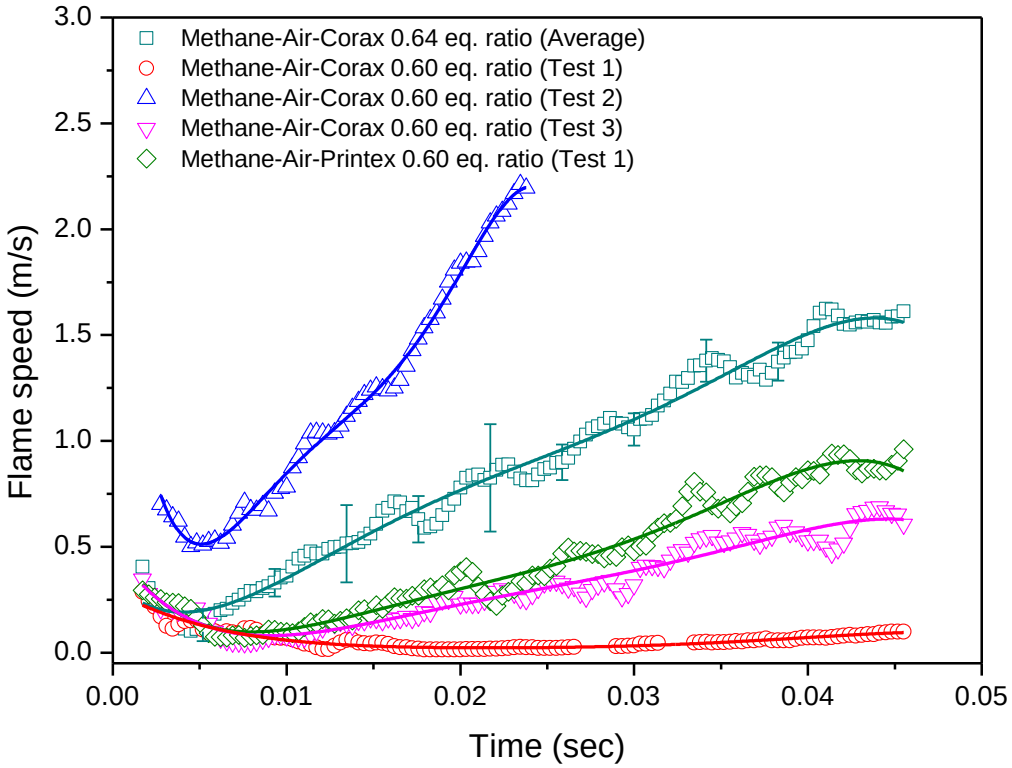

Figure 1: Flame speed variation with time of individual explosion tests of 75 g/m^3 Corax N550/37.5 g/m^3 Printex XE2-methane-air at φ=0.60 and average flame speed variation of 75 g/m^3 Corax N550 methane-air at φ=0.64 (open dots: data ± 2σ, line: polynomial fit).

REFERENCES

Abbasi, T., 2007. Dust explosions–Cases, causes, consequences, and control. *Journal of hazardous materials,* 140**,** 7-44.

ACGIH, 2013. Industrial ventilation: a manual of recommended practice for design.

Agus, E. 2008. *Size-segregated characterisation of urban airborne particulates* PhD, University of Leeds.

Amyotte, P., Chippett, S. & Pegg, M., 1988. Effects of turbulence on dust explosions. *Progress in Energy and Combustion Science,* 14**,** 293-310.

Amyotte, P., Lindsay, M., Domaratzki, R., Marchand, N., Di Benedetto, A. & Russo, P., 2010. Prevention and mitigation of dust and hybrid mixture explosions. *Process Safety Progress,* 29**,** 17-21.

Amyotte, P. R. & Eckhoff, R. K., 2010. Dust explosion causation, prevention and mitigation: An overview. *Journal of Chemical Health and Safety,* 17**,** 15-28.

Anand, S., Mayya, Ys, Yu, M, Seipenbusch, M, Kasper, G, 2012. A numerical study of coagulation of nanoparticle aerosols injected continuously into a large, well stirred chamber. *Journal of Aerosol Science,* 52**,** 18-32.

Andrews, G. & Bradley, D., 1972. Determination of burning velocities: a critical review. *Combustion and Flame,* 18**,** 133-153.

ASTM, 2010. E1226 - 10, Standard Test Method for the Explosibility of Dust Clouds. ASTM Intenrational.

Atzler, F., 1999. Fundamental studies of aerosol combustion. *PhD thesis, Dept. of Mech. Eng., University of Leeds*.

Azubel, M., Koivisto, Jaakko, Malola, Sami, Bushnell, David, Hura, Greg L, Koh, Ai Leen, Tsunoyama, Hironori, Tsukuda, Tatsuya, Pettersson, Mika, Häkkinen, Hannu, 2014. Electron microscopy of gold nanoparticles at atomic resolution. *Science,* 345**,** 909-912.

Baron, P. A., Foley, M. & Maynard, A. D., 2003. *Evaluation of aerosol release during the handling of unrefined single walled carbon nanotube material*, National Technical Information Service.

Baron, P. A. & Willeke, K., 2001. Aerosol fundamentals. *Aerosol measurement: principles, techniques, and applications*.

Beck, H., Glienke, N. & Mohlmann, C., 1997. *Combustion and Explosion Characteristicss of Dusts*, HVBG.

Bekker, C., Kuijpers, E., Brouwer, D. H., Vermeulen, R. & Fransman, W. 2015. Occupational exposure to nano-objects and their agglomerates and aggregates across various life cycle stages; a broad-scale exposure study. *Annals of Occupational Hygiene***,** mev023.

Bello, D., Wardle, Brian L, Yamamoto, Namiko, Guzman Devilloria, Roberto, Garcia, Enrique J, Hart, Anastasios J, Ahn, Kwangseog, Ellenbecker, Michael J, Hallock, Marilyn, 2009. Exposure to nanoscale particles and fibers during machining of hybrid advanced composites containing carbon nanotubes. *Journal of Nanoparticle Research,* 11**,** 231-249.

Bergström, L., 1997. Hamaker constants of inorganic materials. *Advances in Colloid and Interface Science,* 70**,** 125-169.

BGI, I. 2002. Collison Nebulizer - Instructions MRE 1, 3, 6 and 24 jet. *User Manual*

Billinge, K. 1979. The frictional ignition hazard in industry-a survey of reported incidents from 1958 to 1978. *Fire Prevention Science and Technology,* 24**,** 242-250.

Biskos, G., Schmidt-Ott, A., 2012. Airborne Engineered Nanoparticles: Potential Risks and Monitoring Challenges for Assessing their Impacts on Children. *Paediatric Respiratory Reviews,* 13**,** 79-83.

Biskos, G., Reavell, K. & Collings, N., 2005. Description and theoretical analysis of a differential mobility spectrometer. *Aerosol Science and Technology,* 39**,** 527-541.

Bissel, A., Crossley, A. , Dien, J. M., Dobson, P., Klepping, T., Vignes, A., Wehrli, V. ,Wong, K., 2008. What about explosivity and flammability of nanopowders? *(Dissemination Report DR-152-200802-2)*.

Boonruksa, P., Bello, D., Zhang, J., Isaacs, J. A., Mead, J. L. & Woskie, S. R. 2016. Characterization of potential exposures to nanoparticles and fibers during manufacturing and recycling of carbon nanotube reinforced polypropylene composites. *Annals of Occupational Hygiene,* 60**,** 40-55.

Bouillard, J., Vignes, A., Dufaud, O., Perrin, L. & Thomas, D., 2010. Ignition and explosion risks of nanopowders. *Journal of hazardous materials,* 181**,** 873-880.

Bouilly, J., Limam, K., Béghein, C. & Allard, F., 2005. Effect of ventilation strategies on particle decay rates indoors: An experimental and modelling study. *Atmospheric Environment,* 39**,** 4885-4892.

Bradley, D., Gaskell, P. & Gu, X., 1996. Burning velocities, Markstein lengths, and flame quenching for spherical methane-air flames: a computational study. *Combustion and Flame,* 104**,** 176-198.

Bradley, D., Haq, M., Hicks, R., Kitagawa, T., Lawes, M., Sheppard, C. & Woolley, R., 2003. Turbulent burning velocity, burned gas distribution, and associated flame surface definition. *Combustion and Flame,* 133**,** 415-430.

Bradley, D., Lawes, M. & Mansour, M., 2011. Correlation of turbulent burning velocities of ethanol–air, measured in a fan-stirred bomb up to 1.2 MPa. *Combustion and Flame,* 158**,** 123-138.

Bradley, D. & Lung, F. KK., 1987,"Spark ignition and the early stages of turbulent flame propagation,". *Combust. Flame,* 69**,** 71-93.

Brouwer, D., 2010. Exposure to manufactured nanoparticles in different workplaces. *Toxicology,* 269**,** 120-127.

Cambustion, 2005. "DMS500 Fast Particulate Spectrometer". *User manual, Cambustion, Cambridge*.

Cashdollar, K. L., 1993. Minimum explosible dust concentrations measured in 20-L and 1-m3 chambers. *Combustion Science and Technology,* 87**,** 157-171.

Cmbh, D. H., 1994. UP50H/UP100H Ultrasonic processors for laboratories. *Instruction manual*.

CNSI/EICN, 2008. TF20: Tecnai G2 200kV TEM (FEI). *OPERATION MANUAL for Basic TEM*.

Collings, N., Reavell, K., Hands, T., Tate, J.E., 2003. Roadside aerosol measurements with a fast particulate spectrometer. *Proceedings of the JSAE Annual Congress*.

Dahoe, A., Zevenbergen, J., Lemkowitz, S. & Scarlett, B., 1996. Dust explosions in spherical vessels: the role of flame thickness in the validity of the 'cube-root law'. *Journal of Loss Prevention in the Process Industries,* 9**,** 33-44.

Decarlo, P. F., Slowik, Jay G., Worsnop, Douglas R., Davidovits, Paul, Jimenez, Jose L., 2004. Particle morphology and density characterization by combined mobility and aerodynamic diameter measurements. Part 1: Theory. *Aerosol Science and Technology,* 38**,** 1185-1205.

Demou, E., Peter, Philippe, Hellweg, Stefanie, 2008. Exposure to manufactured nanostructured particles in an industrial pilot plant. *Annals of Occupational Hygiene,* 52**,** 695-706.

Demou, E., Stark, W. J. & Hellweg, S. 2009. Particle emission and exposure during nanoparticle synthesis in research laboratories. *Annals of Occupational Hygiene,* 53**,** 829-838.

Di Benedetto, A., Garcia-Agreda, A., Russo, P. & Sanchirico, R., 2011. Combined effect of ignition energy and initial turbulence on the explosion behavior of lean gas/dust-air mixtures. *Industrial & Engineering Chemistry Research,* 51**,** 7663-7670.

Ding, Y., Kuhlbusch, Thomas Aj, Van Tongeren, Martie, Jiménez, Araceli Sánchez, Tuinman, Ilse, Chen, Rui, Alvarez, Iñigo Larraza, Mikolajczyk, Urszula, Nickel, Carmen, Meyer, Jessica, 2016. Airborne engineered nanomaterials in the workplace—a review of release and worker exposure during nanomaterial production and handling processes. *Journal of hazardous materials*.

Dobashi, R., Risk of dust explosions of combustible nanomaterials. Journal of Physics: Conference Series, 2009. IOP Publishing, 012029.

Donnet, J.-B., 1993. *Carbon black: science and technology,* CRC Press.

Dreizin, E. L., 2009. Metal-based reactive nanomaterials. *Progress in Energy and Combustion Science,* 35**,** 141-167.

Dreizin, E. L., 2009. Metal-based reactive nanomaterials. *Progress in Energy and Combustion Science*, 35**,** 141-167.

Du, J. 2002., *Combined algorithms for constrained estimation of finite mixture distributions with grouped data and conditional data.* McMaster University.

Dufaud, O., Perrin, L. & Traore, M., 2008. Dust/vapour explosions: Hybrid behaviours. *Journal of Loss Prevention in the Process Industries,* 21**,** 481-484.

Dufaud, O., Perrin, L., Traore, M., Chazelet, S. & Thomas, D., 2009. Explosions of vapour/dust hybrid mixtures: a particular class. *Powder Technology,* 190**,** 269-273.

Dufaud, O., Vignes, A., Henry, F., Perrin, L. & Bouillard, J. Ignition and explosion of nanopowders: something new under the dust. Journal of Physics: Conference Series, 2011. IOP Publishing, 012076.

ECHA 2012. Guidance on information requirments and chemical safety assessment-Appendix R14-4: Recommendations for nanomaterials, *European Chemical Agency*.

Eckhoff, R., 2003. *Dust explosions in the process industries: identification, assessment and control of dust hazards*, Gulf professional publishing.

Eckhoff, R. K., 2009. Understanding dust explosions. The role of powder science and technology. *Journal of Loss Prevention in the Process Industries,* 22**,** 105-116.

Eckhoff, R. K. Are enhanced dust explosion hazards to be foreseen in production, processing and handling of powders consisting of nano-size particles? Journal of Physics: Conference Series, 2011. IOP Publishing, 012075.

Eckhoff, R. K., 2012. Does the dust explosion risk increase when moving from μm-particle powders to powders of nm-particles? *Journal of Loss Prevention in the Process Industries,* 25**,** 448-459.

Eisenreich, N., Lerner, M. & Vorozhtsov, A. Safety aspects and approaches to fire hazard classification of metal nanopowders. INTERNATIONAL ANNUAL CONFERENCE-FRAUNHOFER INSTITUT FUR CHEMISCHE TECHNOLOGIE, 2008. Berghausen; Fraunhofer-Institut fur Chemische Technologie; 1999.

Elder, A., Lynch, I., Grieger, K., Chan-Remillard, S., Gatti, A., Gnewuch, H., Kenawy, E., Korenstein, R., Kuhlbusch, T. & Linker, F., 2009. Human health risks of engineered nanomaterials. *Nanomaterials: Risks and benefits.* Springer.

EN-14034 2011. Determination of explosion characteristics of dust clouds - Determination of the maximum explosion pressure pmax of dust clouds. European Committee for Standardisation (CEN).

EPA, U. S. 2007. White Paper. *U.S. EPA: Washington, DC, USA, 2007*.

EPA, U. S. 2009. Exposure Factors Handbook 2009 Update (External Review Draft). *U.S. Environmental Protection Agency,* Washington, DC, EPA/600/R-09/052A.

Friedlander, S. K., 1977. Smoke, dust and haze: Fundamentals of aerosol behavior. *New York, Wiley-Interscience, 1977. 333 p.*, 1.

Gao, J., Cao, C.-S., Wang, L., Song, T.-H., Zhou, X., Yang, J. & Zhang, X., 2013. Determination of size-Dependent source emission rate of cooking-generated aerosol particles at the oilheating stage in an experimental kitchen. *Aerosol Air Qual Res,* 13**,** 488-96.

Garcia-Agreda, A., Di Benedetto, A., Russo, P., Salzano, E. & Sanchirico, R., 2011. Dust/gas mixtures explosion regimes. *Powder Technology,* 205**,** 81-86.

Giechaskiel, B., Wang, X., Horn, H.-G., Spielvogel, J., Gerhart, C., Southgate, J., Jing, L., Kasper, M., Drossinos, Y. & Krasenbrink, A., 2009. Calibration of condensation particle counters for legislated vehicle number emission measurements. *Aerosol Science and Technology,* 43**,** 1164-1173.

Gillespie, L., Lawes, M., Sheppard, C. & Woolley, R., 2000. Aspects of laminar and turbulent burning velocity relevant to SI engines. SAE Technical Paper.

Gong, L., Xu, Bin, Zhu, Yifang, 2009. Ultrafine particles deposition inside passenger vehicles. *Aerosol Science and Technology,* 43**,** 544-553.

Gu, X. J., Haq, M. Z., Lawes, M. & Woolley, R., 2000. Laminar burning velocity and Markstein lengths of methane–air mixtures. *Combustion and Flame,* 121**,** 41-58.

Hagendorfer, H., Lorenz, C., Kaegi, R., Sinnet, B., Gehrig, R., Goetz, N. V., Scheringer, M., Ludwig, C. & Ulrich, A., 2010. Size-fractionated characterization and quantification of

nanoparticle release rates from a consumer spray product containing engineered nanoparticles. *Journal of Nanoparticle Research,* 12**,** 2481-2494.

Hallock, M. F., Greenley, P., Diberardinis, L. & Kallin, D., 2009. Potential risks of nanomaterials and how to safely handle materials of uncertain toxicity. *Journal of Chemical Health and Safety,* 16**,** 16-23.

Hamelmann, F. & Schmidt, E., 2003. Methods of estimating the dustiness of industrial powders-a review. *Kona,* 21**,** 7-18.

He, C., Morawska, Lidia, Gilbert, Dale, 2005. Particle deposition rates in residential houses. *Atmospheric Environment,* 39**,** 3891-3899.

Hedmer, M., Isaxon, C., Nilsson, P. T., Ludvigsson, L., Messing, M. E., Genberg, J., Skaug, V., Bohgard, M., Tinnerberg, H. & Pagels, J. H. 2014. Exposure and emission measurements during production, purification, and functionalization of arc-discharge-produced multi-walled carbon nanotubes. *Annals of Occupational Hygiene***,** met072.

Hellweg, S., Demou, E., Bruzzi, R., Meijer, A., Rosenbaum, R. K., Huijbregts, M. A. & Mckone, T. E., 2009. Integrating human indoor air pollutant exposure within life cycle impact assessment. *Environmental science & technology,* 43**,** 1670-1679.

Hertzberg, M., Cashdollar, K. L. & Zlochower, I. A. Flammability limit measurements for dusts and gases: ignition energy requirements and pressure dependences. Symposium (international) on combustion, 1988. Elsevier, 303-313.

Hinds, W. C., 1982. Aerosol technology: properties, behavior, and measurement of airborne particles. *New York, Wiley-Interscience, 1982. 442 p.,* 1.

Hitachi, 2002. Instruction manual for Model SU8230 Field Emission Scanning Electron Microscope *Hitachi high-technology corporation.*

Howard-Reed, C., Wallace, L. A. & Emmerich, S. J., 2003. Effect of ventilation systems and air filters on decay rates of particles produced by indoor sources in an occupied townhouse. *Atmospheric Environment,* 37**,** 5295-5306.

Hristozov, D. & Malsch, I., 2009. Hazards and risks of engineered nanoparticles for the environment and human health. *Sustainability,* 1**,** 1161-1194.

Huang, Y., Risha, G. A., Yang, V. & Yetter, R. A., 2009. Effect of particle size on combustion of aluminum particle dust in air. *Combustion and Flame,* 156**,** 5-13.

Huang, C.-H., Tai, C.-Y., Huang, C.-Y., Tsai, C.-J., Chen, C.-W., Chang, C.-P. & Shih, T.-S. 2010. Measurements of respirable dust and nanoparticle concentrations in a titanium dioxide pigment production factory. *Journal of Environmental Science and Health Part A,* 45**,** 1227-1233.

Humbert, S., Marshall, J. D., Shaked, S., Spadaro, J. V., Nishioka, Y., Preiss, P., Mckone, T. E., Horvath, A., Jolliet, O., 2011. Intake fraction for particulate matter: recommendations for life cycle impact assessment. *Environmental science & technology,* 45**,** 4808-4816.

Hundy, G. F., 1969. Flame propagation in a closed vessel. *PhD thesis, Dept. of Mech. Eng., University of Leeds, 1969*.

Ibaseta, N. & Biscans, B., 2007. Ultrafine aerosol emission from the free fall of TiO_2 and SiO_2 nanopowders. *kona powder and particle journal,* 25**,** 190-204.

ISO/TS-12025 2015. Nanomaterials. Quantification of nano-object release from powders by generation of aerosols. Switzerland ISO copyright office.

Jarosinski, J., Podfilipski, J. & Pu, Y., 2000. Visualization of dust explosion under microgravity conditions. *Combustion Science and Technology,* 158**,** 183-194.

Jensen, K. A., Koponen, I. K., Clausen, P. A. & Schneider, T., 2009. Dustiness behaviour of loose and compacted Bentonite and organoclay powders: What is the difference in exposure risk? *Journal of Nanoparticle Research,* 11**,** 133-146.

John, W., 2001. *Aerosol Measurement,* Chichester, John Wiley & Sons, Inc.

Johnson, D. R., Methner, M. M., Kennedy, A. J. & Steevens, J. A., 2010. Potential for occupational exposure to engineered carbon-based nanomaterials in environmental laboratory studies. *Environmental health perspectives***,** 49-54.

Joint Research Centre, 2013. Synthetic Amorphous Silicon Dioxide (NM-200, NM-201, NM-202, NM-203, NM-204):Characterisation and Physico-Chemical Properties. *European Commission*.

King, M.-F., Noakes, C., Sleigh, P. & Camargo-Valero, M., 2013. Bioaerosol deposition in single and two-bed hospital rooms: A numerical and experimental study. *Building and Environment,* 59**,** 436-447.

Koch, W., 2003. Das dynamische Verhalten von ultrafeinen Aerosolen. *BIA-Report 7/2003***,** 89.

Koivisto, A. J., Palomäki, J. E., Viitanen, A.-K., Siivola, K. M., Koponen, I. K., Yu, M., Kanerva, T. S., Norppa, H., Alenius, H. T. & Hussein, T. 2014. Range-finding risk assessment of inhalation exposure to nanodiamonds in a laboratory environment. *International journal of environmental research and public health,* 11**,** 5382-5402.

Kosinski, P., 2011. Explosion suppression by a cloud of particles: Numerical analysis of the initial processes. *Applied Mathematics and Computation,* 217**,** 5087-5094.

Kosinski, P., Nyheim, R., Asokan, V. & Skjold, T., 2013. Explosions of carbon black and propane hybrid mixtures. *Journal of Loss Prevention in the Process Industries,* 26**,** 45-51.

Kuhlbusch, T., Neumann, S, Fissan, H., 2004. Number size distribution, mass concentration, and particle composition of PM_1, $PM_{2.5}$, and PM_{10} in bag filling areas of carbon black production. *Journal of Occupational and environmental Hygiene,* 1**,** 660-671.

Kuhlbusch, T. A., Asbach, C., Fissan, H., Göhler, D. & Stintz, M., 2011. Nanoparticle exposure at nanotechnology workplaces: a review. *Particle and Fibre Toxicology,* 8**,** 1.

Kulmala, M., Maso, M., Mäkelä, J., Pirjola, L., Väkevä, M., Aalto, P., Miikkulainen, P., Hämeri, K. & O'dowd, C., 2001. On the formation, growth and composition of nucleation mode particles. *Tellus B,* 53**,** 479-490.

Kwok, Q. S., Fouchard, R. C., Turcotte, A. M., Lightfoot, P. D., Bowes, R. & Jones, D. E., 2002. Characterization of aluminum nanopowder compositions. *Propellants, Explosives, Pyrotechnics,* 27**,** 229-240.

Kwon, O., Rozenchan, G. & Law, C., 2002. Cellular instabilities and self-acceleration of outwardly propagating spherical flames. *Proceedings of the Combustion Institute,* 29**,** 1775-1783.

Lai, A. C., 2002. Particle deposition indoors: a review. *Indoor air,* 12**,** 211-214.

Lai, A. C., Byrne, M. A. & Goddard, A. J., 2002. Experimental studies of the effect of rough surfaces and air speed on aerosol deposition in a test chamber. *Aerosol Science & Technology,* 36**,** 973-982.

Lai, A. C. & Chen, F., 2006. Modeling particle deposition and distribution in a chamber with a two-equation Reynolds-averaged Navier–Stokes model. *Journal of Aerosol Science,* 37**,** 1770-1780.

Lai, A. C. K., Nazaroff, William ,W., 2000. Modeling indoor particle deposition from turbulent flow onto smooth surfaces. *Journal of Aerosol Science,* 31**,** 463-476.

Landman, G., 1995. Ignition behaviour of hybrid mixtures of coal dust, methane, and air. *Journal of the South African Institute of Mining and Metallurgy,* 95**,** 45.

Lawes, M., 1987. Effects of turbulence on combustion in engines *PhD thesis, University of Leeds*

Lee, J. H. S., 1988. Dust Explosion Parameters, their Measurement and Use *VDI BERICHTE,* No. 701**,** 113-122.

Lee, S.-B., Lee, J.-H. & Bae, G.-N., 2010. Size response of an SMPS–APS system to commercial multi-walled carbon nanotubes. *Journal of Nanoparticle Research,* 12**,** 501-512.

Lee, J. H., Ahn, K., Kim, S. M., Jeon, K. S., Lee, J. S. & Yu, I. J. 2012. Continuous 3-day exposure assessment of workplace manufacturing silver nanoparticles. *Journal of Nanoparticle Research,* 14**,** 1-10.

Lemkowitz, S. M. & Pasman, H. J., 2014. A Review of the Fire and Explosion Hazards of Particulates. *kona powder and particle journal,* 31**,** 53-81.

Leppänen, M., Lyyränen, J., Järvelä, M., Auvinen, A., Jokiniemi, J., Pimenoff, J. & Tuomi, T., 2012. Exposure to CeO_2 nanoparticles during flame spray process. *Nanotoxicology,* 6**,** 643-651.

Leys, J., Mctainsh, G., Koen, T., Mooney, B. & Strong, C., 2005. Testing a statistical curve-fitting procedure for quantifying sediment populations within multi-modal particle-size distributions. *Earth Surface Processes and Landforms,* 30**,** 579-590.

Li, Q., Lin, B., Li, W., Zhai, C. & Zhu, C., 2011. Explosion characteristics of nano-aluminum powder–air mixtures in 20L spherical vessels. *Powder Technology,* 212**,** 303-309.

Liberman, M., Ivanov, M. & Kiverin, A., 2015. Effects of thermal radiation heat transfer on flame acceleration and transition to detonation in particle-cloud hydrogen flames. *Journal of Loss Prevention in the Process Industries,* 38**,** 176-186.

Lingard, J. J., Agus, E. L., Young, D. T., Andrews, G. E. & Tomlin, A. S., 2006. Observations of urban airborne particle number concentrations during rush-hour conditions: analysis of the number based size distributions and modal parameters. *Journal of Environmental Monitoring,* 8**,** 1203-1218.

Lüttgens, G., 2005. *Statische Elektrizität: begreifen, beherrschen, anwenden; mit 16 Tabellen*, expert-Verlag.

Macdonald, P. D. M. & Green, P. E. J., 1988. *User's guide to program MIX: an interactive program for fitting mixtures of distributions*, Hamilton, Ont.: Ichthus Data Systems.

Malvern, 2013. Zetasizer Nano series user manual. *Nano485 issue 1.1*.

Mandzy, N., Grulke, E. & Druffel, T., 2005. Breakage of TiO_2 agglomerates in electrostatically stabilized aqueous dispersions. *Powder Technology,* 160**,** 121-126.

Mansour, S., M., 2010. Study of premixed combustion rates at elevated pressure and temperature *PhD thesis, Dept. of Mech. Eng., University of Leeds*.

Mark, D., 1998. Atmospheric aerosol sampling. *Atmospheric Particles***,** 29-94.

Maynard, A. D., 2011. Don't define nanomaterials. *Nature,* 475**,** 31-31.

Maynard, A. D. & Aitken, R. J., 2007. Assessing exposure to airborne nanomaterials: current abilities and future requirements. *Nanotoxicology,* 1**,** 26-41.

Maynard, A. D., Baron, P. A., Foley, M., Shvedova, A. A., Kisin, E. R. & Castranova, V., 2004. Exposure to carbon nanotube material: aerosol release during the handling of unrefined single-walled carbon nanotube material. *Journal of Toxicology and Environmental Health, Part A,* 67**,** 87-107.

Maynard, A. D. & Kuempel, E. D., 2005. Airborne nanostructured particles and occupational health. *Journal of Nanoparticle Research,* 7**,** 587-614.

Mazzuckelli, L. F., Methner, M. M., Birch, M. E., Evans, D. E., Ku, B.-K., Crouch, K. & Hoover, M. D. 2007. Identification and characterization of potential sources of worker exposure to carbon nanofibers during polymer composite laboratory operations. *Journal of occupational and environmental hygiene,* 4**,** D125-D130.

Methner, M., 2008. Engineering case reports. Effectiveness of local exhaust ventilation (LEV) in controlling engineered nanomaterial emissions during reactor cleanout operations. *Journal of Occupational and environmental Hygiene,* 5**,** D63-9.

Methner, M., Hodson, L, Dames, a, Geraci, C., 2009. Nanoparticle emission assessment technique (NEAT) for the identification and measurement of potential inhalation exposure to engineered nanomaterials - Part B: Results from 12 field studies. *Journal of Occupational and environmental Hygiene,* 7**,** 163-176.

Methner, M. M. 2010. Effectiveness of a custom-fitted flange and local exhaust ventilation (LEV) system in controlling the release of nanoscale metal oxide particulates during reactor cleanout operations. *International journal of occupational and environmental health,* 16**,** 475-487.

Mönkkönen, P., Koponen, I., Lehtinen, K., Uma, R., Srinivasan, D., Hämeri, K. & Kulmala, M., 2004. Death of nucleation and Aitken mode particles: observations at extreme atmospheric conditions and their theoretical explanation. *Journal of Aerosol Science,* 35**,** 781-787.

Moussa, R. B., Guessasma, M., Proust, C., Saleh, K. & Fortin, J., 2015. Thermal radiation contribution to metal dust explosions. *Procedia Engineering,* 102**,** 714-721.

Nazaroff, W., 2004. Indoor particle dynamics. *Indoor air,* 14**,** 175-183.

NIOSH, 2013. Current strategies for engineering controls in nanomaterial production and downstream handling processes.

Nowack, B., Mueller, N. C., Krug, H. F. & Wick, P., 2014. How to consider engineered nanomaterials in major accident regulations. *Environmental Sciences Europe,* 26**,** 1-10.

Oberdörster, G., Celein, R. M., Ferin, J. & Weiss, B., 1995. Association of particulate air pollution and acute mortality: involvement of ultrafine particles. *Inhalation toxicology,* 7**,** 111-124.

Ogura, I., Sakurai, H. & Gamo, M. Dustiness testing of engineered nanomaterials. Journal of Physics: Conference Series, 2009. IOP Publishing, 012003.

Orion, 2012. Rubber Blacks. *Technical data Europe-Middle East-Africa*.

Ormsby, M., 2005. Turbulent flame developement in a high pressure combustion vessel. *PhD thesis, Dept. of Mech. Eng., University of Leeds*.

Ostiguy, C., 2010. *Engineered nanoparticles: current knowledge about OHS risks and prevention measures*, Institut de recherche Robert-Sauvé en santé et en sécurité du travail.

Pfefferkorn, F. E., Bello, D., Haddad, G., Park, J.-Y., Powell, M., Mccarthy, J., Bunker, K. L., Fehrenbacher, A., Jeon, Y. & Virji, M. A., 2010. Characterization of exposures to airborne nanoscale particles during friction stir welding of aluminum. *Annals of Occupational Hygiene***,** meq037.

Pilão, R., Ramalho, E. & Pinho, C., 2006. Explosibility of cork dust in methane/air mixtures. *Journal of Loss Prevention in the Process Industries*, 19**,** 17-23.

Pilão, R., Ramalho, E. & Pinho, C., 2006. Overall characterization of cork dust explosion. *Journal of hazardous materials*, 133**,** 183-195.

Plitzko, S. 2009. Workplace exposure to engineered nanoparticles. *Inhalation toxicology*, 21**,** 25-29.

Price, P., Stone, R., Collier, T., Davies, M. & Scheer, V., 2006. Dynamic particulate measurements from a DISI vehicle: a comparison of DMS500, ELPI, CPC and PASS. SAE Technical Paper.

Pritchard, D., 2004. *Literature Review: Explosion Hazards Associated with Nanopowders*, Health and Safety Laboratory.

Reavell, K., Hands, T. & Collings, N., 2002. A fast response particulate spectrometer for combustion aerosols. SAE Technical Paper.

Riley, W. J., Mckone, Thomas E, Lai, Alvin Ck., Nazaroff, William W., 2002. Indoor particulate matter of outdoor origin: importance of size-dependent removal mechanisms. *Environmental science & technology*, 36**,** 200-207.

Rim, D., Green, M., Wallace, L., Persily, A. & Choi, J.-I., 2012. Evolution of ultrafine particle size distributions following indoor episodic releases: Relative importance of coagulation, deposition and ventilation. *Aerosol Science and Technology,* 46**,** 494-503.

Santhanam, P., Hoffmann, V., Trunov, M. & Dreizin, E., 2010. Characteristics of aluminum combustion obtained from constant-volume explosion experiments. *Combustion Science and Technology,* 182**,** 904-921.

Schneider, T., Jensen, Keld A, 2009. Relevance of aerosol dynamics and dustiness for personal exposure to manufactured nanoparticles. *Journal of Nanoparticle Research,* 11**,** 1637-1650.

Schneider, T., Brouwer, Derk Henri, Koponen, Ismo Kalevi, Jensen, Keld Alstrup, Fransman, Wouter, Van Duuren-Stuurman, Birgit, Van Tongeren, Martie, Tielemans, Erik, 2011. Conceptual model for assessment of inhalation exposure to manufactured nanoparticles. *Journal of Exposure Science and Environmental Epidemiology,* 21**,** 450-463.

Schneider, T. & Jensen, K. A., 2008. Combined single-drop and rotating drum dustiness test of fine to nanosize powders using a small drum. *Annals of Occupational Hygiene,* 52**,** 23-34.

Seipenbusch, M., Binder, A., Kasper, G., 2008. Temporal evolution of nanoparticle aerosols in workplace exposure. *Annals of Occupational Hygiene,* 52**,** 707-716.

Seipenbusch, M., Yu, Mingzhou, Asbach, Christof, Rating, Uwe, Kuhlbusch, Thomas A. J., Lidén, Göran, 2014. Chapter 4 - From Source to Dose: Emission, Transport, Aerosol Dynamics and Dose Assessment for Workplace Aerosol Exposure A2 - Vogel, Ulla. *In:* Savolainen, K., Wu, Q., Tongeren, M. V., Brouwer, D. & Berges, M. (eds.) *Handbook of Nanosafety*. San Diego: Academic Press.

Skjold, T., 2003. Selected aspects of turbulence and combustion in 20-litre explosion vessels-Developement of experimental apparatus and experimental investigation. *PhD thesis*.

Stahlmecke, B., Wagener, S., Asbach, C., Kaminski, H., Fissan, H. & Kuhlbusch, T. A., 2009. Investigation of airborne nanopowder agglomerate stability in an orifice under various differential pressure conditions. *Journal of Nanoparticle Research,* 11**,** 1625-1635.

Taghiyari, H. R., 2012. Fire-retarding properties of nano-silver in solid woods. *Wood science and technology,* 46**,** 939-952.

Taurozzi, J. S., Hackley, V. A. & Wiesner, M. R., 2012. Preparation of Nanoscale TiO_2 Dispersions in an Environmental Matrix for Eco-Toxicological Assessment. *NIST Special Publication,* 1200**,** 5.

Torrado D., C. N., Pacault S., Dufour A., Glaude P., Murillo C., Dufaud O., 2016. Explosion of gas/carbon blacks nanoparticles mixtures: an approach to assess the role of soot formation. *Chemical Engineering Transactions, 48, 379-384.*

Tsai, C.-J., Lin, G.-Y., Liu, C.-N., He, C.-E. & Chen, C.-W., 2012. Characteristic of nanoparticles generated from different nano-powders by using different dispersion methods. *Journal of Nanoparticle Research,* 14**,** 1-12.

Tsai, C.-J., Liu, C.-N., Hung, S.-M., Chen, S.-C., Uang, S.-N., Cheng, Y.-S. & Zhou, Y., 2012. Novel active personal nanoparticle sampler for the exposure assessment of nanoparticles in workplaces. *Environmental science & technology,* 46**,** 4546-4552.

Tsai, C.-J., Wu, C.-H., Leu, M.-L., Chen, S.-C., Huang, C.-Y., Tsai, P.-J. & Ko, F.-H., 2009. Dustiness test of nanopowders using a standard rotating drum with a modified sampling train. *Journal of Nanoparticle Research,* 11**,** 121-131.

TSI, 2006. Model 3321, Aerodynamic Particle Sizer Spectrometer. *Operation and service manual*.

TSI, 2007. Model 3775, Condensation Particle Counter *Operation and service manual*.

Turkevich, L. A., Dastidar, A. G., Hachmeister, Z. & Lim, M., 2015. Potential explosion hazard of carbonaceous nanoparticles: Explosion parameters of selected materials. *Journal of hazardous materials,* 295**,** 97-103.

Vissotski, A. J., 2012. Developement of an experimental facility for flame speed measurements in powdered aerosols *Thesis of Master of Science, Texas A&M University*

Wallace, L. A., Emmerich, Steven J, Howard-Reed, Cynthia, 2004. Source strengths of ultrafine and fine particles due to cooking with a gas stove. *Environmental science & technology,* 38**,** 2304-2311.

Walser, T., Hellweg, S., Juraske, R., Luechinger, N. A., Wang, J. & Fierz, M., 2012. Exposure to engineered nanoparticles: model and measurements for accident situations in laboratories. *Science of the total environment,* 420**,** 119-126.

Wang, J., Asbach, C., Fissan, H., Hülser, T., Kuhlbusch, T. A., Thompson, D. & Pui, D. Y., 2011. How can nanobiotechnology oversight advance science and industry: examples from environmental, health, and safety studies of nanoparticles (nano-EHS). *Journal of Nanoparticle Research,* 13**,** 1373-1387.

Wang, Y.-F., Tsai, Perng-Jy, Chen, Chun-Wan, Chen, Da-Ren, Hsu, Der-Jen, 2010. Using a modified electrical aerosol detector to predict nanoparticle exposures to different regions of the respiratory tract for workers in a carbon black manufacturing industry. *Environmental science & technology,* 44**,** 6767-6774.

Wehner, B. & Wiedensohler, A., 2003. Long term measurements of submicrometer urban aerosols: statistical analysis for correlations with meteorological conditions and trace gases. *Atmospheric Chemistry and Physics,* 3**,** 867-879.

Worsfold, S. M., Amyotte, P. R., Khan, F. I., Dastidar, A. G. & Eckhoff, R. K., 2012. Review of the explosibility of nontraditional dusts. *Industrial & Engineering Chemistry Research,* 51**,** 7651-7655.

Wu, H.-C., Chang, R.-C. & Hsiao, H.-C., 2009. Research of minimum ignition energy for nano titanium powder and nano iron powder. *Journal of Loss Prevention in the Process Industries,* 22**,** 21-24.

Wu, H.-C., Kuo, Y.-C., Wang, Y.-H., Wu, C.-W. & Hsiao, H.-C., 2010. Study on safe air transporting velocity of nanograde aluminum, iron, and titanium. *Journal of Loss Prevention in the Process Industries,* 23**,** 308-311.

Yang, Y., Mao, P., Wang, Z.-P. & Zhang, J.-H., 2012. Distribution of nanoparticle number concentrations at a nano-TiO2 plant. *Aerosol Air Qual. Res,* 12**,** 934-940.

Yetter, R. A., Risha, G. A. & Son, S. F., 2009. Metal particle combustion and nanotechnology. *Proceedings of the Combustion Institute,* 32**,** 1819-1838.

Zhang, Z. & Chen, Q., 2006. Experimental measurements and numerical simulations of particle transport and distribution in ventilated rooms. *Atmospheric Environment,* 40**,** 3396-3408.

Zhen, G. & Leuckel, W., 1997. Effects of ignitors and turbulence on dust explosions. *Journal of Loss Prevention in the Process Industries,* 10**,** 317-324.

Zhong, K., Yang, X. & Kang, Y., 2010. Effects of ventilation strategies and source locations on indoor particle deposition. *Building and Environment,* 45**,** 655-662.

Zumwalde, R. & Hodson, L., 2009. Approaches to safe nanotechnology: managing the health and safety concerns associated with engineered nanomaterials. *National Institute for Occupational Safety and Health. NIOSH (DHHS) Publication,* 125.